Dynamics of evoked and spontaneous calcium transients in synaptic boutons of neocortical pyramidal neurons

Le Thuy Van Tran

A thesis submitted for the degree of
Doctor of Philosophy
of The Australian National University

October 2017

Except where indicated otherwise, this thesis is my own original work.

Le Thuy Van Tran

24 October 2017

Acknowledgements

I wish to thank, first and foremost, my supervisor, Christian Stricker, for his expertise, encouragement, and enthusiasm. Christian has patiently trained and supported me for 7.5 years, since I was an undergraduate student with little experience in research. He has given me the freedom to design my own projects and work in my own way, while always giving me guidance and making sure that I'm not too far off-track.

I also wish to thank my panel members, John Bekkers, Ehsan Arabzadeh, and Greg Stuart, for their helpful advice. I thank Garry Rodda for invaluable aid around the lab. I thank John McGuigan for teaching me how to make the calcium-buffer solutions and measure the resultant calcium concentrations.

Thanks also to my lab members, especially Debbie Feakes, Adrian Agahari, and Ann Go, for their support and encouragement. Many thanks to Debbie for invaluable discussions during coffee breaks and lunch time, and for proofreading this thesis.

I thank my "Micho" for his love and patience. You have always stood by me and made sure that I'm healthy and happy. I can't wait to start the next chapter of our life together in Europe.

A big thanks to my family and friends. Despite the long distance and infrequent correspondence, I can always feel your love and encouragement.

Finally, I am grateful to the ANU for funding my many years of tertiary education.

Abstract

This thesis presents a characterisation of the dynamics of evoked and spontaneous Ca^{2+} transients in synaptic boutons of neocortical pyramidal neurons.

In response to an action potential (AP), a transient rise in the intracellular Ca^{2+} concentration ($[Ca^{2+}]_i$) causes transmitter release from nerve terminals. As the spatiotemporal dynamics of this Ca^{2+} rise can affect the efficacy and plasticity of synaptic connections, it is essential to understand their determinants. To characterise factors that shape Ca^{2+} transients in neocortical synaptic boutons, layer 5 pyramidal cells in the rat somatosensory cortex were filled through the patch pipette with a fluorescent Ca^{2+} indicator for the measurement of $[Ca^{2+}]_i$.

For accurate calculation of $[Ca^{2+}]_i$ from the fluorescence intensity, the Ca^{2+} binding affinities (K_d) of the indicators were measured *in vitro*, in solutions that were similar to the patch-clamp internal solution. These solutions were made with various concentrations of $CaCl_2$, but a constant concentration of a Ca^{2+} buffer. The resultant free $[Ca^{2+}]$ was measured with a Ca^{2+}-selective macroelectrode. It was found that the K_d values of the Ca^{2+} indicators were considerably different from those previously published or provided by the manufacturers.

Two main determinants of the intracellular Ca^{2+} dynamics are the capacity of endogenous Ca^{2+} buffers and the activity of Ca^{2+} sequestration mechanisms. By measuring the peak amplitude of single AP-evoked Ca^{2+} transients with different concentrations of OGB-1 or OGB-6F, a value of 7 ± 2 was estimated for the Ca^{2+} binding ratio of endogenous buffers. Thus, in response to a single AP and in the absence of exogenous buffers, $[Ca^{2+}]_i$ was raised by 5.3 ± 1.3 μM, with a total change of ~ 50 μM. The rate constant of Ca^{2+} sequestration (0.60 ± 0.03 s^{-1}) was

estimated from the slow decay time constant of the measured transients. The initial fast decay did not prolong when intracellular Ca^{2+} uptake was inhibited, or speed up during repetitive stimulation. These findings suggest that Ca^{2+}-induced Ca^{2+} release (CICR), buffer saturation, and a non-linear Ca^{2+} transporter were not the main cause of the bi-exponential decay. A 3D model of a *bouton en passant* showed that diffusion of Ca^{2+} into the axon was likely the underlying mechanism. During high-frequency stimulation, CICR contributed to a supralinear summation of $[Ca^{2+}]_i$.

Spontaneous increases in $[Ca^{2+}]_i$ have been observed in several nerve terminals. They have been implicated in a number of cellular processes, including Ca^{2+} homeostasis and spontaneous transmitter release. Here, the high-affinity Ca^{2+} indicator OGB-1 was used to monitor small changes in $[Ca^{2+}]_i$. Spontaneous Ca^{2+} transients (sCaTs) were observed at a frequency of ~ 0.2 *per* min. The increase in $[Ca^{2+}]_i$ associated with each sCaT was $1.4 - 2.3$ μM, in the absence of exogenous buffers. As they occurred in the presence of tetrodotoxin, which inhibits AP firing, it was hypothesised that sCaTs arose from Ca^{2+} release from presynaptic stores. In support of this, caffeine increased the average frequency of sCaTs by $90 \pm 30\%$. The amplitude and kinetics of sCaTs identified in caffeine and in the control condition were not different from each other, suggesting that the majority of sCaTs might have been a result of Ca^{2+} release through ryanodine receptors. The functional consequence(s) of sCaTs in neocortical synaptic boutons remains to be determined.

Contents

List of Figures

List of Tables

Abbreviations

$[Ca^{2+}]_{AP}$	The free calcium concentration in a cell or cellular compartment after an AP
$[Ca^{2+}]_i$	The free calcium concentration in a cell, cellular compartment, or solution
$[Ca^{2+}]_{local}$	The local calcium concentration that triggers vesicle fusion
$[Ca^{2+}]_{residual}$	The spatially averaged calcium concentration that remains in a nerve terminal after an AP
$[Ca^{2+}]_{rest}$	The free calcium concentration in a cell or cellular compartment at rest
$[Ca^{2+}]_T$	The total calcium concentration in a cellular compartment or solution
[DCa]	The concentration of Ca^{2+} bound to exogenous buffers
$[D]_T$	Total concentration of exogenous buffers
[ECa]	The concentration of Ca^{2+} bound to endogenous buffers
$[E]_T$	Total concentration of endogenous buffers
$\Delta[Ca^{2+}]_{i,0}$	$\Delta[Ca^{2+}]_i$ in the absence of exogenous buffers
γ	Rate constant of Ca^{2+} sequestration
κ_D	Ca^{2+} binding ratio of exogenous buffers
κ'_D	Incremental Ca^{2+} binding ratio of exogenous buffers
κ_E	Ca^{2+} binding ratio of endogenous buffers
$\Delta F/F_0$	Relative change in fluorescence intensity of a Ca^{2+} indicator upon stimulation
$\tau_{slow,0}$	τ_{slow} of a single AP-evoked Ca^{2+} transient in the absence of exogenous buffers
D_{app}	Apparent diffusion constant of Ca^{2+}
F	Fluorescence intensity of a fluorescent dye

F_0	Fluorescence intensity of a Ca^{2+} indicator prior to stimulation
$K_{0.5}$	Half-maximal activation constant
K_d	Ca^{2+}-binding affinity or dissociation constant of a buffer or fluorescent indicator
k_{off}	Rate constant of Ca^{2+} unbinding from a buffer
k_{on}	Rate constant of Ca^{2+} binding to a buffer
PPF	Paired-pulse facilitation
R_s	Series or access resistance
R_f	Dynamic range of a fluorescent Ca^{2+} indicator
$S\left([Ca^{2+}]_i\right)$	Rate of Ca^{2+} sequestration
t_{AP}	Time of AP onset
t_d	Diffusion time
2-APB	2-Aminoethoxydiphenyl borate
ACSF	Artificial cerebrospinal fluid
AMPA	α-amino-3-hydroxy-5-methyl-4-isoxazole-propionic acid
AP	Action potential
CaM	Calmodulin
cAMP	Cyclic adenosine monophosphate
CICR	Ca^{2+}-induced Ca^{2+} release
CNS	Central nervous system
CPA	Cyclopiazonic acid
D	Exogenous Ca^{2+} buffer(s)
DG	Dentate gyrus
DMSO	Dimethyl sulfoxide
E	Endogenous Ca^{2+} buffer(s)
EC_{50}	Half-maximal effective concentration
EPP	End-plate potential
EPSC	Excitatory postsynaptic current
ER	Endoplasmic reticulum

GECIs	Genetically encoded Ca^{2+} indicators
IC_{50}	Half-maximal inhibiting concentration
iGluR	Ionotropic glutamate receptor
IP_3	Inositol 1,4,5-trisphosphate
IPSC	Inhibitory postsynaptic current
mEPP	Miniature end-plate potential
MFBs	Mossy fibre boutons
mGluR	Metabotropic glutamate receptor
mPSC	Miniature postsynaptic current
NCKX	K^+-dependent Na^+/Ca^{2+} exchanger
NCX	Na^+/Ca^{2+} exchanger
NMDA	N-methyl-D-aspartate
NMJ	Neuromuscular junction
OGB-1	Oregon Green 488 BAPTA-1
PIP_2	Phosphatidylinositol 4,5-bisphosphate
PKC	Protein kinase C
PLC	Phospholipase C
PMCA	Plasmalemmal Ca^{2+}-ATPase
PMT	Photomultiplier tube
PSC	Postsynaptic current
PTP	Post-tetanic potentiation
RIM	Rab3 interacting molecule
RRP	Readily releasable pool
SERCA	Sarco/endoplasmic reticulum Ca^{2+}-ATPase
SM protein	Sec1/Munc18-like protein
SNAP-25	Synaptosomal-associated protein 25
SNARE	Soluble NSF-attachment protein receptor
sPSC	Spontaneous postsynaptic current

SR	Sarcoplasmic reticulum
TTX	Tetrodotoxin
VDAC	Voltage-dependent anion channel
VGCC	Voltage-gated Ca^{2+} channel

Chapter 1

Introduction

1.1 Overview

The transfer of information between neurons is integral to our brain function. Neurons are one of the two main types of cells in the nervous system, the other being glial cells. They communicate with one another through highly specialised points of contact called synapses. The arrival of an action potential at a presynaptic nerve terminal results in a characteristic series of events: the opening of voltage-gated Ca^{2+} channels (VGCCs), which give rise to Ca^{2+} influx, followed by the fusion of synaptic vesicles, the release of neurotransmitter molecules into the synaptic cleft, the activation of specific receptors on the postsynaptic membrane, and finally, the diffusion and uptake of the transmitter. Therefore, the efficacy of synaptic transmission is governed by the number of readily releasable vesicles, the probability of vesicle fusion, and the response of postsynaptic receptors (amplitude and duration) to the released neurotransmitter.

Ca^{2+} is an essential second messenger in all living cells. In neurons, it plays a key role in triggering and regulating synaptic transmission. Not only does Ca^{2+} bridge an electrical stimulation with the molecular machinery that drives vesicle fusion, but it also initiates signalling cascades that enhance or depress transmitter release and the postsynaptic response. In particular, the number of readily releasable vesicles, the probability of vesicle fusion, and the kinetics of transmitter release are all regulated by Ca^{2+} (Rozov *et al.*, 2001; Bollmann and Sakmann, 2005; Wadel *et al.*, 2007; Catterall

et al., 2013). As a result, cellular mechanisms that modulate the intracellular Ca^{2+} concentration $\left([Ca^{2+}]_i\right)$ and dynamics can readily affect synaptic transmission and plasticity.

This thesis aims at characterising factors that shape Ca^{2+} dynamics in nerve terminals of neocortical pyramidal neurons. This chapter will give a background on our current understanding of transmitter release and discuss the mechanisms by which Ca^{2+} controls multiple aspects of synaptic transmission. It will then describe the main determinants of $[Ca^{2+}]_i$, before presenting the organisation of the thesis into the succeeding chapters.

1.2 Synaptic transmission

In the central nervous system (CNS), a pyramidal neuron receives $\sim$ 10,000 synaptic inputs from other neurons (Larkman, 1991). Each of these inputs, generally received along its dendritic branches, causes the membrane potential to depolarise or hyperpolarise. If they together produce a sufficiently strong membrane depolarisation, an all-or-nothing electrical response called action potential (AP) will be generated at the axon initial segment (Coombs *et al.*, 1957; Fuortes *et al.*, 1957; Palmer and Stuart, 2006). This AP will propagate along the axon to its terminals where synaptic transmission initiates.

1.2.1 The nature of synaptic transmission

By the end of the 19th century, largely owing to Ramón y Cajal's histological work on brain tissues, it was generally thought that neurons were discrete cells, connected to each other by points of contact (von Waldeyer-Hartz, 1891). However, it was unclear how information was conveyed across a synapse. For almost the first half of the 20th century, a great debate took place on whether synaptic transmission was electrical or chemical. The idea that nerve fibres, when stimulated, releases a

diffusible substance that produces postsynaptic effects was first suggested by Elliott (1905). A few decades later, Loewi, and Dale and colleagues, provided evidence for this form of transmission by the vagus nerve and at the neuromuscular junction (NMJ), respectively (Loewi, 1924; Dale, 1937). Despite these researchers' work, it remained controversial whether chemical transmission could be fast enough to produce the sub-millisecond delay between a motor nerve impulse and the onset of a muscle response (Eccles, 1990). Eccles *et al.* (1942) finally showed that the release of acetylcholine from motor nerve terminals was sufficient to cause the rapid potential change in the muscle membrane during neuromuscular transmission, thus precluding an involvement of electrical transmission at this synapse.

The introduction of microelectrodes to measure the membrane potential of nerve fibres (Hodgkin and Huxley, 1939; Graham and Gerard, 1946; Cole, 1949; Marmont, 1949), together with the use of electron microscopy to visualise neuronal connections (De Robertis and Bennett, 1955; Palay, 1956; Gray, 1959), rapidly advanced our understanding of transmission between neurons. Both chemical and electrical synapses have been observed and shown to coexist in most, if not all, nervous systems (Pereda, 2014). Key components mediating information transfer across them have also been identified. At a chemical synapse, the pre- and post-synaptic membranes are separated by a $20 - 40$ nm space called synaptic cleft (De Robertis and Bennett, 1955; Palay, 1956). Transmitter molecules are packaged in presynaptic vesicles from which they are released into the synaptic cleft. They then diffuse across the cleft and bind to receptors on the postsynaptic membrane. In contrast, at an electrical synapse, the membranes of the two communicating cells are tightly linked and their cytoplasm connected by clusters of intercellular channels (Bennett *et al.*, 1963; Bennett, 1997). These channels allow ionic currents to flow passively between the two neurons.

This thesis examines the dynamics of the intracellular Ca^{2+} rise associated with neurotransmitter release. The axon terminals studied are known to form chemical synapses onto the dendrites of surrounding neurons (Palay, 1956; Gray, 1959; Markram *et al.*, 1997; Frick *et al.*, 2008). Therefore, from here onwards, unless

otherwise stated, the term synaptic transmission will be used to refer to chemical transmission.

1.2.2 The vesicular hypothesis

Through a series of seminal experiments, Del Castillo and Katz (1954) provided some of our first understanding of the mechanisms underlying transmitter release. They measured miniature end-plate potentials (mEPPs), which occurred randomly at the NMJ in the absence of any stimulation, and compared them to evoked end-plate potentials (EPPs) measured in a low Ca^{2+} external medium. By doing so, they found that the amplitudes of mEPPs were normally distributed, whereas the amplitudes of evoked EPPs displayed a quantised distribution whose peaks were integer multiples of the mean mEPP amplitude. This finding led to the suggestions that transmitter molecules are released in discrete multi-molecular packets, termed quanta, and that the mEPP represents the postsynaptic response to the release of a single quantum. A year later, based on electron microscopic observation of small vesicles inside the motor nerve terminal (Robertson, 1956), Del Castillo and Katz (1955) put forward the vesicular hypothesis, which provides a structural conception for the transmitter quantum. According to this hypothesis, transmitter molecules are packaged in subcellular vesicles from which they are released into the synaptic cleft in an all-or-nothing manner. Thus, the size of a quantum, thereby the amplitude of a mEPP, is determined by the transmitter content of a synaptic vesicle.

Among the first key works in favour of the vesicular hypothesis is a biochemical study showing that synaptic vesicles isolated from the electric organ of *Torpedo* contained a large amount of acetylcholine (Israel *et al.*, 1968). Subsequently, images of synaptic vesicles undergoing stimulation-induced exocytosis were captured in a study that used rapid-freezing techniques in combination with electron microscopy (Heuser *et al.*, 1979). The same study reported a 1:1 relationship between the number of vesicle openings on the presynaptic membrane and the number of released quanta estimated from the postsynaptic response. This supports the idea that a

synaptic vesicle corresponds to a transmitter quantum. Furthermore, recent advances in molecular and genetic techniques have led to the discovery that numerous presynaptic proteins, involved in the trafficking and exocytosis of synaptic vesicles, play an important role in synaptic transmission (Sudhof, 2014). Together, these studies have made the vesicular origin of transmitter release a wide consensus.

The vesicular hypothesis has also received support from electrophysiological studies. A prediction of this hypothesis is that, upon vesicle fusion, the total surface area of the presynaptic membrane will increase, as a result of the vesicle membrane being added to it. Such a change can be tracked by measuring the cell membrane capacitance. Membrane capacitance measurement was first developed by Neher and Marty (1982) to monitor vesicle exocytosis and endocytosis in adrenal chromaffin cells. This technique was later adopted by Sun and Wu (2001), who measured vesicle fusion in response to membrane depolarisation in a large CNS synapse - the calyx of Held. This study elegantly demonstrated a linear relationship between the increase in the presynaptic membrane capacitance and the amplitude of the postsynaptic response, lending further support to the vesicular hypothesis.

1.2.3 Modes of transmitter release

There are three kinetically distinct forms of neurotransmitter release: synchronous, asynchronous, and spontaneous (Fig. 1.1). Both synchronous and asynchronous forms of release result from AP firing (*i.e.* evoked release). However, the former occurs within a few milliseconds, whilst the latter persists for tens of milliseconds to tens of seconds after stimulation. Spontaneous release, on the other hand, occurs in the absence of presynaptic APs.

1.2.3.1 Spontaneous release

Spontaneous transmitter release was first described by Fatt and Katz (1950) at the frog NMJ. Since then, it has been observed in numerous synapses in the

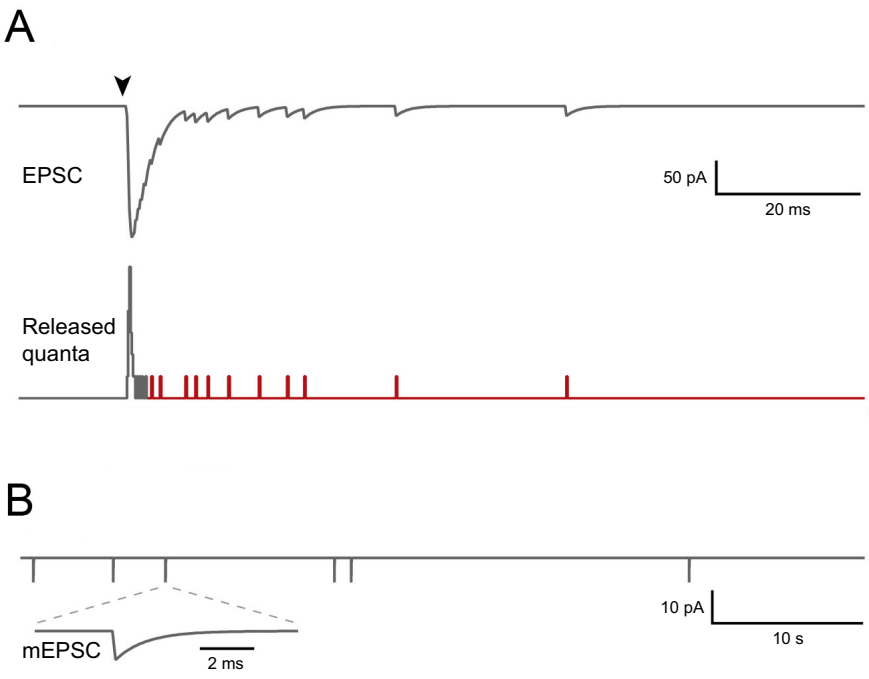

Figure 1.1: Three modes of transmitter release illustrated with simulated data. (A) Top: Stimulation (arrowhead) evokes an excitatory postsynaptic current (EPSC). Bottom: Deconvolution of this current yields the number of released quanta, which reflect two components of release: synchronous (grey) and asynchronous (red). (B) Spontaneous release occurs independently of stimulation, producing miniature inhibitory or excitatory postsynaptic currents (here, mEPSCs). Adapted from Kaeser and Regehr (2014).

CNS. Spontaneous miniature postsynaptic currents/potentials measured in central neurons were initially thought to arise from the continual firing of presynaptic cells in the absence of stimulation (Brock *et al.*, 1952; Hubbard *et al.*, 1967). However, experiments using the voltage-gated Na^+ channel blocker tetrodotoxin (TTX) demonstrated that these miniature currents/potentials were independent of AP firing (Blankenship and Kuno, 1968; Colomo and Erulkar, 1968).

On a per-synapse basis, spontaneous transmitter release occurs at a rather low frequency of 0.01 to 0.1 Hz (Geppert *et al.*, 1994; Frerking *et al.*, 1997; Murthy and Stevens, 1999). Despite this, it has been implicated in a range of physiological processes, including neuronal excitability (Otis *et al.*, 1991; Kombian *et al.*, 2000; Carter and Regehr, 2002), synaptic formation and maintenance (McKinney *et al.*,

1999; Tyler and Pozzo-Miller, 2003; Choi *et al.*, 2014), inhibition of dendritic protein synthesis (Sutton *et al.*, 2004, 2006), and synaptic and homeostatic plasticity (Frank *et al.*, 2006; Lee *et al.*, 2010; Reese and Kavalali, 2015).

1.2.3.2 Synchronous release

Of the three forms of transmitter release, synchronous release is the most extensively studied due to its principal role in fast synaptic transmission. It is also the primary form of release at low-frequency stimulation at most synapses (> 90%; Kaeser and Regehr, 2014). The synchronisation of quantal release evoked by an AP was first revealed by Katz and Miledi (1965b) at the NMJ. By counting the released quanta and measuring their latencies in a low Ca^{2+} external medium, Katz & Miledi showed that transmitter release initiated within a few hundred microseconds of an AP, and that most transmitter quanta were released within the first millisecond.

Unfortunately, the method of counting quanta can only be used when the rate of transmitter release is low, often in non-physiological conditions. To determine the kinetics of transmitter release at synapses with high release rates, a method that involves deconvolution of the evoked postsynaptic current (PSC) with the miniature postsynaptic current (mPSC) was developed by Van der Kloot (1988a,b). Consistent with Katz and Miledi's original observation, this method has demonstrated a high degree of synchrony of AP-evoked transmitter release at a variety of central synapses (Schneggenburger and Neher, 2000; Hefft and Jonas, 2005; Sakaba, 2008; Daw *et al.*, 2009). In fact, following an AP, the rate of transmitter release reaches a peak $10^5 - 10^6$ fold higher than the spontaneous release rate (Lou *et al.*, 2005).

1.2.3.3 Asynchronous release

Asynchronous release can be prominent at some synapses, even after a single AP (Barrett and Stevens, 1972; Iremonger and Bains, 2007; Best and Regehr, 2009). However, for most synapses, this form of transmitter release only becomes apparent

after prolonged moderate- to high-frequency stimulation (Lu and Trussell, 2000; Daw *et al.*, 2009). Unlike its synchronous counterpart, asynchronous transmission is characterised by a period of delayed and desynchronised transmitter release that persists for tens of milliseconds or more after presynaptic membrane depolarisation (Fig. 1.1A). Such persistence makes it ideal for providing sustained modulation of neuronal excitability (Iremonger and Bains, 2007) and network synchrony (Manseau *et al.*, 2010).

1.2.4 Processes underlying synaptic transmission

Neurotransmitters can be broadly divided into two groups: small molecule transmitters (acetylcholine, amino acids, biogenic amines, and gaseous molecules) and neuropeptides. Neocortical pyramidal neurons, which are studied in this thesis, release the amino acid glutamate. They are not known to release neuropeptides. Therefore, this section will only describe processes underlying the release of glutamate into the synaptic cleft (Fig. 1.2).

1.2.4.1 Neurotransmitter synthesis

The main precursor of glutamate is glutamine, which is synthesised in a type of glial cell called astrocytes. Once produced, glutamine is released into the extracellular space for uptake into neurons (Schousboe *et al.*, 2013). In the presynaptic nerve terminals, glutamine is converted to glutamate by the mitochondrial enzyme glutaminase. Glutamate can also be synthesised within the nerve terminals by transamination of α-ketoglutarate, an intermediate of the Krebs cycle (Schousboe *et al.*, 2013).

1.2.4.2 Loading of transmitters into vesicles

Loading of neurotransmitters into synaptic vesicles ($\sim$ 40 nm in diameter) is an active process, energised by the vacuolar H^+-ATPase (Edwards, 2007). This proton pump

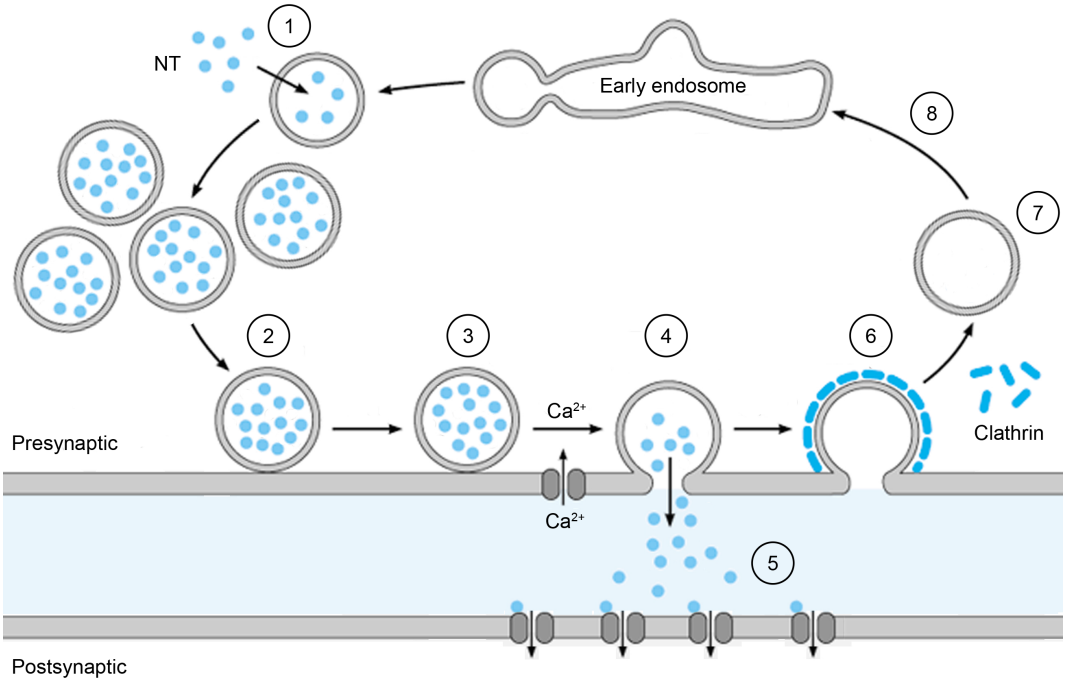

Figure 1.2: Processes underlying synaptic transmission. Step 1: Neurotransmitter molecules (NT) are packaged into synaptic vesicles in the presynaptic terminal. Step 2: Synaptic vesicles are docked at the active zone. Step 3: Docked vesicles are primed to become release-competent. Step 4: Ca^{2+} influx during an AP triggers fusion of docked and primed vesicles. Step 5: Released NT diffuses across the synaptic cleft and binds to postsynaptic receptors. Step 6: Synaptic vesicles are retrieved from the presynaptic membrane by clathrin-mediated endocytosis. Step 7: The new vesicles lose their clathrin coats. Step 8: Vesicles are trafficked to an intermediate endosomal compartment. Adapted from Sudhof (1995).

uses energy released from ATP hydrolysis to transport H^+ into synaptic vesicles. The generated H^+ electrochemical gradient across the vesicle membrane, in turn, enables the vesicular glutamate transporter to transport glutamate into synaptic vesicles (Fig. 1.2, step 1).

1.2.4.3 Vesicle docking, priming, and fusion

In many axon terminals, synaptic vesicles are thought to reside in three functionally distinct pools: a readily releasable pool (RRP), a recycling pool, and a reserve pool (Rizzoli and Betz, 2005). As its name suggests, the RRP constitutes vesicles that are

immediately available to release upon stimulation. It is essential to the speed and synchronicity of evoked transmitter release (Kaeser and Regehr, 2014).

It is generally accepted that, in order to become readily releasable, vesicles need to be "docked" and "primed" (Fig. 1.2, steps 2 and 3, respectively; Rizzoli and Betz, 2005). Docking places vesicles close to the presynaptic membrane, near sites of transmitter release called active zones. Priming then renders docked vesicles competent to fuse with the plasma membrane upon stimulation. During high frequency stimulation, vesicles might enter the primed state without being docked to speed up the replenishment of readily releasable vesicles and sustain transmission (Saviane and Silver, 2006; Verhage and Sorensen, 2008).

The arrival of an AP at the presynaptic terminal activates VGCCs, the opening of which produces an influx of Ca^{2+} into the terminal. The resultant intracellular Ca^{2+} rise causes readily releasable vesicles to fuse with the plasma membrane, releasing neurotransmitters into the synaptic cleft (Fig. 1.2, step 4). As lipid-lipid interactions are the slowest chemical reactions, specific interactions between proteins, and between them and membrane lipids, are required to speed up the process of vesicle fusion. Among the most important proteins are soluble NSF-attachment protein receptors (SNAREs), Sec1/Munc18-like (SM) proteins, synaptotagmins, and Rab3 interacting molecules (RIMs).

SNAREs - the "minimal" fusion machinery. SNAREs are membrane proteins, classified as v-SNAREs if they are expressed on a transport vesicle or t-SNAREs if they are on a target membrane (Malsam *et al.*, 2008). The predominant SNARE proteins in presynaptic terminals are the two t-SNAREs syntaxin-1 and synaptosomal-associated protein 25 (SNAP-25), and the v-SNARE synaptobrevin (also referred to as VAMP; Jahn and Fasshauer, 2012). Like all SNAREs, their cytoplasmic regions contain a conserved 60- to 70-amino acid sequence called the SNARE motif. Fusion of synaptic vesicles occurs when the SNARE motifs of these three SNAREs associate to form a tight bundle of four parallel α-helices, with two

from SNAP-25 and one from either syntaxin-1 or synaptobrevin (Sutton *et al.*, 1998; Stein *et al.*, 2009). As this assembly progresses from the N-termini to the C-termini of the SNAREs ("zippering"), the vesicle and presynaptic membranes are brought into close proximity, promoting their fusion. The energy that is released during SNARE complex formation is thought to fuel membrane fusion (Li *et al.*, 2007a; Wiederhold and Fasshauer, 2009).

An experiment in which cognate v- and t-SNAREs were reconstituted into artificial lipid bilayers showed that they were both necessary and sufficient for membrane fusion (Weber *et al.*, 1998). Consistently, cells with "flipped" SNAREs expressed on their surfaces were found to merge spontaneously (Hu *et al.*, 2003). However, not only was membrane fusion observed in these early experiments Ca^{2+}-independent, but it also occurred at a rate much slower than that required for efficient synaptic transmission. Therefore, besides SNAREs, presynaptic terminals contain other components that regulate vesicle fusion in a Ca^{2+}-dependent manner, facilitate SNARE complex formation, and increase the efficiency of membrane merging upon stimulation (Malsam *et al.*, 2008).

Synaptotagmins - Ca^{2+} sensors. In presynaptic terminals as well as many secretory cells, vesicle fusion is triggered by Ca^{2+} binding to synaptotagmins. Four members of the synaptotagmin family have been found to function as Ca^{2+} sensors for transmitter release. Syt1, Syt2, and Syt9 are primarily localised on synaptic vesicles and responsible for synchronous release (Fernandez-Chacon *et al.*, 2001; Takamori *et al.*, 2006; Sun *et al.*, 2007; Xu *et al.*, 2007), whilst Syt7, which is mainly found on the plasma membrane of neurons, mediates asynchronous transmission (Sugita *et al.*, 2001; Bacaj *et al.*, 2013). Each of these synaptotagmins has two cytoplasmic C2 domains - C2A and C2B, to which two or three Ca^{2+} ions can bind (Perin *et al.*, 1990; Brose *et al.*, 1992). Among the Ca^{2+} sensors for synchronous release, Syt2 mediates release with the fastest kinetics whereas release induced by Syt9 has the slowest rise time (Xu *et al.*, 2007). Syt1, Syt2, and Syt9 are also expressed in different regions of the nervous system (Xu *et al.*, 2007).

Despite many years of research, it remains elusive how Ca^{2+} binding to synaptotagmins triggers vesicle fusion (Chapman, 2008; Jahn and Fasshauer, 2012). A number of studies have illustrated that Ca^{2+}-triggered membrane fusion requires Ca^{2+}-dependent binding of synaptotagmins to SNARE proteins and membrane phospholipids (Zhang *et al.*, 2002; Bhalla *et al.*, 2006; Pang *et al.*, 2006). The interaction between synaptotagmins and anionic phospholipids is primarily electrostatic (Jahn and Fasshauer, 2012). Thus, it occurs at different binding sites on Ca^{2+}-free and Ca^{2+}-bound synaptotagmins (van den Bogaart *et al.*, 2011). It has been proposed that the binding of Ca^{2+}-bound synaptotagmins to plasma membrane anionic phospholipids pulls the vesicle and presynaptic membranes very close together, thereby promoting vesicle fusion (van den Bogaart *et al.*, 2011). At the same time, upon binding of Ca^{2+}-bound synaptotagmins, SNARE proteins might undergo rearrangements that render the SNARE complex fusion-competent (Chapman, 2008).

SM proteins - regulators of the "minimal" fusion machinery. The main SM protein in vertebrate synapses - Munc18-1 - engages in two distinct interactions with SNARE proteins, particularly with syntaxin-1 (Sudhof, 2014). Besides a SNARE motif, syntaxin-1 contains a large N-terminal region that occupies $\sim$ 60% of its total sequence (Misura *et al.*, 2000). This N-terminal region consists of two protein motifs: a short N-terminal peptide called N-peptide, and a larger H_{abc} domain which autonomously forms a three-helix bundle. Prior to SNARE complex formation, syntaxin-1 exists in a closed conformation, in which the H_{abc} domain folds back onto the SNARE motif, making the latter inaccessible to other SNAREs (Dulubova *et al.*, 1999; Misura *et al.*, 2000). Munc18-1 binds to this closed conformation at the H_{abc} domain of syntaxin-1, independently of the syntaxin-1 N-peptide (Hata *et al.*, 1993; Dulubova *et al.*, 1999; Misura *et al.*, 2000). When syntaxin-1 opens to expose its SNARE motif to interaction with other SNAREs, Munc18-1, while remaining attached to syntaxin-1, binds to the N-peptide of syntaxin-1 and the four-helix bundle of the SNARE complex (Dulubova *et al.*, 2007; Hu *et al.*, 2007; Rickman *et al.*, 2007).

Both of these distinct interactions between Munc18-1 and SNARE proteins have been

suggested to perform multiple functions in transmitter release. Binding of Munc18-1 to the closed conformation of syntaxin-1 stabilises the expression of both proteins on the plasma membrane, thereby regulating vesicle priming and the size of the RRP (Gulyas-Kovacs *et al.*, 2007; Gerber *et al.*, 2008; Zhou *et al.*, 2013). It has also been shown to prevent ectopic or premature formation of SNARE complexes, and negatively modulate the rate of vesicle fusion (Medine *et al.*, 2007; Burkhardt *et al.*, 2008; Gerber *et al.*, 2008). On the other hand, binding of Munc18-1 to the open conformation of syntaxin-1 appears to facilitate SNARE protein assembly and speed up membrane fusion (Gulyas-Kovacs *et al.*, 2007; Shen *et al.*, 2007; Burkhardt *et al.*, 2008; Rodkey *et al.*, 2008; Diao *et al.*, 2010; Zhou *et al.*, 2013).

RIMs - coupling the Ca^{2+} signal to the fusion machinery. RIMs are central active zone proteins. They recruit not only synaptic vesicles but also VGCCs to the active zone, thereby reducing the diffusional distance of Ca^{2+} and ensuring the speed of transmitter release (Sudhof, 2013). RIMs participate in vesicle docking by binding to the small GTPase Rab3, the membrane-bound form of which is densely expressed on synaptic vesicles (Fischer von Mollard *et al.*, 1990). At the same time, RIMs, together with their binding proteins, bind directly to P/Q- and N-type VGCCs (Kaeser *et al.*, 2011; Han *et al.*, 2011; Kaeser *et al.*, 2012). Thus, at calyxes of Held where all RIM isoforms were conditionally removed, a reduction in the number of docked vesicles was paralleled by a decrease in the expression of VGCCs in the presynaptic membrane (Kaeser *et al.*, 2011; Han *et al.*, 2011). The presynaptic Ca^{2+} current density and the coupling between VGCCs and synaptic vesicles were also reduced.

Classic model of Ca^{2+}-triggered vesicle fusion. According to a widely accepted model, SNARE/SM complexes are partially assembled during vesicle priming, with full zippering prevented by an energy barrier and/or an interfering protein, most likely complexin and/or synaptotagmin (Jahn and Fasshauer, 2012; Sudhof, 2013, 2014). When $[Ca^{2+}]_i$ rises during an AP, binding of Ca^{2+} to synaptotagmin causes synaptotagmin to bind to plasma membrane phospholipids, change its interaction

with SNARE/SM complexes, and displace complexin. The subsequent formation of a fusion pore is thought to result from the binding of synaptotagmin to plasma membrane phospholipids, although exactly how it occurs remains unknown (Jahn and Fasshauer, 2012; Sudhof, 2014).

1.2.4.4 Neurotransmitter actions

After being released, neurotransmitters diffuse across the synaptic cleft and bind to receptors expressed on the postsynaptic membrane (Fig. 1.2, step 5). Neurotransmitter receptors can be divided into two main groups: ionotropic and metabotropic (Eccles and McGeer, 1979).

Ionotropic receptors are ligand-gated ion channels which open upon neurotransmitter binding and allow the passage of ions. The resultant ionic current could be either excitatory or inhibitory, depending on the ion selectivity of the channels and the electrochemical gradient across the postsynaptic membrane. Excitatory postsynaptic currents (EPSCs) depolarise the membrane potential and thus bring it closer to the AP threshold, whilst inhibitory postsynaptic currents (IPSCs) generally reduce AP firing. Ionotropic glutamate receptors (iGluRs) are non-selective cation channels, the activation of which under physiological conditions produces EPSCs. iGluRs can be further categorised into three major subtypes, named after their selective agonists: α-amino-3-hydroxy-5-methyl-4-isoxazole-propionic acid (AMPA), N-methyl-D-aspartate (NMDA), and kainate (Mayer, 2005).

In general, metabotropic receptors are G-protein coupled receptors, the activation of which initiates second messenger cascades that result in channel opening/closing and/or other cellular effects. Each functional metabotropic glutamate receptor (mGluR) is a homodimer, composed of members of three distinct groups (Niswender and Conn, 2010). Group I mGluRs are coupled to $G_{q/11}$ proteins; their activation promotes hydrolysis of the membrane lipid phosphatidylinositol 4,5-bisphosphate (PIP_2). Group II/III mGluRs are coupled to $G_{i/o}$ proteins; their activation inhibits the production of cyclic adenosine monophosphate (cAMP).

1.2.4.5 Neurotransmitter clearance

For synaptic transmission to be efficient and have a high signal-to-noise ratio, the concentration of neurotransmitters in the synaptic cleft has be to tightly controlled. The removal of glutamate occurs through two processes. First, it can simply diffuse away from the cleft (Clements, 1996; Rusakov and Kullmann, 1998). Second, unbound glutamate molecules are rapidly taken up by the excitatory amino acid transporter (Takahashi *et al.*, 1997). Although this transporter is expressed on presynaptic membranes, its distribution is much more dense on the surface of astrocytic processes that wrap tightly around synapses (Zhou and Danbolt, 2013).

1.2.4.6 Vesicle endocytosis and recycling

To sustain synaptic transmission, particularly during repetitive stimulation, presynaptic terminals must be able to efficiently retrieve synaptic vesicles from the presynaptic membranes. Vesicle endocytosis occurs in two alternative pathways, depending on whether vesicles fully collapse or only "kiss" the presynaptic membranes during transmitter release. A fully fused vesicle has to be retrieved by clathrin-mediated endocytosis (Fig. 1.2, step 6). However, if only a transient, nanometer-sized fusion pore is formed between the vesicle and presynaptic membranes during release, the vesicle can be rapidly retrieved by a direct reversal of the exocytotic process, reloaded with neurotransmitters, and returned to the RRP (Bonanomi *et al.*, 2006; Alabi and Tsien, 2013).

Clathrin-mediated endocytosis initiates with adaptor proteins binding to vesicular membrane proteins (*e.g.* synaptotagmins and neurotransmitter transporters; Diril *et al.*, 2006; Jung and Haucke, 2007; Koo *et al.*, 2011). Clathrin and accessory proteins are subsequently recruited to mediate local invagination of the presynaptic membrane (Jung and Haucke, 2007). This is followed by recruitment of dynamin to the neck of the budding vesicle. Dynamin forms a constricting ring around the neck and mediates membrane fission (Jung and Haucke, 2007). Once free from the

plasma membrane, the new vesicle undergoes clathrin uncoating (Fig. 1.2, step 7). It may then be trafficked to an intermediate endosomal compartment (Fig. 1.2, step 8), or immediately loaded with neurotransmitters and used for transmitter release (Bonanomi *et al.*, 2006).

1.3 Ca^{2+} regulation of transmitter release

In presynaptic nerve terminals, a brief but large increase in $[Ca^{2+}]_i$, in the vicinity of VGCCs, drives synchronous fusion of readily releasable vesicles. By comparison, slowly rising, longer-lasting, and spatially homogeneous elevations regulate asynchronous transmission and several forms of synaptic plasticity. Whether spontaneous transmitter release is driven by a high and short-lived Ca^{2+} elevation near open Ca^{2+} channels, or a smaller and longer-lasting rise, remains unclear.

1.3.1 Ca^{2+} triggering of evoked release

The Ca^{2+} hypothesis of transmitter release was proposed by Katz and Miledi (1967), based on a series of experiments investigating the opposite effects of Ca^{2+} and Mg^{2+} on neuromuscular transmission (Del Castillo and Stark, 1952; Del Castillo and Katz, 1954; Katz and Miledi, 1965a). According to this hypothesis, an influx of Ca^{2+}, upon presynaptic membrane depolarisation, triggers transmitter release. Thus, an intracellular Ca^{2+} rise is required for synaptic transmission, whereas the role of membrane depolarisation in this process is indirect: it facilitates transmitter release by activating VGCCs, thereby increasing the Ca^{2+} permeability of the presynaptic membrane. Such a distinction between Ca^{2+} and presynaptic membrane depolarisation was substantiated by Augustine *et al.* (1985), who reported no direct effect of the latter on AP-evoked release. Subsequent experiments in which photo-labile Ca^{2+} chelators were introduced into presynaptic terminals provided further support to the Ca^{2+} hypothesis (Lando and Zucker, 1994). As photo-labile Ca^{2+}

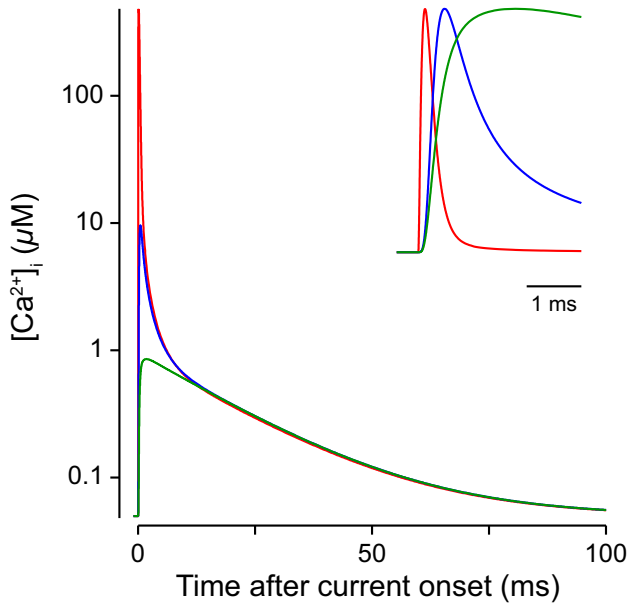

Figure 1.3: Simulated increases in $[Ca^{2+}]_i$ in response to a brief AP-evoked Ca^{2+} current (244 μs half-width). (Inset) The increases in $[Ca^{2+}]_i$ were scaled to the same peak to demonstrate the difference in their time courses. Different colours indicate changes in $[Ca^{2+}]_i$ at different locations from the point source of Ca^{2+} influx: 20 nm (red), 200 nm (blue), and spatially averaged (green).

chelators rapidly release Ca^{2+} ions upon photolysis, these so-called Ca^{2+} uncaging experiments have shown that an elevation in $[Ca^{2+}]_i$ is sufficient to induce transmitter release.

1.3.2 Synchronous release is driven by a localised intracellular Ca^{2+} rise

The idea that transmitter release is triggered by localised and short-lived domains of high $[Ca^{2+}]_i$ developed from theoretical studies 30 years ago (Chad and Eckert, 1984; Simon and Llinas, 1985). By simulating the diffusion of Ca^{2+} ions, these studies revealed the complex spatial and temporal profiles of $[Ca^{2+}]_i$ following the opening of discrete VGCCs. They showed that, in the immediate vicinity of each channel, $[Ca^{2+}]_i$ rises to $\sim$ 100 μM, and it does so within tens of microseconds after the channels have opened (Fig. 1.3, red). Once the channels close, $[Ca^{2+}]_i$ drops back to the resting level very rapidly, in only a few tens of microseconds. In contrast, more than a few hundred nanometres away, $[Ca^{2+}]_i$ rises and falls much more slowly,

taking more than 100 μs after the opening and closing of the channels (Fig. 1.3, blue). Here, $[Ca^{2+}]_i$ also reaches a lower peak, $\sim$ 10 μM or less. As the delay between a presynaptic Ca^{2+} current and the start of the postsynaptic response was found to be $\sim$ 200 μs in the squid giant synapse (Llinas *et al.*, 1981b), it was suggested that readily releasable vesicles were located within 100 nm of VGCCs, and that their fusion was triggered by localised, brief, and yet high Ca^{2+} signals (Simon and Llinas, 1985). This would explain not only the remarkably short delay of evoked release, but also its rapid time course.

1.3.2.1 The Ca^{2+} signal at transmitter release sites

Unfortunately, our current imaging techniques cannot unambiguously resolve the local Ca^{2+} signal that triggers fusion of readily releasable vesicles. This is not only because of the diffraction limit of optical imaging, but also because fluorescent Ca^{2+} indicators, which are commonly used to measure $[Ca^{2+}]_i$, produce signals that are low-pass filtered by their Ca^{2+}-binding and unbinding kinetics (Schneggenburger and Neher, 2005). Therefore, a number of studies have implemented a "reverse approach" to determine the amplitude and time course of the Ca^{2+} signal at transmitter release sites (Fig. 1.4; Schneggenburger and Neher, 2005). Using Ca^{2+} uncaging to induce vesicle fusion, these studies first assess the intracellular Ca^{2+} dependence of transmitter release (Fig. 1.4A-B). A presynaptic terminal loaded with a photo-labile Ca^{2+} chelator is uniformly illuminated to produce spatially homogeneous elevations in $[Ca^{2+}]_i$. This allows the Ca^{2+} signal that the Ca^{2+} sensor for release "sees" to be accurately measured with a low-affinity Ca^{2+} indicator. At the same time, the rate of transmitter release is determined by measuring the resultant change in the presynaptic membrane capacitance or the postsynaptic response. A kinetic model is then formulated to fit the plots of release rate and delay *vs.* $[Ca^{2+}]_i$ (Fig. 1.4C). Finally, the rate of AP-evoked release is measured (Fig. 1.4D), and the local Ca^{2+} signal that drives this release is back-calculated from the kinetic model (Fig. 1.4E). It has been shown that Ca^{2+} uncaging and presynaptic membrane depolarisation trigger release from the same pool of vesicles (Schneggenburger and

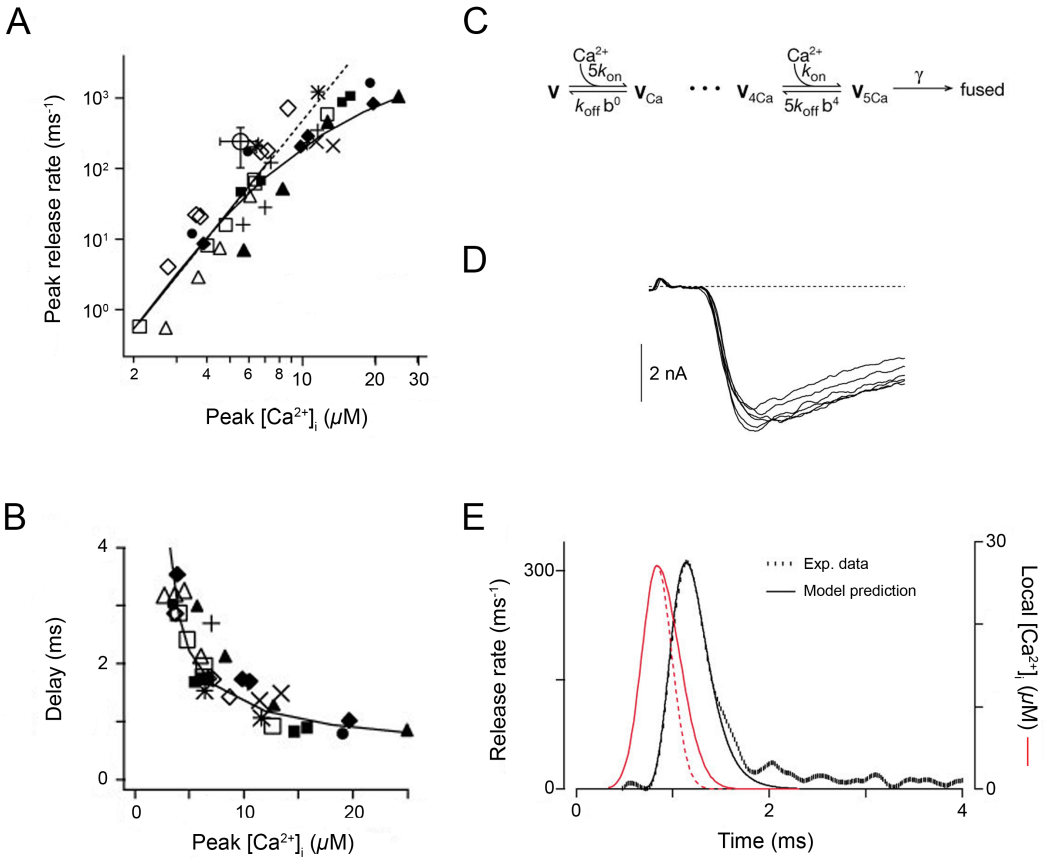

Figure 1.4: The reverse approach of determining the Ca^{2+}signal "seen" by the Ca^{2+}sensor for evoked release. Exemplified here is an experiment in the young calyx of Held by Schneggenburger and Neher (2000). (A-B) The first step is to measure the rate of transmitter release together with synaptic delay as a function of $[Ca^{2+}]_i$. Here, $[Ca^{2+}]_i$ was raised uniformly by uncaging of the photolabile Ca^{2+} chelator DM-nitrophen. At the same time, the resultant transmitter release was assessed by measuring the postsynaptic currents. Dashed line in A indicates a slope of 4.2. (C) A kinetic model is then formulated to fit the data. To account for the steep dependence of release rate on $[Ca^{2+}]_i$, five Ca^{2+} ions needed to bind to the release machinery before vesicle fusion occurred with a rate constant of γ. (D) Experimentally measured postsynaptic currents in response to presynaptic APs. (E) Finally, based on the model in C, the Ca^{2+} signal that produces the measured postsynaptic currents in D is back-calculated (solid red trace). The rate of transmitter release driven by the inferred Ca^{2+} signal (solid black trace) was similar to that obtained experimentally (dashed black trace; obtained by deconvolution of the measured postsynaptic currents). This Ca^{2+} signal was slightly broader than the Ca^{2+} current measured in the calyx of Held during an AP by Borst and Sakmann (1996, dashed red trace). Figure adapted.

Neher, 2000; Sakaba, 2008). Therefore, the kinetic model formulated based on Ca^{2+} uncaging data should provide an appropriate inference of the local Ca^{2+} signal during physiological stimulation.

Thus far, Ca^{2+} uncaging has been used to measure the intracellular Ca^{2+} dependence of transmitter release at three specialised synapses in the mammalian CNS: the calyx of Held - a large glutamatergic synapse located in the auditory brainstem (Bollmann *et al.*, 2000; Schneggenburger and Neher, 2000; Wang *et al.*, 2008; Kochubey *et al.*, 2009), the cochlear inner hair cell afferent synapse, which has ribbon-type active zones and is also glutamatergic (Beutner *et al.*, 2001), and the immature GABAergic cerebellar basket cell terminal (Sakaba, 2008). These experiments have revealed a highly non-linear dependence of the rate of transmitter release on $[Ca^{2+}]_i$. At the calyx of Held and the cerebellar basket cell terminal, the double-logarithmic plot of release rate *vs.* $[Ca^{2+}]_i$ has a slope of $3-5$ when $[Ca^{2+}]_i$ is between 1 and 10 μM (Fig. 1.4A). Such a steep slope could only be explained by the binding of five Ca^{2+} ions to each release machinery (Fig. 1.4C); the binding of each Ca^{2+} ion could, however, be independent (Bollmann *et al.*, 2000) or cooperative (Schneggenburger and Neher, 2000; Sakaba, 2008; Wang *et al.*, 2008; Kochubey *et al.*, 2009). This verifies the classical proposal by (Dodge and Rahamimoff, 1967), who observed a supralinear dependence of evoked release on the extracellular Ca^{2+} concentration, and suggested that a cooperative action of about four Ca^{2+} ions is needed to trigger release of a synaptic vesicle. At the calyx of Held, deletion of Syt2 abolished the steep dependence of evoked release on $[Ca^{2+}]_i$ (Sun *et al.*, 2007; Kochubey and Schneggenburger, 2011). Accordingly, Syt2 serves as a high-cooperativity Ca^{2+} sensor for release, a function it shares with Syt1 (Nagy *et al.*, 2006; Xu *et al.*, 2007).

The reverse approach of determining the local Ca^{2+} signal that triggers transmitter release has shown that the Ca^{2+} sensors for release at the so far examined mammalian central synapses are more sensitive to Ca^{2+} than previously thought. At both the young calyx of Held and the immature cerebellar basket cell terminal, a local Ca^{2+} signal with a peak of $10-25$ μM and a half-width of ~ 0.5 ms produces a change in release rate that mimics AP-evoked transmitter release (Fig. 1.4D-E;

Bollmann *et al.*, 2000; Schneggenburger and Neher, 2000; Sakaba, 2008). As the calyx of Held matures following the onset of hearing in rodents (P12 − 15), the local Ca^{2+} signal becomes larger yet briefer (50 μM peak amplitude and 0.3 ms half-width; Wang *et al.*, 2008; Kochubey *et al.*, 2009). This is in marked contrast to the hundreds of micromolar range of $[Ca^{2+}]_i$ required to trigger transmitter release at the squid giant synapse and at terminals of goldfish retinal bipolar cells (Adler *et al.*, 1991; Heidelberger *et al.*, 1994).

The high sensitivity of transmitter release at the young calyx of Held is supported by an elegant study by Bollmann and Sakmann (2005). In this study, low- to sub-millisecond long elevations in $[Ca^{2+}]_i$ were achieved by photolysis of caged Ca^{2+} in the presence of a high-affinity Ca^{2+} buffer (EGTA or BAPTA). This allowed a direct measurement of the relationship between evoked release and the duration of the Ca^{2+} rise. It was found that the rise time and amplitude of transmitter release increased with an increasing half-width of the Ca^{2+} elevation. The sharp rise in the rate of transmitter release following an AP could only be reproduced experimentally by a Ca^{2+} transient with a peak of ~ 20 μM and a half-width of less than 1 ms. Thus, not only does an intracellular Ca^{2+} rise trigger transmitter release, but the local Ca^{2+} signal at release sites also controls the timing and magnitude of the release.

1.3.2.2 The arrangement of Ca^{2+} channels at the active zone

The variation in the local Ca^{2+} signal between different types of synapses reflects heterogeneity in the coupling between VGCCs and the release machinery. Due to diffusion of Ca^{2+}, a strong local Ca^{2+} signal most likely arises from nearby Ca^{2+} channels, whereas a weaker signal would be "seen" by the Ca^{2+} sensor for release if these channels were located further away. At the frog NMJ, electron microscopy tomography revealed a distance of $\sim$ 20 nm between putative Ca^{2+} channels and docked vesicles (Harlow *et al.*, 2001). Such ultrastructural data are, however, unavailable for most synapses. As a result, the arrangement of VGCCs at the active zone has been indirectly assessed by manipulating the interaction between

Ca^{2+} and the release machinery or by changing the presynaptic Ca^{2+} influx (Fig. 1.5).

The distance between VGCCs and the release machinery. The distance between a readily releasable vesicle and its release-controlling Ca^{2+} channel(s) is commonly probed by comparing the effects of two synthetic Ca^{2+} buffers, EGTA and BAPTA, on transmitter release. The rationale behind this approach is that a Ca^{2+} buffer that can capture Ca^{2+} ions on their way from the Ca^{2+} channel(s) to the Ca^{2+} sensor for release will block synaptic transmission. Although EGTA and BAPTA have similar affinities for Ca^{2+}, the on-rate of Ca^{2+} binding to BAPTA is $\sim$ 100 times faster than that for EGTA. Adler *et al.* (1991) estimated that, under conditions of the squid cytoplasm, 10 mM EGTA binds to Ca^{2+} with a time constant of more than 50 μs, whilst it takes the same concentration of BAPTA less than 1 μs to do so. This, together with mathematical models of Ca^{2+} diffusion, suggests that, if the distance from the Ca^{2+} channel(s) to the Ca^{2+} sensor is more than 100 nm, *i.e.* loose coupling or microdomain signalling, both EGTA and BAPTA will be able to suppress transmitter release (Fig. 1.5A, right). However, if this distance is only a few tens of nanometres, *i.e.* tight coupling or nanodomain signalling, BAPTA will be much more effective at blocking transmission (Fig. 1.5A, left).

This approach was first used at the giant synapse of the squid, where a high concentration of EGTA ($\sim$ 80 mM) had no effect on transmitter release (Adler *et al.*, 1991). In contrast, BAPTA, in the low millimolar range, significantly reduced the postsynaptic potential. Therefore, at this synapse, the distance between VGCCs and the release machinery is most likely only a few tens of nanometres, consistent with a local Ca^{2+} signal of a few hundred micromolars suggested by Llinas *et al.* (1992). Similarly, at the mature calyx of Held and the hippocampal basket cell to granule cell synapse, evoked transmitter release appears to be triggered by Ca^{2+} nanodomains (Fedchyshyn and Wang, 2005; Bucurenciu *et al.*, 2008). Ca^{2+} microdomains, on the other hand, have been suggested to control transmitter release at the young calyx of Held (Borst and Sakmann, 1996; Fedchyshyn and Wang, 2005), the hippocampal

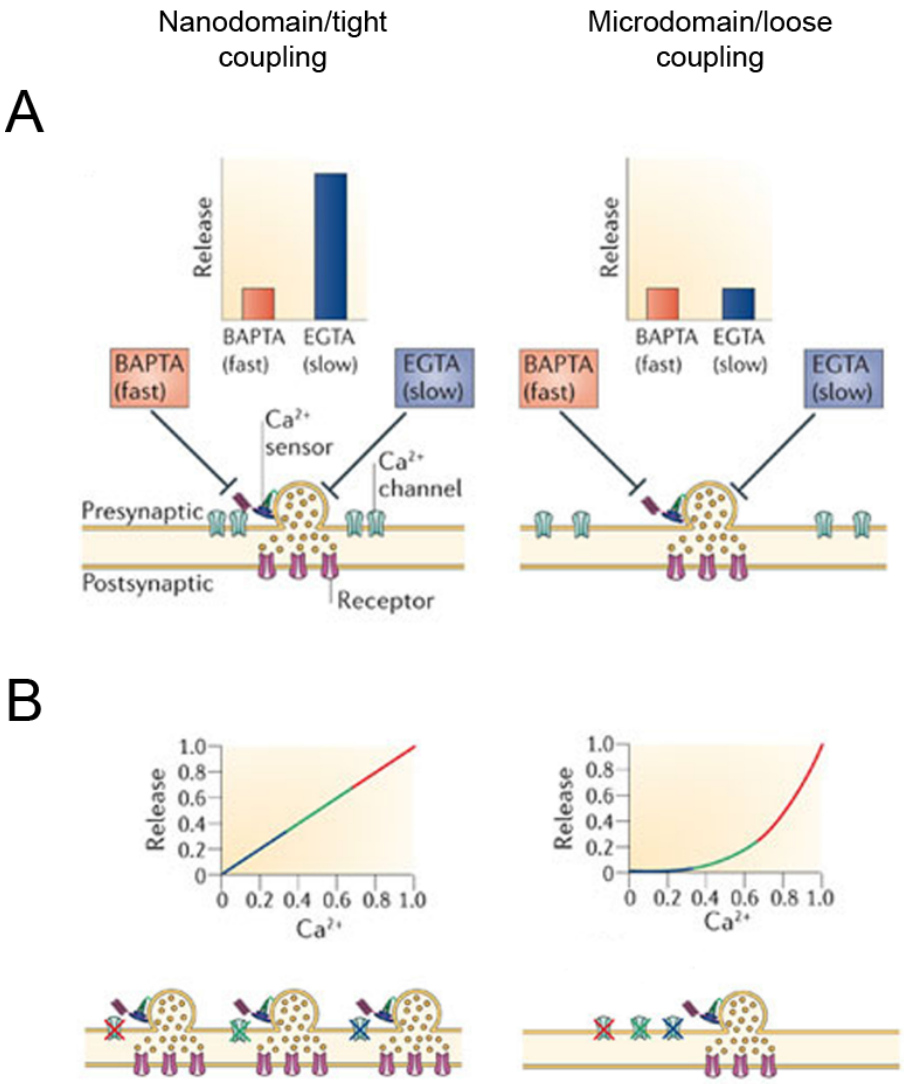

Figure 1.5: Experimental strategies for determining the distance and the number of open VGCCs that mediate transmitter release. (A) To assess the distance between Ca^{2+} channels and the release machinery, two Ca^{2+} buffers with the same Ca^{2+} binding affinity but different on-rates are used. If VGCCs are tightly coupled to Ca^{2+} sensors, only the fast buffer BAPTA will be able to capture Ca^{2+} ions on their way from the former to the latter. In contrast, BAPTA and EGTA will be equally effective at blocking vesicle fusion if coupling between Ca^{2+} channels and sensors are loose. (B) The number of open Ca^{2+} channels that mediate fusion of a vesicle can be estimated by measuring the dependence of transmitter release on presynaptic Ca^{2+} influx in the presence of a slow Ca^{2+} channel blocker. If only one or a few channels are required for vesicle fusion, sequential blockade of Ca^{2+} channels will have a linear effect on the number of vesicles fused. As a result, transmitter release appears proportional to the intracellular Ca^{2+} rise. However, if a large number of open channels mediate fusion of a vesicle, blockade of Ca^{2+} channels will cause transmitter release to decrease supralinearly. Adapted from Eggermann *et al.* (2012).

mossy fibre bouton (Vyleta and Jonas, 2014), and synapses between neocortical layer 5 pyramidal neurons (Ohana and Sakmann, 1998). The finding that signalling at the calyx of Held changes from microdomain to nanodomain during development is consistent with the local Ca^{2+} signals inferred by the reverse approach: as the calyx of Held matures, the Ca^{2+} signal "seen" by the release machinery becomes larger in amplitude and shorter in half-width (Bollmann *et al.*, 2000; Schneggenburger and Neher, 2000; Wang *et al.*, 2008; Kochubey *et al.*, 2009).

The number of VGCCs required for transmitter release. The number of Ca^{2+} channels involved in generating the local Ca^{2+} signal "seen" by each vesicle has also been determined semi-quantitatively. In these experiments, the number of open Ca^{2+} channels is varied, by altering the duration of the presynaptic membrane depolarisation or by addition of a slow Ca^{2+} channel blocker (Eggermann *et al.*, 2012; Wang and Augustine, 2014). The presynaptic Ca^{2+} influx and the corresponding postsynaptic response are then measured and their relationship determined. If the opening of only one VGCC is sufficient to induce vesicle fusion, the amount of release will decrease linearly with the number of open channels (Fig. 1.5B, left). On the other hand, if influx from multiple Ca^{2+} channels is required, a reduction in the number of open channels will cause a supralinear reduction in the postsynaptic response (Fig. 1.5B, right). The power coefficient of this relationship converges to the intrinsic Ca^{2+} cooperativity of transmitter release (~ 4), as more channels involve in generating the local Ca^{2+} signal. Predictably, at synapses where VGCCs are tightly coupled to synaptic vesicles, only $2-3$ open channels trigger transmitter release, and thus, the relationship between release and presynaptic Ca^{2+} influx is close to linearity (Augustine, 1990; Bucurenciu *et al.*, 2010). In contrast, the power coefficient of this relationship is more than 3 at the young calyx of Held, where vesicle fusion is mediated by the opening of ~ 10 loosely coupled VGCCs (Fedchyshyn and Wang, 2005).

Spatial distribution of VGCCs. Electrophysiological studies have provided important information on the distance between VGCCs and the release machinery, and

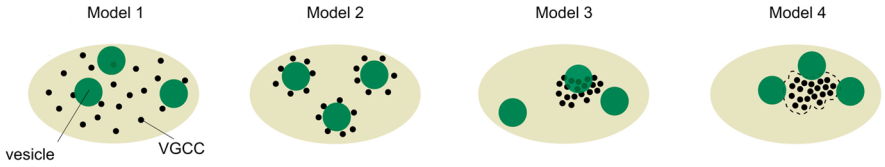

Figure 1.6: Hypothetical topographies of VGCCs and readily releasable vesicles at the active zone. Adapted from Nakamura *et al.* (2015).

the number of open channels required for vesicle fusion. However, they cannot reveal how these channels are distributed at the active zone. A number of topographies have been proposed to describe the relative spatial distribution between Ca^{2+} channels and readily releasable vesicles (Fig. 1.6). These include random distributions of both channels and vesicles (model 1), a ring of channels surrounding each vesicle (model 2), a random distribution of vesicles around a cluster of channels (model 3), and vesicles located just outside a cluster of channels (model 4; Meinrenken *et al.*, 2002; Schneggenburger and Neher, 2005; Scimemi and Diamond, 2012; Ermolyuk *et al.*, 2013; Nakamura *et al.*, 2015). Recent advances in immunogold labelling combined with freeze-fracture replica electron microscopy have led to observations of a non-random distribution of $Ca_V2.1$ or P/Q-type channels in CA3 pyramidal cell axon terminals (Holderith *et al.*, 2012), cerebellar parallel fibre boutons (Indriati *et al.*, 2013), and the calyx of Held (young as well as mature; Nakamura *et al.*, 2015). As a result, models 3 and 4 are more likely to represent the topography of VGCCs and readily releasable vesicles at the active zone of central synapses.

A study by Nakamura *et al.* (2015) suggested that, at the calyx of Held, most of the vesicles that are ready to be released upon an AP are located $15 - 30$ nm from the edge of a VGCC cluster. This is in accordance with model 4, which was termed by the authors as the "perimeter release model". The model was hypothesised based on results from a diverse range of experiments. First, freeze-fracture replica labelling of $Ca_V2.1$ channels revealed clustering of these channels, with each cluster ~ 100 nm wide. Second, presynaptic Ca^{2+} imaging was done to estimate the concentration and Ca^{2+} binding affinity of endogenous Ca^{2+} buffers. Third, the effect of EGTA

on presynaptic Ca^{2+} influx as well as transmitter release was measured. Finally, an experimentally constrained 3D reaction-diffusion model of Ca^{2+} and vesicle fusion was constructed to provide a more precise estimate of the VGCC-sensor distance. This reaction-diffusion model could predict the sensitivity of transmitter release to EGTA if synaptic vesicles were located a few tens of nanometres from the perimeter of a channel cluster. In contrast, a model with a random distribution of synaptic vesicles (model 3) could only reproduce the measured level of EGTA inhibition if each cluster had more than 50 Ca^{2+} channels, much more than that observed experimentally. Based on the labelling efficiency of antibodies and the contribution of $Ca_v2.1$ channels to the presynaptic Ca^{2+} current, the total number of VGCCs *per* cluster was estimated to be $\sim$ 20 on average, for P7 as well as P14 calyxes. Remarkably, the perimeter release model could also explain developmental changes in transmitter release at the calyx of Held: both decreases in the duration and EGTA sensitivity of transmitter release, in mature calyxes, could arise from a shortening of the distance between synaptic vesicles and the perimeter of a channel cluster (from 30 to 20 nm; Nakamura *et al.*, 2015).

1.3.3 Asynchronous release is driven by the global Ca^{2+} elevation

Compared to synchronous release, asynchronous release is much more persistent: it lasts for tens of milliseconds or more after cessation of presynaptic membrane depolarisation (Fig. 1.1A). In a wide range of axon terminals, the slow exogenous Ca^{2+} buffer EGTA markedly reduces the amplitude and duration of asynchronous release, without affecting the synchronous fusion of synaptic vesicles (Cummings *et al.*, 1996; Atluri and Regehr, 1998; Hefft and Jonas, 2005; Iremonger and Bains, 2007; Manseau *et al.*, 2010). Therefore, it is generally acknowledged that asynchronous transmission is triggered by the global, spatially homogeneous $[Ca^{2+}]_i$ that rises and decays slowly upon stimulation (in tens to hundreds of millisecond time scale; Fig. 1.3, green). During a high frequency train of APs, this spatially homogeneous $[Ca^{2+}]_i$ can build up to values in the low micromolar range, making asynchronous release more prominent.

A number of studies have suggested that synchronous and asynchronous release share the same pool of readily releasable vesicles (Hagler and Goda, 2001; Otsu *et al.*, 2004; Sun *et al.*, 2007; Burgalossi *et al.*, 2010; but see Raingo *et al.*, 2012). However, it remains controversial whether the same Ca^{2+} sensor mediates these two forms of evoked release (Neher and Sakaba, 2008; Kochubey *et al.*, 2011). Ca^{2+} uncaging experiments have shown that, at the calyx of Held, as $[Ca^{2+}]_i$ is reduced to the sub-micromolar range, the slope of the double-logarithmic plot of release rate *vs.* $[Ca^{2+}]_i$ becomes less steep (Lou *et al.*, 2005; Sun *et al.*, 2007). At $[Ca^{2+}]_i$ relevant for asynchronous release ($\leq$ 1 μM), the Ca^{2+} cooperativity of release is $1-2$, significantly lower than that for synchronous release. Due to this reduced Ca^{2+} dependence, the rate of transmitter release at sub-micromolar $[Ca^{2+}]_i$ is higher than that predicted by the aforementioned five-site models. As a result, these original models have been modified to allow vesicle fusion in the absence of Ca^{2+} binding and at low levels of $[Ca^{2+}]_i$.

The first revised model proposes that transmitter release occurs even when the release machinery is partially bound (Lou *et al.*, 2005). The rate of release increases in geometric progression with the number of bound Ca^{2+} ions, and the maximal release rate is reached when the release machinery is fully occupied by five Ca^{2+} ions. Thus, the Ca^{2+} cooperativity of release increases gradually as $[Ca^{2+}]_i$ rises from sub- to low-micromolar concentrations.

The second model, on the other hand, proposes the presence of two different Ca^{2+} sensors with different Ca^{2+} binding kinetics (Sun *et al.*, 2007). Besides a sensor with a Ca^{2+} cooperativity of 5 that predominantly triggers rapid release at high levels of $[Ca^{2+}]_i$, another sensor with a slower Ca^{2+} binding rate and a Ca^{2+} cooperativity of 2 mediates release at sub-micromolar $[Ca^{2+}]_i$. Vesicle fusion occurs when either or both Ca^{2+} sensors are fully bound. This model was based on the finding that deletion of Syt2, whilst abolishing synchronous release, did not eliminate asynchronous transmission at the calyx of Held synapse (Sun *et al.*, 2007). Similarly, asynchronous release persisted in cultured cortical and autaptic hippocampal neurons after deletion of Syt1 (Maximov and Sudhof, 2005; Burgalossi *et al.*, 2010). The slope of the

double-logarithmic plot of release rate *vs.* $[Ca^{2+}]_i$ is near linear in Syt1 knockout hippocampal autapses as well as Syt2 knockout calyxes (Burgalossi *et al.*, 2010; Kochubey and Schneggenburger, 2011).

Bacaj *et al.* (2013) demonstrated that a loss of function of Syt7 produced a near-complete inhibition of asynchronous release in Syt1 knockout cultured hippocampal neurons, without affecting transmitter release in wild-type neurons. Such an effect was only rescued by wild-type but not mutant Syt7 that lacked functional Ca^{2+}-binding sites. This indicates that Syt7 functions as a Ca^{2+} sensor for asynchronous release in hippocampal neurons. Consistently, Syt7 has been suggested to complement Syt1 in driving Ca^{2+}-dependent release in chromaffin cells (Schonn *et al.*, 2008). It remains to be determined whether Syt7 also mediates asynchronous release in presynaptic terminals such as the calyx of Held where Syt2 is the main Ca^{2+} sensor for synchronous release.

1.3.4 Ca^{2+} dependence of spontaneous transmitter release

In one of their early experiments, Fatt and Katz (1952) showed that the frequency of mEPPs was relatively independent of the extracellular Ca^{2+} concentration. Thus, spontaneous transmission was generally thought to result from the spontaneous fusion of synaptic vesicles (Katz, 1962). Although a few classic studies demonstrated an influence of extracellular Ca^{2+} on mEPP frequency (Boyd and Martin, 1956; Hubbard, 1961), the role of Ca^{2+} in their generation remains a matter of debate.

Within the last two decades, an increasing number of studies have demonstrated a dependence of spontaneous transmission on Ca^{2+} (Bao *et al.*, 1998; Llano *et al.*, 2000; Simkus and Stricker, 2002a; Xu *et al.*, 2009; Groffen *et al.*, 2010; Goswami *et al.*, 2012; Williams *et al.*, 2012; Ermolyuk *et al.*, 2013). In these studies, removal of the extracellular Ca^{2+}, blockade of VGCCs, and/or addition of exogenous Ca^{2+} buffers (BAPTA and/or EGTA) abolished a significant fraction (> 30%) of miniature postsynaptic currents. As a result, the idea that a considerable amount of

spontaneous transmitter release is triggered by spontaneous fluctuations in $[Ca^{2+}]_i$ has gained general acceptance. It is unclear whether the remaining spontaneous release is truly Ca^{2+}-independent, whether it is triggered by brief and localised elevations in $[Ca^{2+}]_i$ that are incompletely blocked by BAPTA, or whether it is driven by the resting $[Ca^{2+}]_i$ that is unaffected by Ca^{2+} buffering (Kaeser and Regehr, 2014). Ca^{2+}-independent spontaneous release might occur as a consequence of spontaneous energy fluctuations, allowing the energy barrier for vesicle fusion to be overcome (Schneggenburger and Rosenmund, 2015).

The spontaneous opening of VGCCs underlies spontaneous release of GABA at inhibitory synapses onto hippocampal granule cells and those onto cultured neocortical neurons (Goswami *et al.*, 2012; Williams *et al.*, 2012). Each vesicle fusion event requires simultaneous opening of multiple Ca^{2+} channels, either through microdomain or nanodomain signalling. In contrast, spontaneous release of glutamate from cultured hippocampal neurons has been suggested to arise predominantly from individual Ca^{2+} channels that open independently (Ermolyuk *et al.*, 2013). At this synapse, addition of exogenous Ca^{2+} buffers inhibited evoked and VGCC-dependent spontaneous release in similar fashion. A simulation of spontaneous release, utilising the Ca^{2+} sensor for evoked release, showed that $\sim$ 90% of VGCC-dependent mEPSCs could arise from the stochastic opening of single Ca^{2+} channels located within 70 μm of readily releasable vesicles (Ermolyuk *et al.*, 2013).

Besides Ca^{2+} influx, intracellular Ca^{2+} release also drives spontaneous transmission at a variety of synapses. Ca^{2+} can be released from presynaptic stores through the ryanodine and/or inositol 1,4,5-trisphosphate (IP_3) receptor. At inhibitory synapses onto cerebellar Purkinje cells and at excitatory synapses onto neocortical and hippocampal CA3 pyramidal neurons, inhibition of ryanodine and/or IP_3 receptors reduced the frequency of miniature postsynaptic currents (Llano *et al.*, 2000; Emptage *et al.*, 2001; Simkus and Stricker, 2002a). Importantly, spontaneously occurring Ca^{2+} transients that are sensitive to ryanodine have been observed in basket cell terminals onto Purkinje cells and in axon terminals of cultured hippocampal CA3 pyramidal

neurons (Emptage *et al.*, 2001; Conti *et al.*, 2004). In these studies, $[Ca^{2+}]_i$ in the presynaptic nerve terminals was monitored with a high-affinity fluorescent Ca^{2+} indicator in the presence of TTX. Together, these findings provide strong evidence that spontaneous transmitter release can arise from intracellular Ca^{2+} release.

A lot remains controversial about the mechanism(s) of spontaneous release, including the identity of its Ca^{2+} sensor(s) and whether it utilises the same pool of synaptic vesicles as evoked release (Sara *et al.*, 2005; Groemer and Klingauf, 2007; Fredj and Burrone, 2009; Wilhelm *et al.*, 2010). In addition, due to its stochastic nature, the local Ca^{2+} signal(s) that drives spontaneous release is elusive. The fast and high-cooperativity Ca^{2+} sensor Syt1 has been suggested to mediate the majority of Ca^{2+}-dependent spontaneous release from cultured cortical neurons (Xu *et al.*, 2009). This is reasonable if spontaneous transmission is driven by a high and short-lived elevation in $[Ca^{2+}]_i$ near voltage-gated and/or store release Ca^{2+} channels (Ermolyuk *et al.*, 2013). On the other hand, a smaller and longer-lasting rise might be able to trigger spontaneous release through activation of a slower and near-linear Ca^{2+} sensor (Kochubey and Schneggenburger, 2011).

1.3.5 Ca^{2+} regulation of presynaptic plasticity

Synaptic plasticity refers to the ability of synapses to increase or decrease their efficacy over time, given particular stimulation histories. Short-term synaptic plasticity, which occurs on a sub-second to minute timescale, is thought to mediate sensory adaptation, underlie direction selectivity, enable neuronal gain control, and regulate circuit dynamics (Regehr, 2012; Jackman and Regehr, 2017). Long-term synaptic plasticity, which lasts anywhere from minutes to hours, days or years, is the dominant model of learning and memory formation (Collingridge *et al.*, 2010; Nicoll, 2017). Although Ca^{2+} plays a major role in many aspects of long-term synaptic plasticity (Raymond and Redman, 2002; Cavazzini *et al.*, 2005), its induction is predominantly postsynaptic (Cavazzini *et al.*, 2005; Collingridge *et al.*, 2010).

As this thesis examines presynaptic Ca^{2+} dynamics, only presynaptic mechanisms underlying Ca^{2+} regulation of short-term plasticity are described here.

Short-term synaptic plasticity can be divided into three main categories: 1) depression, 2) facilitation, and 3) post-tetanic potentiation. Several features of short-term depression can be explained by the depletion model (Liley and North, 1953; Betz, 1970), according to which, an AP transiently depletes the RRP, and hence, reduces the number of vesicles available to fuse in response to subsequent APs (but see Xu and Wu, 2005; Sullivan, 2007). However, certain presynaptic nerve terminals may be equipped with specialised Ca^{2+}-dependent mechanisms that enhance transmitter release, even when the pool of readily releasable vesicles decreases (Jackman and Regehr, 2017).

1.3.5.1 Synaptic facilitation

Facilitation is a form of short-term synaptic plasticity that boosts transmitter release for tens of milliseconds to seconds (Eccles *et al.*, 1941). As in the case of asynchronous transmitter release, it is widely accepted that synaptic facilitation is a result of the global Ca^{2+} elevation that remains from previous APs (Fig. 1.3, green; Katz and Miledi, 1968; Kamiya and Zucker, 1994; Atluri and Regehr, 1996). This spatially-averaged $[Ca^{2+}]_i$ is often referred to as the residual $[Ca^{2+}]_i$ ($[Ca^{2+}]_{residual}$). However, the molecular mechanism(s) by which $[Ca^{2+}]_{residual}$ induces facilitation remains unknown for many synapses.

According to the residual Ca^{2+} hypothesis proposed by Katz and Miledi (1968), $[Ca^{2+}]_{residual}$ simply adds to the local $[Ca^{2+}]_i$ ($[Ca^{2+}]_{local}$) created by a subsequent AP, thereby increasing the probability of transmitter release. As, in this hypothesis, facilitation and synchronous transmitter release share the same high-cooperativity Ca^{2+} sensor, the extent of paired-pulse facilitation (*PPF*) produced by two closely spaced APs ($\Delta t \leq 100$ ms) can be described as

$$PPF = \frac{([Ca^{2+}]_{local} + [Ca^{2+}]_{residual})^4}{([Ca^{2+}]_{local})^4}. \quad (1.1)$$

It has been argued that a simple addition of $[Ca^{2+}]_{residual}$ to $[Ca^{2+}]_{local}$ cannot account for a large extent of synaptic facilitation (Kamiya and Zucker, 1994; Zucker and Regehr, 2002). This is because, at some synapses, $[Ca^{2+}]_{residual}$ is $\sim$ 100-fold smaller than $[Ca^{2+}]_{local}$ ($\leq$ 1 *vs.* 100 μM, respectively). Thus, a linear sum of $[Ca^{2+}]_{residual}$ and $[Ca^{2+}]_{local}$ would only produce a *PPF* of $\sim$ 4%, a value much smaller than typically measured ($\geq$ 50%; Atluri and Regehr, 1996; Rozov *et al.*, 2001; Jackman *et al.*, 2016). In addition, at the granule cell to Purkinje cell synapse, $[Ca^{2+}]_{residual}$ always decayed more rapidly than did *PPF* (Atluri and Regehr, 1996). Even when the duration of $[Ca^{2+}]_{residual}$ was reduced to less than 20 ms, facilitation still persisted with an intrinsic decay time constant of $\sim$ 40 ms. Due to these disparities, it has been proposed that synaptic facilitation is mediated by a Ca^{2+} binding site with a high affinity but slow kinetics. This binding site is located either on Syt1/Syt2, but different from the low-affinity, fast kinetic sites responsible for synchronous release, or on a Ca^{2+} sensor distinct from Syt1/Syt2 (Kamiya and Zucker, 1994; Bertram *et al.*, 1996; Atluri and Regehr, 1996). In support of this idea, Jackman *et al.* (2016) demonstrated that the high-affinity Ca^{2+} sensor Syt7 is required for facilitation in corticothalamic, hippocampal mossy fibre, Schaffer collateral, and perforant path synapses. Nonetheless, whether Ca^{2+} binding to Syt7 mediates facilitation at other synapses, and if this causes facilitation by increasing the probability of Syt1- or Syt2-mediated release remain to be determined (Jackman and Regehr, 2017).

Recent studies have shown that, for many synapses, the local Ca^{2+} signal at transmitter release sites ($10 - 50$ μM; Bollmann *et al.*, 2000; Schneggenburger and Neher, 2000; Wang *et al.*, 2008; Sakaba, 2008; Kochubey *et al.*, 2009) might not be as large as previously thought ($>$ 100 μM; Simon and Llinas, 1985; Adler *et al.*, 1991). Therefore, a simple addition of $[Ca^{2+}]_{residual}$ to $[Ca^{2+}]_{local}$ can produce a *PPF* much larger than the 4% estimated above. To investigate the extent to which a linear sum of $[Ca^{2+}]_{residual}$ and $[Ca^{2+}]_{local}$ contributed to *PPF*, Felmy *et al.* (2003) used Ca^{2+}

uncaging to homogeneously raise $[Ca^{2+}]_i$ in the calyx of Held, before evoking a brief membrane depolarisation to trigger transmitter release. They found that a linear sum of the pre-elevated $[Ca^{2+}]_i$ and $[Ca^{2+}]_{local}$ could account for almost 30% of the observed facilitation. As the Ca^{2+} sensitivity of transmitter release did not change during Ca^{2+}-dependent synaptic facilitation, Felmy and colleagues argued that facilitation at this synapse is unlikely to be mediated by a high-affinity Ca^{2+} binding site. Facilitation caused by Ca^{2+} binding to such a site would have led to an increased Ca^{2+} sensitivity and/or a reduced synaptic delay. To explain the remaining 70% of the observed facilitation, Felmy and colleagues proposed that $[Ca^{2+}]_{residual}$ partially saturated endogenous fast buffers. As a result, more Ca^{2+} ions remained free during the second stimulation, giving rise to a larger $[Ca^{2+}]_{local}$. Due to the high cooperativity of the Ca^{2+} sensor for release, only an additional 20% increase in $[Ca^{2+}]_{local}$ was sufficient to account for the remaining facilitation. Saturation of endogenous Ca^{2+} buffers, in particular, calbindin-D28k, has also been suggested to underlie synaptic facilitation at the hippocampal mossy fibre synapse (Blatow *et al.*, 2003).

Besides a high-affinity Ca^{2+} binding site and buffer saturation, an activity-dependent increase in Ca^{2+} influx has also been shown to contribute to synaptic facilitation. One mechanism that can increase the presynaptic Ca^{2+} influx is the broadening of the AP waveform (Jackson *et al.*, 1991; Geiger and Jonas, 2000). However, its role in synaptic facilitation is likely restricted to later APs of a long train and to certain synapses (Charlton and Bittner, 1978; Jackman and Regehr, 2017). Independently of AP broadening, P/Q-type Ca^{2+} currents facilitate in response to a pair of brief membrane depolarisations ($\Delta t < 100$ ms; Borst and Sakmann, 1998b; Cuttle *et al.*, 1998). This process arises as a result of Ca^{2+} binding to the C-terminal lobe of calmodulin (CaM), which, although pre-associated with the Ca^{2+} channels, strengthens its interaction with their α_1 pore-forming subunit upon Ca^{2+} binding (DeMaria *et al.*, 2001; Lee *et al.*, 2003). Consequently, the Ca^{2+} channels activate more rapidly and produce a larger Ca^{2+} influx in response to the second depolarisation (Cuttle *et al.*, 1998). It has been shown that, by augmenting the rise in $[Ca^{2+}]_{local}$

evoked by the second AP, facilitation of P/Q-type VGCCs accounts for a significant fraction ($\geq$ 40%) of the observed *PPF* at the calyx of Held (Inchauspe *et al.*, 2004; Ishikawa *et al.*, 2005; Xu and Wu, 2005; Muller *et al.*, 2008). Interestingly, Ca^{2+} binding to the N-terminal lobe of CaM, which causes P/Q-type VGCCs to inactivate (DeMaria *et al.*, 2001; Lee *et al.*, 2003), also plays a major role in short-term depression at the calyx of Held, during low-frequency or after tetanic stimulation (Forsythe *et al.*, 1998; Xu and Wu, 2005).

1.3.5.2 Post-tetanic potentiation

Post-tetanic potentiation (PTP) refers to an increase in synaptic efficacy that follows a long period (seconds to minutes) of high-frequency stimulation (Feng, 1941; Liley and North, 1953; Hughes, 1958). Compared to synaptic facilitation, PTP lasts for much longer: tens of seconds to minutes. At many synapses, a closely related but shorter lasting form of short-term synaptic enhancement, known as augmentation, is also observed (Magleby and Zengel, 1976; Zengel *et al.*, 1980). However, the distinction between augmentation and PTP is often unclear, partly because different synapses show a considerable variability in the number and frequency of APs needed to induce these two processes (Regehr, 2012).

The global accumulation of Ca^{2+} in presynaptic nerve terminals also gives rise to PTP (Kretz *et al.*, 1982; Connor *et al.*, 1986; Delaney *et al.*, 1989; Delaney and Tank, 1994; Kamiya and Zucker, 1994; Regehr *et al.*, 1994; Habets and Borst, 2005; Korogod *et al.*, 2005). Compared to that remaining after a single AP, the $[Ca^{2+}]_{residual}$ following sustained high-frequency stimulation decays much more slowly, taking tens of seconds to minutes to return to the resting level. Such a slow decay time course occurs as a result of Ca^{2+} release from mitochondria (Tang and Zucker, 1997; Lee *et al.*, 2007), or a slow-down, or even a reversal, in the activity of Na^{+}/Ca^{2+} exchangers (Mulkey and Zucker, 1992; Regehr, 1997; Zhong *et al.*, 2001). Although PTP decays in parallel with $[Ca^{2+}]_{residual}$ at many synapses (Connor *et al.*, 1986; Delaney *et al.*, 1989; Delaney and Tank, 1994; Habets and Borst, 2005; Korogod *et al.*,

2005), at the hippocampal mossy fibre and Schaffer collateral synapses, the decay time course of $[Ca^{2+}]_{residual}$ is more rapid than that of PTP (Regehr *et al.*, 1994; Brager *et al.*, 2003). As a result, $[Ca^{2+}]_{residual}$ may induce PTP by activating a slow biochemical cascade that enhances transmitter release (Regehr *et al.*, 1994; Brager *et al.*, 2003; Beierlein *et al.*, 2007).

Even though $[Ca^{2+}]_{residual}$ decays very slowly after tetanic stimulation, its amplitude is still $\sim$ 50-fold smaller than $[Ca^{2+}]_{local}$ at transmitter release site (Regehr *et al.*, 1994; Habets and Borst, 2005; Korogod *et al.*, 2005; Fioravante *et al.*, 2011). Therefore, it is very unlikely that a simple addition of $[Ca^{2+}]_{residual}$ to $[Ca^{2+}]_{local}$ (Eq. 1.1) can give rise to PTP ($\geq$ 100% increase in EPSC amplitude). It is also unlikely that this $[Ca^{2+}]_{residual}$ partially saturates endogenous fast buffers and produces a larger $[Ca^{2+}]_{local}$ in response to a subsequent AP. Instead, $[Ca^{2+}]_{residual}$ has been demonstrated to cause PTP through an increase in AP-evoked Ca^{2+} influx or activation of protein kinase C (PKC). By measuring the rise in the volume-averaged $[Ca^{2+}]_i$ evoked by a single AP, Habets and Borst (2006) showed that, at the calyx of Held, a large fraction of PTP could be accounted for by an increase in the presynaptic Ca^{2+} current. Such an increase, likely caused by Ca^{2+}/CaM-dependent facilitation of P/Q-type VGCCs, had a peak amplitude of 15% and a decay time course similar to that of PTP (Habets and Borst, 2006). The remaining PTP was attributed to a 30% increase in the RRP. A similar increase in the volume-averaged Ca^{2+} elevation evoked by a single AP was also observed by Korogod *et al.* (2007). However, Korogod *et al.* argued that a 15% increase in the global Ca^{2+} elevation could not significantly contribute to PTP, especially because not all of it would trigger transmitter release. Consistent with this idea, it has been shown that activation of Ca^{2+}-dependent PKCα/β is the main mechanism underlying PTP at the calyx of Held ($\sim$ 80%; Korogod *et al.*, 2007; Fioravante *et al.*, 2011). Neither the basal release properties, the $[Ca^{2+}]_{residual}$, nor the AP-evoked Ca^{2+} influx were affected in PKCα/β double knockouts (Fioravante *et al.*, 2011). In addition, the increase in AP-evoked Ca^{2+} influx following tetanic stimulation was unchanged, indicating that the much reduced PTP in knockout animals did not result from impaired facilitation of VGCCs. PKCα/β

may induce PTP by enlarging the RRP (likely via phosphorylation of Munc18-1) and/or increasing the Ca^{2+} sensitivity of vesicle fusion (Yawo, 1999; Wu and Wu, 2001; Korogod *et al.*, 2007; Fioravante *et al.*, 2011).

1.3.5.3 Ca^{2+}-dependent recovery from depression

According to the simplest form of the depletion model, short-term synaptic depression occurs as a result of a slow and constant rate of replenishment of the RRP (Betz, 1970). However, at a number of synapses, recovery from depression is accelerated by high-frequency stimulation (Dittman and Regehr, 1998; Wang and Kaczmarek, 1998; Fuhrmann *et al.*, 2004). As chelation of the intracellular Ca^{2+} with EGTA reduced activity-dependent recovery from depression, it has been suggested that Ca^{2+}, accumulating in the presynaptic terminals during repetitive stimulation, plays a central role in this process (Dittman and Regehr, 1998; Wang and Kaczmarek, 1998; Fuhrmann *et al.*, 2004). In support of this, Hosoi *et al.* (2007) showed that, at the calyx of Held, the rate of recruitment of fast releasing synaptic vesicles increases linearly with the global Ca^{2+} elevation (see also Gomis *et al.*, 1999). This process, which is mediated by CaM, allows fast releasing vesicles to be recruited up to 10× faster than at rest (Sakaba and Neher, 2001; Hosoi *et al.*, 2007). Therefore, Ca^{2+}-dependent vesicle recruitment represents a major mechanism that maintains synaptic transmission under conditions that would otherwise render synapses ineffective. How Ca^{2+}-CaM accelerates vesicle recruitment and whether it accounts for activity-dependent recovery from depression at other synapses remain to be determined.

1.4 Determinants of presynaptic Ca^{2+} dynamics

Factors that regulate the spatiotemporal dynamics of an intracellular Ca^{2+} elevation can be divided into three main categories: the source of Ca^{2+}, Ca^{2+} buffers, and Ca^{2+} sequestration mechanisms. In a presynaptic nerve terminal, an increase in $[Ca^{2+}]_i$ typically arises from Ca^{2+} influx through voltage- or ligand-gated Ca^{2+} channels

(specific as well as non-specific for Ca^{2+}). Ca^{2+} can also be released from intracellular stores through the ryanodine and/or IP_3 receptors (RyR and IP_3R, respectively). Upon their activation, these Ca^{2+} channels allow Ca^{2+} to quickly flow down its electrochemical gradient ($\sim 10^3$ ions/ms), and thus, produce a rapid increase in $[Ca^{2+}]_i$. Through their interactions with Ca^{2+} (binding and unbinding), Ca^{2+} buffers shape the amplitude, spatial distribution, and time course of the Ca^{2+} rise. Finally, active transport mechanisms (and the mitochondrial uniporter) function together to return $[Ca^{2+}]_i$ to the resting level.

1.4.1 Sources of Ca^{2+} influx

1.4.1.1 Voltage-gated Ca^{2+} channels

In most nerve terminals, VGCCs provide the main source of Ca^{2+} for evoked transmitter release. VGCCs are heteromeric complexes, each consisting of an α_1 pore-forming subunit and four associated subunits (α_2, β, or γ). They can be classified into different functional groups, depending on the molecular identity of the α_1 subunit: P/Q-type or $Ca_v2.1$ (containing α_{1A}), N-type or Ca_v 2.2 (α_{1B}), L-type or $Ca_v1.2 - 1.3$ (α_{1C} or α_{1D}, respectively), R-type or $Ca_v2.3$ (α_{1E}), and T-type or $Ca_v3.1 - 3.3$ (α_{1G}, α_{1H}, or α_{1I}, respectively; Catterall, 2011). At neocortical excitatory synapses, evoked transmitter release is predominantly mediated by Ca^{2+} influx through P/Q- and N-type Ca^{2+} channels (Iwasaki *et al.*, 2000; Koester and Sakmann, 2000; Rozov *et al.*, 2001; Millan *et al.*, 2003; Ali and Nelson, 2006).

Voltage-dependent activation and deactivation. Thus far, a direct measurement and detailed characterisation of presynaptic Ca^{2+} currents has only been achieved at two nerve terminals in the mammalian CNS: the calyx of Held and the hippocampal mossy fibre bouton (Borst and Sakmann, 1996, 1998a; Geiger and Jonas, 2000; Bischofberger *et al.*, 2002; Li *et al.*, 2007b). In these terminals, the activation of P/Q- and N-type Ca^{2+} channels depends steeply on the membrane potential and

has a high threshold (at membrane potentials ≥ -40 mV; Borst and Sakmann, 1998a; Bischofberger *et al.*, 2002; Li *et al.*, 2007b). These channels also exhibit rapid activation and deactivation kinetics, with time constants in the sub-millisecond range. As a result, an AP elicits a brief Ca^{2+} current, starting at the peak of the AP and ending before or when the AP repolarisation phase is complete (half-width ≤ 0.5 ms).

All of these findings are consistent with previous measurements of the presynaptic Ca^{2+} current at the squid giant synapse (Llinas *et al.*, 1981a; Augustine and Eckert, 1984; Augustine *et al.*, 1985). However, compared to those in the invertebrate nerve terminal (Pumplin *et al.*, 1981), presynaptic VGCCs in the mammalian CNS are more effectively activated by a single AP, with the peak open probability reaching $70 - 90\%$ of the maximal value (Borst and Sakmann, 1998a; Bischofberger *et al.*, 2002). Nonetheless, because their gating properties are strongly dependent on the membrane potential, any changes in the AP waveform, particularly during high frequency stimulation, will significantly affect the presynaptic Ca^{2+} currents and therefore transmitter release (Jackson *et al.*, 1991; Geiger and Jonas, 2000; Bischofberger *et al.*, 2002).

Ca^{2+}-dependent facilitation and inactivation. As previously mentioned, P/Q-type Ca^{2+} channels show both Ca^{2+}-dependent facilitation and inactivation. During a train of APs, the amplitude to the Ca^{2+} current undergoes a frequency-dependent enhancement, followed by a gradual decline (Cuttle *et al.*, 1998). Based on mutagenesis studies, a model has been proposed in which these two processes involve the two lobes of CaM binding to two adjacent sites on the Ca^{2+} channels: the high-affinity C-terminal lobe binding to an IQ-like domain, and the low-affinity N-terminal lobe to a downstream CaM-binding domain (Catterall, 2011). Thus, a small increase in $[Ca^{2+}]_i$ induces facilitation through the former interaction, whereas a larger Ca^{2+} elevation, during sustained stimulation, causes inactivation through the latter.

Direct interaction with the release machinery. A cytoplasmic region, called the synaptic protein interaction (synprint) site, on P/Q- and N-type Ca^{2+} channels binds directly to SNAP-25 and syntaxin-1A (Sheng *et al.*, 1994; Rettig *et al.*, 1996). This physical link ensures that the VGCCs are positioned close to readily releasable vesicles, thereby reducing the diffusional distance of Ca^{2+} and enhancing the speed and efficacy of transmitter release. In support of this idea, a synprint peptide, which binds to syntaxin and disrupts its interaction with N-type Ca^{2+} channels, inhibits synchronous transmission (Mochida *et al.*, 1996). Rettig *et al.* (1997) showed that this inhibition is caused by a decrease in the Ca^{2+} sensitivity of vesicle fusion, most likely as a result of a longer distance between readily releasable vesicles and open Ca^{2+} channels. P/Q- and N-type Ca^{2+} channels have also been shown to bind directly to Syt1 (Charvin *et al.*, 1997; Sheng *et al.*, 1997).

Although both P/Q- and N-type Ca^{2+} channels can directly interact with the release machinery, at the young calyx of Held, P/Q-type Ca^{2+} channels trigger transmitter release more effectively (Wu *et al.*, 1999). This is because N-type Ca^{2+} channels are diffusely expressed throughout the calyx, even though some of them are present at transmitter release sites (Wu *et al.*, 1999). In contrast, P/Q-type Ca^{2+} channels are predominantly co-localised in clusters with synaptotagmin at the release face. As a result, Ca^{2+} influx through P/Q-type channels drives fusion of readily releasable vesicles more effectively. The different localisation of these VGCCs may reflect competition between them for interaction with SNARE proteins (Rettig *et al.*, 1997; Wu *et al.*, 1999; Cao and Tsien, 2010). N-type Ca^{2+} channels, though not effective at controlling transmitter release, may contribute to the global Ca^{2+} elevation that supports asynchronous transmission and short-term synaptic plasticity (Wu *et al.*, 1999).

1.4.1.2 Presynaptic iGluRs

Although iGluRs are traditionally thought to be located postsynaptically, recent anatomical and electrophysiological studies have demonstrated their presynaptic expression and important roles in synaptic transmission.

Ca^{2+} permeability. In the CNS, most functional iGluRs are homo- or heteromeric complexes of four subunits from the same family (Mayer, 2005). There are four AMPA (GluR1 − 4), seven NMDA (NR1, NR2A − D, and NR3A − B), and five kainate (GluR5 − 7 and KA1 − 2) receptor subunits. Whilst the majority of AMPA receptors are permeable to only Na^+ and K^+, some AMPA and kainate receptors, and all NMDA receptors are also permeable to Ca^{2+}. The Ca^{2+} permeability of AMPA and kainate receptors is governed by the GluR2 and GluR5/6 subunits, respectively; incorporation of a specific GluR2 or GluR5/6 subunit, with glutamine/arginine ribonucleic acid-editing, renders the channel impermeable to Ca^{2+} (Dingledine *et al.*, 1999; Lerma, 2003). Ca^{2+}-permeable AMPA and kainate receptors, together with NMDA receptors, are subject to a voltage-dependent block. Ca^{2+}-permeable AMPA and kainate receptors are blocked by intracellular polyamines at depolarised membrane potentials (−40 to 40 mV; Jonas and Burnashev, 1995). In contrast, at the resting membrane potential of ~ -65 mV, NMDA receptors are partially blocked by extracellular Mg^{2+}, which is relieved upon membrane depolarisation (Mayer *et al.*, 1984; Nowak *et al.*, 1984). Activation of NMDA receptors also requires simultaneous binding of the co-agonist glycine or D-serine (Johnson and Ascher, 1987; Shleper *et al.*, 2005).

Expression and functional consequences. Electrophysiological studies have shown that the expression of presynaptic iGluRs is pathway-specific and developmentally regulated (Engelman and MacDermott, 2004; Banerjee *et al.*, 2016). For instance, within layer 5 of the developing mouse visual cortex (P12 − 20), presynaptic NMDA receptors enhanced transmitter release at synapses made by pyramidal cells onto other pyramidal or Martinotti cells (Buchanan *et al.*, 2012). However, such an effect was absent at synapses made by the same pyramidal cells onto basket cells. Using glutamate uncaging and Ca^{2+} imaging of synaptic boutons of these layer 5 pyramidal neurons, this study showed that the enhancement of glutamate release was likely a result of Ca^{2+} influx through presynaptic NMDA receptors. Consistent with the synapse-specificity of the modulation, the intracellular Ca^{2+} rises produced by somatically evoked APs and glutamate uncaging summed supralinearly in only

$\sim$ 50% of the imaged boutons. Such a supralinear summation presumably indicates expression of NMDA receptors.

It remains unclear how presynaptic NMDA receptors can enhance transmitter release evoked by the first AP in a train. Their maximal activation requires the presence of glutamate as well as membrane depolarisation; the latter is to relieve the Mg^{2+} block. In addition, compared to the AP-evoked Ca^{2+} current mediated by VGCCs, NMDA receptors generally produce a very slowly rising current ($\tau_{rise} = 10 - 50$ ms; Wyllie *et al.*, 1998). Nonetheless, due to their high affinity for glutamate (half-maximal effective concentration or $EC_{50} = 0.5 - 2.0$ μM; Dingledine *et al.*, 1999), presynaptic NMDA receptors might be tonically activated by the ambient glutamate in the synaptic cleft ($0.5 - 5.0$ μM; Sah *et al.*, 1989; Le Meur *et al.*, 2007; Featherstone and Shippy, 2008). Therefore, upon membrane depolarisation which removes the Mg^{2+} block, an increase in the tonic current of presynaptic NMDA receptors might be be able to augment the Ca^{2+} signal generated by VGCCs, and thus, enhance vesicle fusion.

Activation of presynaptic iGluRs can also affect spontaneous transmitter release and synaptic plasticity (Engelman and MacDermott, 2004; Banerjee *et al.*, 2016). At some synapses, the role of presynaptic iGluRs is likely a result of Ca^{2+} influx into the nerve terminals, with or without subsequent Ca^{2+}-induced Ca^{2+} release (see below; Lauri *et al.*, 2003; Rossi *et al.*, 2008; Buchanan *et al.*, 2012; Rossi *et al.*, 2012). However, at many synapses, presynaptic iGluRs modulate multiple aspects of synaptic transmission not by generating a Ca^{2+} current and directly affecting the release machinery. Instead, their activation causes a depolarisation of the nerve terminals or even triggers a second messenger cascade that is independent of ion flow (Engelman and MacDermott, 2004; Banerjee *et al.*, 2016).

1.4.2 Intracellular Ca^{2+} release channels

A major constituent of intracellular Ca^{2+} stores is the smooth endoplasmic reticulum (ER), which is a three-dimensional network formed by an endomembrane. In

neurons, the smooth ER extends from the soma to most compartments, including dendritic spines and presynaptic nerve terminals (Westrum and Gray, 1986; Hartter *et al.*, 1987). In a resting cell, the concentration of free Ca^{2+} in the smooth ER ($[Ca^{2+}]_{ER}$) ranges from 100 μM to 3 mM (Montero *et al.*, 1995; Palmer *et al.*, 2004; de Juan-Sanz *et al.*, 2017), which is three to four orders of magnitude higher than that in the cytoplasm. Ca^{2+} can be released from the smooth ER through ryanodine and/or IP_3 receptors. As Ca^{2+} is an agonist of these receptors, an increase in $[Ca^{2+}]_i$ following their activation will be amplified by further release of Ca^{2+} from intracellular stores. This process, called Ca^{2+}-induced Ca^{2+} release (CICR), was first described in cardiac muscles, in which Ca^{2+} influx through L-type VGCCs causes a large release of Ca^{2+} from the sarcoplasmic reticulum (SR; Fabiato and Fabiato, 1975, 1978).

Presynaptic expression of both IP_3 and ryanodine receptors has been reported in the cerebellum, hippocampus, and neocortex (Sharp *et al.*, 1993; Padua *et al.*, 1996; Llano *et al.*, 2000). Consistent with these observations, CICR has been shown to underlie evoked and spontaneous Ca^{2+} transients in a number of presynaptic nerve terminals (Llano *et al.*, 2000; Emptage *et al.*, 2001; Liang *et al.*, 2002; Conti *et al.*, 2004; Scott and Rusakov, 2006). Whilst the idea that intracellular Ca^{2+} release can trigger spontaneous vesicle fusion is gaining acceptance, its contribution to evoked transmission remains controversial. The extent to which presynaptic stores provides Ca^{2+} for evoked transmitter release may depend on the local environment around transmitter release sites and the experimental protocols used. In particular, studies that reported a role of CICR in synaptic transmission and short-term plasticity were often performed at near physiological temperatures ($30 - 36$ °C in Emptage *et al.*, 2001; Choy, 2011; but room temperature in Galante and Marty, 2003; Lauri *et al.*, 2003), whereas those that showed no effects were done at room temperature (Carter *et al.*, 2002; Breustedt and Schmitz, 2004).

1.4.2.1 Ryanodine receptors

There are three main isoforms of RyRs in mammalian cells. Each of them, coded for by a different gene, forms a large homo-tetrameric complex, with a central ion-conducting pore (Wagenknecht *et al.*, 1989; Fill and Copello, 2002). RyR1 and RyR2 are predominantly expressed in skeletal and cardiac muscles, respectively, whereas RyR3 is found, to some extent, in most tissues. Expression of all three receptor isoforms has been reported in neurons, with RyR2 being the most abundant (Bouchard *et al.*, 2003). Compared to VGCCs, RyRs have a large unitary conductance but a low selectivity for Ca^{2+} (Fill and Copello, 2002).

Bi-phasic dependence on $[Ca^{2+}]_i$. The open probability of RyRs displays a bell-shaped dependence on $[Ca^{2+}]_i$, as they are activated by low $[Ca^{2+}]_i$ ($\geq$ 100 nM) but inhibited when $[Ca^{2+}]_i$ exceeds 100 μM (circles in Fig. 1.7A; Bull and Marengo, 1993; Xu *et al.*, 1996; Chen *et al.*, 1997; Xu and Meissner, 1998). These two processes occur as a result of Ca^{2+} binding to two different cytoplasmic sites on RyRs, one with a high affinity and the other with a low affinity, respectively ($\sim$ 1 μM and 1 mM). A cytoplasmic site that causes inactivation of RyRs at $1-10$ μM of $[Ca^{2+}]_i$ has also been suggested, although its existence has not been conclusively confirmed or dismissed (Fill and Copello, 2002; Laver, 2007).

Modulation. The activation of RyRs is strongly modulated by luminal Ca^{2+}, cytosolic ATP, and cytosolic Mg^{2+} (Fig. 1.7A; Xu *et al.*, 1996; Xu and Meissner, 1998; Fill and Copello, 2002). An increase in $[Ca^{2+}]_{ER}$ or in the concentration of cytosolic ATP promotes the opening of RyRs, whereas high concentrations of cytosolic Mg^{2+} inhibit it. It has been proposed that, in the presence of cytosolic ATP, Ca^{2+} binding to a luminal site on RyRs is sufficient to activate the channels (Laver, 2007). However, the maximal open probability can only be achieved by Ca^{2+} binding to the cytoplasmic activation site. The ubiquitous Ca^{2+} sensor CaM can either activate or inhibit RyR1 and RyR3, at low or high $[Ca^{2+}]_i$, respectively

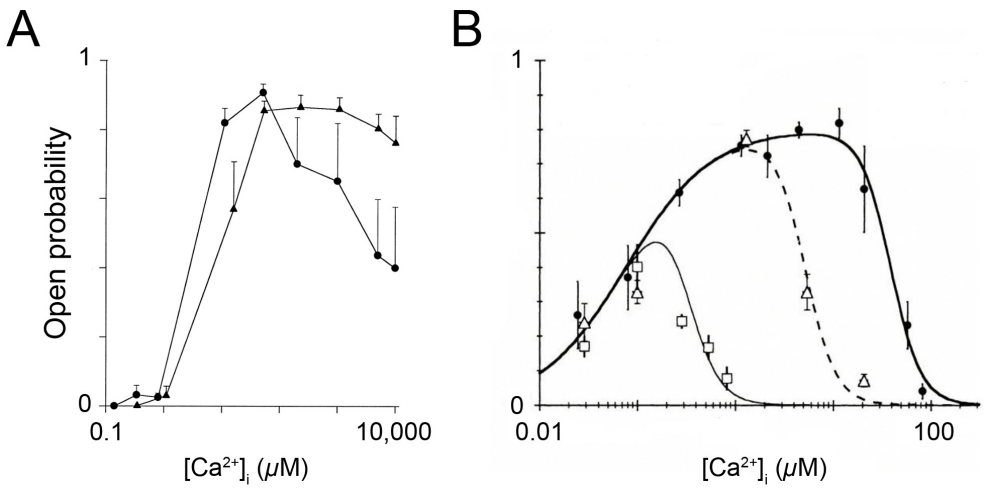

Figure 1.7: The open probability of ryanodine and IP_3 receptors as a function of $[Ca^{2+}]_i$. (A) The open probability of cardiac RyRs determined with or without 2 mM cytosolic Mg^{2+}-ATP (triangles or circles, respectively). Adapted from Xu *et al.* (1996). (B) The open probability of the rat IP_3R-3 measured in the presence of IP_3 (filled circles: 10 μM; triangles: 33 nM; squares: 20 nM). Adapted from Mak *et al.* (2001b).

(Tripathy *et al.*, 1995; Chen *et al.*, 1997; Fruen *et al.*, 2000). For RyR2, only inhibition by Ca^{2+}-CaM has been reported (Fruen *et al.*, 2000).

Pharmacology. Compounds that are commonly used to activate or block RyRs include ryanodine, ruthenium red, and caffeine.

Ryanodine. The plant alkaloid, ryanodine, was first found to promote or inhibit Ca^{2+} release from cardiac myocytes and SR membrane vesicles, in a concentration-dependent manner (10 nM to 10 μM, or $\geq$ 10 μM, respectively; Meissner, 1986; Hansford and Lakatta, 1987; Lattanzio *et al.*, 1987). It binds RyRs with a very high specificity. In fact, RyRs were originally called triad junctional foot proteins, due to their appearance in skeletal muscles under electron microscopy (Franzini-Armstrong, 1975). After being purified from skeletal and cardiac muscles, and found to bind [^{3}H]-ryanodine, RyRs acquired their present name (Inui *et al.*, 1987a,b; Lai *et al.*, 1988).

Subsequent single-channel recordings revealed the presence of high- and low-affinity binding sites for ryanodine on RyRs (Buck *et al.*, 1992). These binding sites have been

proposed to account for the different effects of ryanodine on SR Ca^{2+} release. Ca^{2+} binding to the low-affinity binding site causes a complete closure of the channels, thereby inhibiting Ca^{2+} release at high micromolar concentrations (≥ 200 μM; Buck *et al.*, 1992). Ca^{2+} binding to the high-affinity binding sites, on the other hand, increases the open probability of RyRs, and thus, stimulates Ca^{2+} release at low nanomolar to low micromolar concentrations. However, in this concentration range, the extent to which ryanodine increases Ca^{2+} release is strongly concentration-dependent. This is because, although a low concentration of ryanodine ($5 - 40$ nM) does not affect the single-channel conductance, higher concentrations (50 nM to 70 μM) stabilise the channels in a sub-conducting state ($1/4 - 1/2$ of the maximal conductance). As a result, the magnitude of Ca^{2+} release is reduced with an increasing concentration of ryanodine.

Ruthenium red. Ruthenium red is a very potent inhibitor of SR Ca^{2+} release (half-maximal inhibiting concentration or $IC_{50} = 0.01 - 1$ μM; Chamberlain *et al.*, 1984; Palade, 1987; Ma, 1993). Similar to ryanodine, it modifies the gating and conductance of RyRs by multiple mechanisms, depending on the channel activity, SR membrane potential, and whether it is exposed to the cytosolic or luminal side of RyRs (Xu *et al.*, 1999). However, in contrast to ryanodine, ruthenium red is a highly non-specific blocker of RyRs. It has been shown to inhibit a multitude of Ca^{2+} channels, including VGCCs ($IC_{50} = 1 - 70$ μM; Cibulsky and Sather, 1999), transient receptor potential (TRP) channels ($IC_{50} = 0.1 - 100$ μM; Jia *et al.*, 2004; Voets *et al.*, 2004), and possibly IP_3Rs (Vites and Pappano, 1992).

Caffeine. Caffeine increases the sensitivity of RyRs to both $[Ca^{2+}]_i$ and $[Ca^{2+}]_{ER}$ (Porta *et al.*, 2011), without affecting their single-channel conductance (Rousseau *et al.*, 1988). At rest, when $[Ca^{2+}]_i = 100$ nM and $[Ca^{2+}]_{ER} = 0.1 - 1.0$ mM, caffeine stimulates the opening of RyRs with an EC_{50} of ~ 5 mM (Porta *et al.*, 2011). However, it inhibits IP_3Rs with an IC_{50} of ~ 2 mM (Bezprozvanny *et al.*, 1994).

1.4.2.2 IP_3 receptors

The IP_3R family in mammalian cells also comprises three distinct genes, encoding IP_3R-1, IP_3R-2, and IP_3R-3. Each receptor isoform forms a homo- or hetero-tetramer, again with a central ion-conducting pore (Foskett *et al.*, 2007). All three isoforms have been found expressed in the brain, with IP_3R-1 being the most abundant (Verkhratsky, 2005). Compared to RyRs, IP_3Rs have a similar selectivity for Ca^{2+}, but a two- to three-fold smaller unitary conductance (Fill and Copello, 2002; Foskett *et al.*, 2007).

Bi-phasic dependence on $[Ca^{2+}]_i$. Cytosolic Ca^{2+} is a true agonist of IP_3Rs, whereas IP_3 regulates Ca^{2+}-dependent inhibition of IP_3Rs (Mak *et al.*, 1998). Patch-clamp recordings have shown that, even in the presence of saturating concentrations of IP_3, the open probability of IP_3Rs is still low at a resting $[Ca^{2+}]_i$ of ~ 50 nM (filled circles in Fig. 1.7B; Kaftan *et al.*, 1997; Mak *et al.*, 1998, 2001b; Ionescu *et al.*, 2006). An increase in $[Ca^{2+}]_i$ to less than 1 μM activates IP_3Rs, with the half-maximal open probability achieved at $70 - 210$ nM of cytosolic Ca^{2+}. However, IP_3Rs are inhibited when $[Ca^{2+}]_i$ exceeds $1 - 10$ μM. The sensitivity of these receptors to Ca^{2+}-dependent inhibition is highly variable, even with a saturating concentration of IP_3. In fact, some studies have demonstrated a severe reduction or an absence of inhibition (Foskett *et al.*, 2007). Similar to the proposed inactivation of RyRs at $1 - 10$ μM of $[Ca^{2+}]_i$, the Ca^{2+}-dependent inhibition of IP_3Rs likely serves as a self-regulating mechanism to prevent excessive CICR and Ca^{2+} overload.

Modulation by IP_3. IP_3 is a hydrolytic product of the plasma membrane phospholipid PIP_2 by phospholipase C (PLC). IP_3 regulates the open probability of IP_3Rs by modulating their sensitivity to Ca^{2+}-dependent inhibition, without affecting their activation by Ca^{2+} (Fig. 1.7B; Foskett *et al.*, 2007). At a low or sub-saturating concentration of IP_3, IP_3Rs are inhibited by $0.1 - 1$ μM of $[Ca^{2+}]_i$ (Kaftan *et al.*, 1997; Mak *et al.*, 1998, 2001b; Ionescu *et al.*, 2006). An increase in the concentration of IP_3

causes this inhibition to occur at a higher $[Ca^{2+}]_i$, thereby expanding the range of $[Ca^{2+}]_i$ over which IP_3Rs are active. The IP_3 concentration at which such an effect is half-maximal ranges from 50 nM for *Xenopus* IP_3R-1 and rat IP_3R-3 (Mak *et al.*, 1998, 2001b), 400 nM for insect IP_3Rs (Ionescu *et al.*, 2006), to 10 μM for canine cerebellar IP_3R-1 (Kaftan *et al.*, 1997). The reduced sensitivity of canine cerebellar IP_3R-1 is consistent with the finding that $\geq$ 10 μM of IP_3 was required to induce intracellular Ca^{2+} release in rat cerebellar Purkinje neurons (Khodakhah and Ogden, 1995). In this study, the concentration of IP_3 was raised by flash photolysis of caged IP_3. Therefore, the low sensitivity of store release was not a result of rapid hydrolysis of IP_3, but likely due to a low affinity of the IP_3R. Such a low IP_3-binding affinity of cerebellar IP_3Rs may contribute to the fast kinetics of the observed Ca^{2+} release (Khodakhah and Ogden, 1995).

The fact that IP_3 can modulate the biphasic Ca^{2+} dependence of IP_3Rs means that activation of metabotropic receptors can transform highly localised signals to more global elevations in $[Ca^{2+}]_i$ (Foskett *et al.*, 2007). In the absence of IP_3, the opening of IP_3Rs will most likely produce a small and brief rise in $[Ca^{2+}]_i$. This is because Ca^{2+} released from one channel will suppress the opening of its neighbours. During synaptic activity, activation of metabotropic receptors coupled to $G_{q/11}$ proteins will promote hydrolysis of PIP_2 and lead to an increase in the concentration of IP_3. This will in turn alleviate Ca^{2+}-dependent inhibition of IP_3Rs, enhance intracellular Ca^{2+} release, and give rise to increases in $[Ca^{2+}]_i$ with much higher amplitudes, longer duration, and larger spatial spread (Manita and Ross, 2009; Miyazaki and Ross, 2013).

Other modulators. The activity of IP_3Rs is also regulated by luminal Ca^{2+} and cytosolic ATP. An increase in $[Ca^{2+}]_{ER}$ decreases the open probability of IP_3Rs (Bezprozvanny and Ehrlich, 1994). In comparison, a high concentration of cytosolic ATP increases their sensitivity to Ca^{2+}-dependent activation, thereby extending the range of $[Ca^{2+}]_i$ over which IP_3Rs are open to lower values (Mak *et al.*, 1999, 2001a). Increasing the concentration of cytosolic ATP can also change the sensitivity of Ca^{2+}-dependent inhibition (Mak *et al.*, 1999, 2001a; Tu *et al.*, 2005). Although Ca^{2+} binding

to CaM has been suggested to modulate IP_3R activity, there is little evidence to support this proposition (Foskett *et al.*, 2007).

Pharmacology. Heparin and 2-aminoethoxydiphenyl borate (2-APB) are commonly used to block IP_3R-mediated Ca^{2+} release. Their actions on IP_3Rs are less well-studied than those of ryanodine on RyRs. In addition, unlike ryanodine, these compounds lack specificity.

Heparin. Heparin is a potent blocker of Ca^{2+} release through IP_3Rs, with an IC_{50} of $\sim$ 20 nM (Ghosh *et al.*, 1988). However, at a resting $[Ca^{2+}]_i$ of 100 nM, this concentration of heparin also half-maximally activates RyRs (Bezprozvanny *et al.*, 1993).

2-APB. In rat cerebellar microsomes (*i.e.* ER vesicles), 2-APB inhibits Ca^{2+} release induced by 100 nM of IP_3 ($IC_{50} \sim 40$ μM; Maruyama *et al.*, 1997). However, its effect is likely dependent on the IP_3R isoform and the cytosolic concentration of IP_3 (Bootman *et al.*, 2002). 2-APB also blocks the sarco/endoplasmic reticulum Ca^{2+}-ATPase (SERCA; $IC_{50} \sim 100$ μM; Missiaen *et al.*, 2001) and store-operated Ca^{2+} entry ($IC_{50} \sim 10$ μM; Gregory *et al.*, 2001; Kukkonen *et al.*, 2001). 2-APB additionally modulates a range of TRP channels (IC_{50} or $EC_{50} \geq 10$ μM; Hu *et al.*, 2004; Li *et al.*, 2006). Simkus and Stricker (2002a) showed that, in layer 2 pyramidal neurons of the rat somatosensory cortex, 14 μM of 2-APB produced a maximal inhibition of IP_3R-mediated Ca^{2+} release, without significantly affecting other mechanisms underlying Ca^{2+} homeostasis.

1.4.2.3 Ca^{2+} leak channels

In many cells and cellular compartments, including presynaptic nerve terminals, blockade of SERCA pumps causes a reduction in $[Ca^{2+}]_{ER}$, independently of ryanodine and IP_3 receptors (Camello *et al.*, 2002; de Juan-Sanz *et al.*, 2017). Therefore, it is generally accepted that intracellular Ca^{2+} stores exhibit a passive Ca^{2+} leak. The

rate of this process ranges from 10 to 400 μM/min, depending on the cell type and experimental temperature (Camello *et al.*, 2002). As $[Ca^{2+}]_{ER}$ is typically $0.1 - 3.0$ mM at rest (Montero *et al.*, 1995; Palmer *et al.*, 2004; de Juan-Sanz *et al.*, 2017), the passive Ca^{2+} leak has been thought to cause a complete depletion of Ca^{2+} stores in a few minutes (Camello *et al.*, 2002). However, de Juan-Sanz *et al.* (2017) showed that, in synaptic boutons of cultured hippocampal neurons, although blockade of SERCA pumps caused $[Ca^{2+}]_{ER}$ to decrease with a time constant of 25 s, $\sim 2/3$ of the resting or initial concentration remained, without any further reduction (from $\sim$ 150 to 100 μM).

Several candidates of ER leak channels have been proposed. These include the translocon, a protein complex implicated in the translocation of polypeptides (Flourakis *et al.*, 2006), pannexin-1 (Vanden Abeele *et al.*, 2006), and presenilins (Tu *et al.*, 2006; but see Shilling *et al.*, 2012). Mutations in presenilins have been implicated in the pathogenesis of Alzheimer's disease, likely by impairing the regulation of presynaptic Ca^{2+} dynamics and altering the induction of synaptic plasticity (Zhang *et al.*, 2009).

1.4.3 Endogenous Ca^{2+} buffers

A large fraction of Ca^{2+} ions that enter a nerve terminal is rapidly bound by endogenous Ca^{2+}-binding proteins. These proteins possess different Ca^{2+}-binding sites, predominantly EF-hand motifs, C2 domains, and four annexin repeats (Niki *et al.*, 1996). A large number of endogenous Ca^{2+} binding proteins function as Ca^{2+} sensors, which couple an intracellular Ca^{2+} rise to specific signalling cascades. If expressed at high enough concentrations, Ca^{2+} sensors can also modulate intracellular Ca^{2+} dynamics, and thus, act as Ca^{2+} buffers (Schwaller, 2010; Faas *et al.*, 2011). However, the term "Ca^{2+} buffers" often refer to a small subset of cytosolic proteins with EF-hand motifs, including parvalbumin, calbindin-D28k, and calretinin (Schwaller, 2010).

Table 1.1: Properties of commonly known exogenous and endogenous Ca^{2+} buffers.

	BAPTA[#]	EGTA[#]	Parvalbumin[$]	Calbindin-D28k[&]	Calretinin[+]
k_{on} ($M^{-1}s^{-1}$)	4.5×10^8	2.7×10^6	6×10^6	7.5×10^7	1.8×10^6 (T) 3.1×10^8 (R)
k_{off} (s^{-1})	79	0.5	~ 1	29.5	53 (T) 20 (R)
K_d (μM)	0.18	0.18	$0.15 - 0.25$	0.39	28 (T) 0.068 (R) 1.4 (Apparent)
D_B ($\mu m^2 s^{-1}$)	220	220	$12 - 43$	~ 25	~ 25

[#]Allbritton *et al.* (1992); Naraghi and Neher (1997); Naraghi (1997); [$]Maughan and Godt (1999); Lee *et al.* (2000b); Schmidt *et al.* (2003, 2007); Schwaller (2010); [&]Schmidt *et al.* (2005); Faas *et al.* (2011); [+]Ca^{2+} binding to calretinin is highly cooperative: after the first binding, the state changes from tense (T) to relaxed (R; Faas *et al.*, 2007).

In general, a Ca^{2+} buffer will attenuate an intracellular Ca^{2+} rise and prolong the time it takes for $[Ca^{2+}]_i$ to return to the resting level. Nonetheless, how and the extent to which a Ca^{2+} buffer affects the spatiotemporal dynamics of an intracellular Ca^{2+} rise depends on several parameters, including its concentration, Ca^{2+} binding affinity (K_d), kinetics of Ca^{2+} binding and unbinding (k_{on} and k_{off}, respectively), and mobility (D_B; Table 1.1). These factors, in turn, depend on the specifics of the intracellular environment, particularly the presence of ions or molecules that bind to the protein (Lee *et al.*, 2000b; Schmidt *et al.*, 2005, 2007). In general, Ca^{2+} buffers are more highly expressed in inhibitory interneurons than in excitatory neurons (Hof *et al.*, 1999). However, parvalbumin, calretinin, and calbindin-D28k have all been found in the axons and nerve terminals of some excitatory neurons: parvalbumin ($\sim$ 50 μM) and calretinin at the calyx of Held (Felmy and Schneggenburger, 2004; Muller *et al.*, 2007), and calbindin-D28k in hippocampal mossy fibres ($\sim$ 40 μM; Blatow *et al.*, 2003; Muller *et al.*, 2005).

1.4.3.1 Ca^{2+} binding affinity and kinetics

Similar to EGTA and BAPTA, these endogenous buffers bind Ca^{2+} with a high affinity (Lee *et al.*, 2000b; Nagerl *et al.*, 2000; Faas *et al.*, 2007, 2011). However, whether they modulate the Ca^{2+} signal around open VGCCs, or only affect the slowly rising, global Ca^{2+} elevation, depends on their Ca^{2+} binding rates. At a resting $[Ca^{2+}]_i$ of $50 - 100$ nM, the majority of Ca^{2+}-binding sites on parvalbumin are occupied by Mg^{2+} ($> 80\%$; Olinger *et al.*, 2012). When an AP produces an intracellular Ca^{2+} elevation, Mg^{2+} has to dissociate from these binding sites before Ca^{2+} can bind. As a result, under physiological conditions, parvalbumin has a slow Ca^{2+} on-rate, similar to that of EGTA (Table 1.1). This means that, if readily releasable vesicles are tightly coupled to Ca^{2+} channels, parvalbumin may not be able to interfere with synchronous release (Caillard *et al.*, 2000), unless it is highly expressed ($\sim$ 1 mM; Eggermann and Jonas, 2011). In comparison, calbindin-D28k, which is a faster buffer, likely attenuates $[Ca^{2+}]_{local}$, thereby hindering vesicle fusion (Blatow *et al.*, 2003).

Additionally, a high affinity and fast kinetic buffer, such as calbindin, may promote *PPF*, as its saturation by the residual Ca^{2+} will produce a larger $[Ca^{2+}]_{local}$ in response to a subsequent AP (Klapstein *et al.*, 1998; Rozov *et al.*, 2001; Blatow *et al.*, 2003). In contrast, a slow buffer, such as parvalbumin, accelerates the initial decay of the residual Ca^{2+}, and thus, inhibits *PPF* (Caillard *et al.*, 2000; Collin *et al.*, 2005a; Muller *et al.*, 2007). Nonetheless, such an inhibition would only be present for as long as the incoming Ca^{2+} does not saturate the slow buffer. During sustained high-frequency stimulation, the slow buffer may become saturated (Lee *et al.*, 2000b). This may, in turn, allow synaptic facilitation to occur, unless depression becomes dominant as a result of vesicle depletion or inactivation of the presynaptic Ca^{2+} current (Forsythe *et al.*, 1998; Xu and Wu, 2005).

Although preventing synaptic facilitation, a slow buffer can enhance asynchronous transmitter release. As a result of its slow binding and unbinding kinetics, parvalbumin may accumulate a significant amount of Ca^{2+} during a train of APs. Once the AP train terminates, it acts as a long lasting source of Ca^{2+}, and hence,

prolong the decay time course of the residual Ca^{2+} (Lee *et al.*, 2000b). Consequently, asynchronous transmitter release extends for longer in the presence of parvalbumin (Collin *et al.*, 2005a).

1.4.3.2 Intracellular mobility

The intracellular mobility of an endogenous buffer also determines how it shapes presynaptic Ca^{2+} dynamics, and thus, regulates transmitter release and synaptic plasticity. The diffusion coefficient of free Ca^{2+} is $\sim 220\ \mu m^2 s^{-1}$ (Allbritton *et al.*, 1992). However, in intact cells, its apparent diffusion coefficient is only $10 - 20\ \mu m^2 s^{-1}$, as the majority of Ca^{2+} is bound to endogenous fixed buffers (Allbritton *et al.*, 1992; Gabso *et al.*, 1997). In presynaptic terminals, candidates for endogenous fixed or poorly mobile buffers include negatively charged phospholipid groups on the intracellular face of the presynaptic membrane, active zone proteins with Ca^{2+}-binding sites (*e.g.* synaptotagmins and RIMs), the ubiquitous Ca^{2+} sensor CaM, and membrane-associated Ca^{2+}-binding kinases (Schwaller, 2010; Faas *et al.*, 2011; Eggermann *et al.*, 2012; Matthews and Dietrich, 2015).

Following a Ca^{2+} influx, a fixed or poorly mobile buffer, with fast Ca^{2+} binding kinetics, reduces the spatial spread of Ca^{2+} and prolongs its dwell time around an open channel (Matthews *et al.*, 2013; Delvendahl *et al.*, 2015; Matthews and Dietrich, 2015). As fixed buffers cannot be replenished by means of diffusion, those that are in the vicinity of the channel are prone to saturation (Naraghi and Neher, 1997). Consequently, a subsequent AP may produce a larger increase in $[Ca^{2+}]_{local}$ and lead to synaptic facilitation. However, a high concentration of fixed buffers will slow down the local Ca^{2+} clearance, as they compete with Ca^{2+} transporters for Ca^{2+} binding and reduce the apparent mobility of Ca^{2+}. This may in turn limit the synchronicity of transmitter release during high frequency stimulation (Delvendahl *et al.*, 2015).

In contrast, an intermediately or highly mobile buffer, which shuttles Ca^{2+} away from open channels, will attenuate its local build-up and speed up the global rise

in $[Ca^{2+}]_i$ (Sala and Hernandez-Cruz, 1990; Delvendahl *et al.*, 2015). Parvalbumin, calbindin-D28k, and calretinin all have diffusion coefficients similar to or larger than the apparent diffusion coefficient of Ca^{2+} in intact cells ($12-43$ *vs.* $10-20$ $\mu m^2 s^{-1}$; Allbritton *et al.*, 1992; Gabso *et al.*, 1997; Schmidt *et al.*, 2003, 2005, 2007; Schwaller, 2010). Therefore, they likely accelerate the diffusion and spatial equilibration of Ca^{2+} following a Ca^{2+} influx. In the vicinity of the open channels, Ca^{2+}-bound buffers can be replaced by diffusible free buffers. As a result, a mobile buffer is less likely to saturate than a fixed buffer with the same Ca^{2+} binding affinity and kinetics. By increasing the apparent mobility of Ca^{2+}, a mobile buffer also enables rapid clearance of the local Ca^{2+} rise around VGCCs, and thus, may maintain synchronous transmission during repetitive stimulation.

1.4.3.3 Endogenous Ca^{2+} binding ratio

Unfortunately, the molecular identities of fixed and mobile buffers in most nerve terminals are unknown. To characterise the endogenous buffering capacity, the Ca^{2+} binding ratio of endogenous buffers (κ_E) is often used. This is the ratio of buffer-bound Ca^{2+} (BCa) to free Ca^{2+} following an intracellular Ca^{2+} rise; that is,

$$\kappa_E = \frac{\partial[BCa]}{\partial[Ca^{2+}]_i}.$$

In presynaptic terminals, κ_E has been shown to range from ~ 20 in proximal boutons of dentate gyrus granule cells and cerebellar mossy fibre terminals (Jackson and Redman, 2003; Delvendahl *et al.*, 2015), $20-40$ in the calyx of Held (Helmchen *et al.*, 1996; Neher and Taschenberger, 2013; Babai *et al.*, 2014), ~ 60 in synaptic boutons of cerebellar granule cells (Brenowitz and Regehr, 2007), and ~ 140 in synaptic boutons of neocortical layer 2/3 pyramidal neurons (Koester and Sakmann, 2000), to up to ~ 1000 in cerebellar basket and stellate cell terminals (Collin *et al.*, 2005a). These estimates indicate that, in response to a single AP, $\leq 5\%$ of the Ca^{2+} that enters a nerve terminal remains free.

1.4.4 Ca^{2+} sequestration mechanisms

The turnover rate of an active Ca^{2+} transporter is at least three orders of magnitude smaller than that of a Ca^{2+} channel (*i.e.* $\leq$ 2 ions/ms; Blaustein *et al.*, 2004). Therefore, it is unlikely to affect the peak amplitude of a Ca^{2+} rise evoked by a single AP. However, the activity of a transporter regulates the decay kinetics of this Ca^{2+} transient. By doing so, it also shapes the summation of $[Ca^{2+}]_i$ during repetitive stimulation.

Ca^{2+} can be removed from presynaptic nerve terminals by the plasmalemmal Ca^{2+}-ATPase (PMCA), the sarco/endoplasmic reticulum Ca^{2+}-ATPase (SERCA), the Na^+/Ca^{2+} exchanger (NCX), the K^+-dependent Na^+/Ca^{2+} exchanger (NCKX), and the mitochondrial Ca^{2+} uniporter. Whilst the others are active transporters, the mitochondrial Ca^{2+} uniporter is actually a Ca^{2+} channel (Kirichok *et al.*, 2004). Therefore, it has a much larger turnover rate. These transporters are also different in their Ca^{2+} binding affinities and modulatory mechanisms. As a result, most cells express multiple types of transporters to enable Ca^{2+} regulation under different conditions.

1.4.4.1 Plasmalemmal Ca^{2+}-ATPase

There are four main isoforms of PMCA pumps (PMCA$1-4$), all of which have been found expressed in the cerebral cortex (Stauffer *et al.*, 1995). As its name suggests, PMCA transports Ca^{2+} across the cell membrane, from the cytosol into the extracellular space. It is powered by ATP hydrolysis, with a stoichiometry of one Ca^{2+} ion extruded for each molecule of ATP hydrolysed (Brini and Carafoli, 2011). The $[Ca^{2+}]_i$ at which PMCA pumps are half-maximally activated (that is, $K_{0.5}$) is $10-20$ μM in the resting state, but decreases to ≤ 1 μM upon Ca^{2+}-CaM binding (Brini and Carafoli, 2009). It is likely that, even at a resting $[Ca^{2+}]_i$ of $\sim$ 100 nM, the majority of PMCA pumps are associated with Ca^{2+}-CaM (Vincenzi *et al.*, 1980). This is because their affinity for Ca^{2+}-CaM is $2-50$ nM (Brini and Carafoli, 2009), which

is at least an order of magnitude smaller than the basal concentration of Ca^{2+}-CaM in neuronal tissues ($\sim$ 500 nM, estimated with a total CaM concentration of 100 μM and a K_d value of 13 μM, according to Biber *et al.* 1984 and Faas *et al.* 2011, respectively; consistent with Vincenzi *et al.* 1980). The binding of Ca^{2+}-CaM also increases the maximal transport rate of PMCA pumps by up to four-fold (Preiano *et al.*, 1996).

PMCA was initially found to have a very high affinity for Ca^{2+}, with a $K_{0.5}$ value of $\sim$ 180 nM (DiPolo and Beauge, 1979). Therefore, it has long been attributed to keeping the resting $[Ca^{2+}]_i$ low, at $\sim$ 100 nM (Brini and Carafoli, 2011). However, more recent studies have revealed numerous PMCA isoforms, including splice variants, each with a different affinity for Ca^{2+}-CaM, maximal transport rate, cellular distribution, and/or regulatory mechanism (Strehler and Zacharias, 2001). Accordingly, the multitude of PMCA pumps might have evolved to regulate $[Ca^{2+}]_i$ at rest as well as following stimulation (Brini and Carafoli, 2011). Consistent with this idea, Kim *et al.* (2005) showed that, at the calyx of Held, the rate of Ca^{2+} extrusion by PMCA was yet to reach a maximal level and could still account for $\sim$ 25% of the total Ca^{2+} clearance, after an intracellular Ca^{2+} rise to 1 μM.

1.4.4.2 Sarco/endoplasmic reticulum Ca^{2+}-ATPase

Mammalian cells contain three different genes that code for the three main SERCA isoforms (SERCA1 $-$ 3; Brini and Carafoli, 2009). Only one of them, SERCA2, has been shown to be expressed in the cerebral cortex (Wu *et al.*, 1995; Pelled *et al.*, 2003). Similar to PMCA, SERCA pumps derive energy from ATP hydrolysis, using one ATP molecule to transport two Ca^{2+} ions from the cytosol into the ER lumen (Brini and Carafoli, 2009). Their half-maximal activation constant by cytosolic Ca^{2+} is also in the range of that of PMCA ($K_{0.5}$ = 0.3 $-$ 1.1 μM; Lytton *et al.*, 1992; Pelled *et al.*, 2003).

SERCA is the main Ca^{2+} sequestration mechanism in skeletal muscles (Blaustein *et al.*, 2004). As almost all of the Ca^{2+} required for muscle contraction comes from the SR, not only does the activity of SERCA allow muscle relaxation, but it also ensures

rapid refilling of the SR for subsequent activity. In neurons, a much larger fraction of Ca^{2+} required for synaptic transmission arises from Ca^{2+} influx through VGCCs. Therefore, the relative contribution of SERCA pumps to Ca^{2+} sequestration is likely less than that in skeletal muscles. In fact, Kim *et al.* (2005) showed that SERCA pumps do not contribute to Ca^{2+} sequestration at the calyx of Held. However, blockade of SERCA activity slowed the decay time course of AP-evoked Ca^{2+} transients at synaptic boutons of hippocampal pyramidal neurons and mossy fibre boutons (Emptage *et al.*, 2001; Scott and Rusakov, 2006). In agreement with this, de Juan-Sanz *et al.* (2017) found a significant increase in $[Ca^{2+}]_{ER}$ in synaptic boutons of hippocampal neurons, even in response to a single AP. Therefore, SERCA pumps play an important role in regulating presynaptic Ca^{2+} dynamics. As they constitutively load the ER with Ca^{2+}, these pumps also support intracellular Ca^{2+} release through ryanodine and IP_3 receptors (Brini and Carafoli, 2009).

Pharmacology. Blockade of SERCA pumps is often achieved with thapsigargin or cyclopiazonic acid (CPA). Although a tumour promoter, thapsigargin is the most commonly used blocker, because of its high affinity and specificity for SERCA ($IC_{50} = 1 - 10$ nM; Thastrup *et al.*, 1990; Ma *et al.*, 1999). CPA also inhibits SERCA pumps, without affecting other Ca^{2+} transporters, including PMCA (Seidler *et al.*, 1989). However, it has a lower affinity ($IC_{50} \sim 0.1 - 1$ μM; Soler *et al.*, 1998; Ma *et al.*, 1999).

1.4.4.3 Na^+/Ca^{2+} antiporters

Two distinct gene families code for the main antiporters that mediate Na^+/Ca^{2+} transport in neurons. The SLC8 gene family encodes the Na^+/Ca^{2+} exchangers (NCX), whilst the SLC24 family encodes the less recognised Na^+/Ca^{2+}-K^+ exchangers (NCKX; Brini and Carafoli, 2011). There are three different NCX and at least five different NCKX gene products in mammalian cells ($NCX1 - 3$ and $NCKX1 - 5$, respectively; Altimimi and Schnetkamp, 2007). The expression of

NCX1 − 3 and NCKX2 − 4 has been reported in the cerebral cortex (Lytton *et al.*, 2002; Minelli *et al.*, 2007).

Both NCX and NCKX extract energy from the electrochemical gradient of Na^+ to transport Ca^{2+} across the cell membrane. During each cycle, NCX removes one Ca^{2+} ion in exchange for three Na^+ ions (Blaustein and Lederer, 1999). NCKX, on the other hand, exchanges four Na^+ ions for one Ca^{2+} and one K^+ ion (Altimimi and Schnetkamp, 2007). As it also exploits the outward electrochemical gradient of K^+, NCKX extrudes Ca^{2+} more efficiently than its K^+-independent counterpart, particularly when the electrochemical gradient of Na^+ is low (Schnetkamp, 1995). Compared to Ca^{2+}-ATPases, NCX has a lower affinity for cytosolic Ca^{2+} ($K_{0.5}$ = 0.6 − 3 μM; Blaustein and Lederer, 1999). Consistently, at the calyx of Held, an intracellular Ca^{2+} rise to 0.2 μM was less effectively cleared by NCX than by PMCA (Kim *et al.*, 2005). NCX, however, played a more important role in Ca^{2+} sequestration, when $[Ca^{2+}]_i$ was raised to 2 μM. After the same Ca^{2+} elevation, NCKX also accounted for 42% of the total Ca^{2+} clearance. This suggests that the Ca^{2+} binding affinity of NCKX is likely similar to that of NCX.

The activity of NCX and NCKX is reversible as it depends on the membrane potential and the electrochemical gradients of Na^+ and Ca^{2+} (and K^+ for NCKX). Under physiological conditions and in response to an intracellular Ca^{2+} rise, they predominantly extrude Ca^{2+} and allow $[Ca^{2+}]_i$ to rapidly return to the resting level (Mulkey and Zucker, 1992; Kim *et al.*, 2005). This is commonly referred to as the forward mode of NCX/NCKX. However, during sustained activity, the repetitive activation of voltage-gated Na^+ channels can cause the intracellular concentration of Na^+ to increase significantly, reducing its electrochemical gradient. As a result, NCX/NCKX can reverse and start to transport Ca^{2+} into the cytosol. Similar to the forward mode, the reverse mode operation of NCX also depends on $[Ca^{2+}]_i$ ($K_{0.5}$ = 0.6 − 2 μM; Blaustein and Lederer, 1999). An increase in $[Ca^{2+}]_i$ caused by the reverse mode has been reported at the crayfish NMJ (Zhong *et al.*, 2001) and synaptic boutons of cerebellar granule cells (Regehr, 1997; Roome *et al.*, 2013).

1.4.4.4 Mitochondrial Ca^{2+} uptake

Mitochondrial Ca^{2+} uptake plays a central role in regulating many cellular processes, including energy production and cell death. As mitochondria are double-membrane bound organelles, Ca^{2+} must cross two different membranes to reach the mitochondrial matrix. It is generally accepted that Ca^{2+} can freely flow across the outer mitochondrial membrane (Bianchi *et al.*, 2004). This is because of the abundance of the voltage-dependent anion channel (VDAC), which is mainly expressed in the outer mitochondrial membrane and accounts for almost half of its total protein pool (Linden *et al.*, 1984; Shoshan-Barmatz *et al.*, 2010). Despite its name, the VDAC is poorly selective for anions (Tan and Colombini, 2007). It also has a large conductance, which facilitates the movement of ions and small molecules across the outer mitochondrial membrane.

The mitochondrial Ca^{2+} uniporter is the primary mode of Ca^{2+} transport from the inter-membrane space into the mitochondrial matrix. It is a large complex, consisting of a pore-forming subunit called mitochondrial Ca^{2+} uniporter (MCU), three regulatory subunits (mitochondrial calcium uptake 1 or MICU1, MICU2, and MCUb), and a small membrane-spanning protein (EMRE; Baughman *et al.*, 2011; Kamer and Mootha, 2015; Oxenoid *et al.*, 2016). These proteins are expressed in most mammalian tissues (Plovanich *et al.*, 2013). A paralog of MICU1 and MICU2, called MICU3, is also expressed in the CNS and skeletal muscles, although its function is unclear (Plovanich *et al.*, 2013). According to current models, MICU1 and MICU2 modulate the Ca^{2+} dependence of the uniporter, allowing Ca^{2+} to flow through the MCU pore only when $[Ca^{2+}]_i$ is sufficiently high (Kamer and Mootha, 2015). Their EF-hand motifs are exposed to the inter-membrane space, and thus, can sense $[Ca^{2+}]_i$ (Perocchi *et al.*, 2010; Plovanich *et al.*, 2013). These Ca^{2+} sensors are linked to MCU by EMRE, which is also essential to generating the Ca^{2+} current (Sancak *et al.*, 2013). MCUb is a negative regulator of the uniporter activity (Raffaello *et al.*, 2013).

Due to the mitochondrial membrane potential (-150 to -200 mV), there exists a large electrochemical gradient that drives Ca^{2+} into the mitochondrial matrix. By voltage-clamping the inner mitochondrial membrane, Kirichok *et al.* (2004) demonstrated

that the mitochondrial Ca^{2+} uniporter is a highly selective, inwardly rectifying Ca^{2+} channel. An increase in $[Ca^{2+}]_i$ increases the current amplitude, with a $K_{0.5}$ value of 19 mM (Kirichok *et al.*, 2004). This value is much larger than previously estimated with Ca^{2+} imaging ($10 - 40$ μM; Xu *et al.*, 1997; Colegrove *et al.*, 2000b). This is most likely due to the fact that, under physiological conditions, the flow of Ca^{2+} into the mitochondrial matrix would rapidly dissipate the mitochondrial membrane potential. As the open probability of the uniporter channel decreases with a depolarised membrane potential, the Ca^{2+} influx would reach a maximal level at a lower $[Ca^{2+}]_i$ (Kirichok *et al.*, 2004). At $[Ca^{2+}]_i$ above 100 μM, the Ca^{2+} current is so large that the potential difference across the inner mitochondrial membrane can only be maintained by voltage-clamp.

Ca^{2+} can also be released from mitochondria through the activity of a $Na^+/Li^+/Ca^{2+}$ exchanger (NCLX; Boyman *et al.*, 2013). However, when $[Ca^{2+}]_i$ is elevated, mitochondrial Ca^{2+} uptake dominates, producing a net flux of Ca^{2+} into the mitochondrial matrix (Colegrove *et al.*, 2000a). At the calyx of Held, mitochondria started to take up Ca^{2+} after an intracellular Ca^{2+} rise to more than 2.5 μM (Billups and Forsythe, 2002; Kim *et al.*, 2005). This is consistent with a $K_{0.5}$ value of $10 - 40$ μM (Xu *et al.*, 1997; Colegrove *et al.*, 2000b). As mitochondria are present in nerve terminals (Palay, 1956; Gray, 1959), the mitochondrial uniporter is likely an important regulator of presynaptic Ca^{2+} dynamics, particularly during sustained stimulation.

1.5 Measuring the spatially homogeneous Ca^{2+} rise

Much of our current understanding on Ca^{2+}-dependent mechanisms that underlie transmitter release stems from studies of large- and medium-sized synapses, such as the squid giant synapse (Llinas *et al.*, 1981a; Augustine and Eckert, 1984; Augustine *et al.*, 1985), the calyx of Held (Borst and Sakmann, 1996; Cuttle *et al.*, 1998; Bollmann *et al.*, 2000), and the hippocampal mossy fibre terminal (Geiger and Jonas, 2000; Bischofberger *et al.*, 2002). These nerve terminals allow direct patch-clamp

recordings, and thus, enable the presynaptic membrane potential to be controlled and manipulated.

In contrast, many aspects of Ca^{2+} regulation of transmitter release remain unclear at bouton-type synapses, including nerve terminals of neocortical pyramidal neurons. Due to their small sizes ($\sim$ 1 μm in diameter), routinely patch-clamping these boutons is not possible (yet). Thus far, it has only been achieved in a few studies (Novak *et al.*, 2013), with presynaptic Ca^{2+} currents yet to be systematically characterised. In addition, the local Ca^{2+} signal at transmitter release sites has not been determined. This is because the amplitude and kinetics of transmitter release, elicited by Ca^{2+} uncaging in a small nerve terminal, are not easily measured. These parameters can be determined by measuring the resultant change in the presynaptic membrane capacitance or the postsynaptic current. However, membrane capacitance measurements have not been achieved on small nerve terminals. Regarding the postsynaptic current, as each neocortical neuron forms synaptic contacts onto hundreds to thousands of other cortical cells, identification of the postsynaptic cell that receives input from a specific synapse is also not trivial (although this has been achieved by Koester and Johnston, 2005). Nonetheless, by characterising the sensitivity of transmitter release to EGTA and BAPTA, the coupling distance between readily releasable vesicles and VGCCs has been estimated at some small synapses (Ohana and Sakmann, 1998; Rozov *et al.*, 2001).

Due to technical limitations, most studies that aim at characterising the regulation of transmitter release by Ca^{2+} at small nerve terminals have imaged the spatially averaged intracellular Ca^{2+} rise caused by a single AP. Although it is not the Ca^{2+} signal that triggers synchronous transmitter release, the measured Ca^{2+} transient has been shown to regulate asynchronous transmission, short-term facilitation, post-tetanic potentiation, and recovery from short-term depression (Atluri and Regehr, 1996; Zucker and Regehr, 2002; Neher and Sakaba, 2008). In addition, this spatially averaged Ca^{2+} elevation can reveal valuable information on the expression of Ca^{2+} channels and the buffering capacity of endogenous buffers, both of which play

important roles in regulating the localised Ca^{2+} rise "seen" by the release machinery (Buchanan *et al.*, 2012; Delvendahl *et al.*, 2015).

1.6 Aims of study

This thesis aims at characterising factors that shape the dynamics of AP-evoked and spontaneous Ca^{2+} transients in synaptic boutons of neocortical pyramidal neurons. To achieve this, it has four main objectives:

1. To calibrate the fluorescent Ca^{2+} indicators used to measure $[Ca^{2+}]_i$.
2. To measure the increase in the spatially averaged $[Ca^{2+}]_i$ evoked by a single AP and characterise factors that determine its amplitude and time course.
3. To determine the extent to which Ca^{2+} release from presynaptic stores contributes to AP-evoked Ca^{2+} elevations.
4. To detect and characterise spontaneous Ca^{2+} transients in the absence of AP firing.

1.7 Thesis structure

In this chapter, I have provided the background information and objectives of this thesis. Chapter 2 presents a calibration of the fluorescent Ca^{2+} indicators used for imaging $[Ca^{2+}]_i$ in synaptic boutons of neocortical pyramidal neurons. Chapter 3 presents a characterisation of factors that shape the amplitude and time course of an AP-evoked Ca^{2+} transient. It also describes the summation of $[Ca^{2+}]_i$ during repetitive stimulation and addresses the contribution of intracellular Ca^{2+} release to AP-evoked Ca^{2+} elevations. Chapter 4 presents the detection and characterisation of spontaneous Ca^{2+} transients. Finally, chapter 5 ties all the preceding chapters together and gives a summary of the conclusions.

1.8 Author contribution

I performed all experiments presented in this thesis, except for the measurement of the Ca^{2+} binding affinities of OGB-1, OGB-6F, and OGB-5N, in the presence of Mg^{2+}. These K_d values were measured by Chang Ha Michael Park for a summer research project. They are shown as the results of a preliminary experiment, either in the Discussion of Chapter 2 (OGB-1 and OGB-6F) or in Chapter 3 (OGB-5N).

Chapter 2

Calibration of Ca^{2+} indicators

2.1 Introduction

Ca^{2+} is an essential second messenger in all living cells. An increase in the intracellular Ca^{2+} concentration ($[Ca^{2+}]_i$) can arise from Ca^{2+} influx through voltage- or ligand-gated Ca^{2+} channels, or Ca^{2+} release from intracellular stores. The action of Ca^{2+}- binding proteins and sequestration mechanisms then returns $[Ca^{2+}]_i$ to the resting level. Not only the amplitude, but also the time course of an intracellular Ca^{2+} rise is a determinant of many cellular processes, including those in neurons. In particular, a brief increase in $[Ca^{2+}]_i$ (less than 1 ms long) in the vicinity of voltage-gated Ca^{2+} channels drives synchronous transmitter release, whilst longer-lasting elevations regulate asynchronous transmission, synaptic plasticity, and neuronal development (Zucker and Regehr, 2002; Bollmann and Sakmann, 2005; Kwon and Sabatini, 2011; Kanamori *et al.*, 2013; Kaeser and Regehr, 2014). Therefore, quantification of $[Ca^{2+}]_i$ and characterisation of its dynamics are central to understanding physiological processes that underlie neuronal functions.

A common method for measuring $[Ca^{2+}]_i$ involves the use of fluorescent Ca^{2+} indicators, which can be classified as chemical or genetically encoded Ca^{2+} indicators (GECIs). Chemical indicators are small-molecule fluorophores, each with a Ca^{2+} binding site. The Ca^{2+} binding site of the majority of chemical indicators is based on BAPTA, a synthetic Ca^{2+} buffer with fast Ca^{2+} binding kinetics and a high selectivity for Ca^{2+} over Mg^{2+} (Tsien, 1980; Grynkiewicz *et al.*, 1985; Minta *et al.*, 1989). In

contrast, GECIs are chimeric fluorescent proteins, each consisting of a Ca^{2+}-binding domain (such as calmodulin or troponin C) fused to one or two fluorescent proteins (Miyawaki *et al.*, 1997; Nagai *et al.*, 2001; Mank *et al.*, 2006; Tian *et al.*, 2009; Chen *et al.*, 2013). Although GECIs are increasingly used for imaging of neuronal activity, chemical indicators remain popular in studies that characterise rapid changes in $[Ca^{2+}]_i$, due to their much faster Ca^{2+} binding kinetics (Chen *et al.*, 2013).

Upon Ca^{2+} binding, the excitation and/or emission properties of a chemical Ca^{2+} indicator change (Grynkiewicz *et al.*, 1985; Tsien, 1988; Minta *et al.*, 1989). Ratiometric indicators are those with a shift in the maximum excitation and/or emission wavelength, whilst non-ratiometric indicators exhibit Ca^{2+}-dependent changes in the fluorescence intensity, without any wavelength shift. Compared to their counterparts, ratiometric indicators allow a more accurate quantification of $[Ca^{2+}]_i$. This is because the calculation of $[Ca^{2+}]_i$ from their fluorescence intensities, measured at two excitation/emission wavelengths, corrects for experimental variations such as indicator concentration and optical path length. However, single-photon excitation of most currently available ratiometric indicators requires UV irradiation (< 400 nm), which produces significant autofluorescence from cellular organelles and can cause multiple side-effects (Grynkiewicz *et al.*, 1985). Therefore, non-ratiometric Ca^{2+} indicators, all of which can be excited by visible light ($450 - 600$ nm), are more commonly used to characterise the intracellular Ca^{2+} dynamics in living cells.

The calculation of $[Ca^{2+}]_i$ from the fluorescence intensity of a non-ratiometric Ca^{2+} indicator requires knowledge of three parameters: 1) the dynamic range ($R_f = {}^{F_{max}}/_{F_{min}}$), 2) the Ca^{2+}-binding affinity or dissociation constant (K_d), and 3) the maximum change in fluorescence ($\left({}^{\Delta F}/_{F_0}\right)_{max}$) of the indicator (Lev-Ram *et al.*, 1992; Maravall *et al.*, 2000, also see Section 3.2.6.4). Ideally, these parameters should be measured *in situ*; in this study, they should be measured in synaptic boutons of layer 5 pyramidal neurons. This is because the interaction between Ca^{2+} and a Ca^{2+} chelator - which a Ca^{2+} indicator essentially is - depends on the specifics of the local environment, including ionic strength, pH, temperature, and the presence of other ions or molecules that bind to the chelator (Harkins *et al.*, 1993; Bers *et al.*, 2010).

However, only $(\Delta F/F_0)_{max}$ was measured *in situ* for each bouton imaged (Section 3.2.4). It would be a challenge to measure K_d and R_f of a Ca^{2+} indicator in these synaptic boutons. To determine K_d, $[Ca^{2+}]_i$ would need to be clamped to at least four different levels. Even if K_d was to be measured at the soma, this would still be a difficult and cumbersome task. Similarly, to accurately measure R_f of the high-affinity Ca^{2+} indicator Oregon Green 488 BAPTA-1 (OGB-1; K_d = 170 nM, according to the manufacturer), $[Ca^{2+}]_i$ in a bouton would need to be clamped to less than 10 nM. This is probably impossible considering the long distance between a patch pipette and the bouton ($\geq$ 100 μm).

In this chapter, K_d and R_f of four non-ratiometric Ca^{2+} indicators (OGB-1, OGB-6F, Cal-520, and Fluo-4FF) were measured *in vitro*, in solutions that mimicked the patch-clamp internal solution in terms of ionic strength, pH, and temperature. In these so-called Ca^{2+}-buffer solutions, the free or ionised concentration of Ca^{2+} ($[Ca^{2+}]_i$) was varied by adding different concentrations of $CaCl_2$ to a constant concentration of a Ca^{2+} buffer (EGTA or HEDTA). To avoid errors associated with the calculation of $[Ca^{2+}]_i$ using tabulated constants or freely available computer programs (McGuigan *et al.*, 2007; McGuigan and Stumpff, 2013), the resultant $[Ca^{2+}]_i$ was measured with a Ca^{2+}-selective macroelectrode. The fluorescence of each Ca^{2+} indicator was then measured in these Ca^{2+}-buffer solutions so that its K_d and R_f could be determined.

2.2 Materials and methods

2.2.1 Preparation of Ca^{2+}-buffer solutions

Two sets of Ca^{2+}-buffer solutions, each with a different buffer (EGTA or HEDTA, Sigma-Aldrich, St. Louis, USA), were made such that their ionic strength and pH were similar to those of the patch-clamp internal solution ($\sim$ 170 mM and pH 7.20 $\pm$ 0.01 at 35 $\pm$ 1 °C). Fig. 2.1 shows how these solutions were prepared based on the ratio method (McGuigan *et al.*, 1991). The K-gluconate present in the

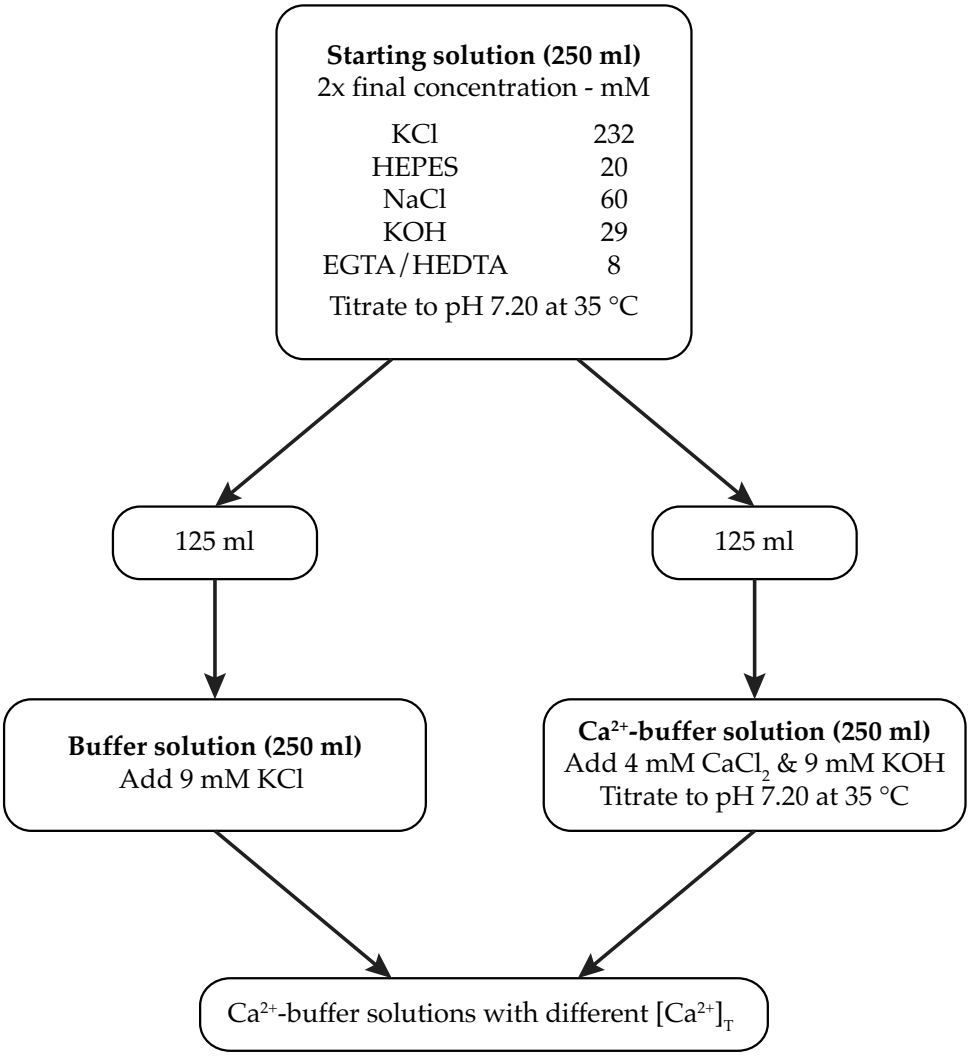

Figure 2.1: Flow chart for preparation of Ca^{2+}-buffer solutions. The initial 250 ml solution contained solutes at 2× the final concentrations. This starting solution was then split into two 125 ml portions used to make buffer and Ca^{2+}-buffer solutions. pH was titrated to 7.20 ± 0.01 at 35 ± 1 °C with 1 M HCl.

patch-clamp solution was substituted by KCl, as the former binds Ca^{2+}, although with a low affinity (K_d ~ 50 mM; Stumpff and McGuigan, 2014; Woehler *et al.*, 2014). Phosphocreatine (disodium salt; 10 mM) was also replaced with NaCl of an equivalent ionic strength (*i.e.* 30 mM), whilst ATP-Mg and GTP were omitted. Mg^{2+} was excluded as it might interfere with the measurement of $[Ca^{2+}]_i$ using the Ca^{2+}-selective macroelectrode.

Table 2.1: Composition of buffer and Ca^{2+}-buffer background solutions, and calibrating solutions.

Compound	Concentration (mM)		
	Buffer solution	Ca^{2+}-buffer solution	Calibrating solutions
KCl	125	116	135
HEPES	10	10	10
NaCl	30	30	30
KOH	14.5	23.5	4.5
EGTA/HEDTA	4	4	0
$CaCl_2$	0	4	0.5, 0.8, 1.5, 2.5, 4.0, 6.0, 8.0, 10.0

For each set of Ca^{2+}-buffer solutions, two background solutions with the same ionic strength and pH were first prepared. Both contained a Ca^{2+} buffer (EGTA or HEDTA; 4 mM), but only one had $CaCl_2$ added to form Ca^{2+}-buffer complexes (4 mM; from 100 mM $CaCl_2$ standard solution, Sigma-Aldrich; Table 2.1). These two solutions were then mixed in the appropriate ratios to give a set of Ca^{2+}-buffer solutions with different total Ca^{2+} concentrations ($[Ca^{2+}]_T$; Table 2.2). This so-called ratio method of making Ca^{2+}-buffer solutions offered two main advantages (McGuigan *et al.*, 2017). First, pH changed minimally when the background solutions were mixed, eliminating the need to measure and adjust pH of individual Ca^{2+}-buffer solutions. Second, the ratio method ensured that the concentrations of all cations and buffers, except for Ca^{2+}, were the same in the final solutions.

2.2.2 Preparation of calibrating solutions

To determine the voltage change *per* decade of a Ca^{2+}-selective macroelectrode, a set of calibrating solutions with no Ca^{2+} buffer added, but with an ionic strength and pH similar to those of Ca^{2+}-buffer solutions, was made (Table 2.1). A background solution with 2× the final concentrations of solutes, but without $CaCl_2$, was first prepared; its pH was titrated to 7.20 ± 0.01 at 35 ± 1 °C with 1 M HCl. Different

Table 2.2: Ratios of Ca^{2+}-buffer and buffer background solutions in the final Ca^{2+}-buffer solutions. Different ratios of Ca^{2+}-buffer and buffer background solutions were mixed to produce solutions with different $[Ca^{2+}]_T$. $[Ca^{2+}]_i$ in these solutions was measured with a Ca^{2+}-selective macroelectrode (2 repeats).

Solution #	Ca^{2+}-EGTA/EGTA	$[Ca^{2+}]_T$ (mM)	$[Ca^{2+}]_i$ (μM)
1	9:1	3.600	5.290 $\pm$ 0.107
2	8:1	3.556	3.725 $\pm$ 0.007
3	7:1	3.500	2.673 $\pm$ 0.030
4	5:1	3.333	1.401 $\pm$ 0.038
5	4:1	3.200	0.989 $\pm$ 0.032
6	3:1	3.000	0.663 $\pm$ 0.024
7	2:1	2.667	0.400 $\pm$ 0.016
8	1.5:1	2.400	0.286 $\pm$ 0.012
9	1:1	2.000	0.182 $\pm$ 0.008
10	1:1.5	1.600	0.118 $\pm$ 0.005
11	1:2	1.333	0.087 $\pm$ 0.004
12	1:4	0.800	0.043 $\pm$ 0.002
13	1:9	0.400	0.019 $\pm$ 0.001

Solution #	Ca^{2+}-HEDTA/HEDTA	$[Ca^{2+}]_T$ (mM)	$[Ca^{2+}]_i$ (μM)
1	19:1	3.800	48.95 $\pm$ 2.41
2	15:1	3.750	40.90 $\pm$ 1.96
3	12:1	3.692	33.93 $\pm$ 1.57
4	9:1	3.600	26.26 $\pm$ 1.16
5	7:1	3.500	20.74 $\pm$ 0.87
6	6:1	3.429	17.90 $\pm$ 0.73
7	5:1	3.333	14.96 $\pm$ 0.59
8	4:1	3.200	12.01 $\pm$ 0.46
9	3:1	3.000	9.02 $\pm$ 0.33
10	2:1	2.667	6.02 $\pm$ 0.21
11	1:1	2.000	3.00 $\pm$ 0.10
12	1:2	1.333	1.50 $\pm$ 0.05
13	1:4	0.800	0.75 $\pm$ 0.02

calibrating solutions were then made by diluting this background solution by two-fold. To these solutions, various amounts of a 100 mM $CaCl_2$ standard solution were added to produce $[Ca^{2+}]_T$ between 0.5 to 10 mM.

2.2.3 Measurement of $[Ca^{2+}]_i$ using a Ca^{2+}-selective macroelectrode

Once calibrating and Ca^{2+}-buffer solutions had been prepared, $[Ca^{2+}]_i$ in these solutions was measured at 35 $\pm$ 1 °C using a Ca^{2+}-selective macroelectrode (Radiometer ISE25Ca, Hach, Colorado, USA). The potential difference between the Ca^{2+} electrode and a 3 M KCl reference electrode (Radiometer REF201) was measured with a pH meter in mV mode (input impedance > 3×10^{12} Ω; Model 1852 mV, TPS Pty. Ltd., Queensland, Australia). All solutions were placed in a 35 °C water bath before and during measurement.

The calibrating solution containing 10 mM $CaCl_2$ was first measured, followed by those with sequentially lower $[Ca^{2+}]_T$. This yielded a calibration curve in the Nernstian range of the Ca^{2+} electrode. Measurement was then done for the set of Ca^{2+}-HEDTA solutions, starting from the solution with the highest $[Ca^{2+}]_T$ to that with the lowest $[Ca^{2+}]_T$. $[Ca^{2+}]_i$ in the set of Ca^{2+}-EGTA solutions was then measured, again starting from the solution with the highest $[Ca^{2+}]_T$. Once all Ca^{2+}-buffer solutions had been measured, $[Ca^{2+}]_i$ in the 10 mM $CaCl_2$ calibrating solution was re-measured to check for potential drift. In all experiments, the electrode potential in the 10 mM $CaCl_2$ calibrating solution stayed constant throughout, indicating that there was no detectable drift. Two independent measurements (*i.e.* on two different days) were obtained.

2.2.4 Fluorescence measurement

The fluorescence intensity of a Ca^{2+} indicator in Ca^{2+}-buffer solutions was measured with a Tecan microplate reader (Infinite® M200 Pro, Männedorf, Switzerland). OGB-1, OGB-6F, and Fluo-4FF were purchased from Life Technologies (Carlsbad, CA,

USA), whilst Cal-520 was from AAT Bioquest, Inc. (Sunnyvale, CA, USA). A small aliquot of each indicator (2 μl) was added to $200 - 400$ μl of different Ca^{2+}-buffer solutions (final concentration of indicator $\sim 10 - 100$ nM). A $100 - 200$ μl sample of each solution was then pipetted into a well of a 96-well plate (Costar®, flat bottom, transparent), in duplicate. The microplate reader was set to 35.0 ± 0.5 °C and the 96-well plate was left in the reader for ~ 10 min before fluorescence measurement was obtained. Samples were excited by 485 nm light and the fluorescence intensity was measured at 525 nm (bandwidth < 9 and 20 nm, respectively). A sample of a Ca^{2+}-buffer solution, with no Ca^{2+} indicator added, was used as a blank. Two to three sets of measurements were done for each indicator.

To measure the maximum fluorescence of OGB-1 and Cal-520, the Ca^{2+}-EGTA background solution, with 4 mM $CaCl_2$ and 4 mM EGTA, was used. $[Ca^{2+}]_i$ in this solution was not measured but could be accurately calculated from Eq. 2.3 based on the optimised values for K_d and $[B]_T$ of EGTA (Table 2.3). To measure the maximum fluorescence of OGB-6F and Fluo-4FF, two additional solutions were made, each by adding a small amount of the 100 mM $CaCl_2$ standard solution to an aliquot of the Ca^{2+}-EGTA background solution to produce a sub-millimolar or millimolar $[Ca^{2+}]_i$; the resultant $[Ca^{2+}]_i$ was also calculated. For all Ca^{2+} indicators, the minimum fluorescence was measured in the EGTA background solution (4 mM EGTA and 0 $CaCl_2$). $[Ca^{2+}]_i$ in this solution was assumed to be 1 nM.

2.2.5 Data analysis

2.2.5.1 Determination of $[Ca^{2+}]_i$ based on the ligand optimisation method

$[Ca^{2+}]_i$ in Ca^{2+}-buffer solutions was determined from the electrode potentials based on the ligand optimisation method (Luthi *et al.*, 1997; McGuigan *et al.*, 2006, 2014). This analysis was implemented in R (version 3.3.1), with the R code kindly provided by James Kay (Department of Statistics, University of Glasglow, UK). To find $[Ca^{2+}]_i$, this method calculates K_d and the purity of EGTA and HEDTA in the prepared

solutions, through an iterative process. More specifically, the following steps were done:

1) Relative potentials (ΔE) were calculated by subtracting the electrode potential in the 10 mM $CaCl_2$ calibrating solution from all measured potentials.

2) ΔE values of the calibrating solutions were plotted against the corresponding pCa. A Nernstian fit to this plot, constrained to pass through 0 at a pCa of 2, provided an estimation of the slope (s) of the Ca^{2+} electrode; that is,

$$\Delta E = 2s - s \times \text{pCa}. \tag{2.1}$$

3) Using Eq. 2.1, pCa or $[Ca^{2+}]_i$ of the Ca^{2+}-buffer solution with the highest $[Ca^{2+}]_T$ was estimated from its ΔE value. K_d of the buffer was in turn estimated as follows:

$$K_d = \frac{[Ca^{2+}]_i \times \left[[B]_T - \left([Ca^{2+}]_T - [Ca^{2+}]_i\right)\right]}{[Ca^{2+}]_T - [Ca^{2+}]_i}, \tag{2.2}$$

where the total buffer concentration ($[B]_T$) was assumed to be 4 mM.

4) With the estimated K_d, $[Ca^{2+}]_i$ in all Ca^{2+}-buffer solutions was calculated as

$$[Ca^{2+}]_i = \frac{-(K_d + [B]_T - [Ca^{2+}]_T) + \sqrt{(K_d + [B]_T - [Ca^{2+}]_T)^2 + 4K_d[Ca^{2+}]_T}}{2}, \tag{2.3}$$

where $[B]_T$ was again assumed to be 4 mM. The calculated $[Ca^{2+}]_i$ was then converted to pCa.

5) The plot of ΔE *vs.* pCa for Ca^{2+}-buffer solutions was fitted with the Nicolsky-Eisenman equation, again constrained to pass through 0 at a pCa of 2. That is,

$$\Delta E = -s \times \log(0.01 + \Sigma) + s \times \log(10^{-\mathrm{pCa}} + \Sigma), \tag{2.4}$$

where Σ represents the total concentration of interfering ions. Here, the slope of the electrode s was a constant, whilst Σ was a free parameter. The residual sum of squares (RSS) of this fit was calculated.

6) $[\mathrm{B}]_\mathrm{T}$, K_d, and Σ were optimised using PORT routines until the best fit to the Nicolsky-Eisenman equation was obtained; *i.e.* RSS reached a minimum. $[\mathrm{B}]_\mathrm{T}$ was constrained to be ≤ 4 mM. Steps $4-5$ were repeated during this optimisation process.

7) The plot of ΔE *vs.* pCa for calibrating solutions was fitted with the Nicolsky-Eisenman equation (Eq. 2.4) using the optimised Σ value. The slope s was re-calculated from this fit.

8) Steps $5-6$ were repeated until the new values for s differed by less than 10^{-6}. Once this criterion had been reached, step 6 was repeated one last time with the final value for s. This yielded a calibration curve for the Ca^{2+}-selective macroelectrode, covering the range of pCa of all solutions (calibrating and Ca^{2+}-buffer solutions; Fig. 2.2). Optimised values for $[\mathrm{B}]_\mathrm{T}$ and K_d were also obtained (Table 2.3). The purity of each Ca^{2+} buffer was calculated by dividing the optimised value for $[\mathrm{B}]_\mathrm{T}$ by 4 mM.

9) $[Ca^{2+}]_\mathrm{i}$ in all Ca^{2+}-buffer solutions was calculated using Eq. 2.3 and the optimised values for $[\mathrm{B}]_\mathrm{T}$ and K_d (Table 2.2).

2.2.5.2 Determination of K_d of Ca^{2+} indicators

K_d of each Ca^{2+} indicator was determined by plotting its fluorescence intensity in Ca^{2+}-buffer solutions (with fluorescence of the no-indicator solution subtracted) as a function of $[Ca^{2+}]_\mathrm{i}$. This plot was then fitted with a Hill equation of the following form:

$$F = F_{\min} + \frac{F_{\max} - F_{\min}}{1 + \frac{K_d}{[Ca^{2+}]_i}}. \tag{2.5}$$

This fit yielded not only K_d but also $F_{\min}$ and $F_{\max}$; the latter parameters allowed R_f to be calculated as $F_{\max}/F_{\min}$. Values for K_d and R_f were determined from the fit to each set of measurement ($2 - 3$ repeats *per* indicator), and then averaged together to give the mean values cited in this thesis (Table 2.4). To generate averaged, normalised fluorescence *vs.* $[Ca^{2+}]_i$ plots (Figs. 2.3A-D), the plots of individual sets of measurement were normalised by dividing by the largest fluorescence measurement in that set, and then averaged together. The averaged plot was refitted with Eq. 2.5; values for K_d and R_f obtained from this fit were less than 5% different from the means mentioned above.

2.3 Results

2.3.1 $[Ca^{2+}]_i$ in Ca^{2+}-buffer solutions

A Ca^{2+}-selective macroelectrode was used to measure $[Ca^{2+}]_i$ in Ca^{2+}-EGTA and Ca^{2+}-HEDTA solutions. Fig. 2.2 shows the potential (ΔE) of each Ca^{2+}-buffer or calibrating solution, relative to that of the 10 mM $CaCl_2$ calibrating solution, as a function of pCa. To generate this plot, the potentials measured with the Ca^{2+} electrode were analysed based on the ligand optimisation method (Section 2.2.3). The voltage change *per* decade of the electrode was first estimated based on the relative potentials of the calibrating solutions (black circles; n = 2). As no Ca^{2+} buffer was present in these solutions, $[Ca^{2+}]_i$ was equal to the respective concentration of $CaCl_2$ ($[Ca^{2+}]_T$; Table 2.1), corresponding to a pCa value from 2 to 3.301. As expected, in this range of pCa, the response of the Ca^{2+} electrode was close to the Nernstian prediction. A Nernstian fit to this part of the plot yielded an estimate of the electrode slope, which was 28.77 $\pm$ 0.06 mV/decade (Eq. 2.1).

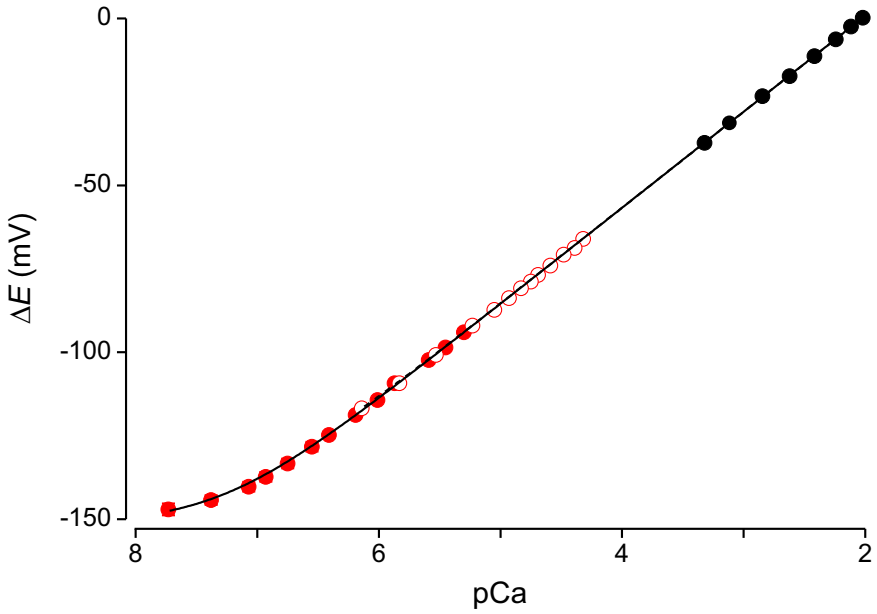

Figure 2.2: Calibration curve of the Ca^{2+}-selective macroelectrode. The electrode potential was measured in a set of calibrating solutions (black circles), a set of Ca^{2+}-HEDTA solutions (red, open circles), and a set of Ca^{2+}-EGTA solutions (red, filled circles). Displayed values (ΔE) are relative potentials, with respect to that of the 10 mM $CaCl_2$ calibrating solution (pCa = 2). The plot of ΔE *vs.* pCa for each set of Ca^{2+}-buffer solutions was fitted with the Nicolsky-Eisenman equation (Eq. 2.4; EGTA: solid curve; HEDTA: dashed curve).

With the assumption that the electrode response remained Nernstian, the pCa values of the Ca^{2+}-EGTA and Ca^{2+}-HEDTA solutions with the highest $[Ca^{2+}]_T$ were calculated from the corresponding ΔE and the estimated slope. This in turn allowed the K_d values of EGTA and HEDTA, and $[Ca^{2+}]_i$ in the remaining Ca^{2+}-buffer solutions, to be estimated (Eqs. 2.2 and 2.3, respectively). However, the detection limit of a Ca^{2+}-selective electrode is typically ≥ 5 μM. As $[Ca^{2+}]_i$ approaches this value, the response of the electrode no longer follows the Nernstian prediction, with the voltage change *per* decade gradually decreasing. Consequently, the calculation of $[Ca^{2+}]_i$ based on a Nernstian fit yielded overestimates of the true $[Ca^{2+}]_i$ (Bers, 1982). To extend the detection limit and accurately determine $[Ca^{2+}]_i$ in Ca^{2+}-buffer solutions, the plot of ΔE *vs.* the estimated pCa values of each set of solutions were fitted with the Nicolsky-Eisenman equation in an iterative process (Eq. 2.4). This process optimised for the total buffer concentration ($[B]_T$), K_d of each buffer, the total

concentration of interfering ions (Σ), and finally, the slope of the electrode (Luthi *et al.*, 1997; McGuigan *et al.*, 2006, 2014). It produced the following best fits:

$$\begin{aligned}\Delta E &= -28.77 \times \log(0.01 + 5.32 \times 10^{-8}) + 28.77 \times \log(10^{-\mathrm{pCa}} + 5.32 \times 10^{-8}) \\ &= 57.54 + 28.77 \times \log(10^{-\mathrm{pCa}} + 5.32 \times 10^{-8})\end{aligned}$$

and

$$\begin{aligned}\Delta E &= -28.77 \times \log(0.01 + 9.84 \times 10^{-8}) + 28.77 \times \log(10^{-\mathrm{pCa}} + 9.84 \times 10^{-8}) \\ &= 57.54 + 28.77 \times \log(10^{-\mathrm{pCa}} + 9.84 \times 10^{-8}),\end{aligned}$$

for Ca^{2+}-EGTA and Ca^{2+}-HEDTA solutions, respectively. These two fits were very consistent with each other, with the former completely overlapping the latter (Fig. 2.2, solid and dashed curves, respectively). Both fits had a regression coefficient $r \geq 0.9996$.

The corresponding optimised values of $[\mathrm{B}]_\mathrm{T}$ and K_d are shown in Table 2.3. As expected, the purity of the buffers was less than 100%, with that of EGTA considerably smaller than the value quoted by the manufacturer (92.5 ± 0.2 *vs.* $\sim$ 97%). In addition, the optimised values of K_d, especially for HEDTA, were different from those estimated by a widely used computer program Maxchelator (2.99 ± 0.09 *vs.* 7.2 μM; WebMaxC Standard version; http://web.stanford.edu/~cpatton/maxc.html; accessed on 08/03/2017); these estimates were for the same pH, ionic strength, and temperature as those in this study. These findings emphasise the importance of measuring $[Ca^{2+}]_\mathrm{i}$ in the Ca^{2+}-buffer solutions with a Ca^{2+}-selective macroelectrode.

Based on the optimised values of $[\mathrm{B}]_\mathrm{T}$ and K_d, the values of $[Ca^{2+}]_\mathrm{i}$ in all Ca^{2+}-buffer solutions could be accurately determined using Eq. 2.3 (Table 2.2). The

Table 2.3: $[B]_T$, purity, and K_d of EGTA and HEDTA. The purity of the buffers, provided by the manufacturer, and values of K_d estimated by the Maxchelator program are also shown.

Buffer	$[B]_T$ (mM)	K_d (μM)		Purity (%)	
		measured	Maxchelator	measured	advertised
EGTA	3.70 ± 0.01	0.155 ± 0.007	0.143	92.5 ± 0.2	~ 97
HEDTA	3.98 ± 0.01	2.99 ± 0.09	7.2	99.5 ± 0.2	≥ 98

corresponding values of pCa are displayed in Fig. 2.2 (EGTA: red, filled circles; HEDTA: open circles). The fact that the plots of ΔE *vs.* pCa for EGTA and HEDTA solutions overlapped each other supports the validity of the ligand optimisation method.

2.3.2 K_d and R_f of Ca^{2+} indicators

The fluorescence intensities of OGB-1, OGB-6F, Cal-520, and Fluo-4FF were measured in Ca^{2+}-buffer solutions with different $[Ca^{2+}]_i$ to determine their K_d and dynamic range (R_f). Figs. 2.3A-D display the normalised fluorescence of these indicators as a function of $[Ca^{2+}]_i$. The consistency in the fluorescence intensity between Ca^{2+}-EGTA and Ca^{2+}-HEDTA solutions (filled and open circles, respectively) verifies the measured values of $[Ca^{2+}]_i$. Each of these plots was fitted with a Hill equation (Eq. 2.5; black curves). The values of K_d and R_f obtained from these fits are shown in Table 2.4.

Figs. 2.3E-F demonstrate the importance of measuring $[Ca^{2+}]_i$ with a Ca^{2+}-selective macroelectrode. In these plots, values for $[Ca^{2+}]_i$ were calculated using

Figure 2.3: Plots of normalised fluorescence *vs.* $[Ca^{2+}]_i$ for OGB-1, Cal-520, OGB-6F, and Fluo-4FF. (A-D) The normalised fluorescence of each indicator was plotted against $[Ca^{2+}]_i$ in Ca^{2+}-EGTA (filled circles) and Ca^{2+}-HEDTA solutions (open circles). The displayed values of $[Ca^{2+}]_i$ were measured with a Ca^{2+}-selective macroelectrode. Each plot has been fitted with a Hill equation (black curves), yielding values of K_d and R_f. (E-F) Same as (A-B) but with values of $[Ca^{2+}]_i$ calculated using Maxchelator. Only values for Ca^{2+}-EGTA solutions were fitted with a Hill equation.

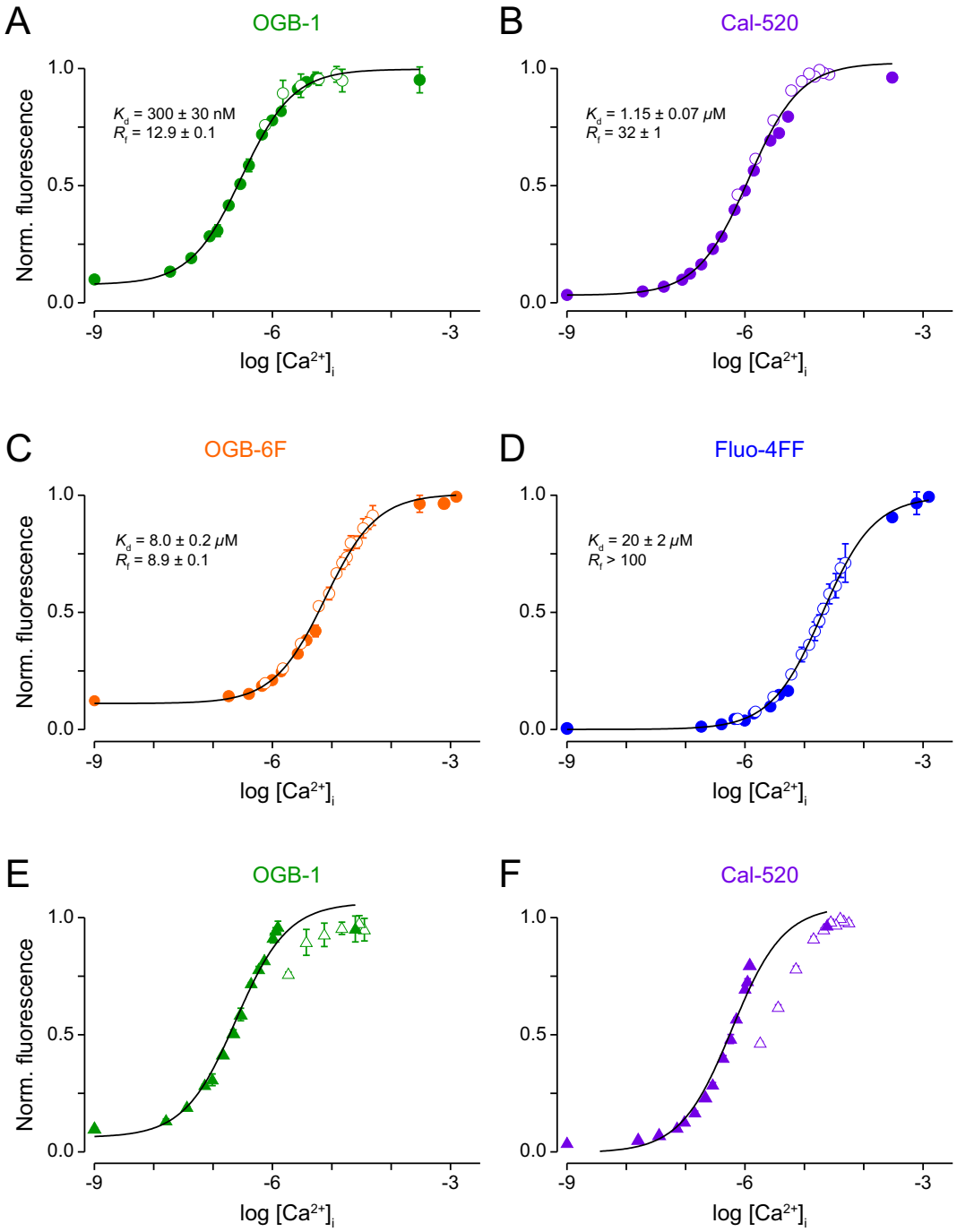

(See previous page for figure legend)

Table 2.4: K_d and R_f of OGB-1, OGB-6F, Cal-520, and Fluo-4FF. Values for K_d and R_f were determined for each batch of an indicator, with 2-3 repeats *per* batch. R_f of Fluo-4FF could not be accurately calculated as its F_{min} was very close to 0. Also shown are the values of K_d obtained from the manufacturers or by previous studies. s.f.: significant figures.

Indicator	Lot #	K_d (μM)		R_f	K_d used for $[Ca^{2+}]_i$ calculation (μM)
		measured	published		
OGB-1	1	0.28 ± 0.04	$0.19 - 0.21$[acd]	12.8 ± 0.8	0.30 (1 s.f.)
	2	0.30 ± 0.03		12.9 ± 0.1	
OGB-6F	1	8.0 ± 0.2	3[ae]	8.9 ± 0.1	8.0 (1 s.f.)
	2	8.4 ± 0.2		8.9 ± 0.4	
Cal-520	1	1.15 ± 0.07	0.32[b]	32 ± 1	not used
Fluo-4FF	1	20 ± 2	8.1[d]	> 100	not used

[a]Life Technologies; [b]AAT Bioquest, Inc.; [c]Maravall *et al.* (2000); [d]Yasuda *et al.* (2004); [e]Brenowitz and Regehr (2007)

the Maxchelator program, with K_d of EGTA and HEDTA shown in Table 2.3. Such a calculation yielded values that were different from those obtained from the electrode potentials. In addition, although the fluorescence intensities of OGB-1 and Cal-520 in some EGTA solutions were similar to those in some HEDTA solutions, the latter solutions had much larger calculated values of $[Ca^{2+}]_i$. The K_d values of OGB-1 and Cal-520 would have been determined as 240 $\pm$ 40 and 600 $\pm$ 90 nM, respectively, if only Ca^{2+}-EGTA solutions were used, if EGTA was assumed to be 100% pure, and if $[Ca^{2+}]_i$ in these solutions were estimated using Maxchelator. These values were smaller than those obtained with the measured $[Ca^{2+}]_i$ values (300 $\pm$ 30 and 1150 $\pm$ 70 nM; p_t = 0.4 and 0.04, respectively).

It has been suggested that K_d and R_f might vary between different batches of a Ca^{2+} indicator, likely due to different levels of impurities (Harkins *et al.*, 1993; Faas and Mody, 2014). As during the course of this study, two batches of OGB-1 and OGB-6F were used for imaging of presynaptic Ca^{2+} dynamics, K_d and R_f were measured for all of them. It was found that values of K_d and R_f did not vary significantly between these batches (Table 2.4). Therefore, only one value of K_d was used for each indicator

to calculate $[Ca^{2+}]_i$ from their fluorescence intensity (Table 2.4).

2.4 Discussion

In this thesis, non-ratiometric Ca^{2+} indicators, including OGB-1, Cal-520, OGB-6F, and Fluo-4FF, were used to image Ca^{2+} dynamics in synaptic boutons of layer 5 pyramidal neurons (Chapters 3 and 4). To accurately calculate $[Ca^{2+}]_i$ from their fluorescence intensities, the K_d values of these indicators were measured in Ca^{2+}-buffer solutions that mimicked the patch-clamp internal solution in terms of pH, ionic strength, and temperature. $[Ca^{2+}]_i$ in these Ca^{2+}-EGTA and Ca^{2+}-HEDTA solutions was measured with a Ca^{2+}-selective macroelectrode to ensure accuracy. When plotted against the measured values of $[Ca^{2+}]_i$, the potentials of the Ca^{2+} electrode as well as the fluorescence intensities of all indicators were consistent between Ca^{2+}-EGTA and Ca^{2+}-HEDTA solutions. This validates the $[Ca^{2+}]_i$ measurements.

2.4.1 The purity and K_d values of EGTA and HEDTA

As has been found by a number of studies (Miller and Smith, 1984; McGuigan *et al.*, 2007; McGuigan and Stumpff, 2013), the purity of EGTA was much smaller than the value quoted by the manufacturer. This was most likely due to "contamination" by water. Miller and Smith (1984) suggested that water is an integral component of the crystal structure of EGTA. Drying at 80 °C for 24 hours did not increase the purity of their sample. There was also no significant water uptake by EGTA under normal shelf-storage conditions. As a result, the purity of EGTA should always be measured in order to accurately determine $[Ca^{2+}]_i$ in Ca^{2+}-EGTA solutions.

Another factor that is critical to the calculation of $[Ca^{2+}]_i$ in Ca^{2+}-buffer solutions is the K_d value of the buffer. The finding that the values of K_d of EGTA and HEDTA were different from those estimated by the widely used Maxchelator program

emphasises the necessity to measure $[Ca^{2+}]_i$ in these solutions (McGuigan *et al.*, 2007; McGuigan and Stumpff, 2013). In fact, many computer programs and tabulated constants provide inaccurate and inconsistent values of $[Ca^{2+}]_i$ in Ca^{2+}-buffer solutions, even when the purity of the buffers has been measured and corrected for (McGuigan and Stumpff, 2013). This is because the association/dissociation constants that underlie the affinity of a buffer for Ca^{2+} are often measured under non-physiological conditions (*e.g.* at a low ionic strength of $\sim$ 100 mM, pH 7.0 and/or $20 - 25$ °C). Therefore, corrections have to be made to determine the apparent Ca^{2+} binding affinity of the buffer in physiologically relevant solutions. Unfortunately, as they involve assumptions and sometimes unavailable data, these corrections are prone to significant errors (Bers *et al.*, 2010; McGuigan *et al.*, 2017).

2.4.2 K_d of Ca^{2+} indicators

The K_d values of OGB-1, Cal-520, OGB-6F, and Fluo-4FF, obtained from the manufacturers or by previous studies, were also much smaller than those measured in this thesis (Table 2.4). Admittedly, different batches of dyes may vary in their purity and thus K_d (Faas and Mody, 2014). However, a major reason for the large variation in K_d values is likely the fact that the manufacturers, in particular Life Technologies, often calibrate fluorescent Ca^{2+} indicators in solutions with a low ionic strength ($\sim$ 100 *vs.* 170 mM in a standard patch-clamp internal solution). However, the Ca^{2+} binding site of these Ca^{2+} indicators is based on BAPTA, the Ca^{2+} binding affinity of which is highly sensitive to the ionic strength (Bers *et al.*, 2010). In fact, an increase in the ionic strength from 100 to 250 mM caused the affinity of Fura-2 for Ca^{2+} to decrease by almost 7-fold (Grynkiewicz *et al.*, 1985).

Additionally, some of the previous studies might have used Ca^{2+}-EGTA solutions to calibrate low-affinity Ca^{2+} indicators, such as OGB-6F and Fluo-4FF (Yasuda *et al.*, 2004; Brenowitz and Regehr, 2007). As the values of K_d of these indicators are not in the optimal buffering range of EGTA, the use of Maxchelator and the assumption of 100% buffer purity would significantly underestimate the true K_d (as shown here for

Cal-520). Moreover, when a solution is not appropriately buffered, the true $[Ca^{2+}]_i$ is highly sensitive to metal contamination, incorrect weighing, and pipetting errors (Patton *et al.*, 2004). Therefore, without measurements, $[Ca^{2+}]_i$ cannot be accurately determined.

2.4.3 Potential effects of intracellular constituents and Mg^{2+}

Although the values of K_d were measured *in vitro*, in the absence of proteins and free Mg^{2+}, they should provide reasonable estimates of the respective K_d values in neocortical pyramidal neurons. It has been shown that certain intracellular constituents, such as myoplasmic proteins, bind to Ca^{2+} indicators and lower their affinities for Ca^{2+} (Konishi *et al.*, 1988; Harkins *et al.*, 1993). However, the interaction between Ca^{2+} indicators and intracellular constituents is much less severe in non-muscle cells (Neher, 2013). In fact, Neher and colleagues reported no difference between the value of K_d of Fura-2 measured in adrenal chromaffin cells and that in a standard intracellular saline (Zhou and Neher, 1993; Oheim, 1995; Neher, 2013; but see Augustine and Neher, 1992). Consistently, the K_d value of OGB-1 measured here is similar to that of its AM-ester in HeLa cells (nucleoplasmic: 320 $\pm$ 60 nM, cytoplasmic 430 $\pm$ 90 nM; Thomas *et al.*, 2000).

The presence of a physiological concentration of free Mg^{2+} has also been suggested to decrease the affinity of Ca^{2+} indicators for Ca^{2+}. This is particularly true for early indicators, such as quin-2 (Tsien *et al.*, 1982). Addition of 1 mM free Mg^{2+} increased the K_d value of quin-2 by almost two-fold. This is because, even though quin-2 binds Ca^{2+} with a 10^4 times higher affinity (100 nM *vs.* 1 mM), the free concentration of Mg^{2+} is also 10^4 times higher than that of Ca^{2+}. As a result, Mg^{2+} strongly competes with Ca^{2+} for quin-2 binding, increasing the K_d value of the latter interaction. However, as the selectivity for Ca^{2+} of newer indicators has been increased to more than 10^5, the presence of $\sim$ 1 mM free Mg^{2+} is unlikely to affect their K_d values, including those of the Fluo and OGB series (Tsien, 1988, 1989). In support of this, a preliminary experiment showed that addition of 0.7 mM free

Mg^{2+}, a concentration found in neurons (Alvarez-Leefmans *et al.*, 1984; Brocard *et al.*, 1993; Li-Smerin *et al.*, 2001), did not significantly affect the K_d values of OGB-1 and OGB-6F (data not shown).

2.4.4 R_f of OGB-1

The measured values of R_f, although similar to those provided by the manufacturer, were considerably larger than *in situ* measurements. For instance, Thomas *et al.* (2000) reported a value of ~ 2.5 for the AM-ester of OGB-1 in HeLa cells. In cultured hippocampal neurons and cerebellar mossy terminals, R_f of OGB-1 ranged from 4 to 6 (Maravall *et al.*, 2000; Delvendahl *et al.*, 2015). Such a significant reduction in R_f (by at least two-fold) has been proposed to result from the interaction between intracellular constituents and Ca^{2+} indicators (Harkins *et al.*, 1993; O'Malley *et al.*, 1999; Thomas *et al.*, 2000). However, caution should be taken to interpret the values of R_f measured in cells or cellular compartments. For a high-affinity indicator such as OGB-1, $[Ca^{2+}]_i$ would need to be reduced to $\sim$ 10 nM to measure its minimum fluorescence intensity. In comparison, for OGB-6F, Fluo-4FF, and other low-affinity indicators, $[Ca^{2+}]_i$ would need to be raised to more than 100 μM to achieve saturation. It is questionable whether $[Ca^{2+}]_i$ in living cells could be accurately clamped to these non-physiological levels. In this study, only R_f of OGB-1 was required so that the resting $[Ca^{2+}]_i$ could be calculated from its fluorescence intensity (Chapter 3). An R_f value of 6, which was the maximum value of R_f measured in neurons (Maravall *et al.*, 2000; Delvendahl *et al.*, 2015), was used for this calculation. With this value, the resting $[Ca^{2+}]_i$ might have been underestimated. However, as explained Section 3.4.1, this was unlikely to significantly affect the estimation of the endogenous Ca^{2+} binding ratio, the rate constant of Ca^{2+} sequestration, and the amplitude and time course of the Ca^{2+} transients in the absence of exogenous buffers.

2.4.5 Implications

The errors associated with calculating $[Ca^{2+}]_i$ in Ca^{2+}-buffer solutions have implications for the published values of the intracellular $[Ca^{2+}]_i$. In particular, in subcellular compartments, including axon terminals and dendritic spines, $[Ca^{2+}]_i$ can increase by ~ 1 μM upon stimulation. Therefore, low-affinity Ca^{2+} indicators such as OGB-6F and Fluo-4FF are increasingly used to measure Ca^{2+} elevations in these compartments (Koester and Sakmann, 2000; Sabatini *et al.*, 2002; Brenowitz and Regehr, 2007; Stocca *et al.*, 2008; Kisfali *et al.*, 2013; Delvendahl *et al.*, 2015). However, to my knowledge, most studies have not properly calibrated these dyes. Their K_d values were either obtained from the manufacturer (who measured them in non-physiological solutions) or measured in calibrating solutions with $[Ca^{2+}]_i$ estimated using computer programs. If the large difference in K_d values is in fact due to inappropriate calibration rather than batch-to-batch variations, then the published values of $[Ca^{2+}]_i$ may have an error of up to 200%. This makes it difficult to interpret not only the published values of $[Ca^{2+}]_i$, but also the values of other parameters that are derived from them (*e.g.* the buffering capacity of endogenous buffers and the number of Ca^{2+} channels that underlie a Ca^{2+} rise). In fact, as shown in Section 3.4.2.1 and Fig. 3.19, the Ca^{2+} binding ratio of endogenous buffers would have been significantly overestimated and the number of VGCCs activated by an AP underestimated, if the published values of K_d of OGB-1 and OGB-6F had been used to determine presynaptic $[Ca^{2+}]_i$. This means that any comparison of $[Ca^{2+}]_i$ and related parameters between different studies is likely misleading.

2.5 Summary

The values of K_d and R_f were determined for OGB-1, Cal-520, OGB-6F, and Fluo-4FF. The use of a Ca^{2+}-selective macroelectrode allowed the purity and K_d of EGTA and HEDTA in the prepared solutions to be measured. This ensured the accuracy of the measured K_d values. Although measured *in vitro*, they provided reasonable estimates

of the respective K_d values in neurons. Therefore, they were used to calculate $[Ca^{2+}]_i$ from the fluorescence intensity of the indicators (Chapters 3 and 4). A smaller value of R_f, compared to that measured *in vitro*, was used to calculate the resting $[Ca^{2+}]_i$ from OGB-1 fluorescence (Chapter 3).

Chapter 3

Dynamics of AP-evoked Ca^{2+} transients in neocortical synaptic boutons

3.1 Introduction

In nerve terminals, the arrival of an action potential (AP) activates voltage-gated Ca^{2+} channels (VGCCs) and causes a brief influx of Ca^{2+} (Katz and Miledi, 1969; Llinas *et al.*, 1981a; Augustine and Eckert, 1984; Borst and Sakmann, 1996, 1998a; Bischofberger *et al.*, 2002). Within $10 - 100$ μs of channel opening and in the vicinity of open channels, localised domains of highly elevated $[Ca^{2+}]_i$ trigger synchronous transmitter release (Chad and Eckert, 1984; Simon and Llinas, 1985; Bollmann *et al.*, 2000; Schneggenburger and Neher, 2000). Once the channels close, Ca^{2+} equilibrates with endogenous fast buffers, and the Ca^{2+} gradient dissipates by diffusion. The spatially homogeneous, residual $[Ca^{2+}]_i$, typically ≤ 1 μM, is removed by Ca^{2+} sequestration mechanisms.

Although the spatially homogeneous $[Ca^{2+}]_i$ does not trigger synchronous transmission, it has been implicated in asynchronous transmitter release and multiple forms of synaptic plasticity (Atluri and Regehr, 1996; Zucker and Regehr, 2002; Neher and

Sakaba, 2008). As a result, factors that underlie the spatially homogeneous Ca^{2+} dynamics have been the focus of many studies since 1980s. These include the endogenous Ca^{2+} buffering capacity and the activity of Ca^{2+} transporters. To estimate these factors, the single-compartment model described by Neher and Augustine (1992) has been widely used. As its name suggests, this model considers a cell or a cellular region as a single compartment in which $[Ca^{2+}]_i$ behaves in a spatially homogeneous manner. With additional assumptions on fast and non-saturable Ca^{2+} buffers, and a linear rate of Ca^{2+} sequestration, the single-compartment model predicts $[Ca^{2+}]_i$ to decay mono-exponentially after a brief Ca^{2+} influx. A mono-exponential decay in $[Ca^{2+}]_i$ has been observed in several nerve terminals, including the calyx of Held and hippocampal mossy fibre synapse (Regehr *et al.*, 1994; Helmchen *et al.*, 1997). However, in a growing number of terminals, the sum of two distinct exponential functions is required to produce a satisfactory fit to the decay phase of AP-evoked Ca^{2+} transients (Tank *et al.*, 1995; Koester and Sakmann, 2000; Collin *et al.*, 2005a; Kim *et al.*, 2005; Muller *et al.*, 2007; Kisfali *et al.*, 2013). Such a deviation from the prediction of the single-compartment model has been attributed to the presence of Ca^{2+} buffers with slow binding kinetics (Collin *et al.*, 2005b; Muller *et al.*, 2007), buffer saturation (Tank *et al.*, 1995), or a non-linear transporter (Regehr, 1997; Kim *et al.*, 2005).

A number of studies have shown that, besides Ca^{2+} influx, intracellular Ca^{2+} release also contributes to synchronous transmitter release and short-term plasticity. Ca^{2+} can be released from presynaptic stores through the ryanodine and/or IP_3 receptor, most likely through the process of Ca^{2+}-induced Ca^{2+} release (CICR). In cerebellar basket cell terminals, synaptic boutons of cultured CA3 pyramidal neurons, and mossy fibre boutons (MFBs) of hippocampal granule cells, AP-evoked Ca^{2+} transients are diminished by pharmacological agents that interfere with Ca^{2+} release (Llano *et al.*, 2000; Emptage *et al.*, 2001; Liang *et al.*, 2002; Scott and Rusakov, 2006). Consistently, at synapses made by basket cells onto Purkinje cells, inhibition of ryanodine receptors (RyRs) affects both the inhibitory postsynaptic current (IPSC) amplitude and the paired-pulse ratio (Galante and Marty, 2003). Similarly, blockade of Ca^{2+} release from presynaptic stores reduces the amplitude of excitatory

postsynaptic currents (EPSCs) in connected pairs of layer 2 pyramidal neurons by $\sim$ 30% (Choy, 2011). However, such an effect has not been observed in cultured CA3 pyramidal neurons, in which inhibition of RyRs affects paired-pulse facilitation but not the EPSC amplitude (Emptage *et al.*, 2001).

In this chapter, AP-evoked Ca^{2+} transients were measured in *boutons en passant* of neocortical pyramidal neurons. Factors that determined the amplitude and time course of the intracellular Ca^{2+} elevations were estimated in accordance with the single-compartment model. Based on these estimations, a 3D reaction-diffusion model was created to simulate the rise in $[Ca^{2+}]_i$ in response to an AP. The simulated transients were compared to their measured counterparts, to elucidate the role of diffusion into the axon in shaping the spatially homogeneous $[Ca^{2+}]_i$. The build-up of $[Ca^{2+}]_i$ during repetitive stimulation was also characterised to provide evidence for CICR in these synaptic boutons.

3.2 Materials, methods, and theory

3.2.1 Animals

$15-20$ day old Wistar rats of either sex were obtained from the Animal Services of the Australian National University (ANU). Animals were housed and handled according to the guidelines of the ANU Animal Experimentation Ethics Committee.

3.2.2 Preparation of acute brain slices

Rats were quickly decapitated with a small animal guillotine (Stoelting Co., Wood Dale, IL, USA; No 51330). The skull was cut along the sagittal suture with a scalpel, and along the coronal and lambdoidal sutures with a pair of sharp-tipped dissecting scissors. A pair of anatomical forceps was used to open the occipital and parietal bones to reveal the brain. With the scalpel, the two cortical hemispheres were then

separated from each other (along the midline), and from the olfactory bulbs at the front and the brainstem at the back. Both hemispheres were removed from the rest of the brain with a spatula and placed in ice-cold artificial cerebrospinal fluid (ACSF) containing (in mM): 125 NaCl, 25 $NaHCO_3$, 1.25 NaH_2PO_4, 2.5 KCl, 2 $CaCl_2$, 1 $MgCl_2$, and 10 glucose, bubbled with Carbogen^{TM} (95% O_2 and 5% CO_2; BOC Limited, North Ryde, NSW, Australia) to obtain a pH of $7.3 - 7.4$ ($\sim$ 310 mOsm). Once cooled, both hemispheres were glued onto the stage of a vibratome (Leica VT 1200S, Leica Biosystems Nussloch GmbH, Nussloch, Germany), with the sagittal cut surfaces down, using cyanoacrylate (Loctite 407, Henkel, Düsseldorf, Germany). The stage was then placed at a forward tilting angle of 15° in the vibratome chamber, which was in turn filled with ice-cold, oxygenated ACSF. The vibratome blade was positioned $\sim$ 3 mm vertically below the top of the two hemispheres, before it was allowed to cut through the brain (0.07 mm/s forward motion with $1.0 - 1.5$ mm horizontal amplitude). 300 μm thick parasagittal slices of the neocortex, with the hippocampus attached, were obtained and placed in a holding chamber containing oxygenated ACSF at 34 °C for 30 min. Slices were subsequently maintained at room temperature until required.

3.2.3 Electrophysiology

Brain slices were placed in a recording chamber and superfused with standard ACSF containing (in mM): 125 NaCl, 25 $NaHCO_3$, 1.25 NaH_2PO_4, 2.5 KCl, 2 $CaCl_2$, 1 $MgCl_2$, and 25 glucose, bubbled with Carbogen^{TM} to obtain a pH of $7.3 - 7.4$ ($\sim$ 320 mOsm). The flow rate of the superfusate was $3 - 4$ ml/min. All experiments were done at 35 $\pm$ 1 °C.

Brain slices were viewed on an upright microscope (LSM 510, Zeiss, Oberkochen, Germany), equipped with a 40$\times$ 1.0 NA objective (Zeiss) and infrared-differential interference contrast optics (Stuart *et al.*, 1993). Whole-cell patch-clamp recordings were obtained from visually identified pyramidal neurons in layer 5 of the somatosensory cortex. Patch pipettes were pulled from borosilicate glass tubes (outer

diameter = 2 mm, inner diameter = 1 mm, length = 75 mm; Hilgenberg GmbH, Malsfeld, Germany; Art.-No 1807502), using a Flaming/Brown micropipette puller (P-97, Sutter Instrument Co., Novato, CA, USA) with a 3 mm box filament. A five-step pulling program was used to produce slowly tapering pipettes. Patch pipettes were filled with an internal solution containing (in mM): 115 K-gluconate, 20 KCl, 10 HEPES, 10 phosphocreatine, 4 ATP-Mg, and 0.3 GTP, titrated with KOH to a pH of 7.3 ($\sim$ 285 mOsm). For fluorescence imaging, a Ca^{2+} indicator and a Ca^{2+}-insensitive dye were both added to the internal solution (Section 3.2.4). When filled, patch pipettes had a tip resistance of $3-6$ MΩ.

Patch pipettes were guided into the recording chamber and towards target cells using an MP-285 manipulator (Sutter Instrument Co.). A positive pressure ($\sim$ 25 mmHg) was applied to the pipette's interior to prevent accumulation of debris on the tip. When the pipette was close to the surface of the target cell, the pressure applied produced a small dimple on the cell's membrane. At this point, the positive pressure was released and a negative pressure (~ -10 mmHg) was applied to promote sealing of the cell membrane to the pipette tip. Once a GΩ seal had formed, brief pulses of suction ($\sim$ 50 mmHg) were applied by mouth to rupture the membrane within the pipette tip and allow access to the cytosol of the target cell. The initial access resistance (R_s) was typically < 20 MΩ.

Voltage- and current-clamp recordings were made with a MultiClamp 700A (Molecular Devices, Sunnyvale, CA, USA; commander version 1.2.10.4). Before a patch pipette was positioned close to the surface of a target cell, the voltage reading on the amplifier was set to zero. Under voltage-clamp, pyramidal cells were held at -70 mV. APs were evoked in current-clamp mode, by applying 2 ms long somatic current injections ($1-3$ nA). Voltage responses were filtered at 10 and digitised at 20 kHz. Membrane potentials have not been corrected for the liquid junction potential, measured to be -12 mV. Experiments were only done in cells which maintained a resting membrane potential of ≤ -60 mV. Data were acquired using custom-made software implemented in Igor Pro 6.2/6.3 (Wavemetrics, Oregon, USA), via an ITC-18 computer interface (InstruTech Corporation, Port Washington, NY, USA). Data were

stored on the hard drive of a MacIntosh PowerMac G5 computer, running Mac OS X 10.5 (Apple Inc., Cupertino, CA, USA). Timings for current and voltage steps were provided by a Master-8 stimulator (A.M.P.I., Jerusalem, Israel).

3.2.4 Confocal Ca^{2+} imaging

Fluorescence imaging was done with a laser-scanning confocal microscope (Zeiss LSM 510), equipped with a 40× 1.0 NA water-immersion objective (Zeiss). Manipulation of all lasers (on/off and intensity) and light paths, together with acquisition of fluorescence images, was done through the LSM 510 software (Zeiss, version 3.2 SP2), which was run on a Windows 2000 workstation.

Cells were filled through the patch pipette with two fluorophores: a Ca^{2+}-insensitive dye (50 μM Alexa Fluor® 568) for imaging of neuronal structures, and a Ca^{2+} indicator ($40-160$ μM OGB-1, $50-500$ μM OGB-6F, 200 μM OGB-5N, 500 μM Fluo-4FF, or 200 μM Cal-520) for measurement of $[Ca^{2+}]_i$. All fluorescent dyes were purchased from Life Technologies (Carlsbad, CA, USA), except for Cal-520, which was from AAT Bioquest, Inc. (Sunnyvale, CA, USA). Unless otherwise stated, cells were filled with the fluorophores for at least 90 min before Ca^{2+} imaging commenced.

In all experiments, Alexa Fluor® 568 and the Ca^{2+}-sensitive fluorophores were excited separately to minimise photo-toxicity. The former was excited by 543 nm light from a helium-neon laser (laser power < 0.1 mW). The emitted fluorescence was long-pass filtered for > 560 nm and measured by a photomultiplier tube (PMT). Ca^{2+}-sensitive indicators were excited using an argon laser (488 nm; laser power < 1 mW), and their fluorescence was long-pass filtered for > 505 nm before being acquired by the same PMT. Bleed-through from Alexa Fluor® 568 into the fluorescence measurement of Ca^{2+}-sensitive indicators would not affect $[Ca^{2+}]_i$ after stimulation calculated based on Eq. 3.5 (Section 3.2.6.4). In contrast, bleed-through from Alexa Fluor® 568 would lead to a slight overestimation of $[Ca^{2+}]_i$ at rest $\left([Ca^{2+}]_{rest}\right)$ calculated from Eq. 3.4 (Section 3.2.6.4). Therefore, in experiments aimed to measure

$[Ca^{2+}]_{rest}$, the fluorescence of OGB-1 (40 μM) was passed through a $500-550$ nm band-pass filter before being acquired.

The fluorescence intensity of Alexa Fluor® 568 was obtained in z-stacks (typically, 1508×1508 pixels *per* frame; pixel size = 150 nm; dwell time = 0.64 μs *per* pixel; z-interval = 2 μm; open pinhole = 10 Airy units; Fig. 3.4A-B). To reduce laser exposure, the fluorescence intensity of a Ca^{2+} indicator was acquired using line scans, drawn across a bouton and perpendicular to its parent axon collateral ($32-44$ pixels *per* line; pixel size = $\sim$ 150 nm; dwell time = 10.24 μs *per* pixel; open pinhole = 12 Airy units; Fig. 3.4C-D). For single APs, line scans were taken every 5 ms if OGB-1 or Cal-520 fluorescence was measured, and every $1-3$ ms if OGB-6F or Fluo-4FF fluorescence was obtained. For $1-2$ s long trains of APs ($10-100$ Hz), line scans were done every $10-100$ ms, unless stated otherwise. When averaging several repeats to improve the signal-to-noise ratio, the inter-repeat interval was $10-30$ s (typically $2-5$ for each measurement). For each cell, $\leq$ 3 boutons, preferentially on different collaterals, were imaged. In experiments with bath application of a pharmacological compound, only $1-2$ boutons were imaged *per* cell.

3.2.5 Pharmacological compounds

To block the sarco/endoplasmic reticulum Ca^{2+} ATPase (SERCA), cyclopiazonic acid (CPA; Alomone Labs, Jerusalem, Israel) was bath-applied for at least 10 min. The stock solution of CPA (50 mM) was made by dissolving 25 mg of CPA in 1.486 ml of dimethyl sulfoxide (DMSO; Sigma-Aldrich, St. Louis, Missouri, USA). On the day that CPA was required for experiments, a small volume of the stock solution was added to the standard ACSF to produce a final concentration of 25 μM.

3.2.6 Data analysis

3.2.6.1 Analysis of electrophysiological data

The voltage threshold of APs recorded at the soma was defined as the membrane potential (V_m) at which dV_m/dt first exceeded 50 $V \cdot s^{-1}$. The AP amplitude was the

difference between the AP threshold and the peak V_m. The AP half-width was defined as the width of the AP, halfway between its threshold and peak.

3.2.6.2 Analysis of Ca^{2+} imaging

Fluorescence data were imported into Igor Pro 6.3, where analysis was done, using a custom-made Zeiss TIFF image reader. Each fluorescence line scan across a bouton ($32 - 44$ pixels) was fitted with a Gaussian function, the y-offset of which was considered to be background fluorescence (Fig. 3.4D, top left). The spatially averaged fluorescence of an imaged bouton (F) was calculated as the average fluorescence of $6 - 10$ pixels, corresponding to $\pm$ 2 standard deviations around the peak of the Gaussian, minus the background fluorescence. The baseline fluorescence (F_0) was determined by averaging over a $15 - 1000$ ms time window immediately before the AP onset (depending on the sampling interval; ≥ 10 time points). The relative change in fluorescence after stimulation $(\Delta F/F_0)$ was calculated by normalising the change in F to F_0.

The decay time course of these fluorescence transients, as well as of the corresponding Ca^{2+} transients, was fitted with either an exponential function $\left(Ae^{-t/\tau}\right)$ or the sum of two exponential functions $\left(A_1e^{-t/\tau_1} + A_2e^{-t/\tau_2}\right)$; for the latter, τ_1 was constrained to be larger than twice the sampling interval ($1 - 3$ ms for OGB-6F and Fluo-4FF; 5 ms for OGB-1 and Cal-520). The decay kinetics of a bouton were considered bi-exponential if 1) $\tau_2 \geq 3 \times \tau_1$, 2) A_1 and A_2 each fell between 0.15 and 0.85 of their sum $(A_1 + A_2)$, and 3) both τ_1 and τ_2 were smaller than the scanning duration after stimulation.

Unless otherwise stated, the peak amplitude of an AP-evoked Ca^{2+} transient was measured as the amplitude of the mono- or bi-exponential fit (A or $A_1 + A_2$). The relative amplitude of the fast decay component of a bi-exponential fit ($\text{amplitude}_{\text{fast}}$) was calculated as $A_1/(A_1+A_2) \times 100\%$. Occasionally, the decay kinetics of transients with bi-exponential fits are presented by the amplitude-weighted decay time constant

τ_w, which was calculated as $\frac{A_1\tau_1+A_2\tau_2}{A_1+A_2}$; for a mono-exponential decay, $\tau_w = \tau$. For 1 or 2 s long trains of APs, ${}^{\Delta F}/_{F_0}$ was measured as the average change over the last 100 or 200 ms of stimulation, respectively, unless stated otherwise.

In experiments in which CPA was added to the superfusate, data were excluded if F_0 changed by more than 30% after the 10 min of solution exchange. Based on this criterion, a total of 4 boutons were excluded: 1 out of 12 boutons measured with Cal-520 (8%), and 3 out of 20 boutons measured with OGB-6F (15%). Additionally, 2 out of 15 boutons measured with Cal-520 in control experiments (no CPA addition; 13%) were also excluded.

3.2.6.3 Determination of $\left({}^{\Delta F}/_{F_0}\right)_{\max}$ *in situ*

OGB-1. The maximal change in fluorescence ($\left({}^{\Delta F}/_{F_0}\right)_{\max}$) of OGB-1 was determined for each bouton imaged, by evoking 2 s long trains of APs at 10 and 20 Hz. According to Maravall *et al.* (2000), if the change in $[Ca^{2+}]_i$ ($\Delta[Ca^{2+}]_i$) is linearly dependent on the AP frequency, the ratio of ${}^{\Delta F}/_{F_0}$ between two different frequencies can be used to estimate $\left({}^{\Delta F}/_{F_0}\right)_{\max}$ of the Ca^{2+} indicator. That is, if v_1 and v_2 are two AP frequencies with ${}^{\Delta[Ca^{2+}]_{v_2}}/_{\Delta[Ca^{2+}]_{v_1}} = {}^{v_2}/_{v_1}$, then

$$\left({}^{\Delta F}/_{F_0}\right)_{\max} = \frac{\left({}^{\Delta F}/_{F_0}\right)_{v_2}}{x_{v_2}}, \tag{3.1}$$

where x_{v_2} ($0 < x_{v_2} < 1$) represents the level of saturation of the Ca^{2+} indicator caused by an AP train at frequency v_2. x_{v_2} in turn can be approximated as

$$x_{v_2} = \frac{1 - Q \times \frac{v_1}{v_2}}{1 - \frac{v_1}{v_2}}, \tag{3.2}$$

where $Q = \frac{\left({}^{\Delta F}/_{F_0}\right)_{v_2}}{\left({}^{\Delta F}/_{F_0}\right)_{v_1}}$.

This analysis requires two conditions. First, $[Ca^{2+}]_i$ changes linearly between v_1 and v_2. Second, the Ca^{2+} indicator is partially saturated during trains of APs at frequencies v_1 and v_2, and thus, the fluorescence F of the indicator during these trains is no longer a linear function of $[Ca^{2+}]_i$. This second criterion is required so that $\frac{(\Delta F/F_0)_{v_2}}{(\Delta F/F_0)_{v_1}} < \frac{\Delta[Ca^{2+}]_{v_2}}{\Delta[Ca^{2+}]_{v_1}}$, making $Q < v_2/v_1$; otherwise, x_{v_2} in Eq. 3.2 would be zero, and as a result, $(\Delta F/F_0)_{max}$ in Eq. 3.1 would be undefined.

However, $\Delta[Ca^{2+}]_i$ was not a linear function of the AP frequency (Fig. 3.16). In particular, in response to 2 s long trains of APs at 10 and 20 Hz, $\Delta[Ca^{2+}]_{20Hz}/\Delta[Ca^{2+}]_{10Hz} = 2.7 \pm 0.3$ (n = 10). Therefore, to calculate $(\Delta F/F_0)_{max}$ of OGB-1 in these boutons, the method described by Maravall *et al.* (2000) was extended to cope with the supralinear summation of $[Ca^{2+}]_i$ during the AP trains. More specifically, without the assumption of linear summation, x_{v_2} and Q have the following relationship:

$$x_{v_2} = \frac{\dfrac{Q\dfrac{\Delta_1}{\Delta_2} - 1}{\dfrac{\Delta_1}{\Delta_2} - 1} - \dfrac{[DCa]_0}{[D]_T}}{1 - \dfrac{[DCa]_0}{[D]_T}}, \tag{3.3}$$

where $\Delta_1 = \Delta[Ca^{2+}]_{v_1}$, $\Delta_2 = \Delta[Ca^{2+}]_{v_2}$, $[DCa]_0$ is the Ca^{2+}-bound concentration of the dye at baseline, and $[D]_T$ is its total concentration (see Appendix A for a derivation of this equation). It can be seen that Eq. 3.3 becomes Eq. 3.2, if $\Delta_2/\Delta_1 = v_2/v_1$ and $[DCa]_0/[D]_T = 0$. Eq. 3.3 was used to calculate the level of saturation of OGB-1 during the AP train at v_2 = 10 Hz (x_{10Hz}). In this calculation,

$$\frac{\Delta[Ca^{2+}]_{20Hz}}{\Delta[Ca^{2+}]_{10Hz}} = \frac{\Delta_1}{\Delta_2} = 2.7$$

and

$$\frac{[DCa]_0}{[D]_T} = \frac{[Ca^{2+}]_{rest}}{K_d + [Ca^{2+}]_{rest}} = \frac{1}{7}.$$

Table 3.1: Level of saturation of OGB-1 during a 2 s long train of APs at 10 Hz ($x_{10\text{Hz}}$).

$[\text{OGB-1}]_\text{T}$ (μM)	$x_{10\text{Hz}}$	n
40	0.66 ± 0.03	18
80	0.63 ± 0.05	15
120	0.68 ± 0.04	13
160	0.71 ± 0.02	29

Here, $[Ca^{2+}]_\text{rest}$ = 50 nM (Section 3.3.2), and K_d = 300 nM (Table 2.4). $\left(\Delta F/F_0\right)_\text{max}$ was then calculated from $\left(\Delta F/F_0\right)_{10\text{Hz}}$ and $x_{10\text{Hz}}$ (Eq. 3.1). Table 3.1 displays the mean values for $x_{10\text{Hz}}$ for different concentrations of OGB-1. There was no significant difference in $x_{10\text{Hz}}$ in the range of OGB-1 concentrations used (p_ANOVA = 0.3).

To verify this method of calculating $\left(\Delta F/F_0\right)_\text{max}$ for OGB-1, $\Delta F/F_0$ of OGB-1 (40 μM) was measured during 2 s long trains of APs at 100 Hz in 10 boutons. As these high-frequency trains of APs raised $[Ca^{2+}]_\text{i}$ to more than 10 μM (Fig. 3.16), it is reasonable to assume that OGB-1 was completely saturated; that is, $\left(\Delta F/F_0\right)_{100\text{Hz}} \approx \left(\Delta F/F_0\right)_\text{max}$. In these boutons, values for $\left(\Delta F/F_0\right)_\text{max}$ calculated from $\left(\Delta F/F_0\right)_{10\text{Hz}}$ and $x_{10\text{Hz}}$ were not different from $\left(\Delta F/F_0\right)_{100\text{Hz}}$ (2.9 ± 0.3 *vs.* 2.7 ± 0.3; p_t = 0.7).

OGB-6F. $\left(\Delta F/F_0\right)_\text{max}$ of OGB-6F was determined for each bouton imaged, by evoking 1 s long trains of APs at 80 and 100 Hz. As $\Delta[Ca^{2+}]_{100\text{Hz}}/\Delta[Ca^{2+}]_{80\text{Hz}}$ was not measured, Eq. 3.3 could not be used to calculate the level of saturation of OGB-6F during these trains. In addition, it was clear that 1 s long trains of APs at 80 Hz and 100 Hz did not cause complete saturation of OGB-6F as its fluorescence was still increasing towards the end of the trains. Higher frequencies (> 100 Hz) could not be reliably used to measure $\left(\Delta F/F_0\right)_\text{max}$ of OGB-6F, because neocortical pyramidal neurons do not sustain firing at these frequencies (Zhu and Connors, 1999). Therefore, to determine $\left(\Delta F/F_0\right)_\text{max}$ of OGB-6F, an upper-bound ($\left(x_{80\text{Hz}}\right)_\text{max}$) and a lower-bound ($\left(x_{80\text{Hz}}\right)_\text{min}$) were calculated for its level of saturation during the 80 Hz AP train. $\left(x_{80\text{Hz}}\right)_\text{max}$ was found by assuming that $\left(\Delta F/F_0\right)_{100\text{Hz}} = \left(\Delta F/F_0\right)_\text{max}$; thus, $\left(x_{80\text{Hz}}\right)_\text{max} = \frac{\left(\Delta F/F_0\right)_{80\text{Hz}}}{\left(\Delta F/F_0\right)_{100\text{Hz}}}$.

Table 3.2: Level of saturation of OGB-6F during a 1 s long train of APs at 80 Hz (x_{80Hz}).

$[OGB\text{-}6F]_T$ (μM)	x_{80Hz}	n
50	0.70 ± 0.05	13
100	0.73 ± 0.04	15
200	0.71 ± 0.05	10
500	0.57 ± 0.04	12

On the other hand, $(x_{80Hz})_{min}$ was found by assuming that $[Ca^{2+}]_i$ changed linearly between 80 and 100 Hz; that is, $\Delta[Ca^{2+}]_{100Hz}/\Delta[Ca^{2+}]_{80Hz} = 100/80 = 5/4$. Eq. 3.2 was used to calculate $(x_{80Hz})_{min}$ as $[DCa]_0/[D]_T \approx 0$ for OGB-6F. The level of saturation of OGB-6F at 80 Hz (x_{80Hz}) was then calculated as the mean of $(x_{80Hz})_{max}$ and $(x_{80Hz})_{min}$. $(\Delta F/F_0)_{max}$ was subsequently calculated from $(\Delta F/F_0)_{80Hz}$ and x_{80Hz} (Eq. 3.1). Table 3.2 displays the mean values for x_{80Hz}. There was no significant difference in x_{80Hz} in the range of OGB-6F concentrations used (p_{ANOVA} = 0.06).

To verify this method of calculating $(\Delta F/F_0)_{max}$ for OGB-6F, $\Delta F/F_0$ of OGB-6F (50 μM) was measured in response to local application of the Ca^{2+}-ionophore ionomycin (0.3 mM). Among 10 boutons to which ionomycin was applied, only 5 boutons had values for $(\Delta F/F_0)_{ionomycin}$ larger than $(\Delta F/F_0)_{100Hz}$ (4.0 ± 0.2 *vs.* 3.5 ± 0.1; p_t = 0.03). In these boutons, values for $(\Delta F/F_0)_{max}$ calculated from $(\Delta F/F_0)_{80Hz}$ and x_{80Hz} were not significantly different from $(\Delta F/F_0)_{ionomycin}$ (5.1 ± 0.4 *vs.* 4.0 ± 0.2; p_t = 0.06). The tendency for the calculated $(\Delta F/F_0)_{max}$ to be larger than $(\Delta F/F_0)_{ionomycin}$ was consistent with the observation that prolonged application of ionomycin caused cell swelling/beading and a gradual reduction in fluorescence intensities, presumably due to leakage of fluorescent dyes out of the cells or dilution by the increased volume (data not shown). Because of this, $(\Delta F/F_0)_{ionomycin}$ would be smaller than the true $(\Delta F/F_0)_{max}$. Similarly, it is likely that $(\Delta F/F_0)_{ionomycin}$ was measured after substantial dye leakage in the other 5 boutons with $(\Delta F/F_0)_{ionomycin} < (\Delta F/F_0)_{100Hz}$.

3.2.6.4 Determination of $[Ca^{2+}]_i$

$[Ca^{2+}]_{rest}$ was calculated from $(\Delta F/F_0)_{max}$ of the high-affinity Ca^{2+} indicator OGB-1 as follows (Maravall *et al.*, 2000):

$$[Ca^{2+}]_{rest} = K_d \times \left(\frac{1 - R_f^{-1}}{(\Delta F/F_0)_{max}} - R_f^{-1} \right). \tag{3.4}$$

Here, R_f of OGB-1 was assumed to be 6 as had been measured in hippocampal neurons and cerebellar MFBs (Maravall *et al.*, 2000; Delvendahl *et al.*, 2015).

$[Ca^{2+}]_i$ after stimulation was calculated from $\Delta F/F_0$ of OGB-1 or OGB-6F as follows (Lev-Ram *et al.*, 1992):

$$[Ca^{2+}]_i = \frac{[Ca^{2+}]_{rest} + K_d \times \frac{\Delta F/F_0}{(\Delta F/F_0)_{max}}}{1 - \frac{\Delta F/F_0}{(\Delta F/F_0)_{max}}}. \tag{3.5}$$

For all calculations, $[Ca^{2+}]_{rest} = 50$ nM (Section 3.3.2). It can be seen in Eq. 3.5 that, as $\Delta F/F_0$ approaches $(\Delta F/F_0)_{max}$, the denominator approaches 0, thereby subjecting the calculated $[Ca^{2+}]_i$ to large errors. Accordingly, only measurements with $\Delta F/F_0 \leq 0.8 \times (\Delta F/F_0)_{max}$ were used for calculation of $\Delta[Ca^{2+}]_i$. Based on this criterion, two out of 13 boutons (15%) imaged with 40 μM OGB-1 and four out of 22 boutons (18%) imaged with 80 μM OGB-1 were excluded from further analysis.

3.2.6.5 Statistical analysis

Values were given as mean ± standard error (S.E.M). Error bars also indicate S.E.M. In each box-and-whisker plot, the ends of the whiskers represent the minimum and maximum values of the respective data set. Unless stated otherwise, statistical comparisons between different experimental conditions were performed with the

Student's *t*-test or one-way ANOVA analysis, and linear correlation assessed using Pearson's *r*. $p_t < 0.05$, $p_{ANOVA} < 0.05$, and $p_{Pr} < 0.05$ were considered significant.

To assess whether $^{\Delta F}/_{F_0}$ and $\Delta[Ca^{2+}]_i$ in response to an AP or a train of APs decayed mono- or bi-exponentially, changes measured in different boutons using the same concentration of a Ca^{2+} indicator were pooled and averaged. The decay time course of this average response was fitted with an exponential function $\left(Ae^{-t/\tau}\right)$ or the sum of two distinct exponential functions $\left(A_1e^{-t/\tau_1} + A_2e^{-t/\tau_2}\right)$. As a mono-exponential fit is "nested" within a bi-exponential fit (*i.e.*, a bi-exponential fit can be transformed into a mono-exponential fit by making either A_1 or A_2 zero), an *F*-test was used to compare the two fits. The *F*-statistic was calculated as the ratio of the weighted sums of squared errors (χ^2) of the fits (Motulsky and Christopoulos, 2004; Costa *et al.*, 2010). The null hypothesis that the sum of two exponential functions did not provide a significantly better fit than a single exponential function was rejected if $p_F < 0.05$.

To assess whether $\Delta[Ca^{2+}]_i$ reached a plateau during a 2 s long train of APs, changes measured in different boutons using the same stimulation frequency and the same concentration of a Ca^{2+} indicator were pooled and averaged. The lower envelope of the average response was fitted with an exponential function $\left(A \times (1 - e^{-t/\tau})\right)$ or the sum of an exponential function and a linear function $\left(A_1 \times (1 - e^{-t/\tau}) + A_2t\right)$. The statistical comparison was then done with an *F*-test, as described above.

3.2.7 Theory

3.2.7.1 Estimation of endogenous Ca^{2+} binding ratio and sequestration rate

Formulation of a single-compartment model. The single-compartment model described by Neher and Augustine (1992) was used to estimate the Ca^{2+} binding ratio of endogenous buffers and the rate of Ca^{2+} sequestration. This model considers a cell or a cellular region as a compartment in which $[Ca^{2+}]_i$ is spatially homogeneous and diffusion is fast and negligible (assumption 1). Thus, it addresses the time

course of the global Ca^{2+} elevation following membrane depolarisation, rather than the spatiotemporal dynamics of the Ca^{2+} signal around Ca^{2+} channels (Helmchen and Tank, 2015). With rapid equilibration of Ca^{2+}, $\Delta[Ca^{2+}]_i$ in this compartment is determined only by Ca^{2+} influx, buffering, and sequestration (Fig. 3.1A). Only a fraction of the Ca^{2+} ions that enter this compartment will appear as free Ca^{2+}; the rest will be chelated by Ca^{2+} buffers. This model includes two main pools of buffers: a pool of endogenous buffers E and a pool of exogenously introduced buffers D. Here, D mainly consisted of the Ca^{2+} dye. The dynamics of $[Ca^{2+}]_i$ after a brief Ca^{2+} pulse at time t_{AP} are described by the following differential equation:

$$\frac{d[Ca^{2+}]_i}{dt} = k_{off}[ECa] - k_{on}[E][Ca^{2+}]_i + k_{off}[DCa] - k_{on}[D][Ca^{2+}]_i + \Delta[Ca^{2+}]_T \delta(t - t_{AP}) - S\left([Ca^{2+}]_i\right), \quad (3.6)$$

where [ECa] and [DCa] represent the concentrations of Ca^{2+} ions bound to E and D, respectively, k_{on} and k_{off} are the Ca^{2+} on- and off-rates of the respective buffer, $\Delta[Ca^{2+}]_T$ indicates the total increase in Ca^{2+} concentration, and $S\left([Ca^{2+}]_i\right)$ describes the rate at which Ca^{2+} is removed. Here, it is assumed that Ca^{2+} influx is instantaneous; that is, its duration is brief compared to the time course of Ca^{2+} sequestration (assumption 2). Therefore, the Ca^{2+} pulse is modelled by a δ-function. The first four terms on the right-hand side of Eq. 3.6 can be replaced by the rate of change of [ECa] and [DCa] over time as follows:

$$\frac{d[ECa]}{dt} = -k_{off}[ECa] + k_{on}[E][Ca^{2+}]_i, \quad (3.7)$$

and

$$\frac{d[DCa]}{dt} = -k_{off}[DCa] + k_{on}[D][Ca^{2+}]. \quad (3.8)$$

Substituting Eqs. 3.7 and 3.8 into Eq. 3.6 yields

$$\frac{d[\mathrm{Ca}^{2+}]_\mathrm{i}}{dt} + \frac{d[\mathrm{ECa}]}{dt} + \frac{d[\mathrm{DCa}]}{dt} = \Delta[\mathrm{Ca}^{2+}]_\mathrm{T}\delta(t - t_\mathrm{AP}) - S\left([\mathrm{Ca}^{2+}]_\mathrm{i}\right). \tag{3.9}$$

This equation simply describes the conservation of Ca^{2+}: the change in the total calcium concentration (free and buffered; left-hand side) equals the difference between Ca^{2+} influx and sequestration (right-hand side). [ECa] can be quantified by the Ca^{2+} binding ratio of endogenous buffers (κ_E), which is the ratio of E-bound Ca^{2+} to free Ca^{2+} following an increase in $[Ca^{2+}]_\mathrm{i}$; that is,

$$\kappa_\mathrm{E} = \frac{\partial[\mathrm{ECa}]}{\partial[\mathrm{Ca}^{2+}]_\mathrm{i}}. \tag{3.10}$$

If the reactions between Ca^{2+} and endogenous buffers are sufficiently fast so that they are always at equilibrium (assumption 3), then [ECa] can be replaced by

$$[\mathrm{ECa}] = \frac{[\mathrm{E}]_\mathrm{T}[\mathrm{Ca}^{2+}]_\mathrm{i}}{[\mathrm{Ca}^{2+}]_\mathrm{i} + K_\mathrm{d,E}}, \tag{3.11}$$

where $[\mathrm{E}]_\mathrm{T}$ is the total concentration of endogenous buffers and $K_\mathrm{d,E}$ represents their apparent Ca^{2+} binding affinity. Differentiating [ECa] with respect to $[Ca^{2+}]_\mathrm{i}$ yields

$$\begin{aligned}
\kappa_\mathrm{E} &= \frac{\partial[\mathrm{ECa}]}{\partial[\mathrm{Ca}^{2+}]_\mathrm{i}} \\
&= \frac{[\mathrm{E}]_\mathrm{T}([\mathrm{Ca}^{2+}]_\mathrm{i} + K_\mathrm{d,E}) - [\mathrm{E}]_\mathrm{T}[\mathrm{Ca}^{2+}]_\mathrm{i}}{([\mathrm{Ca}^{2+}]_\mathrm{i} + K_\mathrm{d,E})^2} \\
&= \frac{[\mathrm{E}]_\mathrm{T}K_\mathrm{d,E}}{([\mathrm{Ca}^{2+}]_\mathrm{i} + K_\mathrm{d,E})^2}.
\end{aligned} \tag{3.12}$$

Similarly, the Ca^{2+} binding ratio of exogenous buffers (κ_D) can be expressed as

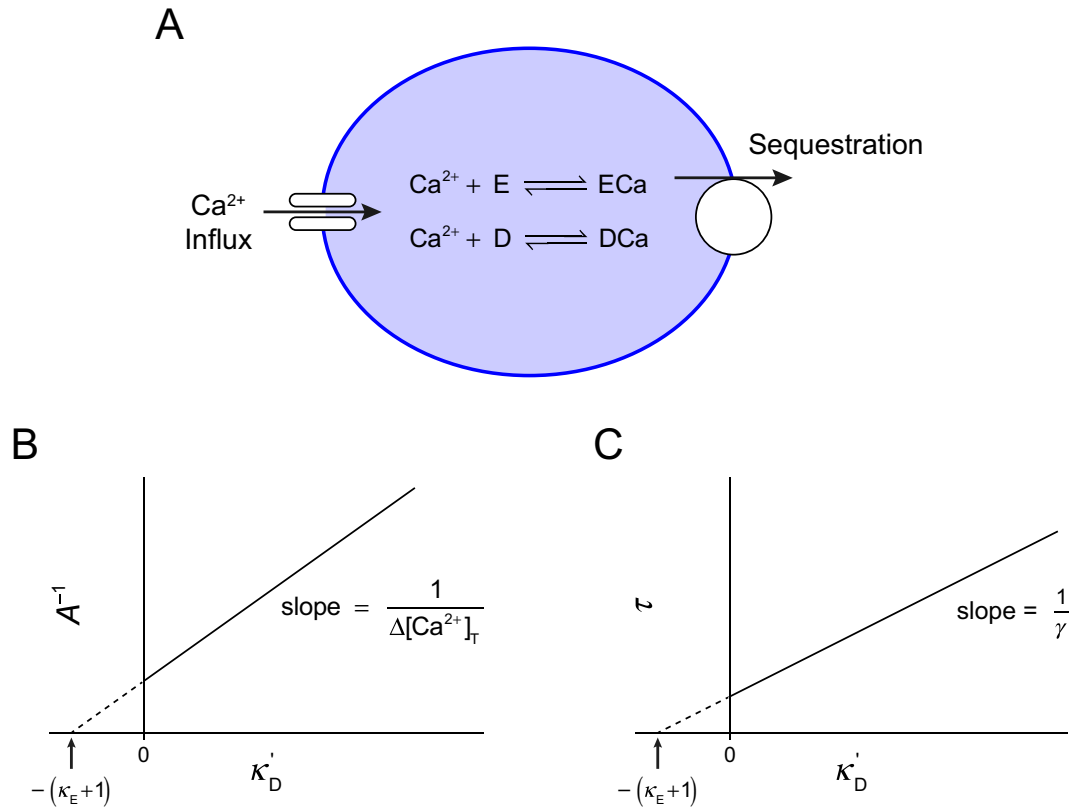

Figure 3.1: Schematic and predictions of a single-compartment model. (A) Schematic of the model described by Neher and Augustine (1992). A cell or a cellular region is considered as a compartment in which $[Ca^{2+}]_i$ is spatially homogeneous. Two pools of Ca^{2+} buffers with fast kinetics are present: a pool of endogenous buffers E and a pool of exogenous buffers D. Ca^{2+} is removed from this compartment by a linear sequestration mechanism. (B) The single-compartment model predicts a linear relationship between the inverse of the peak amplitude of an AP-evoked Ca^{2+} transient (A^{-1}) and the Ca^{2+} binding ratio of exogenous buffers (κ'_D). Characterisation of this relationship allows estimation of the endogenous Ca^{2+} binding ratio κ_E from the x-intercept and the total change in Ca^{2+} concentration ($\Delta[Ca^{2+}]_T$) from the slope. (C) The single-compartment model also predicts a linear relationship between the decay time course of the Ca^{2+} transient (τ) and κ'_D. Characterisation of this relationship allows estimation of κ_E from the x-intercept and γ from the slope. Extrapolation of these two plots to $\kappa'_D = 0$ further yields values of A and τ in the absence of exogenous buffers.

$$\kappa_D = \frac{\partial[DCa]}{\partial[Ca^{2+}]_i} = \frac{[D]_T K_{d,D}}{([Ca^{2+}]_i + K_{d,D})^2}, \tag{3.13}$$

assuming that exogenous Ca^{2+} buffers also have fast Ca^{2+} binding kinetics compared to the rate of Ca^{2+} sequestration. Substituting Eqs. 3.10 and 3.13 into Eq. 3.9 yields

$$\frac{d[Ca^{2+}]_i}{dt}(1 + \kappa_E + \kappa_D) = \Delta[Ca^{2+}]_T \delta(t - t_{AP}) - S\left([Ca^{2+}]_i\right). \tag{3.14}$$

In Eqs. 3.12 and 3.13, it can be seen that both κ_E and κ_D increase as $[Ca^{2+}]_i$ decreases. κ_E reaches a maximum value of $[E]_T/K_{d,E}$ and κ_D approaches $[D]_T/K_{d,D}$ at $[Ca^{2+}]_i$ levels well below $K_{d,E}$ and $K_{d,D}$, respectively. The single-compartment model assumes that $[Ca^{2+}]_i$ after the brief Ca^{2+} pulse is much smaller than $K_{d,E}$ and $K_{d,D}$ so that κ_E and κ_D can be considered as constants (assumption 4). In addition, it is assumed that $S\left([Ca^{2+}]_i\right)$ is linearly dependent on $\Delta[Ca^{2+}]_i$; that is, $S\left([Ca^{2+}]_i\right) = \gamma \times \Delta[Ca^{2+}]_i$, where γ represents the rate constant of Ca^{2+} sequestration (assumption 5). With this assumption, Eq. 3.14 can be re-written as

$$\frac{d[Ca^{2+}]_i}{dt}(1 + \kappa_E + \kappa_D) = \Delta[Ca^{2+}]_T \delta(t - t_{AP}) - \gamma \times \Delta[Ca^{2+}]_i. \tag{3.15}$$

With κ_E and κ_D being constants, and $t_{AP} = 0$, the analytical solution of Eq. 3.15 is an exponential function:

$$\Delta[Ca^{2+}]_i(t) = [Ca^{2+}]_i(t) - [Ca^{2+}]_{rest} = Ae^{-t/\tau}, \tag{3.16}$$

for $t \geq 0$ (Helmchen *et al.*, 1996). The amplitude A of this function, which is the peak amplitude of $\Delta[Ca^{2+}]_i$, can be obtained by integrating Eq. 3.15 over the short period of Ca^{2+} influx (Neher and Augustine, 1992), yielding

$$A \times (1 + \kappa_E + \kappa_D) = \Delta[Ca^{2+}]_T. \tag{3.17}$$

In this integration, the second term on the right-hand side of Eq. 3.15 has been neglected, assuming that the integration time is short compared to the time course of Ca^{2+} sequestration (*i.e.* assumption 2). Consequently,

$$A = \frac{\Delta[Ca^{2+}]_T}{1 + \kappa_E + \kappa_D}. \tag{3.18}$$

The decay time constant τ can be obtained by solving the following equation:

$$\frac{d[Ca^{2+}]_i}{dt}(1 + \kappa_E + \kappa_D) = -\gamma \times \Delta[Ca^{2+}]_i, \tag{3.19}$$

yielding

$$\tau = \frac{1 + \kappa_E + \kappa_D}{\gamma}. \tag{3.20}$$

According to Eqs. 3.18 and 3.20, the inverse of the peak amplitude of $\Delta[Ca^{2+}]_i$ (A^{-1}) and τ are both linearly dependent on the Ca^{2+} binding ratios of buffers. More specifically, the peak amplitude of an AP-evoked Ca^{2+} transient is reduced and its decay time course prolonged with larger values of κ_E and κ_D, that is with increasing buffer concentrations or higher Ca^{2+} binding affinities (smaller values of K_d). Intuitively, this can be understood by considering that, as κ_E or κ_D increases, a larger fraction of Ca^{2+} ions is chelated, thereby decreasing the fraction of free Ca^{2+} ions and $\Delta[Ca^{2+}]_i$. In addition, Ca^{2+} ions that are bound to buffers have to unbind before they can be sequestered. Therefore, an increase in κ_E or κ_D will slow down the decay time course of the Ca^{2+} transient.

In contrast, the time integral of the Ca^{2+} transient, given by the product of A and τ, is independent of the total Ca^{2+} binding ratio (Helmchen *et al.*, 1996); that is,

$$\int_{t_{AP}}^{\infty} \Delta[Ca^{2+}]_i(t)dt = A\tau = \frac{\Delta[Ca^{2+}]_T}{\gamma}. \tag{3.21}$$

Whilst Ca^{2+} influx adds Ca^{2+} and sequestration mechanisms remove Ca^{2+} from the compartment, Ca^{2+} buffers only act as temporary storage sites for Ca^{2+}. As a result, Ca^{2+} buffering does not affect the time integral of the Ca^{2+} transient.

Estimation of κ_E and γ. The "added-buffer" method was used to estimate κ_E and γ based on the single-compartment model (Neher, 1995). According to Eqs. 3.18 and 3.20, these parameters can be estimated by plotting A^{-1} and τ against κ_D. Experimentally, κ_D can be varied by adding different concentrations of a fluorescent Ca^{2+} indicator or by adding indicators with different Ca^{2+} binding affinities (Eq. 3.13). As κ_D of fluorescent Ca^{2+} indicators, in particular of high-affinity indicators such as OGB-1, is not quite constant in the range of $[Ca^{2+}]_i$ often measured in synaptic boutons and dendrites, κ_D is generally replaced by $\kappa_D^{'}$. The latter is the incremental Ca^{2+} binding ratio of exogenous buffers (Neher and Augustine, 1992):

$$\kappa_D^{'} = \frac{\Delta[DCa]}{\Delta[Ca^{2+}]_i} = \frac{[D]_T K_{d,D}}{([Ca^{2+}]_{rest} + K_{d,D})([Ca^{2+}]_{AP} + K_{d,D})}, \tag{3.22}$$

where $[Ca^{2+}]_{rest}$ and $[Ca^{2+}]_{AP}$ represent $[Ca^{2+}]_i$ before and at the peak of an elevation. A plot of A^{-1} *vs.* $\kappa_D^{'}$ will allow estimation of κ_E and $\Delta[Ca^{2+}]_T$ (Fig. 3.1B). Similarly, by plotting τ against $\kappa_D^{\prime}$, κ_E and γ can be estimated (Fig. 3.1C). Extrapolation of these two plots to $\kappa_D^{'} = 0$ further yields values of A and τ in the absence of exogenous buffers. Here, exogenous buffers included not only fluorescent Ca^{2+} indicators but also gluconate and nucleotides (ATP and GTP) present in the internal solution. The latter compounds gave an additional κ of ~ 5 (See Table 3.3 for total concentrations and K_d values), which was added to all $\kappa_D^{'}$ values.

Assumptions of the single-compartment model. Since the solution of Eq. 3.15 is an exponential function (Eq. 3.16), the single-compartment model predicts $[Ca^{2+}]_i$ after stimulation to decay mono-exponentially. However, in the imaged boutons, the sum of two distinct exponential functions provided a significantly better fit to the

decay time course of AP-evoked Ca^{2+} transients, than a single exponential function (Fig. 3.6A). This suggests that at least one of the assumptions underlying the single-compartment model was violated.

As mentioned previously, the single-compartment model of Ca^{2+} dynamics is based on five assumptions: 1) Ca^{2+} gradients and diffusion can be neglected, 2) Ca^{2+} influx is instantaneous, 3) Ca^{2+} and buffers are always at equilibrium, 4) Ca^{2+} buffers have constant Ca^{2+} binding ratios, and 5) the rate of Ca^{2+} removal is linearly dependent on $\Delta[Ca^{2+}]_i$. Among these assumptions, assumption 2 is the most justifiable: compared to Ca^{2+} sequestration which occurred on the timescale of a few tens to hundreds of milliseconds, the presynaptic Ca^{2+} influx evoked by an AP could be considered instantaneous. This is supported by the finding that, in the calyx of Held and hippocampal MFBs, the Ca^{2+} current evoked by an AP is less than 1 ms long (Borst and Sakmann, 1996, 1998a; Bischofberger *et al.*, 2002).

The assumption of spatial homogeneity (assumption 1) is also justifiable within the imaged boutons due to their small sizes ($r \sim 0.5$ μm). Following an AP-evoked Ca^{2+} influx, Ca^{2+} gradients should dissipate within a characteristic diffusion time (t_d) defined by

$$t_d = \frac{r^2}{6D_{app}}, \tag{3.23}$$

where D_{app} is the apparent diffusion coefficient of Ca^{2+} (Helmchen and Tank, 2015). It takes into account the binding of Ca^{2+} to Ca^{2+} buffers, particularly endogenous fixed buffers. For $r = 0.5$ μm and a D_{app} value of 20 $\mu m^2 s^{-1}$ (Gabso *et al.*, 1997), $t_d \simeq 2$ ms. In the presence of exogenous Ca^{2+} buffers, which are highly mobile compared to endogenous buffers (Table 3.3; Gabso *et al.*, 1997), D_{app} increases and thus t_d would be even smaller. As this diffusion time was at least an order of magnitude smaller than the time course of Ca^{2+} sequestration, spatial gradients of $[Ca^{2+}]_i$ within these boutons were negligible during the decay phase of an AP-evoked Ca^{2+} transient.

However, diffusion of Ca^{2+} out of a bouton into its parent axon could reduce the peak amplitude of the Ca^{2+} transient and speed up its decay time course.

Deviations from a mono-exponential decay time course could also arise from the presence of an endogenous Ca^{2+} buffer with slow binding kinetics (assumption 3 is invalid), saturation of Ca^{2+} buffers (assumption 4 is invalid), a non-linear Ca^{2+} sequestration mechanism (assumption 5 is invalid), and/or CICR (Neher, 1995; Tank *et al.*, 1995; Helmchen and Tank, 2015). Even though these conditions could significantly alter the decay time course of an AP-evoked Ca^{2+} transient, its peak amplitude, which was reached within 3 ms of AP initiation, would be minimally affected, unless Ca^{2+} buffers were saturated. Therefore, a plot of A^{-1} *vs.* $\kappa_D^{'}$ would provide a more accurate and reliable estimate of κ_E than would a plot of τ *vs.* $\kappa_D^{'}$ (Neher and Augustine, 1992; Lee *et al.*, 2000b). Saturation of exogenously introduced Ca^{2+} indicators were taken into account in the former plot by using $\kappa_D^{'}$ instead of κ_D. Strictly speaking, κ_E estimated with this method represents the fraction of Ca^{2+} ions that have been "buffered away" at the peak of an AP-evoked Ca^{2+} transient. Therefore, it reflects the capacity of only endogenous fast buffers.

It should be noted here that all of the exogenously introduced buffers had fast Ca^{2+} binding and unbinding kinetics, compared to the rate of Ca^{2+} sequestration. The rate at which each buffer bound Ca^{2+}, determined as the product of k_{on} and [D], was $\geq 10^4$ s^{-1} (Table 3.3). Similarly, the slowest unbinding rate, which was of the high-affinity indicator OGB-1 ($k_{off} \simeq 130$ s^{-1}; Table 3.3), was still around an order of magnitude faster than the rate of sequestration ($\tau > 50$ ms corresponding to a rate of 20 s^{-1} for Ca^{2+} transients measured with OGB-1). Therefore, Ca^{2+} was largely at equilibrium with exogenous buffers.

3.2.7.2 Linear summation of $[Ca^{2+}]_i$ during trains of APs

During a train of APs with a constant time interval (Δt), Ca^{2+} transients evoked by individual APs will summate if Δt is shorter than the time it takes each transient

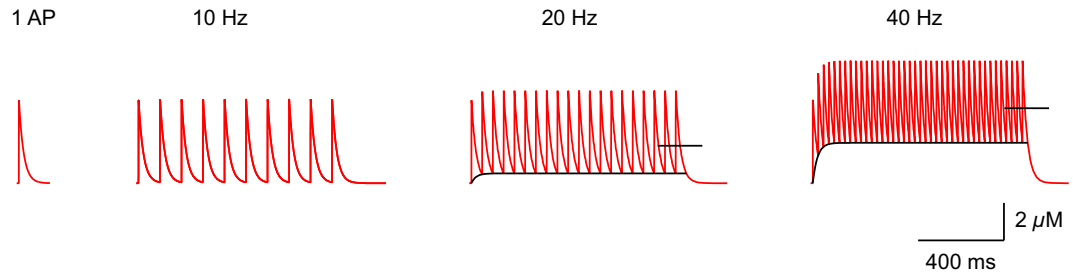

Figure 3.2: Simulated summation of $[Ca^{2+}]_i$ during 1 s long trains of APs. The lower envelope of the Ca^{2+} build-up at $20-40$ Hz has been fitted with an exponential function (black curves). Black lines indicate the average change in $[Ca^{2+}]_i$ during steady state ($\Delta[Ca^{2+}]_{ss}$).

to decay ($\Delta t \leq 2\tau$). Linear summation of $[Ca^{2+}]_i$ occurs when: 1) Ca^{2+} influx and $\Delta[Ca^{2+}]_T$ *per* AP are constant, 2) the rate of Ca^{2+} sequestration remains linearly dependent on $\Delta[Ca^{2+}]_i$, and 3) Ca^{2+} buffers are not saturated (Helmchen and Tank, 2015). Under these conditions, each Ca^{2+} transient raises $[Ca^{2+}]_i$ by the same amount A and has the same decay time constant τ (Fig. 3.2). The $[Ca^{2+}]_i$ above resting level immediately before the $(n+1)^{\text{th}}$ AP (B_n) is given by a geometric series (Regehr *et al.*, 1994); that is,

$$B_n = A \sum_{i=1}^{n} e^{-i\Delta t/\tau} \tag{3.24}$$

$$= A \times \frac{1 - e^{-n\Delta t/\tau}}{e^{\Delta t/\tau} - 1}. \tag{3.25}$$

This equation shows that, during a high-frequency train of APs and under the assumption of linear summation, the lower envelope of $[Ca^{2+}]_i$ builds up exponentially with a time constant of $\tau_{\text{rise}} = \tau$, independent of the AP frequency (black curves in Fig. 3.2). As $n \to \infty$, B_n approaches a maximum value of

$$B_{\max} = A \times \frac{1}{e^{\Delta t/\tau} - 1}. \tag{3.26}$$

This steady state level is reached when Ca^{2+} influx and sequestration are in equilibrium: the drop in $[Ca^{2+}]_i$ during Δt is counterbalanced by an increase by

A produced by the next AP (Helmchen *et al.*, 1996). During this state, $[Ca^{2+}]_i$ above the resting level fluctuates between a lower level given by B_{max} and an upper level given by

$$A_{max} = B_{max} + A \tag{3.27}$$

$$= A \times \frac{1}{1 - e^{-\Delta t/\tau}}. \tag{3.28}$$

The average change in $[Ca^{2+}]_i$ during this steady state ($\Delta[Ca^{2+}]_{ss}$; solid lines in Fig. 3.2) is in turn

$$\Delta[Ca^{2+}]_{ss} = \frac{1}{\Delta t} \int_0^{\Delta t} A_{max} e^{-t/\tau} dt \tag{3.29}$$

$$= \frac{A\tau}{\Delta t} \tag{3.30}$$

$$= A\tau v_{AP}, \tag{3.31}$$

where $v_{AP} = 1/\Delta t$ is the AP frequency (Tank *et al.*, 1995; Helmchen *et al.*, 1996). According to Eq. 3.31, $\Delta[Ca^{2+}]_{ss}$ is a linear function of v_{AP}, with the proportionality constant being the time integral $A\tau$ of a single AP-evoked Ca^{2+} transient. As this integral is determined by $\Delta[Ca^{2+}]_T$ *per* AP and the rate constant of Ca^{2+} sequestration (Eq. 3.21), $\Delta[Ca^{2+}]_{ss}$ is independent of Ca^{2+} buffering (Helmchen and Tank, 2015). More specifically, whilst Ca^{2+} buffers shape the dynamics of each Ca^{2+} transient, they do not affect the steady state level of $[Ca^{2+}]_i$ during high-frequency AP trains. An increase in the total concentration of Ca^{2+} buffers or a decrease in their K_d will reduce the amplitude and prolong the decay time course of individual Ca^{2+} transients, without changing $\Delta[Ca^{2+}]_{ss}$. Similarly, $\Delta[Ca^{2+}]_{ss}$ is not affected by saturation of Ca^{2+} buffers or by the presence of a buffer with slow Ca^{2+} binding kinetics (Tank *et al.*, 1995; Lee *et al.*, 2000b).

To assess whether $[Ca^{2+}]_i$ summed linearly during 2 s long trains of APs, the average changes in $[Ca^{2+}]_i$ during the last $200 - 500$ ms of stimulation were compared to

the predicted $\Delta[Ca^{2+}]_{ss}$ (Eq. 3.31). Because in most experiments, $[Ca^{2+}]_i$ had yet to return to $[Ca^{2+}]_{rest}$ by the end of the imaging periods, the time integral of a single AP-evoked Ca^{2+} transient was determined from values obtained by fitting its decay time course; that is, the time integral was calculated as $A\tau$ if its decay was exponential, and $A_1\tau_1 + A_2\tau_2$ if it decayed bi-exponentially.

3.2.7.3 Diffusion of Ca^{2+} into the axon

The single-compartment model described by Neher and Augustine (1992) was extended to investigate how diffusion of Ca^{2+} out of a bouton into the connecting axon shaped the presynaptic Ca^{2+} dynamics. As a starting point, $[Ca^{2+}]_i$ in a cylindrical structure with a constant radius r was examined. Only longitudinal diffusion along the x-axis was considered; given the small diameter of axon collaterals ($< 0.5\ \mu$m), Ca^{2+} and buffers should be at spatial equilibrium in the radial direction. The temporal dynamics of $[Ca^{2+}]_i$ at position x ($Ca(x,t)$) in this cylinder, after a brief Ca^{2+} current $I(x,t)$, are described by the following differential equation:

$$\frac{\partial Ca}{\partial t} = k_{off}[ECa] - k_{on}[E][Ca^{2+}]_i + k_{off}[DCa] - k_{on}[D][Ca^{2+}]_i + \frac{2}{r}K_\infty I(x,t) - S\left([Ca^{2+}]_i\right) + D_{Ca}\frac{\partial^2 Ca}{\partial x^2}, \quad (3.32)$$

where $2/r$ is the surface to volume ratio of the cylinder, K_∞ represents the proportionality constant between $I(x,t)$ and the resultant increase in $[Ca^{2+}]_T$, and D_{Ca} is the diffusion coefficient of free Ca^{2+} ions (Zador and Koch, 1994). Eq. 3.32 is an extension of Eq. 3.6, with the last term on the right-hand side describing how diffusion causes $[Ca^{2+}]_i$ to change over time (Fick's second law). Again, the first four terms on the right-hand side of Eq. 3.32 can be replaced by the rate of change of [ECa] and [DCa] over time as follows:

$$\frac{\partial \mathrm{ECa}}{\partial t} = -k_{\mathrm{off}}[\mathrm{ECa}] + k_{\mathrm{on}}[\mathrm{E}][\mathrm{Ca}^{2+}]_{\mathrm{i}}, \tag{3.33}$$

and

$$\frac{\partial \mathrm{DCa}}{\partial t} = -k_{\mathrm{off}}[\mathrm{DCa}] + k_{\mathrm{on}}[\mathrm{D}][\mathrm{Ca}^{2+}]_{\mathrm{i}} + D_{\mathrm{DCa}}\frac{\partial^2 \mathrm{DCa}}{\partial x^2}, \tag{3.34}$$

where D_{DCa} is the diffusion coefficient of Ca^{2+} ions bound to D. Here, endogenous buffers are assumed to be fixed whilst exogenously introduced buffers are mobile (Zhou and Neher, 1993; Gabso *et al.*, 1997). Thus, diffusion does not affect the rate of change of [ECa] over time, whilst Ca^{2+} ions bound to D can diffuse out of the bouton, most likely with a diffusion coefficient equal to that of D itself (that is, $D_{\mathrm{DCa}} = D_{\mathrm{D}}$). Substituting Eqs. 3.33 and 3.34 into Eq. 3.32 yields

$$\frac{\partial \mathrm{Ca}}{\partial t} + \frac{\partial \mathrm{ECa}}{\partial t} + \frac{\partial \mathrm{DCa}}{\partial t} = \frac{2}{r}K_{\infty}I(x,t) - S\left([\mathrm{Ca}^{2+}]_{\mathrm{i}}\right) + D_{\mathrm{Ca}}\frac{\partial^2 \mathrm{Ca}}{\partial x^2} + D_{\mathrm{D}}\frac{\partial^2 \mathrm{DCa}}{\partial x^2}. \tag{3.35}$$

Compared to Eq. 3.9, this equation states that $\Delta[\mathrm{Ca}^{2+}]_{\mathrm{T}}$ is determined not only by Ca^{2+} influx and sequestration, but also by diffusion of Ca^{2+} (free or bound to mobile buffers). Under the assumptions of chemical equilibrium, non-saturable buffers, and a linear rate of Ca^{2+} sequestration (assumptions $3-5$ of the single-compartment model), Eq. 3.35 can be simplified as

$$\frac{\partial \mathrm{Ca}}{\partial t}(1 + \kappa_{\mathrm{E}} + \kappa_{\mathrm{D}}) = \frac{2}{r}\left(K_{\infty}I(x,t) - \gamma \times [\mathrm{Ca}^{2+}]_{\mathrm{i}}\right) + (D_{\mathrm{Ca}} + D_{\mathrm{D}}\kappa_{\mathrm{D}})\frac{\partial^2 \mathrm{Ca}}{\partial x^2}. \tag{3.36}$$

Dividing both sides of this equation by $(1 + \kappa_{\mathrm{E}} + \kappa_{\mathrm{D}})$ yields

$$\frac{\partial \mathrm{Ca}}{\partial t} = \frac{2}{r} \times \left(\frac{K_\infty I(x,t) - \gamma \times [\mathrm{Ca}^{2+}]_\mathrm{i}}{1 + \kappa_\mathrm{E} + \kappa_\mathrm{D}} \right) + D_\mathrm{app} \frac{\partial^2 \mathrm{Ca}}{\partial x^2}, \tag{3.37}$$

where the apparent diffusion coefficient $D_\mathrm{app} = (D_\mathrm{Ca} + D_\mathrm{D}\kappa_\mathrm{D})/(1 + \kappa_\mathrm{E} + \kappa_\mathrm{D})$ (Gabso *et al.*, 1997). According to Gabso *et al.* (1997), after a brief Ca^{2+} current at $x = 0$ and $t = 0$, this equation has a solution of the following form:

$$\Delta[\mathrm{Ca}^{2+}]_\mathrm{i}(x,t) = [\mathrm{Ca}^{2+}]_\mathrm{i}(x,t) - [\mathrm{Ca}^{2+}]_\mathrm{rest} = y(x,t)e^{-t/\tau}, \tag{3.38}$$

with

$$y(x,t) = \frac{A_0}{\sqrt{4\pi D_\mathrm{app} t}} \exp\left(\frac{-x^2}{4D_\mathrm{app} t} \right) \tag{3.39}$$

and

$$\tau = \frac{r}{2\gamma}(1 + \kappa_\mathrm{E} + \kappa_\mathrm{D}). \tag{3.40}$$

A_0 in Eq. 3.39 depends on the Ca^{2+} current. To find its value, I integrate $\Delta[\mathrm{Ca}^{2+}]_\mathrm{i}(x,t)$ from $x = -\infty$ to ∞, and evaluate this integral at time t shortly after $t_\mathrm{AP} = 0$. That is,

$$\int_{-\infty}^{\infty} \Delta[\mathrm{Ca}^{2+}]_\mathrm{i}(x,t)dx = \int_{-\infty}^{\infty} \left[\frac{A_0}{\sqrt{4\pi D_\mathrm{app} t}} \exp\left(\frac{-x^2}{4D_\mathrm{app} t} \right) e^{-t/\tau} \right] dx \tag{3.41}$$

$$= \frac{A_0}{\sqrt{4\pi D_\mathrm{app} t}} e^{-t/\tau} \int_{-\infty}^{\infty} \exp\left(\frac{-x^2}{4D_\mathrm{app} t} \right) dx. \tag{3.42}$$

Let $u^2 = x^2/(4D_\mathrm{app} t)$. Then $dx = \sqrt{4D_\mathrm{app} t} \times du$. Accordingly,

$$\int_{-\infty}^{\infty} \Delta[\mathrm{Ca}^{2+}]_{\mathrm{i}}(x,t)dx = \frac{A_0}{\sqrt{\pi}} e^{-t/\tau} \int_{-\infty}^{\infty} \exp\left(-u^2\right) du \tag{3.43}$$

$$= A_0 e^{-t/\tau}. \tag{3.44}$$

At time $t = t_{\mathrm{AP}} + \delta t = \delta t$ with δt being infinitesimally small,

$$\int_{-\infty}^{\infty} \Delta[\mathrm{Ca}^{2+}]_{\mathrm{i}}(x,t)dx|_{t=\delta t} = A_0. \tag{3.45}$$

Assuming that Ca^{2+} has yet to be sequestered at this time,

$$\int_{-\infty}^{\infty} \Delta[\mathrm{Ca}^{2+}]_{\mathrm{i}}(x,t)dx|_{t=\delta t} = \frac{N_{\mathrm{Ca}}}{\pi r^2(1+\kappa_{\mathrm{E}}+\kappa_{\mathrm{D}})}, \tag{3.46}$$

where N_{Ca} is the total number of moles of Ca^{2+} ions that enter the bouton. Therefore,

$$A_0 = \frac{N_{\mathrm{Ca}}}{\pi r^2(1+\kappa_{\mathrm{E}}+\kappa_{\mathrm{D}})}. \tag{3.47}$$

This means that, in a cylindrical structure, $\Delta[\mathrm{Ca}^{2+}]_{\mathrm{i}}$ at any position x is

$$\Delta[\mathrm{Ca}^{2+}]_{\mathrm{i}}(x,t) = \frac{N_{\mathrm{Ca}}}{\pi r^2(1+\kappa_{\mathrm{E}}+\kappa_{\mathrm{D}})\sqrt{4\pi D_{\mathrm{app}} t}} \exp\left(\frac{-x^2}{4D_{\mathrm{app}} t}\right) e^{-t/\tau}. \tag{3.48}$$

However, in this study, only $\Delta[\mathrm{Ca}^{2+}]_{\mathrm{i}}$ within a bouton was of interest. In response to an AP, Ca^{2+} predominantly entered through clusters of VGCCs in the presynaptic membrane (Holderith *et al.*, 2012; Nakamura *et al.*, 2015). As explained above, the spatial gradient of Ca^{2+} within the imaged boutons was negligible during the decay phase of the Ca^{2+} transient. Therefore, diffusion of Ca^{2+} into the axon could be simplified as diffusion away from an instantaneous point source. In other words, $\Delta[\mathrm{Ca}^{2+}]_{\mathrm{i}}$ within a bouton could be approximated by

$$\Delta[\mathrm{Ca}^{2+}]_\mathrm{i}(0,t) = \frac{N_\mathrm{Ca}}{\pi r^2(1+\kappa_\mathrm{E}+\kappa_\mathrm{D})\sqrt{4\pi D_\mathrm{app} t}} e^{-t/\tau}.$$

The extent to which diffusion into the axon shaped the decay kinetics of $\Delta[\mathrm{Ca}^{2+}]_\mathrm{i}$ within a bouton could be understood by differentiating this equation, yielding

$$\begin{aligned}
\frac{d[\mathrm{Ca}^{2+}]_\mathrm{i}}{dt} &= -\frac{N_\mathrm{Ca}}{\pi r^2(1+\kappa_\mathrm{E}+\kappa_\mathrm{D})\sqrt{4\pi D_\mathrm{app}}}\left[\frac{1}{\tau\sqrt{t}}e^{-t/\tau} + \frac{1}{2\sqrt{t^3}}e^{-t/\tau}\right] \\
&= -\frac{N_\mathrm{Ca}}{\pi r^2(1+\kappa_\mathrm{E}+\kappa_\mathrm{D})\sqrt{4\pi D_\mathrm{app} t}} e^{-t/\tau}\left(\frac{1}{\tau}+\frac{1}{2t}\right) \\
&= -\left(\frac{1}{\tau}+\frac{1}{2t}\right) \times \Delta[\mathrm{Ca}^{2+}]_\mathrm{i} \\
&= -\frac{1}{\tau} \times \Delta[\mathrm{Ca}^{2+}]_\mathrm{i} - \frac{1}{2t} \times \Delta[\mathrm{Ca}^{2+}]_\mathrm{i}. \qquad (3.49)
\end{aligned}$$

The first term on the right-hand side of Eq. 3.49 describes the rate of change of $\Delta[\mathrm{Ca}^{2+}]_\mathrm{i}$ in a truly single compartment where diffusion is negligible (Eq. 3.19). The second term describes the rate of change due to diffusion in the absence of Ca^{2+} transporters (that is, $\gamma = 0$). Unlike the former, the latter is not a linear function of $\Delta[\mathrm{Ca}^{2+}]_\mathrm{i}$. In addition, although both terms decrease in magnitude during the decay phase (as $\Delta[\mathrm{Ca}^{2+}]_\mathrm{i}$ decreases), the second term decreases much more rapidly (due to the factor $1/t$). This means that the relative contribution of diffusion to the rate of decay decreases over time. It also decreases if τ decreases and the first term in Eq. 3.49 becomes more dominant. Accordingly, if diffusion of Ca^{2+} into the axon occurs soon after an influx, and if τ is large, diffusion will play a major role in Ca^{2+} removal, causing the rate of decay to deviate significantly from a linear relationship with $\Delta[\mathrm{Ca}^{2+}]_\mathrm{i}$. A large τ in turn occurs when $\kappa_\mathrm{E}+\kappa_\mathrm{D}$ is large or γ is small (Eq. 3.40). However, as t increases, the deviation from linearity will become smaller. Eventually, the rate of decay will be linearly dependent on $\Delta[\mathrm{Ca}^{2+}]_\mathrm{i}$, reflecting the activity of Ca^{2+} transporters.

Intuitively, the relative contribution of diffusion to the decay kinetics of $\Delta[\mathrm{Ca}^{2+}]_\mathrm{i}$ in a *bouton en passant* is smaller than that indicated by Eq. 3.49. The reduced diameter

of the axon, compared to that of the bouton, restricts the escape of Ca^{2+}. This causes the rate of change by diffusion to decrease with thinner axons (Fig. 3.11D). Based on 3D simulations, it was found that, if the diameters of the bouton and the axon were 1.0 and 0.2 μm, respectively, the maximum rate of change by diffusion was only 3% of that in a cylindrical structure with a constant diameter (all values corrected for the peak amplitude of $\Delta[Ca^{2+}]_i$; data not shown). Despite this, diffusion into the axon still played a major role in shaping the presynaptic Ca^{2+} dynamics in the presence of exogenous mobile buffers (Figs. 3.11E-F).

3.2.8 Modelling

All simulations were performed using CalC (Calcium Calculator) computer software, version 6.8.6 (Matveev *et al.*, 2002). This software uses a finite-difference scheme to solve partial differential equations governing the spatiotemporal dynamics of $[Ca^{2+}]_i$. Data from the simulations were further analysed in Igor Pro 7.01. Both CalC and Igor Pro were executed on a Mac mini computer, running Mac OS X 10.10.

To simulate AP-evoked Ca^{2+} dynamics in synaptic boutons of layer 5 pyramidal cells, a 3D model of a bouton with an axon attached to it was created (Fig. 3.11A). Key parameters of the model were constrained based on measurements obtained in this thesis as well as previous studies (Table 3.3). The modelled bouton had a spherical morphology, centred at (0,0,0) and 0.5 μm in radius. The axon attached to it was cylindrical, with a diameter of $0.1 - 0.4$ μm in the y- and z-axes, and a length of 20 μm on each side of the bouton along the x-axis. The number of grids was 190, 50, and 50 in the x-, y-, and z-axes, respectively. Within the bouton, each grid corresponded to a cube of $\sim 20 \times 20 \times 20$ nm. To reduce simulation time, the size of each successive grid outside the bouton was stretched along the x-axis by a factor of 1.06. The CalC accuracy parameter was 1×10^{-5}; smaller values did not change simulation results.

Table 3.3: Model parameters for simulations of presynaptic Ca^{2+} dynamics.

Parameters		Value	Unit	Reference/Note
Geometry	Grid size at bouton	~ 20	nm	Smaller grids did not change results
	Grid size at ends of axon	≤ 1.1	μm	Successive grids were stretched by 1.06
	Bouton radius	0.5	μm	Romand *et al.* (2011)
	Axon diameter	$0.1 - 0.4$	μm	Rollenhagen and Lübke (personal comm.)
	Axon length	40	μm	Longer axons did not change results
Free Ca^{2+}	D_{Ca}	220	$\mu m^2 s^{-1}$	Allbritton *et al.* (1992)
	$[Ca^{2+}]_{rest}$	0.05	μM	measured (Section 3.3.2)
Ca^{2+} current	Radius	50	nm	Nakamura *et al.* (2015)
	Number of Ca^{2+} ions	15,762	ions	calculated with $\Delta[Ca^{2+}]_T = 50$ μM (measured)
	Amplitude	-18.6	pA	
	Half-width	244	μs	consistent with Borst and Sakmann (1998a)
Ca^{2+} extrusion	$\gamma_{extrusion}$	0.06	$\mu m \cdot ms^{-1}$	estimated; at bouton only
Ca^{2+} uptake	γ_{uptake}	0.07	ms^{-1}	estimated; homogeneously distributed
Hypothetical endogenous buffer	C_M	1000	μM	$= K_d \times \kappa_E$ with $\kappa_E = 10$ (measured)
	K_d	100	μM	Xu *et al.* (1997)
	k_{on}	5×10^8	$M^{-1}s^{-1}$	Delvendahl *et al.* (2015)
	k_{off}	2.5×10^4	s^{-1}	$= K_d \times k_{on}$
	D_E	0	$\mu m^2 s^{-1}$	buffer is fixed

Gluconate	C_M	115	mM	used in experiments
	K_d	57	mM	Woehler *et al.* (2014)
	k_{on}	1×10^8	$M^{-1}s^{-1}$	Woehler *et al.* (2014)
	k_{off}	5.7×10^6	s^{-1}	$= K_d \times k_{on}$
	$D_{gluconate}$	220	$\mu m^2 s^{-1}$	Woehler *et al.* (2014)
ATP	C_M	580	μM	calculated with $[Mg^{2+}]_T = [ATP]_T = 4$ mM, and $K_{d,Mg}$ = 100 μM (Baylor and Hollingworth, 1998)
	K_d	200	μM	Baylor and Hollingworth (1998)
	k_{on}	1×10^9	$M^{-1}s^{-1}$	Hammes and Levison (1964)
	k_{off}	2×10^5	s^{-1}	$= K_d \times k_{on}$
	D_{ATP}	220	$\mu m^2 s^{-1}$	Naraghi and Neher (1997)
OGB-1	C_M	$36 - 144$	μM	used in experiments
	K_d	0.3	μM	measured
	k_{on}	4.5×10^8	$M^{-1}s^{-1}$	$\approx k_{on}$ of BAPTA (Naraghi, 1997)
	k_{off}	1.35×10^2	s^{-1}	$= K_d \times k_{on}$
	D_{OGB-1}	100	$\mu m^2 s^{-1}$	$\approx D_{Fura-2}$ (Gabso *et al.*, 1997)
OGB-6F	C_M	$45 - 450$	μM	used in experiments
	K_d	8	μM	measured
	k_{on}	4.5×10^8	$M^{-1}s^{-1}$	$\approx k_{on}$ of BAPTA
	k_{off}	3.6×10^3	s^{-1}	$= K_d \times k_{on}$
	D_{OGB-6F}	100	$\mu m^2 s^{-1}$	$\approx D_{Fura-2}$

3.2.8.1 Presynaptic Ca^{2+} current

The AP-evoked Ca^{2+} current was modelled as a skewed gamma distribution with the following probability density function:

$$f(t) = N_{Ca} \times 2e \times \frac{\beta^{\alpha} \times (t - t_0)^{\alpha-1} \times \exp(-\beta \times (t - t_0))}{\Gamma(\alpha)},$$

where N_{Ca} represents the total number of Ca^{2+} ions that entered the bouton, e is the elementary charge, α is the shape parameter of the distribution, β is the inverse scale factor, and t_0 is the time of current onset. For an α value of 2, $\Gamma(\alpha) = \Gamma(2) = 1$, and thus

$$f(t) = N_{Ca} \times 2e \times \beta^2 \times (t - t_0) \times \exp(-\beta \times (t - t_0)).$$

For the half-width of this current to be in the range of that of the presynaptic Ca^{2+} current measured at the calyx of Held (Borst and Sakmann, 1998a), β was chosen to be 0.1 s^{-1}, corresponding to a half-width of 244 μs. With $N_{Ca} = 15,762$, which is the number of Ca^{2+} ions that would produce a $\Delta[Ca^{2+}]_T$ of 50 μM in a sphere of $r = 0.5$ μm, the modelled Ca^{2+} current had a peak amplitude of -18.6 pA (Fig. 3.11B). The source of the Ca^{2+} current had a spatial radius of 50 nm, which was about half of the width of an active zone (Nakamura *et al.*, 2015). It was positioned on the surface of the bouton at $(0, -0.5, 0)$ μm.

3.2.8.2 Ca^{2+} sequestration

Following an intracellular rise, Ca^{2+} was extruded by a pump or sequestered by a homogeneously distributed uptake mechanism. The value of γ estimated based on the single-compartment model represents the action of all Ca^{2+} sequestration mechanisms on the volume-averaged $\Delta[Ca^{2+}]_i$ within the imaged boutons. This

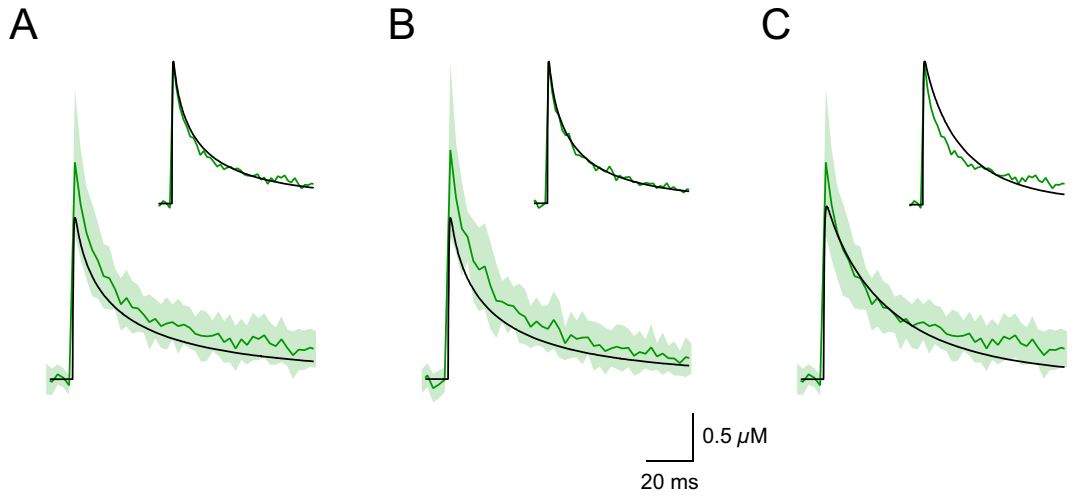

Figure 3.3: Estimation of the rate constants of Ca^{2+} sequestration mechanisms. (A) A transient, simulated with an axon diameter of 0.4 μm, $\gamma_{extrusion} = 0.06$ μm·ms^{-1}, and γ_{uptake} = 0 (black), was superimposed with the average Ca^{2+} transient measured in the presence of CPA (green; n = 15). (Inset) The simulated transient was peak-scaled to match the measured transient. (B) Similar to A but with $\gamma_{uptake} = 0.07$ ms^{-1} and the average Ca^{2+} transient measured before addition of CPA. (C) Similar to A but with an axon diameter of 0.2 μm and $\gamma_{extrusion} = 0.08$ μm·ms^{-1}. Shaded areas represent mean $\pm$ 1 SD.

estimation does not take into account the fact that the activity of a Ca^{2+} transporter depends on the local $[Ca^{2+}]_i$. It also does not differentiate between the action of Ca^{2+} transporters and the escape of Ca^{2+} through diffusion into the axon. Therefore, the rate constants corresponding to the action of the membrane pump and intracellular uptake ($\gamma_{extrusion}$ and γ_{uptake}, respectively) were approximated based on the effect of CPA on the decay time course of single AP-evoked Ca^{2+} transients (measured with 100 μM OGB-6F in the patch pipette).

$\gamma_{extrusion}$ was estimated first, by increasing its value from 0, in steps of 0.01 μm·ms^{-1}. The simulated transient was compared to the average Ca^{2+} transient measured in the presence of CPA (black *vs.* green, respectively; Fig. 3.3A). After scaling its peak amplitude to match that of the measured transient (inset), the residual sum of squares (*RSS*) was calculated. The minimum value of *RSS* was obtained when $\gamma_{extrusion} = 0.06$ μm·ms^{-1}. γ_{uptake} was then estimated, by increasing its value in steps of 0.01 ms^{-1}. The simulated transient was compared to the average Ca^{2+} transient

measured before addition of CPA (Fig. 3.3B). Again, after scaling its peak to match that of the measured transient (inset), *RSS* was calculated. The smallest *RSS* was obtained when $\gamma_{\text{extrusion}} = 0.06$ μm·ms^{-1} and $\gamma_{\text{uptake}} = 0.07$ ms^{-1}. All of these simulations were done in the presence of 90 μM OGB-6F (see Section 3.3.1) and with an axon diameter of 0.4 μm. The measured time courses were better reproduced with this axon diameter than with a thinner axon (Fig. 3.3C).

3.2.8.3 Boundary conditions

The Ca^{2+} pump was distributed on the surface of the bouton. The boundary along the axon was reflective (*i.e.* zero flux), and those at the ends were clamped to $[Ca^{2+}]_{\text{rest}}$. When the Ca^{2+} pump was additionally distributed along the axon (on all sides, except at the ends), the simulated Ca^{2+} transient still exhibited an initial fast decay, although the relative amplitude of this component ($\text{amplitude}_{\text{fast}}$) was reduced (from 47 to 32% in the presence of 90 μM OGB-6F and with an axon diameter of 0.4 μm). As there is evidence for clustering of the plasmalemmal Ca^{2+}-ATPase at the active zones (Blaustein *et al.*, 2002), the rate of Ca^{2+} extrusion along the axon was unlikely to be as fast as that at the bouton.

3.2.8.4 Calculation of volume-averaged $\Delta[Ca^{2+}]_i$

In simulations with exogenous buffers present, $\Delta[Ca^{2+}]_i$ in the bouton was calculated from the Ca^{2+}-free concentration of the fluorescent indicator ([D]) as follows:

$$\Delta[Ca^{2+}]_i = \frac{K_d \times \left(1 - \frac{[D]}{[D]_T}\right)}{\frac{[D]}{[D]_T}} - [Ca^{2+}]_{\text{rest}}.$$

The volume-averaged [D] was calculated by averaging 61 uniformly distributed points along the $i(1,0,0)$, $i(0,1,0)$, or $i(0,0,1)$ axis, with $i \in \mathbb{R}$, and $|x|$, $|y|$, and $|z|$

≤ 0.5 μm. In a model with only the bouton and no connecting axon, this calculation gave a value of [D] equal to that obtained using the CalC default parameter for the volume-averaged [D].

In simulations with no exogenous buffers, the volume-averaged $[Ca^{2+}]_i$ in the bouton was calculated by averaging $[Ca^{2+}]_i$ at 475 uniformly distributed points on the planes that contain two of the aforementioned axes, with $|x|$, $|y|$, and $|z| \leq 0.35$ μm. In a model with only the bouton and no connecting axon, this calculation yielded a value of $[Ca^{2+}]_i$ equal to that obtained using the CalC default parameter for the volume-averaged $[Ca^{2+}]_i$, but only at time $t \geq 2$ ms after the AP onset. Since the spatial gradient of Ca^{2+} took longer to dissipate in the presence of only fixed endogenous buffers, for smaller time points, this calculation yielded a value of $[Ca^{2+}]_i$ slightly smaller than the default parameter.

3.3 Results

The spatially averaged $[Ca^{2+}]_i$ in neocortical synaptic boutons was measured with confocal microscopy. Whole-cell patch-clamp recordings were obtained from visually identified pyramidal neurons in layer 5 (mostly 5A) of the rat somatosensory cortex. These cells were filled through the patch pipette with Alexa Fluor® 568 (50 μM) and a fluorescent Ca^{2+} indicator (OGB-1, OGB-6F, OGB-5N, Fluo-4FF, or Cal-520). Approximately 20 min after break-in, the fluorescence of Alexa Fluor® 568 was acquired to reveal the morphology of the patched cell (Figs. 3.4A-B). The cell was confirmed to be a pyramidal neuron if it had a pyramidal-shaped soma, a pronounced apical dendrite, and spines lining all dendrites. The majority of the imaged cells had a thin apical dendrite and a main axon that was intact within 200 μm from the soma. Within this distance, the main axon gave rise to several axon collaterals, with some extending horizontally and remaining in layer 5, whilst others extending in an oblique fashion into the supragranular layers (layers $1-3$) or down to layer 6. Occasionally, a collateral that ran almost parallel to the apical dendrite

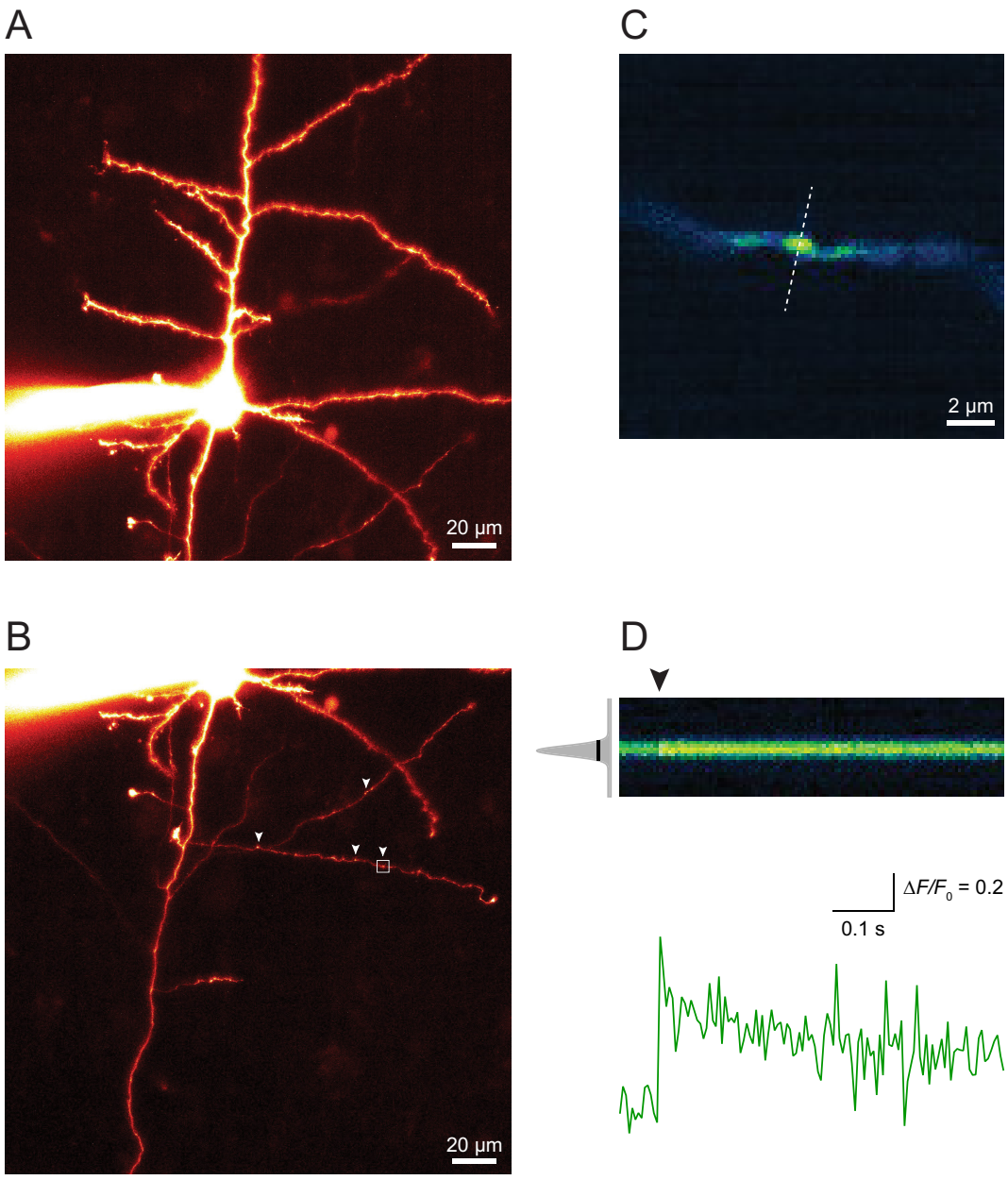

Figure 3.4: Ca^{2+} imaging of synaptic boutons. (A) A layer 5 pyramidal cell visualised using fluorescence of Alexa Fluor® 568. (B) Synaptic boutons (arrowheads) were identified along its axon collaterals. (C) A magnified view of one of the boutons (inside square in B) showing fluorescence of OGB-1 at rest. (D) Top: Acquisition of line scans across this bouton (dashed line in C) over time revealed an increase in OGB-1 fluorescence in response to an AP evoked at the soma. Arrowhead indicates time of AP onset. Each line scan was fitted with a Gaussian function (*e.g.* left), and the spatially averaged fluorescence of the bouton (F) was calculated as the average fluorescence of all pixels $\pm$ 2 SD around the peak of the Gaussian (black bar inside fit), minus the background fluorescence (y-offset of fit). Bottom: The relative change in F over time.

was also seen. Cells that fired in bursts were not imaged to ensure that single APs could be reliably evoked.

Synaptic boutons (~ 1 μm in diameter) were identified along 1st to 3rd order axon collaterals ($100 - 300$ μm from the soma; Fig. 3.4C). Most of them were confined to layer 5 and vertically below the respective soma (*i.e.* further away from the pia). As axonal varicosities have been shown to represent synapses (Gray, 1959; Markram *et al.*, 1997; Lubke *et al.*, 2000), the imaged boutons most likely contained synaptic vesicles and formed functional release sites onto other layer 5 cells. Consistent with this, their $[Ca^{2+}]_i$ increased rapidly and strongly in response to a somatically evoked AP (Fig. 3.4D; typically, AP threshold = -44 ± 2 mV, amplitude = 77 ± 2 mV, and half-width = 0.68 ± 0.03 ms; n = 24 cells). Only boutons that displayed a rapid and clear fluorescence increase (within 5 ms of AP onset; > 95%) were used for further analysis.

3.3.1 Equilibration time course of fluorophores

The extent to which a drug affected the dynamics of presynaptic Ca^{2+} transients could only be determined accurately if the concentration of the Ca^{2+} indicator in the imaged bouton changed minimally during the recording period (*i.e.* 10 min of solution exchange). Therefore, it was important to measure the amount of time it took for the indicator concentration in the bouton to reach a steady state. To achieve this, the fluorescence intensity of both Alexa Fluor® 568 and OGB-1 (80 μM) in a chosen bouton was measured over time, starting from 30 to 150 min after break-in and at an increasing interval between 10 to 30 min. At the same time, the relative change in OGB-1 fluorescence ($\Delta F/F_0$) in response to an AP evoked at the soma was also measured (Fig. 3.4D). To reduce laser exposure, the fluorescence intensity of both dyes was acquired using line scans drawn across the bouton and perpendicular to its parent axon collateral (Fig. 3.4C). Additionally, in these experiments, each measurement at each time point was only performed once (*i.e.* no repeat).

Figs. 3.5A-B show the averaged, normalised fluorescence of Alexa Fluor® 568 and OGB-1 over time in 15 boutons of layer 5 pyramidal neurons (210 $\pm$ 10 μm from the soma). To generate these plots, the measured fluorescence of each dye was normalised by dividing it by the maximum fluorescence measurement obtained from the same bouton; the normalised values were subsequently averaged together. Note that the maximum values in these plots were less than 1 as the maximum fluorescence measurement of each bouton occurred at a slightly different time ($\geq$ 60 min after break-in). The fluorescence of both dyes increased rapidly after break-in and reached a plateau after $\sim$ 90 min. An exponential fit to the averaged plots gave an equilibration time constant of 33 $\pm$ 2 and 41 $\pm$ 4 min for Alexa Fluor® 568 and OGB-1, respectively ($p_{\mathrm{Pr}} \leq 0.01$ with log-level regression analysis). These values were not different from the mean values calculated from the equilibration time constants of individual boutons (38 $\pm$ 5 and 43 $\pm$ 5 min; $p_{\mathrm{t}} \geq 0.3$; ranging from 7 to 78 min, and 14 to 82 min, respectively). There was also no difference in the equilibration time constant between Alexa Fluor® 568 and OGB-1 ($p_{\mathrm{pt}} = 0.3$). Additionally, there was no correlation between the equilibration time constants and the distance of the imaged boutons from the somata, likely due to variations in the access resistance, axonal branching, and the thickness of the axon collaterals ($p_{\mathrm{Pr}} \geq 0.7$; data not shown).

Fig. 3.5C demonstrates the effect of the equilibration time on $^{\Delta F}/_{F_0}$ of OGB-1 in response to an AP. All of the 15 boutons imaged had fluorescence transients with bi-exponential decay kinetics. A nested model comparison between mono- and bi-exponential fits showed that the former was rejectable for all measured time points (dashed and solid black curves, respectively; $p_{\mathrm{F}} \leq 0.005$). As the equilibration time increased, the peak amplitude of $^{\Delta F}/_{F_0}$ decreased, whilst its decay time course became longer. This was expected because of the binding of Ca^{2+} to the fluorescent indicator: over time, as the concentration of OGB-1 in the imaged bouton increased, less of the Ca^{2+} ions that entered the bouton during an AP would remain free and available for sequestration, making the presynaptic Ca^{2+} transient smaller in amplitude and longer in time course.

Figs. 3.5D-G summarise the change in the peak amplitude and decay time course

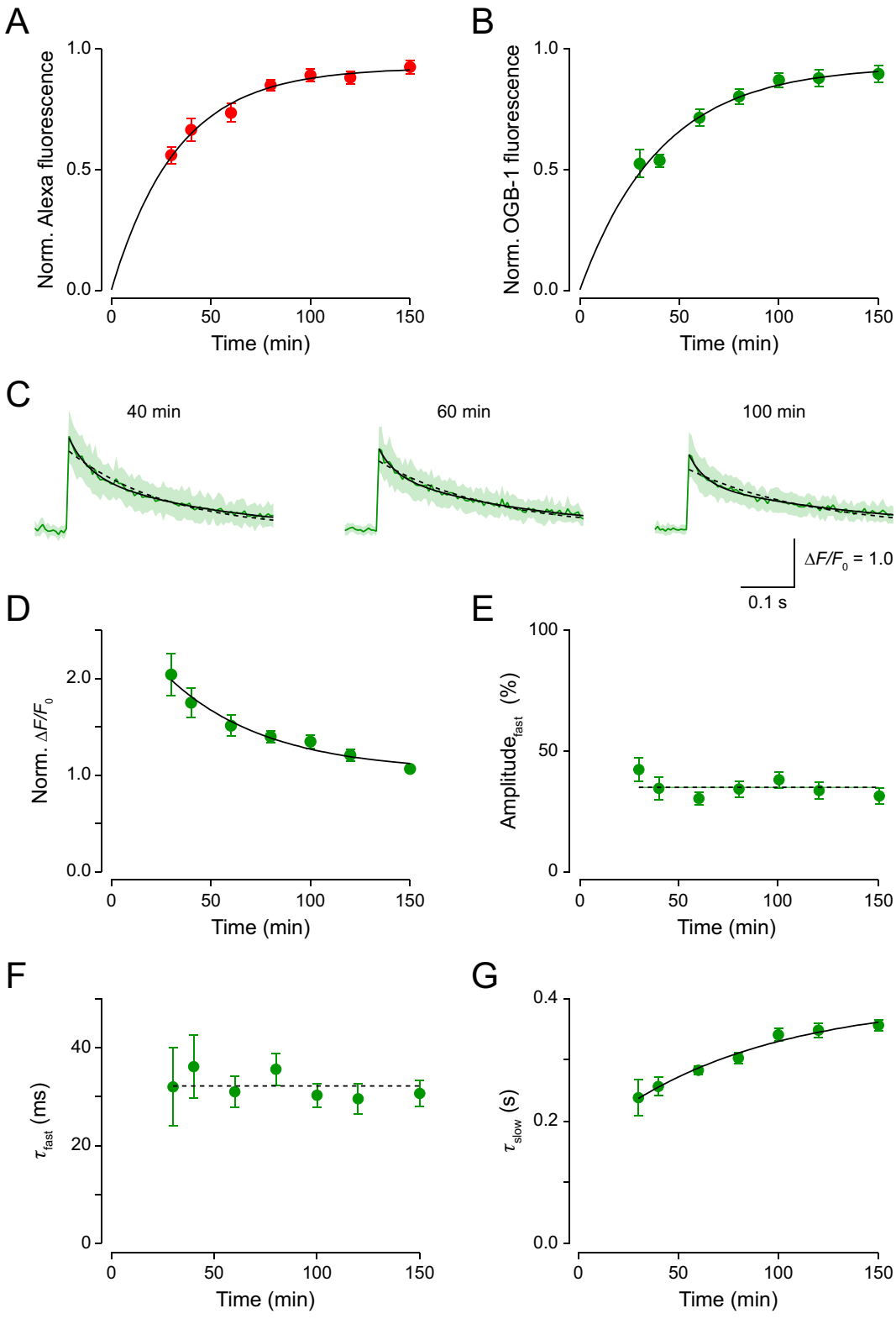

(See next page for figure legend)

Figure 3.5: Equilibration time course of fluorescent dyes. (A-B) The normalised fluorescence of Alexa Fluor® 568 and OGB-1, plotted as a function of equilibration time (n = 15). Plots have been fitted with an exponential function constrained to include (0,0). (C) $^{\Delta F}/_{F_0}$ in response to an AP measured at the indicated time points. Each trace (solid, green) is an average of fluorescence transients of 15 boutons. Shaded areas represent mean ± 1 SD. Each decay phase has been fitted with an exponential function (dashed) and the sum of two distinct exponential functions (solid, black). (D-G) The normalised peak amplitude of $^{\Delta F}/_{F_0}$, amplitude$_{\text{fast}}$, τ_{fast}, and τ_{slow}, plotted as a function of equilibration time. In D and G, plots have been fitted with an exponential function. Dashed line indicates no correlation (E-F).

of $^{\Delta F}/_{F_0}$ over time. Each measured amplitude was normalised by dividing it by the minimum amplitude obtained from the same bouton; the normalised values were subsequently averaged together. The minimum normalised amplitude in this averaged plot was more than 1 as the minimum value of $^{\Delta F}/_{F_0}$ occurred at a slightly different time for each bouton ($\geq$ 60 min after break-in). An exponential fit to the averaged, normalised plot of the peak amplitude yielded a time constant of 50 ± 16 min (Fig. 3.5D; p_{Pr} = 0.0002 with log-level regression analysis). Similarly, an exponential fit to the averaged plot of the slow decay time constant (τ_{slow}) yielded a time constant of 81 ± 29 min (Fig. 3.5G; p_{Pr} = 0.0006 with log-level regression analysis). Interestingly, the relative amplitude as well as the time constant of the fast decay component (amplitude$_{\text{fast}}$ and τ_{fast}, respectively) did not change over time (Figs. 3.5E-F; $p_{\text{Pr}} \geq 0.2$). This indicates that the bi-exponential decay time course was unlikely to arise from either wash-out of intracellular constituents or wash-in of the patch pipette filling solution.

The measured equilibration time courses appeared much longer than those reported by early studies that characterised the Ca^{2+} dynamics in small synaptic boutons (Koester and Sakmann, 2000; Jackson and Redman, 2003). However, they are consistent with more recent studies, in which more than 60 min of equilibration time was required for the indicator concentration to reach a steady state in distant nerve terminals or remote regions of dendrites (> 100 μm from the soma; Scott and Rusakov, 2006; Eilers and Konnerth, 2009; Kisfali *et al.*, 2013). Due to the long equilibration time constant of OGB-1 (41 ± 4 min; Fig. 3.5B), layer 5 pyramidal neurons were filled with the fluorophore (or another Ca^{2+} indicator) for at least

90 min before the extent to which a drug affected AP-evoked Ca^{2+} transients was assessed. In most cases, the concentration of OGB-1 in the imaged boutons, at 90 min after whole-cell break-in, reached only $\sim$ 90% of that in the pipette filling solution (assuming that the final steady-state value was equal to the dye concentration in the patch pipette). However, according to Figs. 3.5D-G, after this time, $^{\Delta F}/_{F_0}$ should change minimally during a period of 10 min required for solution exchange (< 10% in both amplitude and decay time constants).

3.3.2 $[Ca^{2+}]_{rest}$

$[Ca^{2+}]_{rest}$ was calculated from the maximum fluorescence $\left(^{\Delta F}/_{F_0}\right)_{max}$ of the high-affinity Ca^{2+} indicator OGB-1 (40 μM; Eq. 3.4). The latter was measured *in situ* using a 2 s long train of APs evoked at 100 Hz. Based on this method, $[Ca^{2+}]_{rest}$ in synaptic boutons of layer 5 pyramidal neurons was 53 $\pm$ 13 nM (n = 10; ranging from 15 to 158 nM). This value is in the range of $[Ca^{2+}]_{rest}$ measured at the calyx of Held and cerebellar MFBs (Helmchen *et al.*, 1997; Delvendahl *et al.*, 2015).

3.3.3 Ca^{2+} transients evoked by an AP decayed bi-exponentially

The "added-buffer" method was used to estimate the Ca^{2+} binding ratio of endogenous buffers (κ_E) and the rate constant of Ca^{2+} sequestration (γ; Neher, 1995). This method takes advantage of the fact that fluorescent Ca^{2+} indicators are essentially Ca^{2+} buffers. Thus, they compete with endogenous buffers and transporters, and alter the amplitude and time course of presynaptic Ca^{2+} transients. By loading synaptic boutons with different concentrations of a Ca^{2+} indicator, or with indicators with different Ca^{2+} binding affinities, the relationship between presynaptic Ca^{2+} dynamics and the exogenous Ca^{2+} binding ratio (κ_D) can be characterised (Fig. 3.1). This then allows κ_E, γ, and the presynaptic Ca^{2+} dynamics in the absence of any exogenous buffers (*i.e.* unperturbed Ca^{2+} dynamics) to be estimated.

Here, layer 5 pyramidal neurons were filled through the patch pipette with either OGB-1 (40, 80, 120, or 160 μM) or OGB-6F (50, 100, 200, or 500 μM). AP-evoked Ca^{2+} transients were measured around $90 - 100$ min after whole-cell break-in. For synaptic boutons loaded with OGB-1, $^{\Delta F}/_{F_0}$ was measured in response to an AP and two 2 s long trains of APs, each at 10 and 20 Hz. For those loaded with OGB-6F, $^{\Delta F}/_{F_0}$ was measured in response to an AP and two 1 s long trains of APs, each at 80 and 100 Hz. $^{\Delta F}/_{F_0}$ measured during the AP trains was used to estimate $\left(^{\Delta F}/_{F_0}\right)_{\max}$ (Section 3.2.6.3), which in turn allowed the calculation of $\Delta[Ca^{2+}]_i$ in response to an AP (Eq. 3.5).

Fig. 3.6A displays the average Ca^{2+} transients evoked by a single AP, each measured with a different concentration of OGB-1 or OGB-6F (green or orange, respectively; $n = 11 - 29$ for each concentration). Consistent with previous studies (Koester and Sakmann, 2000; Jackson and Redman, 2003), these transients reached a peak within $2 - 3$ ms of the AP onset. One intriguing observation from this set of experiments was that the decay of most Ca^{2+} transients was not well approximated by a single exponential function ($Ae^{-t/\tau}$; dashed curves). Instead, based on the set of criteria described in Section 3.2.6.2, the sum of two distinct exponential functions ($A_1e^{-t/\tau_1} + A_2e^{-t/\tau_2}$; solid curves) was required to fit most of them (80% of the imaged boutons). A nested model comparison between mono- and bi-exponential fits showed that the former was rejectable for all indicator concentrations used ($p_F \leq 10^{-4}$).

Figs. 3.6B-E summarise the effect of indicator concentration on the amplitude and decay time course of the single AP-evoked Ca^{2+} transients. Note that the total concentration of OGB-1 and OGB-6F ($[D]_T$) was assumed to be 90% of that in the pipette filling solution, as explained in Section 3.3.1. As expected, Ca^{2+} transients measured with the high-affinity indicator OGB-1 were smaller in amplitude and longer in time course compared to those measured with a similar concentration of OGB-6F. In addition, the peak amplitude of the transients decreased while their τ_{slow} prolonged with an increase in the indicator concentration (Figs. 3.6B and E, respectively; OGB-1: $p_{Pr} = 0.06$ for both parameters; OGB-6F: $p_{Pr} \leq 0.03$). Although

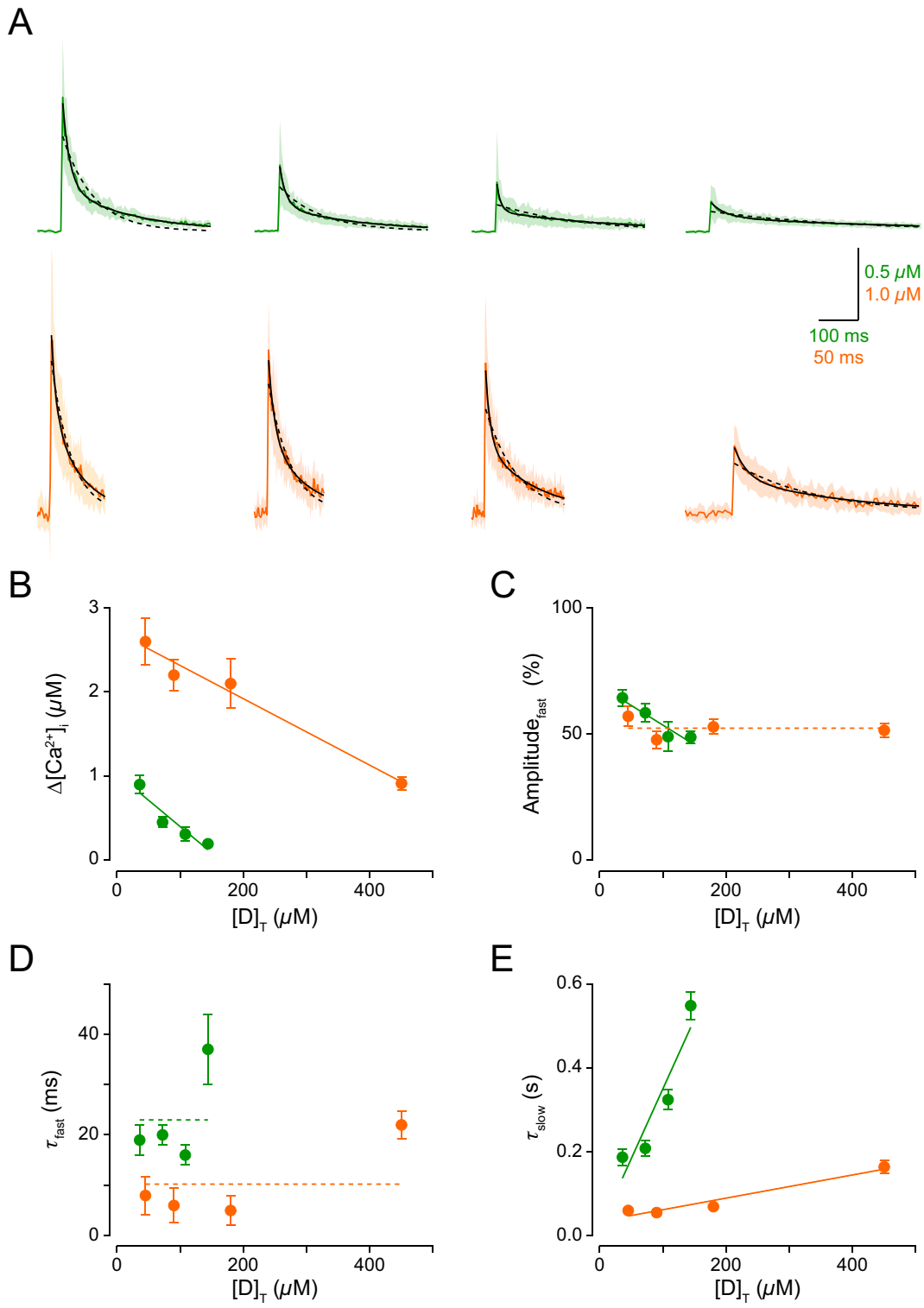

(See next page for figure legend)

Figure 3.6: Characteristics of single AP-evoked Ca^{2+} transients measured with OGB-1 (green) and OGB-6F (orange). (A) The average Ca^{2+} transients evoked by single APs, measured with different concentrations of OGB-1 and OGB-6F (increasing concentration from left to right). Each trace is an average of transients of $11-29$ boutons. Shaded areas represent mean $\pm$ 1 SD. Each decay phase was fitted with a single exponential function (dashed) and the sum of two exponential functions (solid, black). (B-E) The peak amplitude of $\Delta[Ca^{2+}]_i$, $\text{amplitude}_{\text{fast}}$, τ_{fast}, and τ_{slow}, plotted as a function of indicator concentration ($[D]_T$). Plots were fitted with linear regression. Dashed lines indicate no correlation.

τ_{fast} was independent of OGB-1 concentration (Fig. 3.6D; $p_{\text{Pr}} = 0.3$), $\text{amplitude}_{\text{fast}}$ decreased as more OGB-1 was added (Fig. 3.6C; $p_{\text{Pr}} = 0.048$). This was most likely because of saturation of OGB-1: a higher OGB-1 concentration would produce a smaller $\Delta[Ca^{2+}]_i$, which in turn would reduce the extent of its saturation and hence $\text{amplitude}_{\text{fast}}$. In contrast, $\text{amplitude}_{\text{fast}}$ as well as τ_{fast} were both independent of OGB-6F concentration ($p_{\text{Pr}} \geq 0.11$). This suggests that OGB-6F was not significantly saturated by $\Delta[Ca^{2+}]_i$ evoked by a single AP and that saturation of exogenous Ca^{2+} buffers was not the main cause of the observed bi-exponential decay time course.

3.3.4 Estimation of κ_E and γ based on the single-compartment model

To estimate κ_E and γ, the measured Ca^{2+} transients were analysed based on the single-compartment model (Neher and Augustine, 1992; Helmchen and Tank, 2015). κ_E was determined by plotting the inverse of their peak amplitudes $\left(\left(\Delta[Ca^{2+}]_i\right)^{-1}\right)$ against the incremental Ca^{2+} binding ratio of exogenous buffers (κ'_D; Eq. 3.22). κ'_D was used in place of κ_D to take into account saturation of OGB-1. Again, in this calculation, the total concentration of exogenous buffers was assumed to be 90% of that in the pipette filling solution.

Fig. 3.7A shows $\left(\Delta[Ca^{2+}]_i\right)^{-1}$ as a function of κ'_D. Here, each data point indicates the average values of $\left(\Delta[Ca^{2+}]_i\right)^{-1}$ and κ'_D of Ca^{2+} transients measured with a different concentration of OGB-1 or OGB-6F (green or orange, respectively). This plot was fitted with a regression line, with weights inversely proportional to the respective standard errors. Extrapolation to $\kappa'_D = 0$ yielded a y-intercept of $0.19 \pm 0.05\ \mu M^{-1}$.

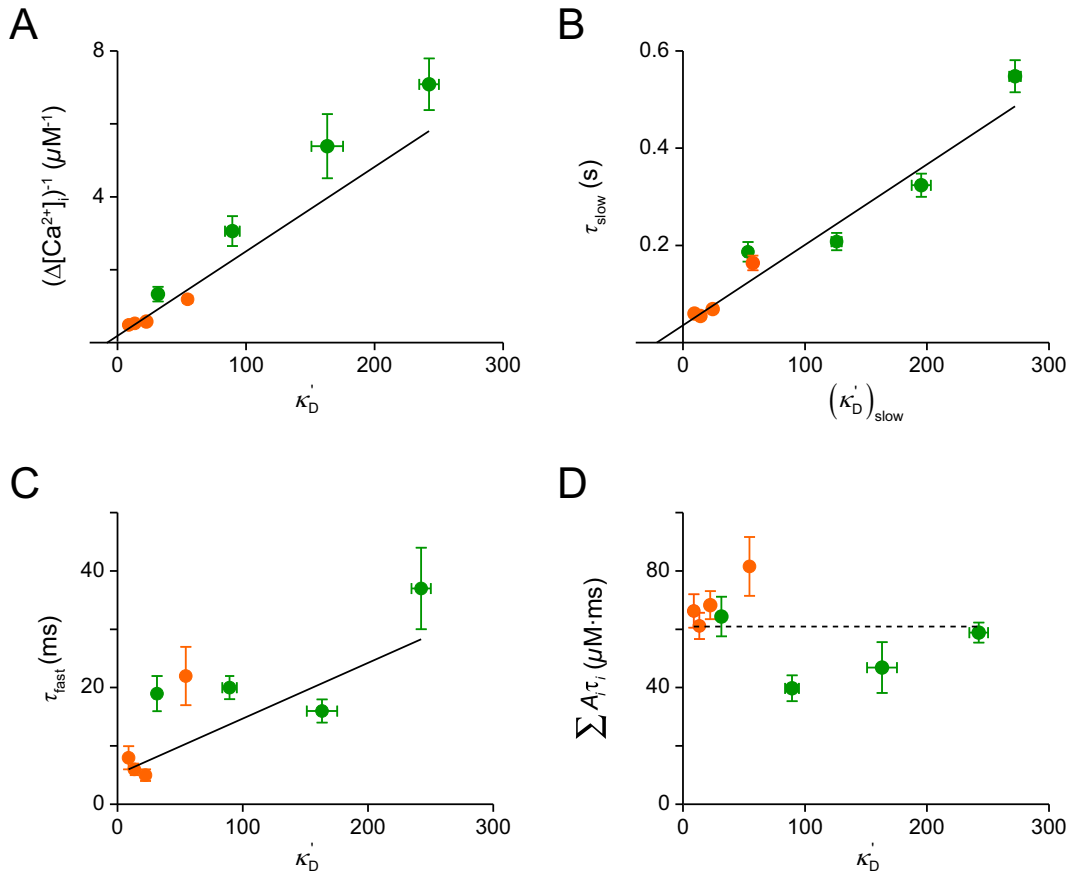

Figure 3.7: Dependence of AP-evoked Ca^{2+} dynamics on the Ca^{2+} binding ratio of exogenous buffers. (A) $\left(\Delta[Ca^{2+}]_i\right)^{-1}$ plotted against κ_D'. (B) τ_{slow} plotted against $\left(\kappa_D'\right)_{slow}$. (C) τ_{fast} plotted against κ_D'. (D) The time integral of the transients ($\sum A_i\tau_i$) plotted against κ_D'. In all plots, each data point represents the average values of Ca^{2+} transients measured with a different concentration of OGB-1 or OGB-6F (green or orange, respectively; $n = 11 - 29$). In A-C, each plot was fitted with a weighted regression line. Dashed line indicates no correlation (D).

The inverse of this value, which was 5.3 ± 1.3 μM, provided an estimate of the peak amplitude of a single AP-evoked Ca^{2+} transient in the absence of exogenous buffers ($\Delta[Ca^{2+}]_{i,0}$). The inverse of the slope of the regression line gave an estimate of 43 ± 3 μM for the total rise in $[Ca^{2+}]_i$ immediately after an AP ($\Delta[Ca^{2+}]_T$). κ_E was estimated from the x-intercept to be 7 ± 2. This suggests that, at the peak of an AP-evoked Ca^{2+} transient, there were ~ 7 Ca^{2+} ions bound to endogenous buffers, for each Ca^{2+} ion that remained free.

In this figure, the data points for OGB-1 and OGB-6F appeared inconsistent of each other. This was mainly because different sampling intervals were used to measure their fluorescence intensities. More specifically, OGB-1 fluorescence was sampled every 5 ms, whilst that of OGB-6F was acquired every $1-3$ ms. Due to the relatively long sampling interval, the amplitudes of $\Delta[Ca^{2+}]_i$ measured with OGB-1 were most likely smaller than the true peak amplitudes. This is supported by the fact that the Ca^{2+} transients measured with OGB-6F reached a peak within $2-3$ ms of the AP onset. Such an underestimation of $\Delta[Ca^{2+}]_i$ would have produced values of $\left(\Delta[Ca^{2+}]_i\right)^{-1}$ that were larger than the true values. This, together with the fact that the values measured with OGB-6F had more weight on the fit, caused the data points of OGB-1 to lie above the regression line.

According to the single-compartment model, γ can also be determined by plotting the decay time constant of an AP-evoked Ca^{2+} transient against κ_D' (Fig. 3.1). As described earlier, most of the measured Ca^{2+} transients decayed bi-exponentially. However, the slow rather than the fast initial decay of these transients was predominantly shaped by the activity of Ca^{2+} transporters (explained in Section 3.3.5). Therefore, to determine γ, τ_{slow} was plotted against the incremental Ca^{2+} binding ratio of exogenous buffers during the slow decay phase $\left(\left(\kappa_D'\right)_{slow}\right)$. $\left(\kappa_D'\right)_{slow}$ was calculated based on Eq. 3.22, with $[Ca^{2+}]_{AP}$ being the amplitude of the slow decay component. Ca^{2+} transients with mono-exponential decays (20%) were excluded from this plot.

Fig. 3.7B shows τ_{slow} as a function of $\left(\kappa_D'\right)_{slow}$. Again, each data point indicates the average values of τ_{slow} and $\left(\kappa_D'\right)_{slow}$ of Ca^{2+} transients measured with a different

concentration of OGB-1 or OGB-6F. Extrapolation of the weighted regression line to $\left(\kappa_D'\right)_{slow} = 0$ yielded a y-intercept of 36 ± 4 ms, which was τ_{slow} of the unperturbed Ca^{2+} transient ($\tau_{slow,0}$). The slope of the regression line provided an estimate of γ_{slow} of 0.60 ± 0.03 ms^{-1}. κ_E estimated from the x-intercept was 21 ± 3, significantly larger than that obtained from the plot of $\left(\Delta[Ca^{2+}]_i\right)^{-1}$ *vs.* κ_D' (p_t = 0.002). This suggests that a larger fraction of Ca^{2+} ions was bound to endogenous buffers during the slow decay phase than at the peak of the Ca^{2+} transients.

To provide a deeper understanding of the mechanism(s) underlying the initial fast decay, τ_{fast} was plotted as a function of κ_D' (Fig. 3.7C). Similar to τ_{slow}, τ_{fast} was linearly dependent on κ_D' (p_{Pr} = 0.01). The slope of the weighted regression line yielded an estimate of γ_{fast} of 10 ± 1 ms^{-1}, a value more than 10-fold larger than γ_{slow}. This suggests that, immediately after the peak of an intracellular Ca^{2+} rise, a highly non-linear process took place and allowed Ca^{2+} to rapidly escape the imaged boutons.

Fig. 3.7D shows the average time integral of the Ca^{2+} transients as a function of κ_D'. The time integral of each transient was calculated from values obtained by fitting its decay time course (that is, $A\tau$ for a mono-exponential fit and $A_1\tau_1 + A_2\tau_2$ for a bi-exponential fit). Consistent with the fact that Ca^{2+} buffers only act as temporary storage sites for Ca^{2+}, the time integral was independent of κ_D' (p_{Pr} = 0.3). The average time integral was 61 ± 5 μM·ms, which was similar to the ratio between the estimated values of $\Delta[Ca^{2+}]_T$ and γ (72 ± 6 μM·ms; Eq. 3.21). This is consistent with the opposite roles of Ca^{2+} influx and sequestration in determining the dynamics of an AP-evoked Ca^{2+} transient.

3.3.5 Blockade of SERCA prolonged the late but not the initial decay

The observed bi-exponential decay kinetics, together with the different estimates of κ_E (Fig. 3.7, A *vs.* B), indicate that at least one of the assumptions underlying the single-compartment model was violated in the imaged boutons. Multi-exponential

decays, which have been reported in a variety of cells and cellular compartments, can arise from buffer saturation (Tank *et al.*, 1995), slowly binding Ca^{2+} buffers (Lee *et al.*, 2000a,b; Collin *et al.*, 2005a; Muller *et al.*, 2007), a non-linear rate of Ca^{2+} sequestration (Regehr, 1997; Kim *et al.*, 2005), or Ca^{2+}-induced Ca^{2+} release (CICR; Sankaranarayanan *et al.*, 2016). However, the mechanism(s) underlying the bi-exponential decay time course observed in nerve terminals of neocortical pyramidal neurons is still unknown (layer 2/3; Koester and Sakmann, 2000). Here, I sought to explain the decay kinetics of AP-evoked Ca^{2+} transients in synaptic boutons of layer 5 pyramidal neurons.

Whether CICR gave rise to the observed decay time course was first investigated. Whilst all of the other factors accelerate $[Ca^{2+}]_i$ decay immediately after an AP, a delayed source of Ca^{2+} through CICR would oppose the action of Ca^{2+} transporters and cause the late decay kinetics to deviate from the initial rate of decay. In other words, if CICR were the principal factor underlying a bi-exponential decay, the activity of Ca^{2+} transporters would mainly determine its initial phase. To investigate this, Ca^{2+} transients evoked by single APs were measured in the presence of cyclopiazonic acid (CPA), a blocker of SERCA pumps. It was hypothesised that, if Ca^{2+} sequestration was the main mechanism underlying the initial decay phase, an inhibition on the rate of Ca^{2+} sequestration through blockade of SERCA would increase τ_{fast} of the Ca^{2+} transients.

Fig. 3.8A shows AP-evoked Ca^{2+} transients measured with OGB-6F (100 μM) in a synaptic bouton, before and after 10 min application of CPA (25 μM; bath-applied; red *vs.* blue, respectively). It can be seen that both the amplitude and the initial decay time course were not considerably affected by CPA. However, CPA seemed to prolong the late decay phase.

Figs. 3.8B-E summarise the effect of CPA on the amplitude and decay kinetics of AP-evoked Ca^{2+} transients in 15 different boutons. Twelve of them (80%) had Ca^{2+} transients that always decayed bi-exponentially ($p_F \leq 10^{-8}$). The decay time course of Ca^{2+} transients measured in the remaining three boutons was bi-exponential in

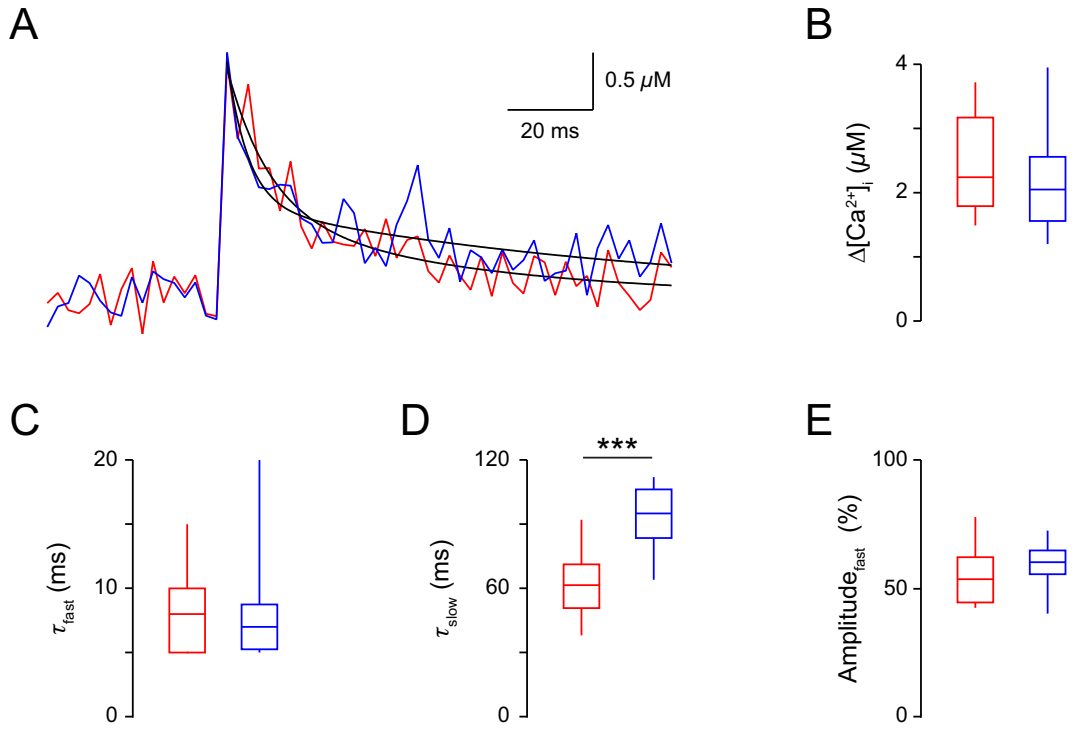

Figure 3.8: Blockade of SERCA pump prolonged the late but not the initial decay phase. (A) Ca^{2+} transients evoked by an AP measured with OGB-6F (100 μM) in a synaptic bouton, before (red) and after 10 min application of CPA (blue). Each trace is an average of 5 repeats. Each decay time course was fitted with the sum of two distinct exponential functions (black curves). (B-E) The peak amplitude of $\Delta[Ca^{2+}]_i$, τ_{fast}, τ_{slow}, and $amplitude_{fast}$ before and after CPA addition. n = 15 in (B) and 12 in (C-E). *** $p_t < 0.001$.

the control condition, but became mono-exponential after CPA addition. The decay kinetics of these boutons were thus excluded in Figs. 3.8C-E. On average, CPA did not significantly alter the peak amplitude of the Ca^{2+} transients (p_{pt} = 0.09; 2.4 $\pm$ 0.2 *vs.* 2.1 $\pm$ 0.2 μM in control and CPA, respectively). It also did not affect $amplitude_{fast}$ and τ_{fast} ($p_{pt} \geq 0.16$; 55 $\pm$ 3 *vs.* 59 $\pm$ 2%, and 8 $\pm$ 1 ms in both conditions). However, τ_{slow} increased by 55 $\pm$ 11% from 63 $\pm$ 5 to 93 $\pm$ 4 ms (p_{pt} = 0.0006). These findings suggest that SERCA contributed to Ca^{2+} sequestration and that the activity of Ca^{2+} transporters was not the main factor that determined the initial decay time course of the Ca^{2+} transients. Accordingly, the observed bi-exponential decay was unlikely to arise from CICR opposing the action of Ca^{2+} sequestration.

3.3.6 The decay kinetics did not speed up during repetitive stimulation

To assess the level of saturation of endogenous Ca^{2+} buffers, Ca^{2+} transients were measured in response to a single AP and a train of 5 APs at 50 Hz. It was hypothesised that, if endogenous Ca^{2+} buffers were significantly saturated, a larger rise in $[Ca^{2+}]_i$ during repetitive stimulation would increase the degree of saturation, thereby yielding Ca^{2+} transients with faster decay kinetics and larger $\Delta[Ca^{2+}]_i$ *per* AP (Tank *et al.*, 1995; Jackson and Redman, 2003). The low-affinity Ca^{2+} indicator Fluo-4FF (500 μM; $K_d = 20 \pm 2$ μM) was used for this set of experiments to avoid saturation of the indicator, which would also speed up the decay kinetics. However, as $[Ca^{2+}]_i$ in synaptic boutons could not be raised to a level sufficient for the measurement of $(\Delta F/F_0)_{max}$ of Fluo-4FF ($\geq$ 100 μM), $\Delta[Ca^{2+}]_i$ could not be calculated from the corresponding $\Delta F/F_0$.

Fig. 3.9A displays Fluo-4FF fluorescence transients measured in a synaptic bouton in response to a single AP and a train of 5 APs at 50 Hz (left and middle, respectively). Similar to Ca^{2+} transients measured with OGB-1 and OGB-6F, the decay time course of these fluorescence transients was bi-exponential ($p_F \leq 10^{-13}$). A peak-scaled comparison of the transient evoked by the single AP and that evoked by the 5th

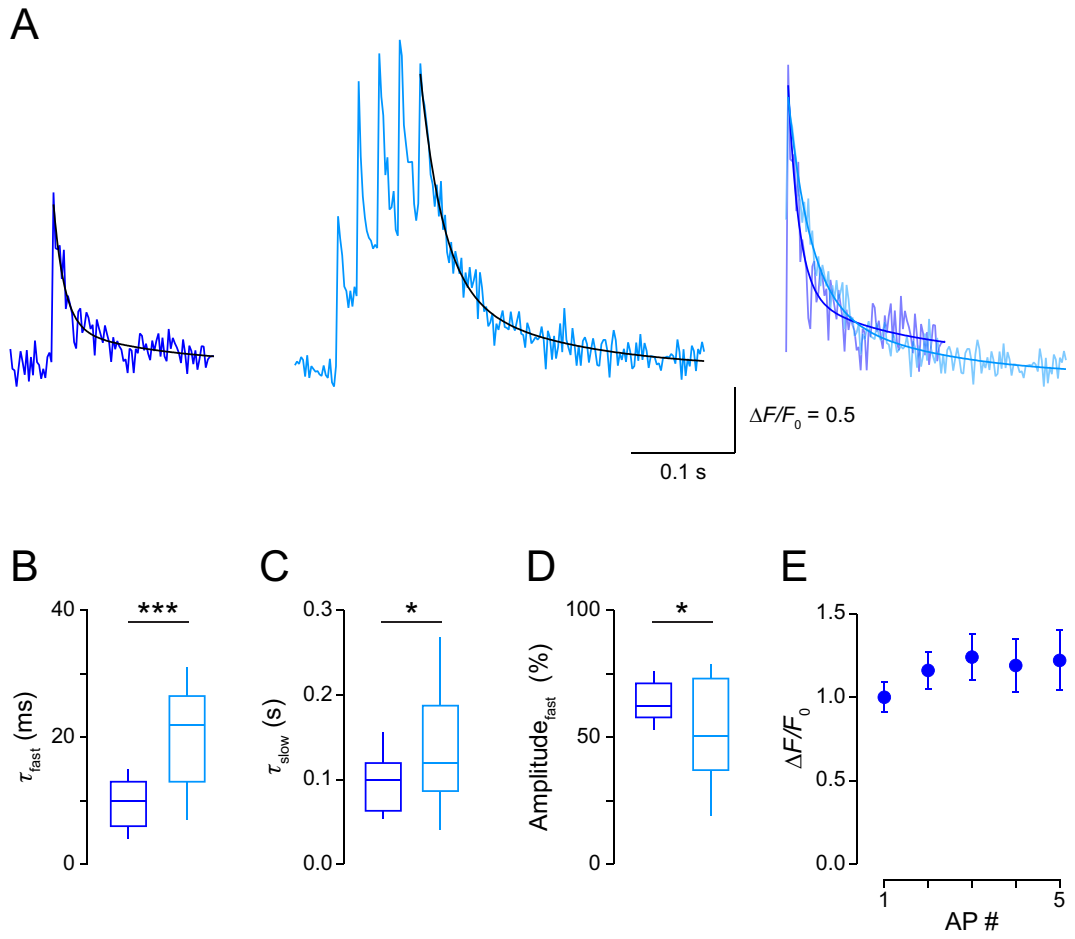

Figure 3.9: $^{\Delta F}/_{F_0}$ measured with Fluo-4FF during repetitive stimulation. (A) $^{\Delta F}/_{F_0}$ of Fluo-4FF (500 μM) measured in a synaptic bouton in response to an AP (left) and 5 APs evoked at 50 Hz (middle). Each trace is an average of 2 repeats. Each decay time course was fitted with the sum of two exponential functions (black curves). For easy comparison of the decay kinetics, the transient evoked by a single AP was peak-scaled to match that evoked by the 5th AP in the train (right); the respective bi-exponential fits are also shown. (B-D) τ_{fast}, τ_{slow}, and amplitude$_{fast}$ after a single AP *vs.* the 5th AP. (E) The average $^{\Delta F}/_{F_0}$ *per* AP, plotted as a function of the AP number. n = 13 in (B-E). * $p_t < 0.05$; *** $p_t < 0.001$.

AP in the train shows that, in contrast to the above hypothesis, the decay time course slowed down during repetitive stimulation (Fig. 3.9A, right).

Figs. 3.9B-D summarise the change in the decay kinetics of Fluo-4FF fluorescence after the AP train (n = 13). Both τ_{fast} and τ_{slow} increased after the 5th AP, whilst amplitude$_{fast}$ became smaller ($p_t \leq 0.04$; τ_{fast} from 10 $\pm$ 1 to 20 $\pm$ 2 ms; τ_{slow} from 94 $\pm$ 10 to 139 $\pm$ 18 ms; amplitude$_{fast}$ from 64 $\pm$ 2 to 53 $\pm$ 5%). In addition, $^{\Delta F}/_{F_0}$ *per* AP did not change during repetitive stimulation (p_{Pr} = 0.12; Fig. 3.9E). Together, these findings suggest that endogenous Ca^{2+} buffers were not significantly saturated in the measured range of $[Ca^{2+}]_i$.

Although Fluo-4FF was used in this set of experiments to avoid indicator saturation, the fact that $\Delta[Ca^{2+}]_i$ could not be calculated from the corresponding $^{\Delta F}/_{F_0}$ could potentially be problematic. This is because, if $[Ca^{2+}]_i$ upon stimulation approached its K_d value, the fluorescence change of Fluo-4FF would no longer be a linear function of $\Delta[Ca^{2+}]_i$. In other words, ΔF would become smaller for the same $\Delta[Ca^{2+}]_i$ and the decay time course of the fluorescence transient would be prolonged compared to that of the underlying Ca^{2+} transient. These non-linear changes in the fluorescence transient might have masked a potential increase in $\Delta[Ca^{2+}]_i$ *per* AP and a more rapid decay time course caused by buffer saturation. However, it can be estimated that, in the presence of 500 μM Fluo-4FF (which yielded a κ_D of $\sim$ 25, slightly larger than κ_D' of 200 μM OGB-6F), a single AP raised $[Ca^{2+}]_i$ by $\sim$ 2 μM. The peak amplitude of $^{\Delta F}/_{F_0}$ in response to a train of 5 APs evoked at 50 Hz was 2.2 $\pm$ 0.2 times that evoked by a single AP. Therefore, $[Ca^{2+}]_i$ immediately after the AP train would only be around $\sim$ 5 μM, a value four-fold smaller than the K_d value of Fluo-4FF (20 $\pm$ 2 μM; Table 2.4). Accordingly, the measured fluorescence transients of Fluo-4FF were most likely proportional to the intracellular Ca^{2+} elevations.

To consolidate the idea that endogenous Ca^{2+} buffers were not saturated by $\Delta[Ca^{2+}]_i$ evoked by an AP, $[Ca^{2+}]_i$ during repetitive stimulation was measured with OGB-6F (500 μM) so that $\Delta[Ca^{2+}]_i$ could be calculated from the corresponding $^{\Delta F}/_{F_0}$. Fig. 3.10A displays Ca^{2+} transients measured in a synaptic bouton in response to

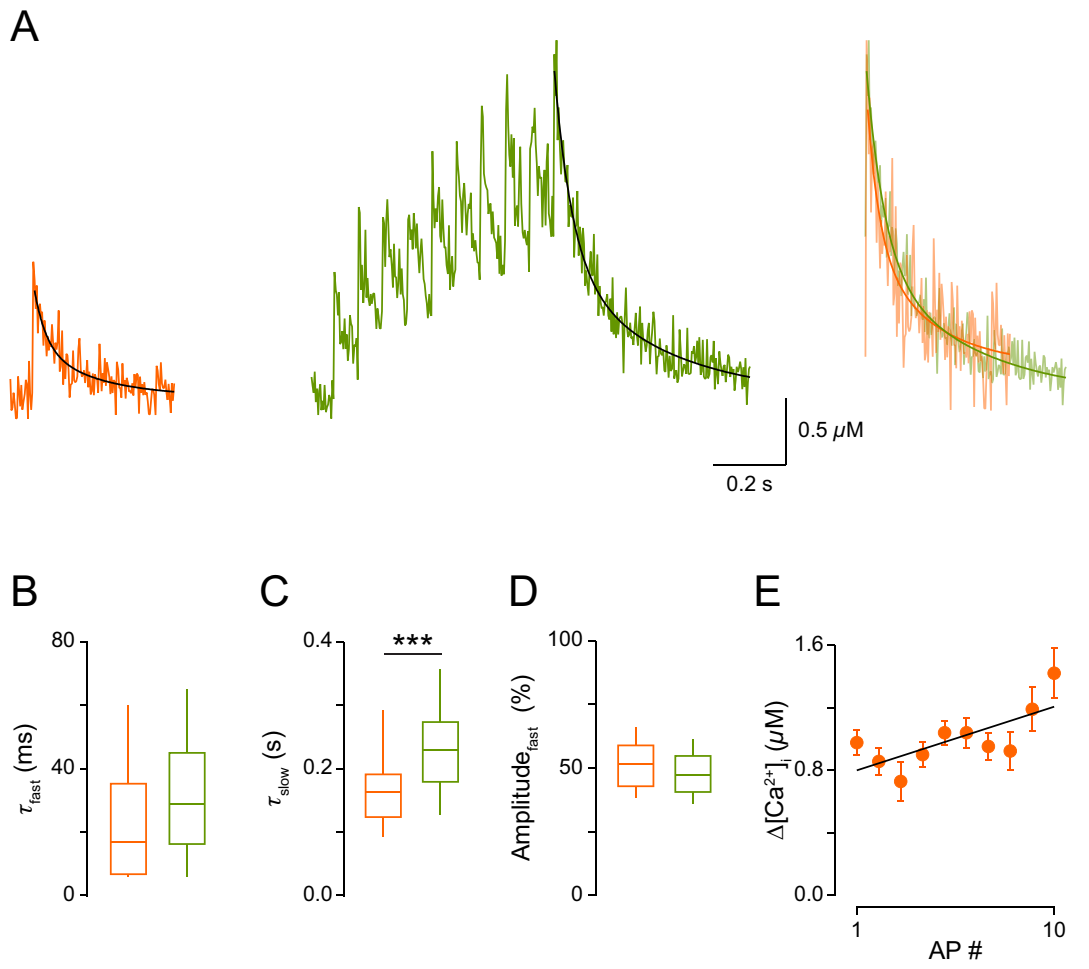

Figure 3.10: Ca^{2+} transients measured with OGB-6F during repetitive stimulation. (A) Ca^{2+} transients measured with OGB-6F (500 μM) in a synaptic bouton in response to an AP (left) and 10 APs evoked at 15 Hz (middle). Each trace is an average of 3 repeats. Each decay time course was fitted with the sum of two exponential functions (black curves). For easy comparison of the decay kinetics, the transient evoked by a single AP was peak-scaled to match that evoked by the 10^{th} AP in the train (right); the respective bi-exponential fits are also shown. (B-D) τ_{fast}, τ_{slow}, and $amplitude_{fast}$ after a single AP *vs.* the 10^{th} AP. (E) The average $\Delta[Ca^{2+}]_i$ *per* AP, plotted as a function of the AP number. This plot was fitted with linear regression. n = 12 in (B-E).

a single AP and a train of 10 APs evoked at 15 Hz (left and middle, respectively). Again, following both types of stimulation, $[Ca^{2+}]_i$ still decayed bi-exponentially ($p_F \leq 10^{-4}$). After the transient evoked by the single AP was peak-scaled to match that evoked by the 10^{th} AP in the 15 Hz train, a slight broadening of the decay time course during repetitive stimulation was also revealed (Fig. 3.10A, right).

Figs. 3.10B-D compare the average decay kinetics of $[Ca^{2+}]_i$ following a single AP and the 15 Hz train (n = 12). Both τ_{fast} and $amplitude_{fast}$ did not change after the AP train ($p_t \geq 0.08$; τ_{fast}: 23 ± 5 *vs.* 31 ± 5 ms; $amplitude_{fast}$: 53 ± 3% *vs.* 48 ± 2% after a single AP and 10 APs, respectively). However, τ_{slow} increased by 48 ± 12% from 164 ± 15 to 234 ± 19 ms (p_t = 0.002). $\Delta[Ca^{2+}]_i$ *per* AP also increased during the train, at a rate of 45 ± 16 nM/AP (p_{Pr} = 0.02; Fig. 3.10E).

These findings lend further support to the conclusion above, that is, in synaptic boutons of layer 5 pyramidal neurons, $\Delta[Ca^{2+}]_i$ evoked by a single AP did not significantly saturate endogenous Ca^{2+} buffers. Together with the prolongation of Fluo-4FF fluorescence transients following repetitive stimulation, they also argue against a speed up in the activity of Ca^{2+} transporters at a higher $[Ca^{2+}]_i$ (or the presence of a transporter with a rate supralinearly dependent on $[Ca^{2+}]_i$). Therefore, neither buffer saturation nor a non-linear rate of Ca^{2+} sequestration was the main cause of the observed bi-exponential decays.

3.3.7 Diffusion of Ca^{2+} into the axon sped up the initial decay

Due to the small sizes of the imaged boutons and the fact that most, if not all of them, were *boutons en passant*, it was hypothesised that diffusion into the axon allowed Ca^{2+} to rapidly escape, thereby speeding up the initial decay time course of $[Ca^{2+}]_i$ within the bouton. To investigate the role of diffusion, a 3D reaction-diffusion model of a bouton, with an axon attached to it, was created (Fig. 3.11A). The bouton was modelled as a sphere, with a radius of 0.5 μm. The axon was modelled as a cylinder, with a diameter varied between 0.1, 0.2, and 0.4 μm. These values

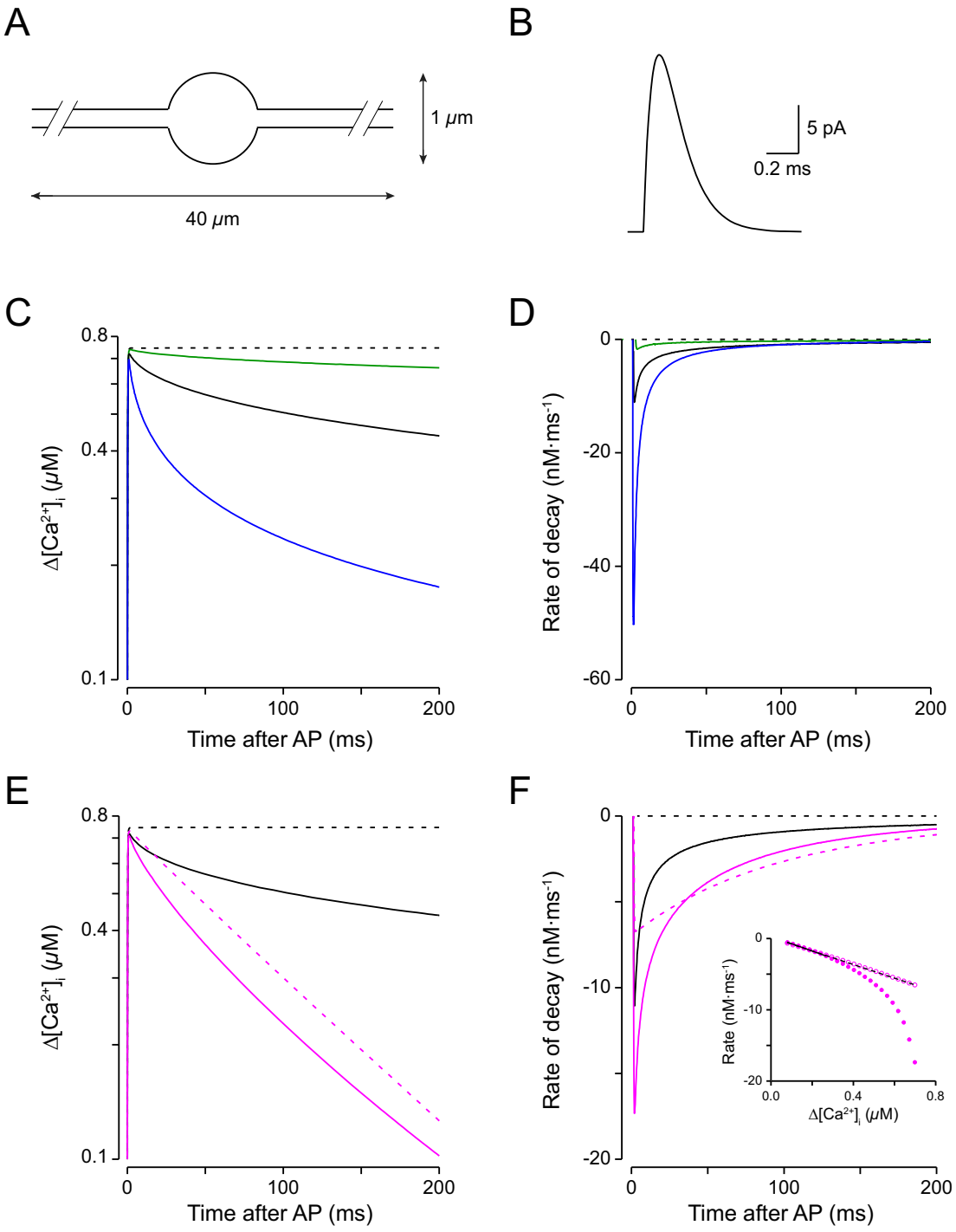

(See next page for figure legend)

Figure 3.11: Diffusion of Ca^{2+} into the axon sped up the initial decay of Ca^{2+} transients. (A) A visualisation of the modelled bouton. (B) The simulated Ca^{2+} current. (C) $\Delta[Ca^{2+}]_i$ in the modelled bouton, with the rate of decay determined solely by diffusion of Ca^{2+} into the axon. The axon diameter was 0.1 (green), 0.2 (black), or 0.4 μm (blue). Dashed line indicates $\Delta[Ca^{2+}]_i$ in a bouton with no connecting axon. (D) The rate of decay, obtained by differentiating the respective traces in C. (E) $\Delta[Ca^{2+}]_i$ in a bouton with an axon diameter of 0.2 μm (solid), or with no connecting axon (dashed), without or with Ca^{2+} transport (black *vs.* pink). (F) The corresponding rate of decay, plotted against time or $\Delta[Ca^{2+}]_i$ (inset). Plots in inset were fitted with a linear regression.

represent the range of axon diameters of layer 5 pyramidal neurons (minimum, mean, and maximum, respectively; Rollenhagen and Lübke, personal communication). To understand how diffusion into the axon shaped the dynamics of $\Delta[Ca^{2+}]_i$ within the bouton, an additional model with only the bouton was included. In these 3D models, Ca^{2+} was buffered by an endogenous fixed buffer and a pool of exogenous mobile buffers. The concentrations, K_d, Ca^{2+} binding and unbinding rates, and diffusion coefficients of these buffers were derived from the experimental values or obtained from the literature (Table 3.3). Following an AP-evoked Ca^{2+} current that increased $[Ca^{2+}]_T$ within the bouton by 50 μM (Fig. 3.11B), Ca^{2+} was extruded by a pump or sequestered by a homogeneously distributed uptake mechanism. Both mechanisms operated at a rate linearly dependent on the local $\Delta[Ca^{2+}]_i$. The corresponding rate constants ($\gamma_{extrusion}$ and γ_{uptake}) were approximated based on the decay time courses measured with and without CPA (Section 3.2.8.2).

Figs. 3.11C-D demonstrate the effect of diffusion on the amplitude and time course of single AP-evoked Ca^{2+} transients, simulated in the presence of 450 μM OGB-6F. In this set of simulations, Ca^{2+} within the bouton could only escape by diffusion into the axon; both membrane transport and intracellular uptake were zero. As expected, Ca^{2+} could not escape if there was no connecting axon (dashed line), and the Ca^{2+} transients decayed more rapidly with increasing axon diameters: 0.1 (green), 0.2 (black), and 0.4 μm (blue). The escape of Ca^{2+} was particularly rapid within $\sim$ 10 ms after the AP onset, when the gradient of Ca^{2+} between the bouton and the axon was high. After this time, the rate of decay due to diffusion reduced to $\leq$ 40% of the maximal rate. This is consistent with the fact that the rate of change by diffusion

decreases inversely with time (Section 3.2.7.3). As a result, the rate of Ca^{2+} decay was not a linear function of $\Delta[Ca^{2+}]_i$, causing the decay time course to deviate from a single exponential function (Fig. 3.11C).

In Fig. 3.11E, single AP-evoked Ca^{2+} transients, simulated in the absence of membrane pumps and intracellular uptake, were compared to those simulated in their presence (black *vs.* pink). The axon was 0.2 μm in diameter (solid) or non-existent (dashed). Expectedly, the activity of Ca^{2+} transporters increased the rate of decay of $[Ca^{2+}]_i$ (Fig. 3.11F). Without a connecting axon, the maximal rate of decay increased from 0 to 7 nM·ms^{-1} (in magnitude). With an axon diameter of 0.2 μm, it increased from 11 to 17 nM·ms^{-1}. Therefore, diffusion of Ca^{2+} into the axon accounted for $\sim 11/17$ or 60% of the initial Ca^{2+} removal. This shows that, even when Ca^{2+} sequestration mechanisms were active, the rate of decay immediately after the AP onset was still significantly determined by diffusion into the axon. This is consistent with the fact that the maximal rate of decay caused solely by Ca^{2+} transporters was smaller than that caused solely by diffusion (7 *vs.* 11 nM·ms^{-1} in magnitude, respectively). Accordingly, in the presence of exogenous buffers, the activity of Ca^{2+} transporters was not fast enough to capture all Ca^{2+} ions and prevent them from escaping into the axon. As a significant fraction of Ca^{2+} ions were able to diffuse out of the bouton, the rate of decay was non-linearly dependent on $\Delta[Ca^{2+}]_i$ (filled circles in Fig. 3.11F inset). In contrast, without a connecting axon, the rate of Ca^{2+} removal was always linearly dependent on $\Delta[Ca^{2+}]_i$ (open circles). Thus, diffusion of Ca^{2+} out of the imaged boutons was likely the main factor that caused the Ca^{2+} transients to deviate from a mono-exponential decay.

Fig. 3.11F (inset) supports the finding that blockade of SERCA prolonged the late, but not the initial decay phase of single AP-evoked Ca^{2+} transients. As the extent to which Ca^{2+} diffused into the axon decreased with time, the contribution of Ca^{2+} transporters became more prominent (Section 3.2.8.2). Consequently, once $\Delta[Ca^{2+}]_i$ decreased to $\sim$ 40% of the peak amplitude, the rate of decay was a linear function of $\Delta[Ca^{2+}]_i$. The slope of this linear relationship (solid line) was similar to that in the absence of a connecting axon (dashed line). This indicates that, at $\Delta[Ca^{2+}]_i$ below

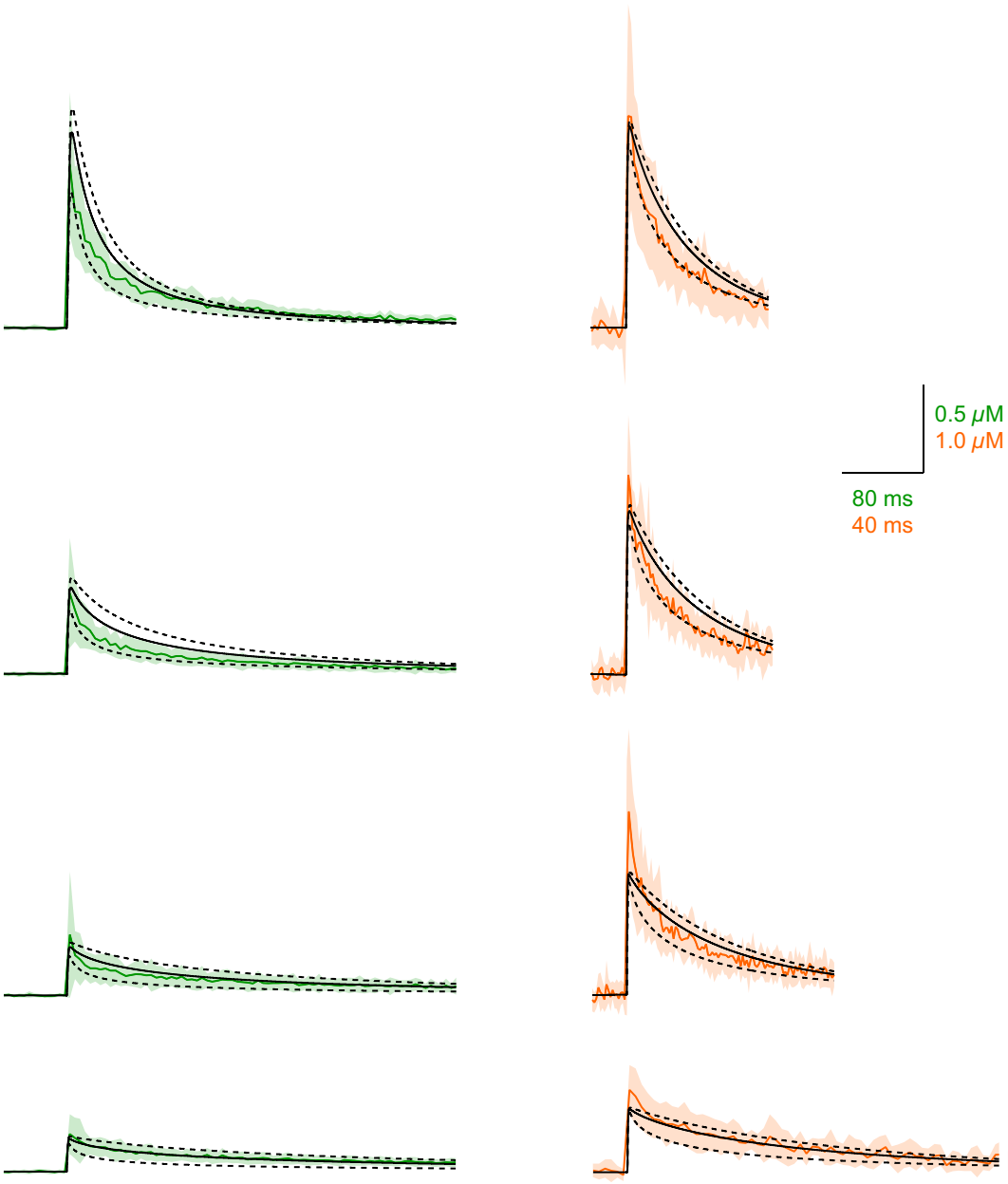

Figure 3.12: Simulated Ca^{2+} transients evoked by a single AP. In each sub-figure, the averaged single AP-evoked Ca^{2+} transient, measured with a different concentration OGB-1 (green) or OGB-6F (orange), was superimposed with the corresponding transients obtained from 3D models of different axon diameters: 0.1 (dashed, outer), 0.2 (solid), or 0.4 μm (dashed, inner). Shaded areas represent mean $\pm$ 1 SD.

$\sim$ 40% of the peak amplitude, the rate of Ca^{2+} removal was mainly determined by Ca^{2+} sequestration mechanisms.

Fig. 3.12 compares single AP-evoked Ca^{2+} transients, obtained from the 3D models of different axon diameters, to those measured in synaptic boutons of layer 5 pyramidal neurons (Fig. 3.6A). In each sub-figure, data were obtained with a different concentration of OGB-1 (green) or OGB-6F (orange), with the simulated data indicating the volume-averaged $\Delta[Ca^{2+}]_i$ within the modelled bouton (black). As the axon diameter increased from 0.1 to 0.4 μm, the peak amplitude of the simulated Ca^{2+} transients decreased, whilst their initial decay kinetics sped up. Even with a very thin axon of 0.1 μm in diameter (outer dashed trace), the decay time course of the simulated Ca^{2+} transients did not become mono-exponential. However, all of the measured time courses were better reproduced when the modelled axon had a diameter of 0.2 or 0.4 μm (solid or inner dashed trace, respectively). This is consistent with the fact that the imaged boutons were mostly from 1st to 2nd order axon collaterals. Therefore, the connecting axons were likely to be $\geq$ 0.2 μm in diameter. For all indicator concentrations used, the dynamics of the simulated and measured transients were remarkably similar to each other, even though the values of $\gamma_{extrusion}$ and γ_{uptake} were approximated based solely on τ_{slow} measured with 100 μM OGB-6F in the patch pipette. This emphasises the consistency between the measured Ca^{2+} transients. Together, the results in Figs. 3.11 and 3.12 suggest that diffusion of Ca^{2+} into the axon played a major role in shaping the decay kinetics of AP-evoked Ca^{2+} transients in the imaged boutons.

3.3.8 Evaluation of model parameters and the single-compartment model

The simulated Ca^{2+} transients (Fig. 3.12) were analysed based on the single-compartment model to assess the appropriateness of the parameters used in the 3D models (Table 3.3). This also allowed an examination of whether the single-compartment model provided accurate estimates of the unperturbed Ca^{2+} dynamics in a small *bouton en passant*. In each of Figs. 3.13A-D, the experimentally measured

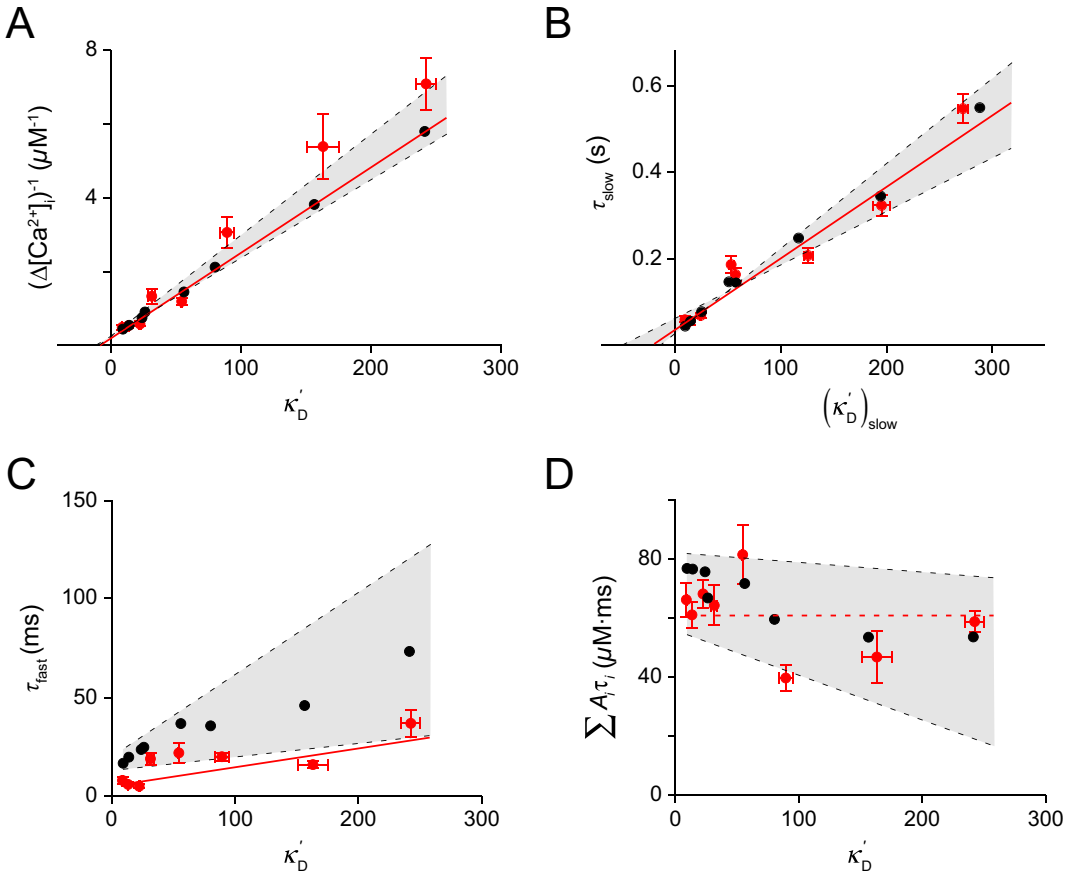

Figure 3.13: Analysis of the simulated Ca^{2+} transients based on the single-compartment model. In each plot, simulation results, obtained with an axon diameter of 0.2 (black circles), 0.1 or 0.4 μm (dashed lines), were superimposed with experimental data (red).

values (red; Fig. 3.7) were superimposed with simulation results. Black circles represent simulated data obtained with an axon diameter of 0.2 μm, whilst dashed black lines indicate linear fits to the data obtained with an axon diameter of 0.1 or 0.4 μm.

Unexpectedly, the values of κ_E and $\Delta[Ca^{2+}]_{i,0}$ obtained from the plot of $\left(\Delta[Ca^{2+}]_i\right)^{-1}$ *vs.* κ'_D were rather insensitive to the variation in axon diameters (Fig. 3.13A). With a K_d value of 100 μM and a total concentration of 1 mM, the modelled endogenous buffer provided a maximum κ_E value of $[E]_T/K_d = 10$. Therefore, following a presynaptic Ca^{2+} current that yielded a $\Delta[Ca^{2+}]_T$ of 50 μM, the peak amplitude of $\Delta[Ca^{2+}]_{i,0}$ in the modelled bouton was approximately $50/(10+1)$ or 4.5 μM. In

agreement with this, for an axon diameter of 0.2 μm, a linear fit to the plot of $\left(\Delta[Ca^{2+}]_i\right)^{-1}$ *vs.* κ_D' yielded a κ_E value of 9 $\pm$ 1, and a $\Delta[Ca^{2+}]_{i,0}$ value of 4.2 $\pm$ 0.4 μM. These values were not different from those obtained with an axon diameter of 0.1 or 0.4 μm, indicating that diffusion of Ca^{2+} into the axon did not significantly reduce the peak amplitude of AP-evoked Ca^{2+} transients in the absence of exogenous buffers. They were also in the range of those estimated from the measured Ca^{2+} transients (7 $\pm$ 2 and 5.3 $\pm$ 1.3 μM, respectively; red line). These findings suggest that, in the range of axon diameters of layer 5 pyramidal neurons and in the absence of endogenous buffer saturation, the single-compartment model provided accurate estimates of κ_E and $\Delta[Ca^{2+}]_{i,0}$.

In contrast, the single-compartment model provided only a rough estimate of $\Delta[Ca^{2+}]_T$ evoked by a single AP. Despite a constant presynaptic Ca^{2+} current, the value of $\Delta[Ca^{2+}]_T$, obtained from the slope of the plot of $\left(\Delta[Ca^{2+}]_i\right)^{-1}$ *vs.* κ_D', was 47 $\pm$ 1, 44 $\pm$ 1, and 37 $\pm$ 1 μM for an axon diameter of 0.1, 0.2, and 0.4 μM, respectively (Fig. 3.13A). Such an inverse relationship between the estimated value of $\Delta[Ca^{2+}]_T$ and the axon diameter was most likely because, the thicker the axon, the more Ca^{2+} ions escaped from the bouton before the spatially averaged $[Ca^{2+}]_i$ reached its peak (Fig. 3.12). However, the fraction of Ca^{2+} ions that escaped decreased with increasing concentrations of OGB-1 or OGB-6F (due to a speed up in spatial equilibration and an increase in the absolute binding rate, or $k_{on} \times [D]$, of the dye). This means that, with a larger value of κ_D', the relative reduction in $\Delta[Ca^{2+}]_i$ due to an increase in axon diameter became smaller, making the corresponding difference in $\left(\Delta[Ca^{2+}]_i\right)^{-1}$ larger. Consequently, the slope of the plot of $\left(\Delta[Ca^{2+}]_i\right)^{-1}$ *vs.* κ_D' increased with increasing axon diameters, yielding smaller estimates of $\Delta[Ca^{2+}]_T$ ($=$ slope^{-1}). Surprisingly, the value of $\Delta[Ca^{2+}]_T$ estimated with the mean axon diameter (0.2 μm) was the same as that obtained with the measured Ca^{2+} transients (44 $\pm$ 1 *vs.* 43 $\pm$ 3 μM, respectively). This suggests that the value of $\Delta[Ca^{2+}]_T$ provided by the single-compartment model was an underestimate of the true $\Delta[Ca^{2+}]_T$ evoked by a single AP, which was likely $\sim$ 50 μM in these boutons.

Similarly, the single-compartment model provided only a rough estimate of γ. This

is because the model does not take into account the fact that the activity of a Ca^{2+} transporter depends on the local $\Delta[Ca^{2+}]_i$, not the volume-averaged $\Delta[Ca^{2+}]_i$. Furthermore, diffusion into the axon, which contributed significantly to the total Ca^{2+} removal, caused the rate of decay to be non-linearly dependent on $\Delta[Ca^{2+}]_i$ (Fig. 3.11F). This violated one of the assumptions of the single-compartment model. As a result, the values of $\gamma_{extrusion}$ and γ_{uptake} had to be approximated based on the measured values of τ_{slow} in the control condition and after addition of CPA, instead of the estimated value of γ_{slow} (Section 3.2.8.2). Consistent with the remarkable similarity in the decay time courses between the simulated and measured transients (Fig. 3.12), the plot of τ_{slow} *vs.* $\left(\kappa_D'\right)_{slow}$ obtained with the measured transients (red) lied reasonably well within the grey area defined by the simulated values (Fig. 3.13B). A linear fit to the simulated data, with the mean axon diameter (0.2 μm; black circles), yielded a γ_{slow} of 0.64 $\pm$ 0.02 ms^{-1} and a $\tau_{slow,0}$ of 38 $\pm$ 7 ms, both of which were similar to those obtained with the measured Ca^{2+} transients (0.60 $\pm$ 0.03 ms^{-1} and 36 $\pm$ 4 ms, respectively; red line). Interestingly, the value of κ_E estimated from the x-intercept of this plot (23 $\pm$ 5) was larger than that obtained from the corresponding plot of $\left(\Delta[Ca^{2+}]_i\right)^{-1}$ *vs.* κ_D' (9 $\pm$ 1), but in the range of that obtained with the measured transients (21 $\pm$ 3). This finding further supports the idea that diffusion of Ca^{2+} into the axon was the main mechanism that caused the measured transients to deviate from the prediction of the single-compartment model.

The plot of τ_{fast} *vs.* κ_D' obtained with the measured Ca^{2+} transients did not lie as well within the grey area defined by the simulated values (Fig. 3.13C). This was likely because, compared to τ_{slow}, τ_{fast} was measured based on a smaller number of data points, and thus, more prone to random sampling. The values of τ_{fast} were also much more sensitive to the variation in axon diameters, consistent with the rapid rate of diffusion during the initial decay phase (Figs. 3.11C-F). A linear fit to the simulated data, with the mean axon diameter, yielded a value of γ_{fast} roughly in the range of that obtained with the measured transients (5 ± 1 *vs.* 10 ± 1 ms^{-1}, respectively).

Similar to τ_{fast}, there was a large variation in the time integral of a single AP-evoked Ca^{2+} transient between axon diameters of 0.1 and 0.4 μm (Fig. 3.13D). Even

with the same diameter, $\sum A_i\tau_i$ decreased considerably with increasing values of κ_D'. These phenomena likely arose from the diffusion of Ca^{2+}, particularly those bound to buffer molecules, out of the bouton. The thicker the axon or the higher the concentration of mobile buffers, the more Ca^{2+} ions were carried away and remained "unseen" by sequestration mechanisms that operated within the bouton. In contrast, without a connecting axon, Ca^{2+} is only temporarily "stored" by buffers, and all of the ions that enter the bouton during an AP will be taken up and removed by a transporter. Therefore, $\sum A_i\tau_i$ is independent of κ_D' in a truly single compartment, where diffusion is negligible. The lack of a linear correlation between the measured values of $\sum A_i\tau_i$ and κ_D' (p_{Pr} = 0.3) was likely due to variations in the geometry of the imaged boutons and their connecting axons.

Together, the results in Figs. 3.12 and 3.13 show that the parameters used in the 3D reaction-diffusion models produced quite accurate predictions of single AP-evoked Ca^{2+} transients in synaptic boutons of layer 5 pyramidal neurons. They also suggest that, in the absence of endogenous buffer saturation, the single-compartment model provided accurate estimates of κ_E and $\Delta[Ca^{2+}]_{i,0}$, but only rough estimates of $\Delta[Ca^{2+}]_T$ and γ in small boutons.

3.3.9 Modelling Ca^{2+} transients in an unperturbed bouton

As the 3D model with a connecting axon quite accurately reproduced the spatially averaged $[Ca^{2+}]_i$ in the presence of exogenous buffers, I used it to simulate Ca^{2+} dynamics in an unperturbed bouton. Fig. 3.14A displays simulated Ca^{2+} transients, evoked by a single AP, in the absence of exogenous buffers. Again, the axon diameter was varied between 0.1 (green), 0.2 (black), and 0.4 μm (blue). Consistent with the estimate of $\Delta[Ca^{2+}]_{i,0}$ based on the single-compartment model (4.2 $\pm$ 0.4 μM; Fig. 3.13A), the peak amplitude of the Ca^{2+} transients was 4.6 μM, independent of the axon diameter. This supports the use of the single-compartment model to estimate $\Delta[Ca^{2+}]_{i,0}$ in the imaged boutons.

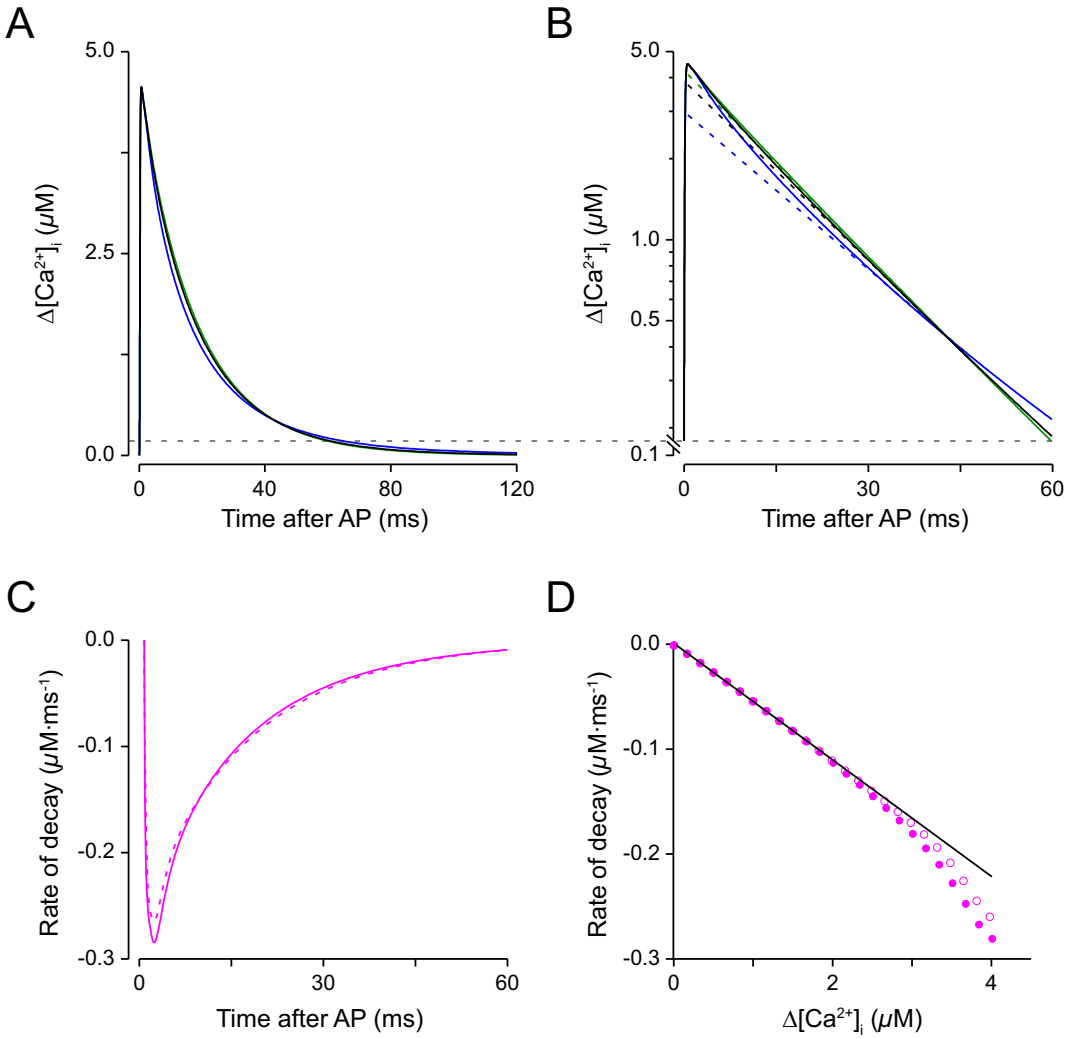

Figure 3.14: Single AP-evoked Ca^{2+} transients in an unperturbed bouton. (A-B) Simulated Ca^{2+} transients evoked by a single AP in the absence of exogenous buffers. The connecting axon was 0.1 (green), 0.2 (black), or 0.4 μm (blue) in diameter. Dashed lines in B indicate mono-exponential fits to the decay time courses between 30 and 50 ms, extrapolated back to the time of peak amplitude. (C-D) The rate of decay of $\Delta[Ca^{2+}]_i$ in an unperturbed bouton with an axon diameter of 0.2 μm (solid/filled circles), or with no connecting axon (dashed/open circles), plotted against time or $\Delta[Ca^{2+}]_i$. Solid line in D indicates a linear fit to the values at $\Delta[Ca^{2+}]_i < 2$ μM.

Again, the decay time course of the Ca^{2+} transients was not truly mono-exponential (Fig. 3.14B). However, based on the difference between the maximal rates of decay with a 0.2 μm thick axon *vs.* without an axon (Fig. 3.14C; solid *vs.* dashed; -280 *vs.* -260 nM·ms^{-1}, respectively), it was estimated that diffusion of Ca^{2+} into the axon accounted for only $\sim$ 7% of the initial Ca^{2+} clearance. Thus, the relative contribution of diffusion was much smaller than that in the presence of exogenous buffers ($\sim$ 60%; Fig. 3.11F). This was expected because exogenous buffers competed with Ca^{2+} transporters for Ca^{2+} binding, thereby decreasing the effective rate of Ca^{2+} sequestration. Without them, the total Ca^{2+} binding ratio of all buffers was much reduced ($\kappa_E + \kappa_D = 9$ *vs.* 65 in the presence of 450 μM OGB-6F). This allowed Ca^{2+} transporters, operated within the bouton, to capture the majority of Ca^{2+} ions and prevent them from escaping into the axon. Consequently, the rate of decay deviated less from a linear relationship with $\Delta[Ca^{2+}]_i$ (Fig. 3.14D; filled circles). A fit to the linear part of this plot yielded a slope of 0.056 $\pm$ 0.001 ms^{-1} (solid line; for $\Delta[Ca^{2+}]_i \leq 2$ μM). Multiplying this by a factor of 11, which was the maximum value of (κ_E + 1), gave a value of 0.61 $\pm$ 0.01 ms^{-1} for the rate constant γ of Ca^{2+} sequestration (Eq. 3.19). As this is similar to the value of γ_{slow} obtained from the plot of τ_{slow} *vs.* $\left(\kappa'_D\right)_{slow}$ (0.64 $\pm$ 0.02 ms^{-1}; Fig. 3.13B), the estimated γ_{slow} mainly represents the action of Ca^{2+} transporters on the volume-averaged $\Delta[Ca^{2+}]_i$.

Interestingly, even without a connecting axon (Fig. 3.14D; open circles), the relationship between the initial rate of decay and $\Delta[Ca^{2+}]_i$ still deviated slightly from linearity. This arose from the low apparent mobility of Ca^{2+} in the presence of only fixed endogenous buffers. The apparent diffusion coefficient of Ca^{2+} (D_{app}) was $\sim$ five-fold smaller in the absence of exogenous buffers than in their presence (14 *vs.* $60 - 75$ μm^{2}s^{-1}; data not shown; consistent with Allbritton *et al.*, 1992 and Gabso *et al.*, 1997). As a result of this, the Ca^{2+} gradient took longer to dissipate after an AP-evoked Ca^{2+} influx ($\sim$ 3 *vs.* < 1 ms; Eq. 3.23). Before spatial homogeneity was achieved, the activity of membrane pumps and intracellular uptake was non-linearly dependent on the volume-averaged $\Delta[Ca^{2+}]_i$, even though it was a linear function of the local $\Delta[Ca^{2+}]_i$.

A bi-exponential fit to the decay time course of the simulated Ca^{2+} transient, with the mean axon diameter, yielded a τ_{fast} of 6 ms and a τ_{slow} of 19 ms (black trace in Fig. 3.13A). The difference between these values and those estimated based on the single-compartment model (16 ± 2 and 38 ± 7 ms, respectively; Figs. 3.13B-C) was most likely a result of the non-linear relationship between the rate of decay by diffusion and $\Delta[Ca^{2+}]_i$. Regardless, both analyses suggest that, in an unperturbed synaptic bouton of layer 5 pyramidal neurons, $[Ca^{2+}]_i$ was rapidly removed and thus returned to the resting level within 100 ms following a single AP.

3.3.10 CPA, coupled with a train of APs, did not affect $\Delta[Ca^{2+}]_i$ amplitude

In synaptic boutons of cultured CA3 pyramidal neurons, blockade of CICR by either ryanodine or CPA (20 and 30 μM, respectively) reduced the amplitude of Ca^{2+} transients evoked by a single AP by 30% (Emptage *et al.*, 2001). These blockers interfere with intracellular Ca^{2+} release through different mechanisms: whilst a high concentration of ryanodine directly inhibits the RyR-dependent store release, prolonged application of the SERCA pump blocker CPA causes depletion of Ca^{2+} stores, which are thought to continuously leak Ca^{2+}. However, in this thesis, bath application of CPA for 10 min did not affect the amplitude of Ca^{2+} transients evoked by a single AP (Fig. 3.8).

One reason for the lack of effect of CPA on the amplitude of the measured Ca^{2+} transients could be the use of the relatively low affinity Ca^{2+} indicator OGB-6F. The contribution of CICR to AP-evoked Ca^{2+} transients described by Emptage *et al.* (2001) was measured with OGB-1, the Ca^{2+} binding affinity of which is about 25-fold higher than that of OGB-6F (Table 2.4). Therefore, the role of presynaptic Ca^{2+} stores in shaping AP-evoked Ca^{2+} transients was re-assessed with Cal-520 (200 μM), a BAPTA-based Ca^{2+} indicator with a K_d value in the range of $\Delta[Ca^{2+}]_i$ caused by a single AP (Table 2.4). Cal-520 was preferred to OGB-1 as the latter was significantly saturated following a single AP (see Section 3.3.3). In addition, with a higher signal-to-noise ratio and a larger dynamic range than OGB-1 (Tada *et al.*, 2014, and Table

2.4, respectively), Cal-520 was potentially more suitable to the measurement of small changes in the amplitude of Ca^{2+} transients.

Fig. 3.15A shows the experimental protocol for measuring the extent to which CICR contributed to Ca^{2+} transients evoked by a single AP. CPA (25 μM) was bath-applied for 10 min to prevent refilling of intracellular Ca^{2+} stores. Additionally, a train of 200 APs was evoked at 10 Hz at 8 min after CPA addition to promote store emptying. Control experiments in which CPA was not added were also performed to gauge the stability of the evoked Ca^{2+} transients. In some experiments, DMSO, which was used as the solvent for the CPA stock solution, was added to the superfusate to check if it affected the Ca^{2+} response. As the data from control experiments with and without DMSO were not different from each other (n = 7 *vs.* 6; $p_t \geq 0.13$), they were pooled.

Fig. 3.15B (left) displays Cal-520 fluorescence transients measured in a control experiment with DMSO application. In this synaptic bouton, addition of DMSO together with a train of 200 APs did not considerably affect the amplitude or decay time course of $^{\Delta F}/_{F_0}$ evoked by an AP. In contrast, in another bouton to which CPA was applied, the amplitude of $^{\Delta F}/_{F_0}$ was reduced and its decay time course prolonged (Fig. 3.15B, right). As $\left(^{\Delta F}/_{F_0}\right)_{max}$ of Cal-520 was not measured in these experiments, $\Delta[Ca^{2+}]_i$ was not be calculated from the corresponding $^{\Delta F}/_{F_0}$.

Figs. 3.15C-G summarise the effect of CPA, together with the 10 Hz train of APs, on the amplitude and decay kinetics of $^{\Delta F}/_{F_0}$ of Cal-520. In the set of control experiments (n = 13), the decay kinetics of the fluorescence transients never changed: 11 boutons (85%) had fluorescence transients that always decayed bi-exponentially ($p_F \leq 10^{-10}$), and the remaining two boutons had transients that always decayed mono-exponentially. In the set of experiments with CPA (n = 11), the decay time course of fluorescence transients measured in one bouton was bi-exponential before and mono-exponential after CPA addition. Except one with mono-exponential decay kinetics all throughout, the remaining nine boutons (82%) always had bi-exponential decay kinetics ($p_F \leq 10^{-9}$). As boutons with mono-exponential decays were excluded from Figs. 3.15D-F, the amplitude-weighted decay time constants

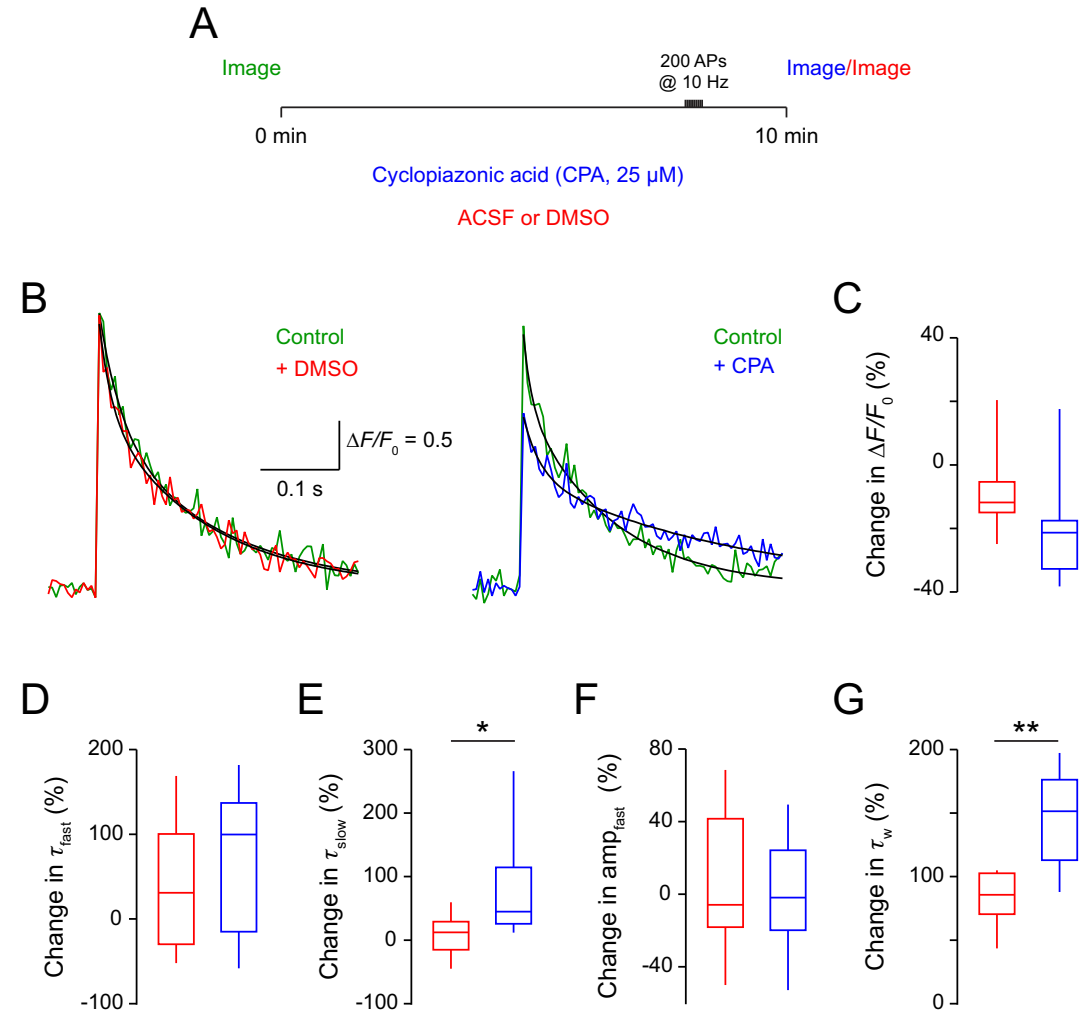

Figure 3.15: Addition of CPA together with a train of APs did not affect the amplitude of $^{\Delta F}/_{F_0}$ of Cal-520 following an AP. (A) Experimental protocol to assess the contribution of presynaptic Ca^{2+} stores to AP-evoked Ca^{2+} transients. (B) $^{\Delta F}/_{F_0}$ evoked by single APs in two different boutons before (green) and after 10 min of DMSO or CPA application (25 μM; red and blue, respectively). Each trace is an average of $3-4$ repeats, with decay time course fitted with the sum of two exponential functions (black curves). (C-G) The average change in peak amplitude, τ_{fast}, τ_{slow}, $\text{amplitude}_{\text{fast}}$, and τ_{w} in control experiments (red; n = 13) and after addition of CPA (blue; n = 11).

(τ_w) of all fluorescence transients were plotted in Fig. 3.15G so that the extent to which CPA affected the decay kinetics in all boutons could be assessed (for a mono-exponential decay, $\tau_w = \tau$).

On average, after 10 min of solution exchange (with or without DMSO, but no CPA), and a train of 200 APs at 10 Hz, the peak amplitude of $^{\Delta F}/_{F_0}$ evoked by an AP decreased by 9.5 $\pm$ 3.0%, from 2.2 $\pm$ 0.2 to 2.0 $\pm$ 0.2 (p_{pt} = 0.001), whilst its τ_{fast}, amplitude$_{fast}$, τ_{slow}, and τ_w were all unchanged ($p_{pt} \geq 0.3$). Addition of CPA increased τ_{slow} by 77 $\pm$ 27%, from 139 $\pm$ 12 to 230 $\pm$ 21 ms (p_{pt} = 0.004; control *vs.* CPA experiments: p_t= 0.04). τ_w was also increased by 81 $\pm$ 20%, from 82 $\pm$ 5 to 141 $\pm$ 11 ms (p_{pt} = 0.0002; control *vs.* CPA experiments: p_t= 0.003). However, although the peak amplitude of $^{\Delta F}/_{F_0}$ decreased after CPA addition (p_{pt} = 0.007; from 2.0 $\pm$ 0.3 to 1.6 $\pm$ 0.2), this reduction was not different from that observed in control experiments ($p_t = 0.2$). CPA also did not affect τ_{fast} and amplitude$_{fast}$ ($p_{pt} \geq 0.09$; control *vs.* CPA experiments: $p_t \geq 0.3$). These findings suggest several possibilities. First, presynaptic Ca^{2+} stores might have been insufficiently emptied. Second, the contribution of store release to Ca^{2+} transients evoked by single APs was relatively small (expected to be $\sim$ 10%; see Discussion) and might not be readily resolved by the experimental design and tools in this study.

It should be noted that, although the baseline fluorescence (F_0) of Cal-520 increased by 13 $\pm$ 5% after CPA application (p_{pt} = 0.03), this increase was not different from that seen in control experiments (12 $\pm$ 4%; p_t = 0.9). In another set of experiments, F_0 of OGB-1 (160 μM) was also unchanged after 10 min of CPA application (n = 6; p_{pt} = 0.4; data not shown). This is in contrast to studies in synaptic boutons of cultured CA3 pyramidal neurons and hippocampal mossy fibres, in which blockade of SERCA caused a significant increase in F_0 of OGB-1 (Emptage *et al.*, 2001; Scott and Rusakov, 2006).

3.3.11 $[Ca^{2+}]_i$ summed supralinearly during high-frequency stimulation

It remains controversial whether CICR contributes to the presynaptic Ca^{2+} dynamics following a single AP. Whilst blockade of intracellular Ca^{2+} release was found

to reduce $\Delta[Ca^{2+}]_i$ evoked by a single AP in synaptic boutons of cultured CA3 pyramidal neurons (Emptage *et al.*, 2001), it had no effect on the peak amplitude of $^{\Delta F}/_{F_0}$ evoked by a short extracellular stimulus in parallel fibre to Purkinje cell, hippocampal associational-commissural, mossy fibre, and Schaffer collateral synapses (Carter *et al.*, 2002). In fact, most studies that provide evidence for CICR in presynaptic terminals only measured the extent to which store release augmented $\Delta[Ca^{2+}]_i$ caused by repetitive stimulation ($\geq$ 4 brief stimuli evoked at $\geq$ 20 Hz; Llano *et al.*, 2000; Liang *et al.*, 2002; Scott and Rusakov, 2006). Thus, the build-up of $[Ca^{2+}]_i$ during trains of APs was characterised to find evidence for CICR in synaptic boutons of layer 5 pyramidal neurons.

Fig. 3.16A displays $\Delta[Ca^{2+}]_i$ in a bouton in response to a single AP, and 2 s long trains of APs evoked at $10 - 40$ Hz. In this set of experiments, the low affinity Ca^{2+} indicator OGB-6F (100 μM) was used to minimise dye saturation but still allow the calculation of $[Ca^{2+}]_i$. As the fluorescence of OGB-6F was sampled at 50 Hz during these AP trains, the peak amplitude of $\Delta[Ca^{2+}]_i$ associated with individual APs was not sampled. It can be seen that, during the AP trains at 10 and 20 Hz, a steady state was reached within 1 s of the first AP. During this state, $[Ca^{2+}]_i$ fluctuated around a plateau level (black lines), which was dependent on the AP frequency. In contrast, $[Ca^{2+}]_i$ in this bouton never reached a steady state during the 2 s long trains of APs at 30 and 40 Hz, but kept increasing with the stimulus number.

Fig. 3.16B shows the average intracellular Ca^{2+} elevations pooled from 10 different boutons. Consistent with previous observations, the average Ca^{2+} transient evoked by a single AP decayed bi-exponentially ($p_F = 9 \times 10^{-8}$; $\tau_{fast} = 6 \pm 1$ ms; $\tau_{slow} = 58 \pm 3$ ms; $amplitude_{fast} = 50 \pm 7\%$). Similarly, the decay kinetics of all Ca^{2+} elevations evoked by repetitive stimulation, except those at 12.5 and 40 Hz ($p_F \geq 0.06$; $\tau =$ 122 and 113 ms, respectively), were bi-exponential ($p_F \leq 0.03$; τ_{fast} from 40 to 110 ms; τ_{slow} from 350 to 860 ms; $amplitude_{fast}$ from 72% to 91%). However, the decay time course after the AP trains was longer than that in response to a single AP (Fig. 3.16C; coloured *vs.* black, respectively). This could have been caused by a number of factors, including the longer sampling interval (20 *vs.* 1.5 ms, respectively), a

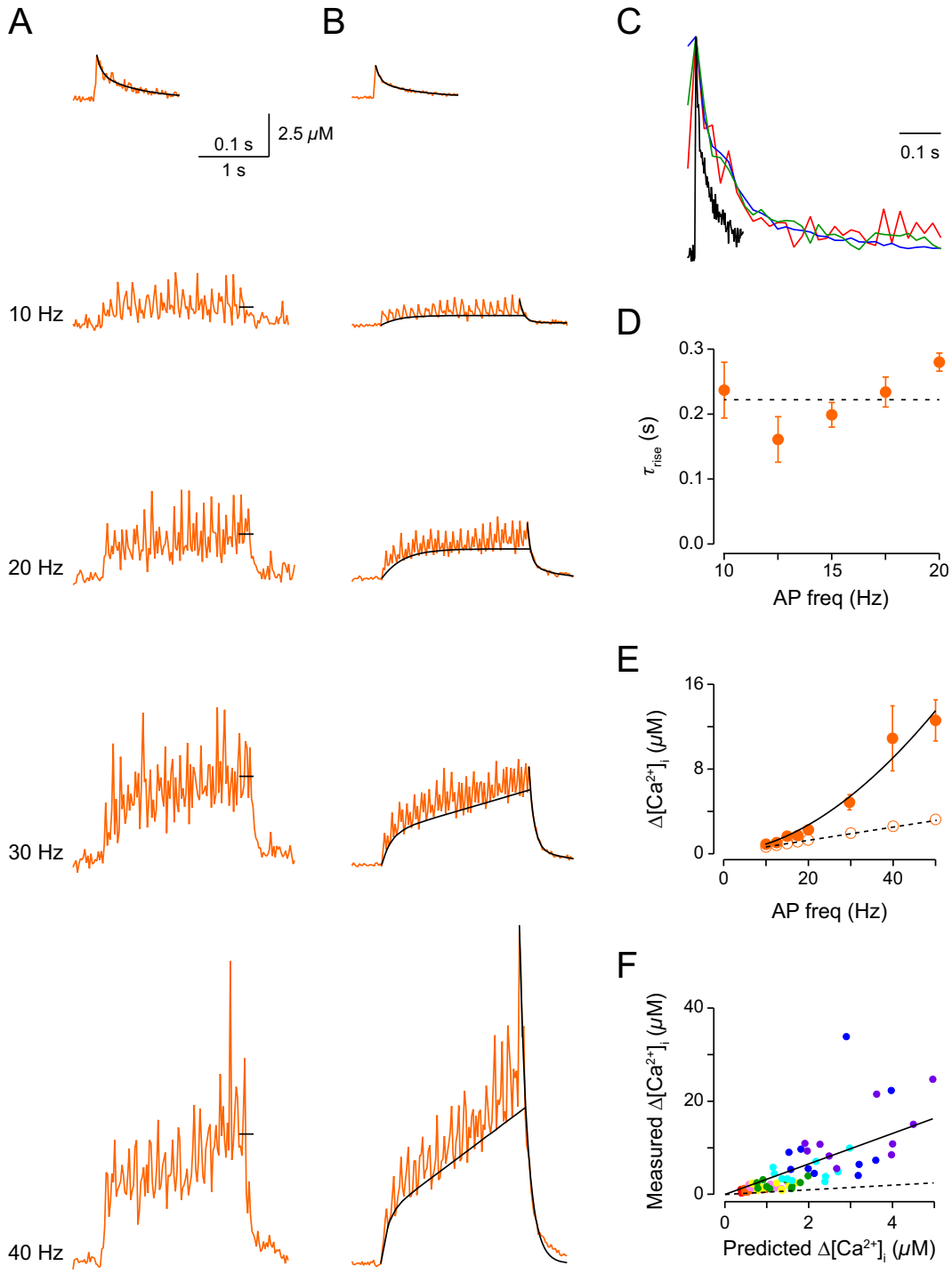

(See next page for figure legend)

Figure 3.16: Summation of $[Ca^{2+}]_i$ during 2 s long trains of APs. (A) $\Delta[Ca^{2+}]_i$ in a synaptic bouton in response to a single AP, and a train of APs evoked at $10 - 40$ Hz. Each trace is an average of $2 - 3$ repeats, measured with OGB-6F (100 μM). The decay of the Ca^{2+} transient evoked by an AP was fitted with the sum of two exponential functions. Black lines indicate the average $[Ca^{2+}]_i$ during the last 200 ms of stimulation. (B) The average $\Delta[Ca^{2+}]_i$ from 10 boutons. Each decay time course was fitted with the sum of two exponential functions (1 AP, and $10 - 30$ Hz), or a single exponential function (40 Hz). The lower envelope of $\Delta[Ca^{2+}]_i$ during AP trains was fitted with an exponential function ($10 - 20$ Hz) or the sum of an exponential function and a linear function ($30 - 40$ Hz). (C) Overlay of the decay time courses of the average Ca^{2+} elevations in response to a single AP (black), or a 2 s long train evoked at 10 (red), 20 (green), or 40 Hz (blue). Traces were aligned at the time of the last AP, with peak amplitudes scaled to the same value. (D) τ_{rise} plotted against AP frequency. Dashed line represents the average τ_{rise}. (E) The average $\Delta[Ca^{2+}]_i$ during the last 200 ms of stimulation (filled circles), and the predicted $\Delta[Ca^{2+}]_i$ calculated based on Eq. 3.31 (open circles), plotted against AP frequency. Plots were fitted with either a power function (solid) or a regression line (dashed). (F) The average $\Delta[Ca^{2+}]_i$ during the last 200 ms of stimulation, plotted against the predicted values. This plot was fitted with a linear function (solid), constrained to go through (0,0). Each colour indicates a different AP frequency: 10 (red), 12.5 (orange), 15 (pink), 17.5 (yellow), 20 (green), 30 (light blue), 40 (dark blue), and 50 Hz (purple). Dashed line represents the line of identity.

reduction in the rate at which Ca^{2+} diffused into the axons (due to decreased spatial gradients during repetitive stimulation), saturation of Ca^{2+} transporters, and/or CICR. Nonetheless, the decay time course after the AP trains was independent of the stimulation frequency ($p_{Pr} \geq 0.11$).

To assess whether a steady state level was reached during the 2 s long trains of APs, the lower envelope of the average intracellular Ca^{2+} elevations was fitted with either an exponential function or the sum of an exponential function and a linear function. A nested model comparison between these two fits showed that the former was satisfactory for AP trains between 10 and 20 Hz ($p_F \geq 0.3$), but was rejectable for AP trains at 30, 40, and 50 Hz ($p_F \leq 0.03$). Fig. 3.16D demonstrates that, during the AP trains at $10 - 20$ Hz, the time constant of the intracellular Ca^{2+} rise (τ_{rise}) was independent of the AP frequency ($p_{Pr} = 0.3$). The average value of τ_{rise} was 220 ± 20 ms (dashed line), significantly larger than τ_{slow} of the average single AP-evoked Ca^{2+} transient (58 ± 3 ms; $p_t < 10^{-4}$). In contrast, for the AP trains above 20 Hz, the slope of the linear fit to the late rising phase appeared dependent on the stimulation frequency. More specifically, the slope at 40 Hz was ~ 2.5-fold larger than that at 30

Hz (3.18 $\pm$ 0.04 *vs.* 1.28 $\pm$ 0.03 μM/s), although it was not different from that at 50 Hz (3.16 $\pm$ 0.04 μM/s; p_t = 0.7; data not shown). These results indicate that, during 2 s long trains of APs at frequencies $\leq$ 20 Hz, the rate of Ca^{2+} sequestration was able to match that of Ca^{2+} influx, allowing $[Ca^{2+}]_i$ to reach a steady state after $\sim$ 500 ms. However, at frequencies above 20 Hz, $[Ca^{2+}]_i$ was never removed at a rate as fast as that of Ca^{2+} influx (and CICR), causing it to continuously rise with subsequent APs.

In Fig. 3.16E, the average $\Delta[Ca^{2+}]_i$ during the last 200 ms of stimulation was plotted as a function of AP frequency (filled circles; black lines in Fig. 3.16A). To assess whether $[Ca^{2+}]_i$ summed linearly, the values of $\Delta[Ca^{2+}]_i$ produced by linear superposition of single AP-evoked transients were also plotted (open circles; Eq. 3.31). The fact that all the measured values of $\Delta[Ca^{2+}]_i$, particularly at frequencies above 20 Hz, were larger than the predicted values indicates supralinear summation of $[Ca^{2+}]_i$ during repetitive stimulation.

To further evaluate the degree of linearity of summation, for each bouton imaged, the average values of $\Delta[Ca^{2+}]_i$ during the last 200 ms of stimulation were plotted against the predicted values (Fig. 3.16F); here, each colour indicates a different stimulation frequency. Consistent with the continuous rise in $[Ca^{2+}]_i$ during high-frequency AP trains, a linear fit to this plot was significantly different from the line of identity ($p_{ANCOVA} < 10^{-5}$; solid *vs.* dashed line, respectively). This emphasises that $[Ca^{2+}]_i$ summed supralinearly during repetitive stimulation, potentially even at frequencies below 20 Hz. Such a build-up of Ca^{2+} could not have arisen from buffer saturation as Ca^{2+} buffers do not determine the steady-state or average $\Delta[Ca^{2+}]_i$ during a long train of APs (Tank *et al.*, 1995 and see Section 3.2.7.2). Instead, the underlying mechanism might have been facilitation of presynaptic Ca^{2+} currents, activation of CICR, and/or saturation of Ca^{2+} sequestration.

3.3.12 Ca^{2+} current facilitation could not explain supralinear summation

At neocortical excitatory synapses, Ca^{2+} influx through N- and P/Q-type Ca^{2+} channels provides the main source of Ca^{2+} for evoked transmitter release (Iwasaki

et al., 2000; Koester and Sakmann, 2000; Millan *et al.*, 2003; Ali and Nelson, 2006). It has been shown, at the calyx of Held, that P/Q-type Ca^{2+} currents undergo facilitation when activated repetitively at a frequency higher than 10 Hz (Cuttle *et al.*, 1998). To investigate whether the supralinear summation of $[Ca^{2+}]_i$ arose from facilitation of presynaptic Ca^{2+} influx, $\Delta[Ca^{2+}]_i$ associated with individual APs during a 40 Hz train was measured. In this set of experiments, the low-affinity Ca^{2+} indicator OGB-5N (200 μM; $K_d \sim 30$ μM, preliminary experiment - data not shown) was used to avoid saturation of exogenous Ca^{2+} buffers, which would also affect $\Delta[Ca^{2+}]_i$ *per* AP. As its K_d value is about three-fold larger than the average $\Delta[Ca^{2+}]_i$ during the last 200 ms of the 40 Hz train (11 $\pm$ 3 μM; Fig. 3.16E), OGB-5N would not be significantly saturated. However, as $[Ca^{2+}]_i$ in synaptic boutons could not be raised to a level sufficient for measurement of $(\Delta F/F_0)_{max}$ of OGB-5N (> 100 μM), $\Delta[Ca^{2+}]_i$ could not be calculated from the corresponding $\Delta F/F_0$.

Fig. 3.17A displays $\Delta F/F_0$ of OGB-5N measured in a synaptic bouton in response to a 2 s long train of APs at 40 Hz. To measure the amplitude of $\Delta F/F_0$ associated with individual APs, the fluorescence of OGB-5N was sampled every 5 ms. Similar to Ca^{2+} transients measured with other fluorescent Ca^{2+} indicators, the decay time course of OGB-5N fluorescence transients following the AP train was bi-exponential (p_F = 0.01; $\tau_{fast} = 45 \pm 14$ ms; $\tau_{slow} = 286 \pm 104$ ms; $amplitude_{fast}$ = 63 $\pm$ 9%). It can be seen, in this bouton, that the change in $\Delta F/F_0$ associated with individual APs was largely constant throughout the AP train. However, the lower envelope of the fluorescence measurement (black curve) rose continuously and never reached a steady state. In Fig. 3.17B, the rate at which $\Delta F/F_0$ decayed following each AP was plotted against the corresponding peak amplitude; the former was calculated from the difference between each peak and the following trough (20 ms interval). Despite the continuous rise in $[Ca^{2+}]_i$, the rate of decay remained linearly dependent on $\Delta[Ca^{2+}]_i$ (p_{Pr} = 0.0005).

Similar features are apparent in Fig. 3.17C, which shows the average $\Delta F/F_0$ of OGB-5N measured in seven different boutons. To assess whether a steady state level was reached, the lower envelope of the average $\Delta F/F_0$ was fitted with either an exponential

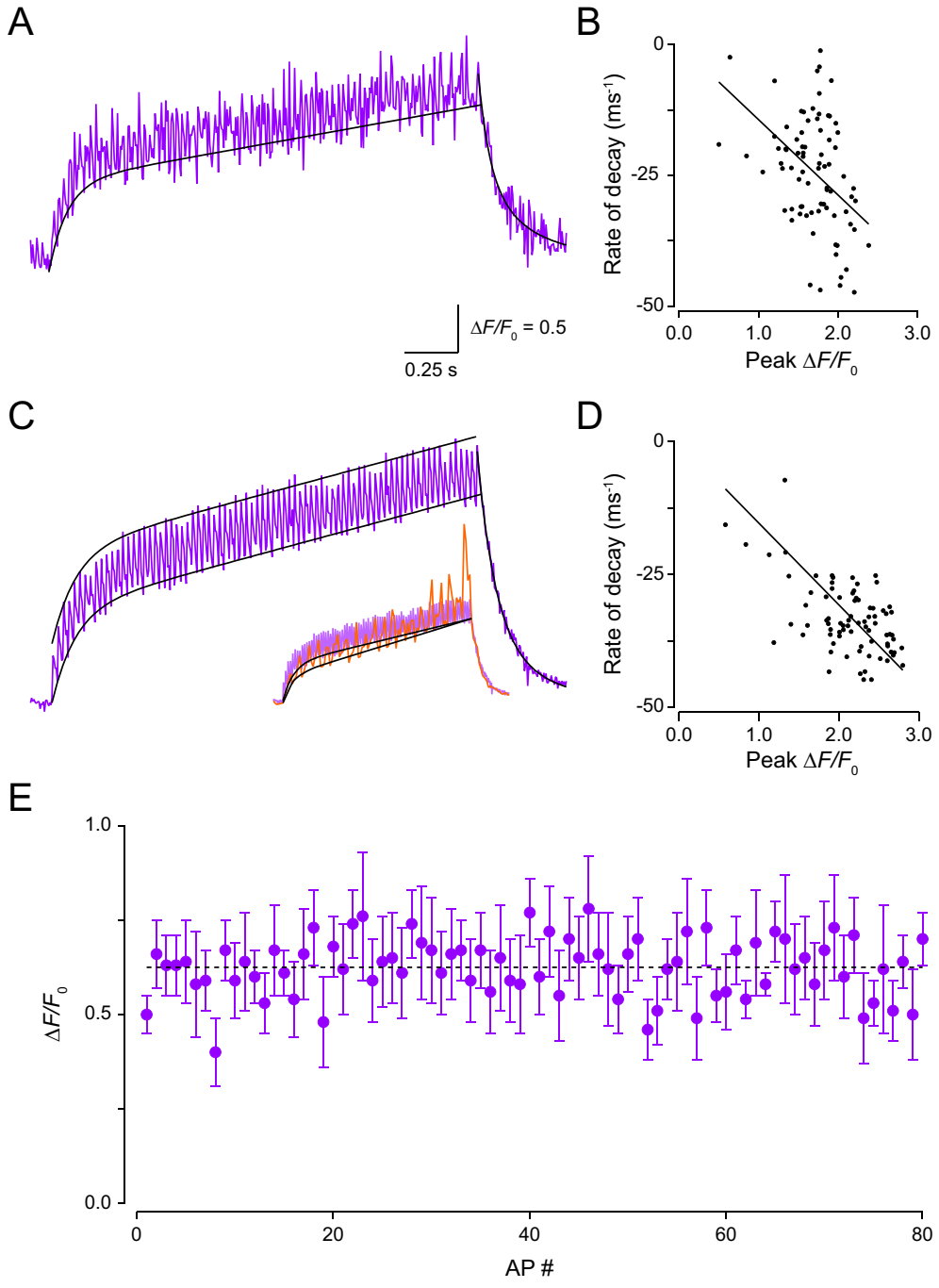

(See next page for figure legend)

Figure 3.17: Continuous rise in $[Ca^{2+}]_i$ during repetitive stimulation was not caused by facilitation of presynaptic Ca^{2+} currents. (A) $\Delta F/F_0$ of OGB-5N (200 μM) measured in a synaptic bouton in response to a 2 s long train of APs evoked at 40 Hz (2 repeats). (B) The rate of decay of $\Delta F/F_0$ following each AP, plotted against the corresponding peak amplitude, for the bouton illustrated in A. (C) The average $\Delta F/F_0$ of OGB-5N pooled from 7 boutons. Inset: The average $\Delta F/F_0$ of OGB-5N was overlaid with the corresponding average $\Delta[Ca^{2+}]_i$ from Fig. 3.16B. Traces were scaled by the peak amplitudes of their lower envelopes. (D) Same as B but with values calculated from the average trace in C. (E) The average $\Delta F/F_0$ *per* AP, plotted against the AP number. The decay time courses in A and C were fitted with the sum of two exponential functions, and the lower envelopes with the sum of an exponential function and a linear function. The upper envelope in C was calculated from the fit to the lower envelope and the average $\Delta F/F_0$ *per* AP (dashed line in E). In B and D, plots were fitted with a linear regression, constrained to go through (0,0).

function (not shown) or the sum of an exponential function and a linear function (lower black curve). A nested model comparison between these two fits showed that the former was rejectable ($p_F = 5 \times 10^{-13}$), consistent with the corresponding Ca^{2+} elevation measured with OGB-6F (inset). Despite this, each AP produced a constant change in $\Delta F/F_0$ ($p_{Pr} = 0.96$; Fig. 3.17E). The average value of $\Delta F/F_0$ *per* AP was 0.63 $\pm$ 0.01 (dashed line). Adding this value to the fit of the lower envelope produced a perfect fit to the upper envelope of the average $\Delta F/F_0$ in Fig. 3.17C (upper black curve; $p_{\chi^2} = 1$).

Together, these findings suggest that the supralinear summation of $[Ca^{2+}]_i$ during high-frequency stimulation did not arise from facilitation of presynaptic Ca^{2+} currents. Instead, it might have been a result of saturation of Ca^{2+} sequestration and/or activation of CICR. However, in all but one bouton imaged, the rate at which $\Delta F/F_0$ decayed following each AP was linearly dependent on the peak amplitude (Fig. 3.17D; $p_{Pr} \leq 0.006$). This indicates that, during the 40 Hz AP train, the rate of Ca^{2+} sequestration did not significantly saturate.

3.3.13 Blockade of SERCA attenuated supralinear summation

To determine whether the supralinear summation of $[Ca^{2+}]_i$ arose from saturation of Ca^{2+} sequestration, the build-up of $[Ca^{2+}]_i$ during AP trains was measured

when SERCA pumps were blocked with CPA. It was hypothesised that, if a Ca^{2+} sequestration mechanism was saturated, a reduction in the rate of sequestration through blockade of SERCA would put further strain on this mechanism, causing it to become saturated at lower stimulation frequencies. As a result, $[Ca^{2+}]_i$ would sum even more supralinearly.

Fig. 3.18A displays $\Delta[Ca^{2+}]_i$ in a synaptic bouton in response to a single AP, and 2 s long trains of APs evoked at $10-40$ Hz, before and after application of CPA (25 μM; bath-applied for 10 min; red and blue, respectively). To minimise laser exposure, fluorescence of OGB-6F (100 μM) was sampled at 100 ms intervals during the AP trains. Although the peak amplitudes of $\Delta[Ca^{2+}]_i$ associated with individual APs could not be resolved, the low sampling frequency was sufficient for characterising the build-up of $[Ca^{2+}]_i$ during repetitive stimulation. Consistent with previous experiments, in this bouton, CPA did not considerably affect the peak amplitude and fast decay component of the Ca^{2+} transient evoked by a single AP, but prolonged its τ_{slow} by 96%, from 57 to 112 ms. As a result, the time integral ($A_1\tau_1 + A_2\tau_2$) of this Ca^{2+} transient increased by 38%, from 106 to 147 μM·ms. Due to the prolonged decay time course and increased time integral of the single AP-evoked transient, it was expected that, during repetitive stimulation, $[Ca^{2+}]_i$ would build up to a level

Figure 3.18: Blockade of SERCA pump reduced supralinear summation of $[Ca^{2+}]_i$ during repetitive stimulation. (A) $\Delta[Ca^{2+}]_i$ in a synaptic bouton in response to an AP, and 2 s long trains of APs at $10-40$ Hz before and after addition of CPA (25 μM; red and blue, respectively). Each trace is an average of $2-3$ repeats, measured with OGB-6F (100 μM). The decay time course of the Ca^{2+} transients evoked by an AP was fitted with the sum of two exponential functions. (B) The average change in peak amplitude, τ_{slow}, τ_w, and $\sum A_i\tau_i$ of a single AP-evoked Ca^{2+} transient after addition of CPA (n = 9). (C) The average $\Delta[Ca^{2+}]_i$ during the last 500 ms of stimulation (filled circles), and the predicted $\Delta[Ca^{2+}]_i$ calculated based on Eq. 3.31 (open circles), plotted against AP frequency. Plots were fitted with either a power function (solid) or linear regression (dashed). (D) The averaged $\Delta[Ca^{2+}]_i$ during the last 500 ms of stimulation, plotted against the predicted values. (E) The averaged, normalised $\Delta[Ca^{2+}]_i$ at 40 Hz measured in CPA plotted against that measured before CPA addition. In D-E, plots were fitted with a linear regression constrained to go through (0,0). Black dashed lines represent the line of identity.

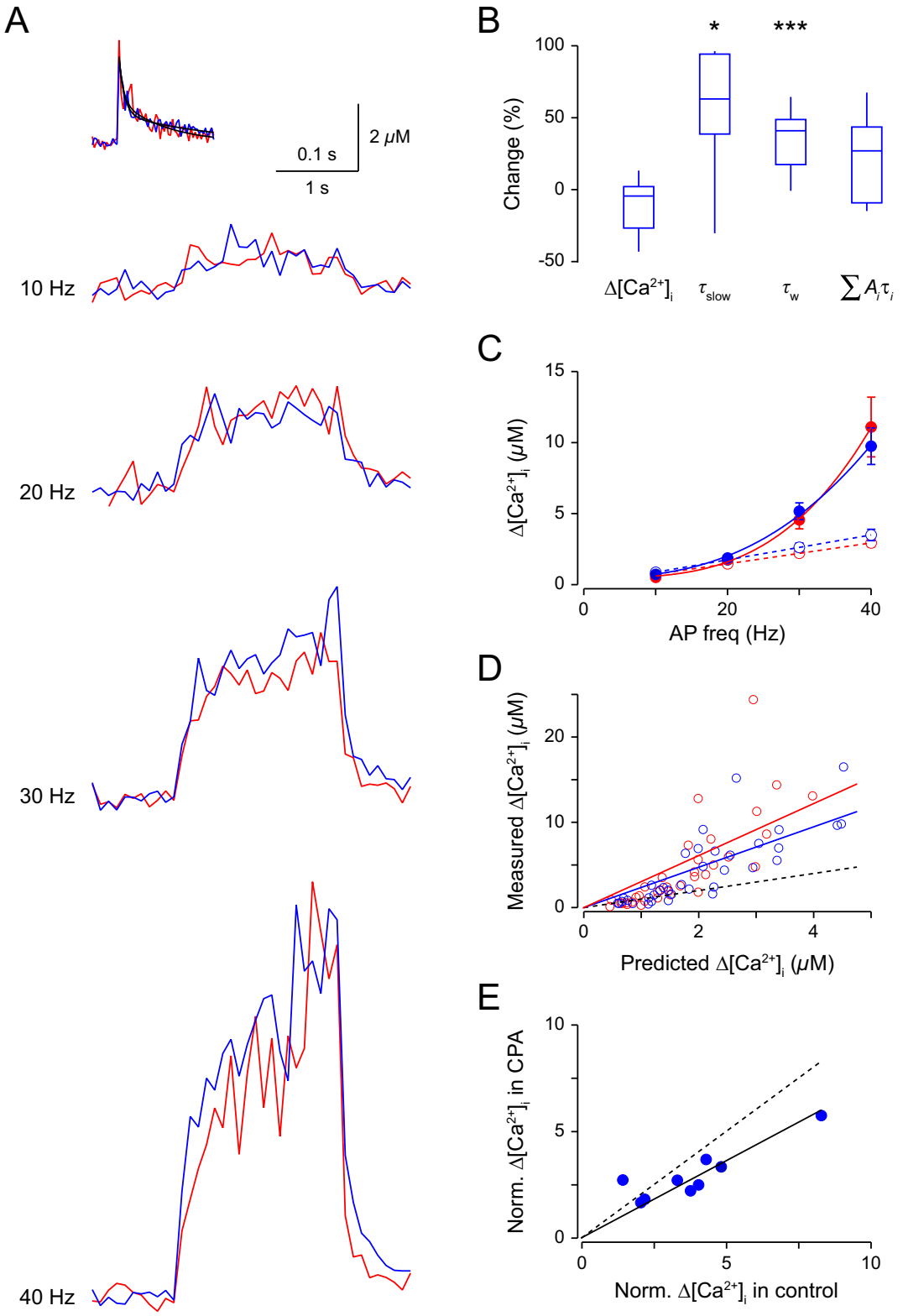

(See previous page for figure legend)

higher than that during the control condition. However, $\Delta[Ca^{2+}]_i$ evoked by the $10 - 40$ Hz AP trains did not increase after addition of CPA.

Fig. 3.18B summarises the effect of CPA on the amplitude and decay kinetics of single AP-evoked Ca^{2+} transients in 9 different boutons. Seven of them (78%) had Ca^{2+} transients that always decayed bi-exponentially ($p_F \leq 10^{-5}$). The decay time course of Ca^{2+} transients measured in the remaining two boutons was bi-exponential in the control condition, but became mono-exponential after CPA addition. The decay kinetics of these boutons were thus excluded in the average change in τ_{slow}, but included in the average change in τ_w shown in Fig. 3.18B. On average, CPA did not affect the peak amplitude of the Ca^{2+} transients (p_{pt} = 0.15; 2.3 $\pm$ 0.2 *vs.* 2.1 $\pm$ 0.2 μM). It also did not affect amplitude$_{fast}$ or τ_{fast} ($p_{pt} \geq 0.4$; 54 $\pm$ 5 *vs.* 58 $\pm$ 4%, and 8 $\pm$ 2 *vs.* 8 $\pm$ 1 ms, respectively; data not shown). However, after addition of CPA, τ_{slow} and τ_w increased by 58 $\pm$ 17 and 35 $\pm$ 7%, respectively ($p_{pt} \leq 0.03$; from 63 $\pm$ 6 to 94 $\pm$ 7 ms, and 32 $\pm$ 1 to 43 $\pm$ 2 ms). Despite this, the time integral of the single AP-evoked Ca^{2+} transient ($\sum A_i \tau_i$) did not significantly increase (p_{pt} = 0.08; 74 $\pm$ 7 *vs.* 88 $\pm$ 10 μM·ms).

Fig. 3.18C summarises the effect of CPA on the build-up of $[Ca^{2+}]_i$ during the 2 s long trains of APs. In this figure, the average values of $\Delta[Ca^{2+}]_i$ during the last 500 ms of stimulation, before and after addition of CPA, were plotted as a function of AP frequency (filled circles). The values of $\Delta[Ca^{2+}]_i$ produced by a linear superposition of single AP-evoked transients were also plotted (open circles). It can be seen that, despite blockade of SERCA, $[Ca^{2+}]_i$ did not build up to a level higher than that during the control condition. This suggests that the continuous rise in $[Ca^{2+}]_i$ was unlikely to arise from significant saturation of a Ca^{2+} sequestration mechanism.

To assess the extent of summation after CPA application, for each bouton imaged, the average values of $\Delta[Ca^{2+}]_i$ during the last 500 ms of stimulation were plotted against the predicted values (Fig. 3.18D). Consistent with previous experiments, most of the values measured in the control condition lied above the line of identity ($p_{ANCOVA} < 10^{-5}$), indicating supralinear summation of $[Ca^{2+}]_i$. Summation was

also supralinear in the presence of CPA ($p_{\mathrm{ANCOVA}} < 10^{-5}$). However, the extent of "supra-linearity" was not increased after its addition ($p_{\mathrm{ANCOVA}} = 0.06$), again arguing against significant saturation of Ca^{2+} sequestration.

Interestingly, in Fig. 3.18D, the average values of $\Delta[Ca^{2+}]_i$ measured in CPA appeared to lie closer to the line of identity than those measured in the control condition, particularly for $\Delta[Ca^{2+}]_i$ evoked by higher stimulation frequencies. To elucidate whether blockade of SERCA decreased the extent of summation during the 40 Hz train, the degree of supra-linearity of summation was calculated by normalising each measured value of $\Delta[Ca^{2+}]_i$ to its corresponding predicted value. In Fig. 3.18E, the degree of supra-linearity of summation in the presence of CPA is compared to that in the control condition; each data point represents an imaged bouton. A linear regression through the data points yielded a fit that was different from the line of identity ($p_{\mathrm{ANCOVA}} = 0.02$), indicating a reduction in the extent of summation by $28 \pm 2\%$. Together with the linear rate of Ca^{2+} decay (Figs. 3.17B and D), these findings suggest that the continuous rise in $[Ca^{2+}]_i$ during high-frequency stimulation was unlikely caused by significant saturation of Ca^{2+} sequestration. Instead, the fact that the build-up of $[Ca^{2+}]_i$ during the 40 Hz train decreased after blockade of SERCA implicates CICR as an underlying mechanism.

3.4 Discussion

In this study, factors underlying the presynaptic Ca^{2+} dynamics in layer 5 pyramidal neurons were characterised by measuring single AP-evoked Ca^{2+} transients with different concentrations of fluorescent indicators. A surprisingly low Ca^{2+} binding ratio of endogenous buffers was found, together with a large amount of Ca^{2+} ions entering the boutons in response to a single AP. However, there was no evidence to suggest that endogenous Ca^{2+} buffers were saturated. Based on experimental results and 3D reaction-diffusion models, it can be concluded that the initial fast decay of the measured Ca^{2+} transients was predominantly caused by diffusion of Ca^{2+} into

the connecting axon. Despite a high and linear rate of Ca^{2+} sequestration, $[Ca^{2+}]_i$ summed supralinearly during high-frequency trains of APs. Blockade of SERCA reduced the extent of summation, implicating a role of CICR.

3.4.1 $[Ca^{2+}]_{rest}$ of 50 nM

Based on the fluorescence intensity of OGB-1 before and after a 2 s long train of APs at 100 Hz, $[Ca^{2+}]_{rest}$ was found to be 53 ± 13 nM. The presence of exogenous buffers in the imaged boutons should not affect this measurement. This is because $[Ca^{2+}]_{rest}$ is established by passive Ca^{2+} fluxes and active sequestration mechanisms, all of which are unaffected by the extent of Ca^{2+} buffering (Neher, 1998). Consistent with this idea, Jackson and Redman (2003) found no correlation between $[Ca^{2+}]_{rest}$ and the concentration of OGB-1 present in synaptic boutons of granule cells in the dentate gyrus (DG).

The measured value of $[Ca^{2+}]_{rest}$ is in the range of that measured in the calyx of Held (39 ± 7 nM; Helmchen *et al.*, 1997), cerebellar MFBs (57 ± 7 nM; Delvendahl *et al.*, 2015), Purkinje cell dendrites and soma (47 ± 9 and 34 ± 3 nM, respectively; Llano *et al.*, 1994; but 95 ± 15 nM; Hashimoto *et al.*, 1996), and dendrites of CA1 pyramidal cells (53 ± 7 nM; Pohle and Bischofberger, 2014). However, it is considerably lower than $[Ca^{2+}]_{rest}$ in proximal boutons of DG granule cells (74 ± 9 nM; Jackson and Redman, 2003), hippocampal MFBs (116 ± 20 nM; Scott and Rusakov, 2006), neurohypophysial nerve endings (145 ± 22 nM; Stuenkel, 1994), and skeletal muscle fibres (106 ± 2 nM; Williams *et al.*, 1990). These values may reflect variability in the regulation of $[Ca^{2+}]_{rest}$ between different cells and cellular compartments, most likely due to differential expression of Ca^{2+} leak channels and transporters. However, some of their differences could have also been caused by the different experimental methods and assumptions, including those used to calibrate the fluorescent Ca^{2+} indicators (see Chapter 2 discussion).

In this study, $[Ca^{2+}]_{rest}$ was calculated based on the assumption that R_f of OGB-1 in the imaged boutons was 6, a value measured in cultured rat hippocampal

neurons and cerebellar MFBs (Maravall *et al.*, 2000; Delvendahl *et al.*, 2015). The fact that this value was almost two-fold smaller than that measured *in vitro* (Table 2.4; also see Maravall *et al.*, 2000) could be because of interactions between OGB-1 and intracellular constituents (Harkins *et al.*, 1993; O'Malley *et al.*, 1999). If such interactions were however weak and the lowered value of R_f measured *in situ* was caused by insufficient clamping of $[Ca^{2+}]_i$ to desired levels, then the calculated value of $[Ca^{2+}]_{rest}$ was an underestimate of the true value. An R_f value of 12.8, as measured *in vitro* (Table 2.4), would have yielded an almost two-fold larger value of $[Ca^{2+}]_{rest}$ (91 $\pm$ 15 nM).

It should be noted here that, although $[Ca^{2+}]_{rest}$ could not be precisely determined, the estimation of κ_E, γ, and unperturbed Ca^{2+} dynamics based on the single-compartment model was unlikely to be significantly affected. For a value of $[Ca^{2+}]_{rest}$ between 50 and 90 nM, the values of $\Delta[Ca^{2+}]_i$ as well as κ'_D calculated from the fluorescence intensity of OGB-6F changed by less than 1% (Eqs. 3.5 and 3.22, respectively). Larger deviations were obtained for the values of $\Delta[Ca^{2+}]_i$ and κ'_D calculated with OGB-1 fluorescence ($\leq$ 10 and 18%, respectively). However, κ_E, γ, $\Delta[Ca^{2+}]_T$, and $\Delta[Ca^{2+}]_{i,0}$ were estimated based on weighted linear fits, with weights inversely proportional to the respective standard errors (Figs. 3.7A-B). As a result, they were predominantly determined by values calculated from OGB-6F fluorescence. This made them, to some extent, insensitive to uncertainties in $[Ca^{2+}]_{rest}$.

3.4.2 A low κ_E and a large $\Delta[Ca^{2+}]_{i,0}$ associated with a single AP

The present results indicate that, in synaptic boutons of layer 5 pyramidal neurons, a single AP caused $[Ca^{2+}]_T$ to increase by $\sim$ 50 μM. However, due to the presence of endogenous fast buffers with a κ_E of 7 $\pm$ 2, the concentration of free Ca^{2+} or $[Ca^{2+}]_{i,0}$ increased by only 5.3 $\pm$ 1.3 μM.

3.4.2.1 Comparison with other presynaptic terminals

The value of κ_E in the imaged boutons is considerably smaller than many of those found in previous studies (Table 3.4). In contrast, the values of both $\Delta[Ca^{2+}]_T$ and $\Delta[Ca^{2+}]_{i,0}$ are larger than those previously estimated (but see Koester and Sakmann, 2000 and Ermolyuk *et al.*, 2013). These variations may reflect variability in the surface area to volume ratio, and the expression of Ca^{2+} channels and buffers, between different types of nerve terminals (Collin *et al.*, 2005a; Matthews *et al.*, 2013). Differences in channel density and buffer capacity have also been observed in synaptic boutons of the same type (Brenowitz and Regehr, 2007). As Ca^{2+} channels and buffers can influence both the local Ca^{2+} signal at transmitter release sites and the spatially homogeneous Ca^{2+} rise, differences in their expression are likely to contribute to the variable properties of synaptic transmission and short-term plasticity.

Differences in the experimental conditions and methods could also contribute to the large ranges of κ_E, $\Delta[Ca^{2+}]_T$, and $\Delta[Ca^{2+}]_{i,0}$. In particular, it was found that the estimated values of κ_E, $\Delta[Ca^{2+}]_T$, and $\Delta[Ca^{2+}]_{i,0}$ were highly sensitive to the K_d values of the Ca^{2+} indicators. When $\Delta[Ca^{2+}]_i$ was calculated with published values of K_d of OGB-1 and OGB-6F (200 nM and 3 μM, respectively; Maravall *et al.*, 2000; Brenowitz and Regehr, 2007), both of which were smaller than the measured values (300 nM and 8 μM), the resultant values of $\Delta[Ca^{2+}]_i$ in response to an AP were much reduced. Consequently, the values of $\left(\Delta[Ca^{2+}]_i\right)^{-1}$ and κ'_D were both increased, and the plot of $\left(\Delta[Ca^{2+}]_i\right)^{-1}$ *vs.* κ'_D was shifted to the left (open circles in Fig. 3.19A). A linear fit to this plot yielded an estimate of 24 $\pm$ 4 for κ_E, 29 $\pm$ 2 μM for $\Delta[Ca^{2+}]_T$, and 1.2 $\pm$ 0.1 μM for $\Delta[Ca^{2+}]_{i,0}$ (dashed line). These values were considerably different from those estimated using the measured K_d values, indicating that the inappropriate use of published K_d values could lead to an overestimation of κ_E and an underestimation of $\Delta[Ca^{2+}]_T$ and $\Delta[Ca^{2+}]_{i,0}$. Unless Ca^{2+} indicators are properly calibrated, a comparison of values of κ_E, $\Delta[Ca^{2+}]_T$, and $\Delta[Ca^{2+}]_{i,0}$ obtained by different research groups is likely misleading.

Table 3.4: Values of κ_E, $\Delta[Ca^{2+}]_{i,0}$, $\Delta[Ca^{2+}]_T$, and γ measured in axon terminals of different excitatory cells. All measurements were done in response to a single AP at $\sim$ 35 °C. PCs: pyramidal cells; GCs: granule cells. [c] calculated as the product of $(\kappa_E + 1)$ and $\Delta[Ca^{2+}]_{i,0}$.

Type of terminals	κ_E	$\Delta[Ca^{2+}]_{i,0}$ (μM)	$\Delta[Ca^{2+}]_T$ (μM)	γ (ms^{-1})	Reference
Layer 5 PCs	7 ± 2	5.3 ± 1.3	~ 50	0.60 ± 0.03	This study
Layer 2/3 PCs	140	$0.5 - 1.0$	$70 - 140^c$	2.6	Koester and Sakmann (2000)
Dentate gyrus GCs	20	1.0	30	0.5	Jackson and Redman (2003)
Cerebellar GCs	56 ± 12	0.5 ± 0.1	$15 - 45$		Brenowitz and Regehr (2007)
Cerebellar MFBs	17 $[-20, 70]$	0.2	4^c	0.3	Delvendahl *et al.* (2015)
Calyx of Held	$20 - 40$	$0.5 - 0.9$	$10 - 13$	0.9	Helmchen *et al.* (1997); Neher and Taschenberger (2013); Babai *et al.* (2014)

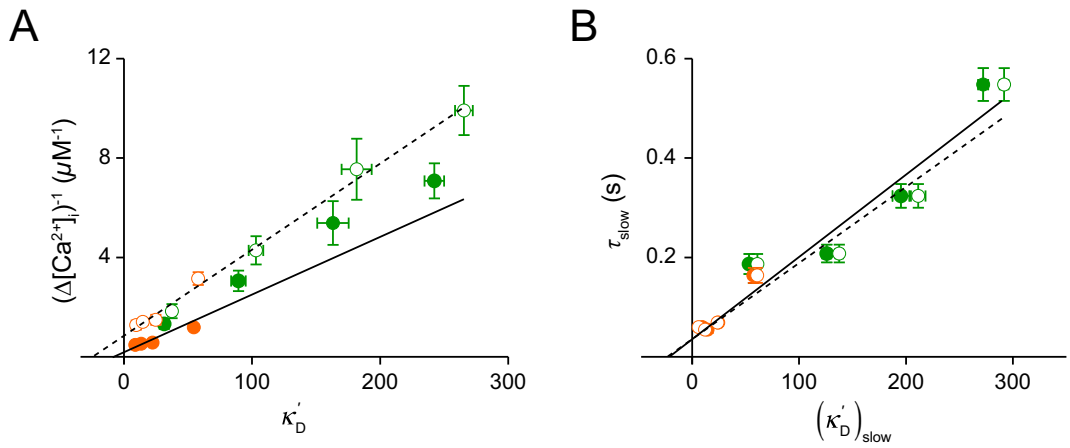

Figure 3.19: Estimation of κ_E, $\Delta[Ca^{2+}]_T$, γ, and unperturbed Ca^{2+} dynamics based on measured *vs.* published values of K_d of fluorescent Ca^{2+} indicators (filled *vs.* open circles, respectively) . (A) $\left(\Delta[Ca^{2+}]_i\right)^{-1}$ plotted against κ'_D. (B) τ_{slow} plotted against $\left(\kappa'_D\right)_{slow}$. Each plot was fitted with a weighted regression line.

In contrast, the estimated value of γ_{slow} was quite insensitive to the K_d values of the Ca^{2+} indicators. Fig. 3.19B compares the plots of τ_{slow} *vs.* $\left(\kappa'_D\right)_{slow}$ obtained from the measured and published values of K_d (filled and open circles, respectively). It can be seen that the values of τ_{slow}, primarily determined by the ratio between $\Delta F/F_0$ and $(\Delta F/F_0)_{max}$ (Eq. 3.5), were unaffected by the different values of K_d. On the contrary, the values of $\left(\kappa'_D\right)_{slow}$ calculated based on the published K_d values were larger, causing the plot of τ_{slow} *vs.* $\left(\kappa'_D\right)_{slow}$ to shift slightly to the right. A linear fit to this plot yielded an estimate of 0.65 ± 0.03 ms^{-1} for γ_{slow}, 23 ± 3 for κ_E, and 37 ± 4 ms for $\tau_{slow,0}$ (dashed line). These values are not significantly different from those estimated using the measured K_d values. Consistently, the value of γ_{slow} in the imaged boutons is in the range of that found in other presynaptic nerve terminals in the CNS (see Table 3.4).

It should be noted here that the low value of κ_E was unlikely due to significant "wash-out" of endogenous fast buffers. In a set of experiments in which κ_E was measured for individual boutons and within 60 min of break-in (in accordance with Helmchen *et al.*, 1996), it was found to range from -55 to 67, with a mean value of 8 ± 8 ($n = 14$; data not shown). Similar values of κ_E have been reported in individual

MFBs (Delvendahl *et al.*, 2015). This finding supports the low value of κ_E obtained from the population means (Fig. 3.7A) and argues against significant "wash-out" of endogenous fast buffers.

3.4.2.2 The number of Ca^{2+} channels activated during an AP

The present results allow a rough estimate of the number of Ca^{2+} channels that were activated in response to a single AP. With a value of $\Delta[Ca^{2+}]_T$ of ~ 50 μM, and assuming that the average volume of the imaged boutons was 0.36 μm^3 (Rollenhagen and Lübke, personal communication), a total of $\sim$ 10,000 Ca^{2+} ions entered these boutons. As there was no evidence for CICR following a single AP, the majority of these ions entered through VGCCs. To approximate the number of VGCCs that were open, their mean unitary current was assumed to be 0.3 pA (for an external $[Ca^{2+}]$ of 2 mM, a membrane potential of -30 mV at which the presynaptic Ca^{2+} current reaches its peak, and at 35 °C; Gollasch *et al.*, 1992; Borst and Sakmann, 1998a). With a mean opening time of 200 μs (Borst and Sakmann, 1998a), the opening of each VGCC let in $\sim$ 200 Ca^{2+} ions. Accordingly, a single AP activated $\sim$ 50 VGCCs in these synaptic boutons.

Although this value is only a rough estimate, it is in agreement with previous suggestions in synaptic boutons of layer 2/3 pyramidal neurons (40 channels with 5,500 ions; Koester and Sakmann, 2000), cultured hippocampal pyramidal cells (40 channels with 3,500 ions; Ermolyuk *et al.*, 2013), and cerebellar granule cells ($20-125$ channels with 6,000$-$19,000 ions; Brenowitz and Regehr, 2007). Even in larger presynaptic terminals with multiple release sites, a similar number of VGCCs has been proposed to open at each release site in response to a single AP (hippocampal MFBs: 20 channels with 10,000 ions *per* site, Bischofberger *et al.*, 2002; calyx of Held: 60 channels with 13,000 ions *per* site; Borst and Sakmann, 1996). However, not all of these channels necessarily contribute to synchronous transmitter release. A small fraction of them, especially R-type VGCCs, might be required to support asynchronous release, sustain transmitter release during repetitive stimulation, and

promote the induction of synaptic plasticity (Atluri and Regehr, 1998; Breustedt *et al.*, 2003; Li *et al.*, 2007b).

3.4.2.3 No evidence for saturation of endogenous buffers

A small value of κ_E may mean that endogenous Ca^{2+} buffers were saturated. However, there was no evidence to suggest that the spatially averaged Ca^{2+} rise in response to a single AP caused saturation of endogenous buffers. A larger rise in $[Ca^{2+}]_i$ during repetitive stimulation did not decrease τ_{fast} or increase $amplitude_{fast}$. In addition, during 2 s long trains of APs evoked at $10 - 20$ Hz, the time course of the intracellular Ca^{2+} rise (that is, τ_{rise}) was independent of the stimulation frequency. If endogenous buffers had been significantly saturated, more and more Ca^{2+} ions would have remained free after each AP, causing τ_{rise} to decrease with increasing AP frequencies. Nevertheless, the possibility that, within 100 nm of open VGCCs, endogenous Ca^{2+} buffers were saturated by the local $[Ca^{2+}]_i$ cannot be excluded.

When measured with OGB-6F, $\Delta[Ca^{2+}]_i$ *per* AP increased during a train of 10 APs evoked at 15 Hz. However, without a concurrent speed up in the decay kinetics, this increase was unlikely a result of buffer saturation. Instead, it could have been caused by facilitation of the presynaptic Ca^{2+} current (Cuttle *et al.*, 1998) or CICR (Llano *et al.*, 2000; Emptage *et al.*, 2001; Liang *et al.*, 2002; Scott and Rusakov, 2006). In support of this, a 2 s long AP train evoked at 15 Hz produced an increase in $[Ca^{2+}]_i$ that was slightly larger than expected with linear summation (Figs. 3.16E-F). The corresponding τ_{rise} was also longer than predicted. These two effects could not have arisen from buffer saturation. An increase in $\Delta[Ca^{2+}]_i$ *per* AP was not observed in the fluorescence transients of Fluo-4FF (Fig. 3.9E), likely because of the low affinity of this indicator for Ca^{2+}.

3.4.2.4 Candidates for endogenous fast buffers

It is unknown which Ca^{2+} binding protein(s) expressed in the imaged boutons gave rise to the measured value of κ_E. Based on the range of $\Delta[Ca^{2+}]_i$ observed in this

study, its K_d value was most likely larger than 5 μM, corresponding to a total concentration of more than 35 μM. Low-affinity buffers have also been suggested in the calyx of Held, synaptic boutons of cerebellar granule cells, and cerebellar MFBs (Habets and Borst, 2006; Brenowitz and Regehr, 2007; Delvendahl *et al.*, 2015). In adrenal chromaffin cells, Xu *et al.* (1997) reported a K_d value of ~ 100 μM by titrating endogenous buffers; a total concentration of 4 mM of such a low-affinity buffer would need to be present to produce a κ_E of 40 in these cells. However, many of the commonly known endogenous Ca^{2+} buffers, particularly parvalbumin, calbindin, and calretinin, have much smaller K_d values, ranging from 50 nM to less than 2 μM (Lee *et al.*, 2000b; Nagerl *et al.*, 2000; Faas *et al.*, 2007, 2011). In agreement with the absence of buffer saturation, none of these proteins are expressed in neocortical pyramidal neurons after the second postnatal week (Hof *et al.*, 1999). Low-affinity Ca^{2+} sensors such as calmodulin could potentially contribute to the measured κ_E value and modulate presynaptic Ca^{2+} dynamics, if they are expressed at sufficiently high concentrations (Faas *et al.*, 2011).

3.4.2.5 Endogenous buffers with slow Ca^{2+} binding kinetics?

A number of observations suggest the possible presence of a buffer with slow Ca^{2+} binding kinetics. These include the initial fast decay of AP-evoked Ca^{2+} transients and the discrepancy between the values of κ_E estimated from the plot of $\left(\Delta[Ca^{2+}]_i\right)^{-1}$ *vs.* κ'_D and that of τ_{slow} *vs.* $\left(\kappa'_D\right)_{slow}$ (7 ± 2 and 21 ± 3, respectively; Figs. 3.7A-B). If a buffer has not equilibrated with Ca^{2+} before a sequestration mechanism starts, it will appear to sequester Ca^{2+} and thus speed up the decay kinetics (Atluri and Regehr, 1998). Once an equilibrium is reached, $[Ca^{2+}]_i$ decays at a slower rate, determined by the activity of Ca^{2+} transporters and the total Ca^{2+} binding ratios. This produces not only bi-exponential decay kinetics, but also a larger Ca^{2+} binding ratio during the decay phase than at the peak of the Ca^{2+} transient. As a result, in the presence of a slow buffer, the value of κ_E estimated from the plot of τ_{slow} *vs.* $\left(\kappa'_D\right)_{slow}$ is larger than that estimated from the plot of $\left(\Delta[Ca^{2+}]_i\right)^{-1}$ *vs.* κ'_D (Lee *et al.*, 2000a,b). In addition, during 2 s long trains of APs evoked at $10 - 20$ Hz, the time it took $[Ca^{2+}]_i$ to reach

a steady state was longer than τ_{slow} of single AP-evoked transients. Such prolonged rise times are also indicative of a buffer that slowly equilibrates with Ca^{2+} (Lee *et al.*, 2000b).

Muller *et al.* (2007) provided convincing evidence that, at the calyx of Held, the bi-exponential decay time course of AP-evoked Ca^{2+} transients was caused by the presence of ~ 50 μM of the slow Ca^{2+} buffer parvalbumin. The intracellular Ca^{2+} rise, in response to a single AP, decayed with a τ_{fast} of 25 ± 7 ms, a value in the range of those measured in this thesis (Fig. 3.7C). However, expression of parvalbumin has not been observed in neocortical pyramidal neurons (Hof *et al.*, 1999). In support of this, intracellular Ca^{2+} elevations of more than 2 μM evoked by a train of APs still decayed bi-exponentially (Fig. 3.10). If the initial fast decay had been caused by parvalbumin, which binds Ca^{2+} with a very high affinity ($K_d \sim 50$ nM), it would have been significantly reduced or abolished after repetitive stimulation (Lee *et al.*, 2000b; but see Muller *et al.*, 2007). This, together with the finding that diffusion of Ca^{2+} into the axon could satisfactorily account for the initial fast decay and the different estimates of κ_E, argues against the presence of a significant concentration of a slow buffer. As the fast decay kinetics of fluorescence transients measured with OGB-1 did not change with equilibration time (Figs. 3.5E-F), the absence of a significant contribution of a slow buffer was unlikely due to it being "washed-out", as has been observed at the calyx of Held (Muller *et al.*, 2007). Accordingly, it can be concluded that the prolonged rise times during the 2 s long trains of APs at $10 - 20$ Hz were not caused by Ca^{2+} binding to a slow buffer. Instead, they could have arisen from CICR (discussed below).

3.4.3 Ca^{2+} sequestration

Following a single AP-evoked Ca^{2+} influx, Ca^{2+} in the imaged boutons was rapidly removed, not only by Ca^{2+} transporters but also by diffusion into the connecting axon collaterals. Addition of exogenous buffers, which competed with Ca^{2+} transporters for Ca^{2+} binding, reduced the effectiveness of the latter in sequestering

Ca^{2+}. This allowed a significant fraction of Ca^{2+} ions to escape into the axon, causing the rate of decay to deviate from a linear relationship with $\Delta[Ca^{2+}]_i$. In the absence of exogenous buffers, Ca^{2+} transporters were the main determinant of the decay kinetics, although diffusion of Ca^{2+} into the axon still caused the initial rate of decay be non-linearly dependent on $\Delta[Ca^{2+}]_i$. The rapid activity of Ca^{2+} transporters, with a rate constant of 0.60 ± 0.03 ms^{-1}, and the small κ_E allowed $[Ca^{2+}]_i$ to return to the resting level within 100 ms after a single AP.

3.4.3.1 Diffusion into the axon

This is the first study to demonstrate that diffusion of Ca^{2+} into the axon plays an important role in shaping the decay time course of AP-evoked Ca^{2+} transients in small *boutons en passant*. A similar role of diffusion has been shown for dendritic spines, in which the escape of Ca^{2+} through the spine neck contributes to Ca^{2+} clearance (Majewska *et al.*, 2000; Noguchi *et al.*, 2005). The effect of diffusion was most prominent in the presence of exogenous buffers, causing the initial rate of decay to be much faster than that determined solely by Ca^{2+} transporters. In support of this, blockade of SERCA with CPA increased τ_{slow}, but did not affect τ_{fast} or amplitude$_{fast}$ of single AP-evoked Ca^{2+} transients. The lack of effect of CPA on the initial decay phase could have resulted from a reduced Ca^{2+} binding ratio and/or activation of an additional transporter. However, as the peak amplitude of the Ca^{2+} transients remained unchanged, the total Ca^{2+} binding ratio did not decrease. In addition, an increase in $\Delta[Ca^{2+}]_i$ caused by repetitive stimulation did not speed up the initial decay kinetics. Therefore, it was unlikely that, after application of CPA, an additional sequestration mechanism became activated and counteracted the reduced rate of Ca^{2+} uptake into intracellular stores. Accordingly, in the presence of exogenous buffers, the initial fast decay of the presynaptic Ca^{2+} transients was largely caused by a factor different from the action of Ca^{2+} transporters. However, once $\Delta[Ca^{2+}]_i$ decayed to $\sim$ 50% of the peak amplitude, the rate of decay was predominantly determined by Ca^{2+} transport.

The role of diffusion was supported by a 3D reaction-diffusion model, in which the presence of a connecting axon ($0.1 - 0.4$ μm in diameter) caused the rate of decay of $[Ca^{2+}]_i$ to deviate from a linear relationship with $\Delta[Ca^{2+}]_i$. As its parameters were based on measurements acquired in this thesis or previous studies, this model provided realistic representations of the Ca^{2+} transients measured in response to a single AP. In fact, an analysis of the simulated transients based on the single-compartment model yielded results that were in the range of those obtained from the measurements. In this model, factors that could give rise to a multi-exponential decay time course were excluded, except for diffusion of Ca^{2+} into the axon. More specifically, a brief Ca^{2+} current was the only source of the intracellular Ca^{2+} rise, with no Ca^{2+} influx or release occurring during its decay phase. In addition, the endogenous Ca^{2+} buffer, which had a low affinity ($K_d = 100$ μM; Xu *et al.*, 1997) and a fast Ca^{2+} binding rate, was not saturated by the spatially averaged Ca^{2+} rise (peak amplitude ≤ 5 μM). The rate at which Ca^{2+} was extruded or taken up into intracellular stores was also linearly dependent on $\Delta[Ca^{2+}]_i$. Therefore, diffusion of Ca^{2+} into the axon was the only mechanism that could produce the initial fast decay of the simulated Ca^{2+} transients in the presence of exogenous buffers.

Two main reasons underlay the large contribution of diffusion to the initial rate of decay of the measured Ca^{2+} transients. The first was the small size of the imaged boutons, which allowed Ca^{2+} to escape into the axon shortly after an AP-evoked Ca^{2+} influx (≤ 3 ms after the AP onset). Due to the high spatial gradient of Ca^{2+} between the boutons and their connecting axons at this point in time, the rate of Ca^{2+} diffusion was large. This caused the initial rate of decay to be non-linearly dependent on $\Delta[Ca^{2+}]_i$ within the boutons.

The second reason for the clear effect of diffusion was the presence of exogenous buffers in the patch-clamp internal solution. Compared to their endogenous counterparts, exogenous buffers are highly mobile, with large diffusion coefficients ($D = 0 - 10$ *vs.* $100 - 220$ $\mu m^2 s^{-1}$, respectively; Table 3.3; Allbritton *et al.*, 1992; Zhou and Neher, 1993; Gabso *et al.*, 1997). Due to the small κ_E of endogenous buffers, even a small concentration of exogenous buffers, particularly those with a high affinity for

Ca^{2+}, would significantly increase the apparent mobility of Ca^{2+} and accelerate its diffusion out of the boutons. In addition, by increasing the total Ca^{2+} binding ratio, exogenous buffers reduced the effective rate of Ca^{2+} sequestration. This allowed more Ca^{2+} ions to elude Ca^{2+} transporters, operated within the boutons, and escape into the axon. As a result, immediately after an AP-evoked Ca^{2+} influx, diffusion accounted for $\sim 60\%$ of the total rate of Ca^{2+} clearance.

According to the 3D model, diffusion had only a small impact on the rate of decay of an unperturbed Ca^{2+} transient ($\sim 7\%$ of the initial rate). This was due to the presence of only fixed endogenous buffers and a much stronger effective rate of Ca^{2+} sequestration. Unfortunately, with the experimental methods used, this study could not identify whether the measured value of κ_E was accounted for by only fixed buffers, or a mixture of fixed and mobile buffers. Mobile buffers, if present, were unlikely to be completely "washed-out" due to the long distance between the patch pipette and the imaged boutons. Whether a mobile buffer speeds up the diffusion of Ca^{2+} depends on its diffusion coefficient (Matthews and Dietrich, 2015). A buffer with a D value smaller than D_{app} of Ca^{2+} in the presence of only fixed buffers (*i.e.* 14 $\mu m^2 s^{-1}$ in the simulations) would further restrict Ca^{2+} diffusion. Due to their large molecular weight, endogenous Ca^{2+} buffers are generally not as mobile as the exogenous buffers ($D = 12 - 43$ $\mu m^2 s^{-1}$; Schwaller, 2010). However, unless they interact with intracellular fixed proteins or the cytoskeleton, their diffusion coefficients are still slightly larger than D_{app} of Ca^{2+} in the presence of only fixed buffers. Therefore, they would increase the impact of diffusion. In addition, highly mobile Ca^{2+}-binding molecules, such as ATP and other nucleotide, would also accelerate the diffusion of Ca^{2+} and strengthen its role in shaping the Ca^{2+} dynamics in small *boutons en passant*.

To provide more direct evidence for the role of diffusion, future research could measure $[Ca^{2+}]_i$ along the connecting axon in response to an AP. If a significant amount of Ca^{2+} escapes a bouton into the axon, $[Ca^{2+}]_i$ in the axon and within $1 - 3$ μm of the bouton should increase after stimulation. An axonal Ca^{2+} rise that stems from diffusion of Ca^{2+} from the bouton should have a much slower rise time than

that caused by activation of VGCCs. In addition, soon after the AP, $[Ca^{2+}]_i$ along the axon should display a spatial gradient, with high concentrations closer to the bouton. However, the presence of nearby boutons may mask such a Ca^{2+} gradient, especially if Ca^{2+} sequestration occurs along the axon.

3.4.3.2 Contribution of SERCA

The finding that addition of CPA increased τ_{slow} of single AP-evoked Ca^{2+} transients suggests a role of SERCA in presynaptic Ca^{2+} clearance. As blockade of SERCA did not affect the peak amplitudes and therefore the total Ca^{2+} binding ratios, the relative contribution of SERCA can be estimated based on the change in τ_{slow} and the inverse relationship between τ_{slow} and γ_{slow} (Eq. 3.20). As diffusion of Ca^{2+} into the axon contributed minimally to late decay phase of the Ca^{2+} transients, γ_{slow} represents the pooled activity of all Ca^{2+} sequestration mechanisms. With τ_{slow} increased from 63 $\pm$ 5 to 93 $\pm$ 4 ms after CPA addition, and a γ_{slow} value of 0.60 $\pm$ 0.03 ms^{-1} in the control condition, the value of γ_{slow} with CPA present was 0.41 $\pm$ 0.04 ms^{-1}. Accordingly, the action of SERCA accounted for 32 $\pm$ 8% of the total Ca^{2+} sequestration, similar to that in synaptic boutons of CA3 pyramidal neurons (Emptage *et al.*, 2001) and hippocampal MFBs (Scott and Rusakov, 2006). However, as I did not investigate whether the application of CPA (25 μM) for 10 min fully abolished SERCA activity, this value might be an underestimate of the relative contribution of SERCA following a single AP-evoked Ca^{2+} influx.

3.4.3.3 No evidence for saturation of Ca^{2+} sequestration

Besides SERCA, the Na^+/Ca^{2+} exchanger, Na^+/Ca^{2+}-K^+ exchanger, and plasmalemmal Ca^{2+} ATPase were likely to account for most of the remaining 68 $\pm$ 7% of the total rate of Ca^{2+} sequestration, during the slow decay phase of a single AP-evoked Ca^{2+} transient. Although the activity of these transporters is half-maximal at $[Ca^{2+}]_i \leq 3$ μM (DiPolo and Beauge, 1979; Lytton *et al.*, 1992; Blaustein and Lederer,

1999; Pelled *et al.*, 2003), there was no evidence that the rate of Ca^{2+} sequestration approached a maximum value during high-frequency trains of APs. A 2 s long train evoked at 40 Hz elevated $[Ca^{2+}]_i$ to as high as 10 μM. Despite this, the rate of decay of individual AP-evoked Ca^{2+} transients was linearly dependent on the corresponding peak amplitude (Figs. 3.17B and D). This, together with the finding that blockade of SERCA did not enhance the supralinear build-up of $[Ca^{2+}]_i$, argues against significant saturation of Ca^{2+} sequestration.

Activation of the mitochondrial uniporter during repetitive stimulation might have prevented the rate of Ca^{2+} sequestration from reaching a plateau at high levels of $[Ca^{2+}]_i$. At the calyx of Held, Ca^{2+} uptake by mitochondria was activated in response to intracellular Ca^{2+} elevations ≥ 2.5 μM (Kim *et al.*, 2005). As a result, when $[Ca^{2+}]_i$ was increased to 4 μM, mitochondrial uptake accounted for $\sim 25\%$ of the total rate of Ca^{2+} clearance. Such a large contribution is quite surprising, as the mitochondrial uniporter has a very low affinity for Ca^{2+}. In fact, the rate of mitochondrial uptake is only half-maximal when $[Ca^{2+}]_i$ is ≥ 10 μM (Xu *et al.*, 1997; Colegrove *et al.*, 2000b). Due to the assumption of a constant κ_E in their study, Kim *et al.* (2005) might have overestimated the contribution of mitochondrial uptake. Despite this, the facts that mitochondria are a common feature of nerve terminals (Palay, 1956; Gray, 1959), including synaptic boutons of layer 5 pyramidal neurons (Rollenhagen and Lübke, personal communication), that they have a large capacity but low affinity for Ca^{2+} uptake (Xu *et al.*, 1997), and that they start sequestering a considerable amount of Ca^{2+} at $[Ca^{2+}]_i \geq 2.5$ μM (Kim *et al.*, 2005), support the finding that the rate of Ca^{2+} sequestration did not saturate during the 40 Hz AP train.

3.4.4 Supralinear summation during trains of APs

Despite the rapid rate of Ca^{2+} sequestration in response to a single AP-evoked Ca^{2+} influx, $[Ca^{2+}]_i$ never stopped rising during 2 s long trains of APs evoked at $30 - 50$ Hz. In the presence of 100 μM OGB-6F in the patch pipette, a single AP-evoked Ca^{2+} transient decayed with a τ_{slow} of ~ 60 ms. If $\Delta[Ca^{2+}]_T$ *per* AP remained constant

and the rate of Ca^{2+} sequestration was linearly dependent on $\Delta[Ca^{2+}]_i$, then $[Ca^{2+}]_i$ should have plateaued within 100 ms of the first AP, independent of the stimulation frequency. The fact that $[Ca^{2+}]_i$ did not reach a steady state suggests that, even though the rate of Ca^{2+} decay increased linearly with $\Delta[Ca^{2+}]_i$, it was never able to match the rate at which Ca^{2+} entered the cytosol. Therefore, $\Delta[Ca^{2+}]_T$ *per* AP was unlikely to remain constant during repetitive stimulation.

3.4.4.1 Role of CICR in supralinear summation

The finding that blockade of SERCA reduced the extent to which $[Ca^{2+}]_i$ summed during the 40 Hz AP train provides direct evidence that CICR contributes to the supralinear summation of $[Ca^{2+}]_i$. Due to a basal leak of Ca^{2+} from intracellular stores, prolonged inhibition of SERCA by CPA might have caused a small reduction in store $[Ca^{2+}]$ (Beck *et al.*, 2004; de Juan-Sanz *et al.*, 2017). As a consequence, less Ca^{2+} was released and thus accumulated in the boutons during the AP train. Admittedly, the supra-linearity of summation was only slightly reduced by CPA. However, it was unlikely that presynaptic Ca^{2+} stores were completely depleted after 10 min of bath application of CPA (discussed below). Therefore, CICR might have persisted and contributed to the remaining build-up of $[Ca^{2+}]_i$.

Intracellular Ca^{2+} release most likely arose from activation of RyRs. Although IP_3Rs could have been involved, their activation is typically inhibited by $[Ca^{2+}]_i$ above $1-10$ μM (Foskett *et al.*, 2007). Both ryanodine and IP_3 receptors have been found expressed in a range of presynaptic terminals, including those in the cerebellum, hippocampus, and neocortex (Sharp *et al.*, 1993; Padua *et al.*, 1996). As RyRs are activated by $[Ca^{2+}]_i$ as low as 100 nM (McPherson *et al.*, 1991; Xu *et al.*, 1996; Xu and Meissner, 1998), it is conceivable that a small amount of Ca^{2+} was also released during 2 s long trains of APs evoked at $10-20$ Hz, during which $[Ca^{2+}]_i$ was elevated to ≥ 1 μM. In support of this, the time it took $[Ca^{2+}]_i$ to reach steady states during these trains was longer than expected with a constant $\Delta[Ca^{2+}]_T$ *per* AP and a linear rate of Ca^{2+} sequestration.

A similar role of CICR has been reported in Purkinje cells (Llano *et al.*, 1994), in which activation of RyRs caused $\Delta[Ca^{2+}]_i$ to be supralinearly dependent on the Ca^{2+} current integral. Blockade of RyRs reduced the build-up of $[Ca^{2+}]_i$ during sustained membrane depolarisation, whereas stimulation of RyRs enhanced it (Llano *et al.*, 1994). Ca^{2+} release through RyRs has also been suggested in other presynaptic terminals, including hippocampal MFBs and cerebellar basket cell terminals (Llano *et al.*, 2000; Liang *et al.*, 2002; Scott and Rusakov, 2006).

Interestingly, de Juan-Sanz *et al.* (2017) suggested that, although the ER regulates presynaptic Ca^{2+} dynamics, it does so not by releasing Ca^{2+} but by modulating Ca^{2+} influx. By measuring the concentration of Ca^{2+} in ER stores ($[Ca^{2+}]_{ER}$) in synaptic boutons of cultured hippocampal neurons, they found no evidence for Ca^{2+} release from the ER in response to a single AP as well as a train of 20 APs evoked at 20 Hz. Following bath application of CPA, $[Ca^{2+}]_{ER}$ decreased with a time constant of 25 s, whereas the amplitude of $\Delta[Ca^{2+}]_i$ evoked by a single AP decreased with a time constant of 150 s. These findings led to the conclusion that the reduction in $\Delta[Ca^{2+}]_i$ was not a result of attenuated Ca^{2+} release, but caused by a decrease in Ca^{2+} influx. Upon depletion of ER stores, the ER Ca^{2+} sensor STIM1 formed clusters at synaptic boutons and presumably inhibited presynaptic VGCCs (de Juan-Sanz *et al.*, 2017). However, the idea that Ca^{2+} is not released from the presynaptic ER in response to stimulation is inconsistent with the finding that inhibition of ryanodine or IP_3 receptors reduced the amplitude of presynaptic Ca^{2+} transients and even affected transmitter release (Emptage *et al.*, 2001; Liang *et al.*, 2002; Galante and Marty, 2003; Scott and Rusakov, 2006; Cowan and Stricker, unpublished). Moreover, de Juan-Sanz *et al.* (2017) measured $[Ca^{2+}]_{ER}$ with a sampling interval of $50 - 100$ ms and with genetically encoded Ca^{2+} indicators, which have relatively slow Ca^{2+} binding kinetics (Chen *et al.*, 2013). Therefore, any brief and rapid release of Ca^{2+} that occurred within 10 ms of an AP might have remained undetected.

Lack of CICR in response to a single AP. Despite the contribution of CICR to the supralinear build-up of $[Ca^{2+}]_i$ during repetitive stimulation, there was no evidence

for its presence in response to a single AP. Blockade of SERCA did not reduce the peak amplitude of $\Delta[Ca^{2+}]_i$ evoked by single APs, even when store emptying was promoted with a 20 s long AP train. This may appear contradictory to the finding that, in connected pairs of layer 2 pyramidal neurons, bath application of CPA, together with membrane depolarisation, reduced the amplitude of EPSCs by $\sim$ 30% (Choy, 2011). The same effect was also seen in connected pairs of layer 5 pyramidal neurons (Cowan and Stricker, unpublished). However, assuming a fourth power relationship between $\Delta[Ca^{2+}]_i$ and transmitter release (Dodge and Rahamimoff, 1967), a 30% reduction in EPSC amplitudes corresponds to a decrease in $\Delta[Ca^{2+}]_i$ of only 9%. Such a small change might not be readily detectable by the experimental design and tools used in this study.

Kinetics and regulation of CICR. The kinetics of CICR and its dependence on the stimulation frequency remain to be carefully studied. However, because the decay kinetics of $\Delta[Ca^{2+}]_i$ did not slow down with increasing frequencies (Fig. 3.16C), it can be inferred that intracellular Ca^{2+} release did not significantly outlast the AP trains. This is consistent with the finding that Ca^{2+} release from cardiac sarcoplasmic reticulum vesicles was brief, with a rate as high as 100 s^{-1} (Sanchez *et al.*, 2003). In addition, as the linear rise of $\Delta[Ca^{2+}]_i$ at 50 Hz was not different from that at 40 Hz, the magnitude of intracellular Ca^{2+} release was unlikely to increase significantly at frequencies above 40 Hz. In support of this, it was found that the open probability of RyRs increased steeply as $[Ca^{2+}]_i$ rose from 1 to 10 μM, but remained constant at $[Ca^{2+}]_i$ above $\sim$ 20 μM (Xu *et al.*, 1996). As the 2 s long AP train at 40 Hz increased $[Ca^{2+}]_i$ to $\sim$ 11 μM (Fig. 3.16E), a higher frequency train was unlikely to produce much more Ca^{2+} release.

3.4.4.2 No evidence for contribution of Ca^{2+} current facilitation

Unlike CICR, facilitation of the presynaptic Ca^{2+} current did not play a major role in the supralinear summation of $[Ca^{2+}]_i$. Due to the low Ca^{2+} binding affinity of OGB-5N, an increase in $\Delta[Ca^{2+}]_i \leq 1$ μM might have been unresolved. However, without a

concurrent, observable increase in the amplitude of $^{\Delta F}/_{F_0}$ associated with individual APs, the continuous rise in its fluorescence intensity during the 40 Hz train was unlikely caused by an increase in the amount of Ca^{2+} influx *per* AP. Following an AP, the presynaptic Ca^{2+} current mediated by P/Q- and N-type channels is less than 1 ms long (Borst and Sakmann, 1996, 1998a; Bischofberger *et al.*, 2002). Therefore, AP-evoked Ca^{2+} influx most likely finished before OGB-5N fluorescence reached its peak, measured 5 ms after somatic current injection. Even the Ca^{2+} current through the less common R-type channels, which have relatively slow activation and deactivation kinetics, terminates within 3 ms of the AP onset (Li *et al.*, 2007b). As a result, in the absence of an observable increase in $\Delta[Ca^{2+}]_i$ *per* AP, the continuous rise in $[Ca^{2+}]_i$ was unlikely caused by Ca^{2+} current facilitation.

3.4.4.3 Other factors underlying supralinear summation

The fact that blockade of SERCA did not abolish the supralinear build-up of $[Ca^{2+}]_i$ seems to suggest the involvement of an additional mechanism(s). These include a slow down or reversal of Ca^{2+} transporters, a delayed source of Ca^{2+} due to diffusion from neighbouring boutons, or activation of presynaptic NMDA receptors. Alternatively, bath application of CPA for 10 min might not have depleted presynaptic Ca^{2+} stores and thereby allowed CICR to persist.

Although the rate of $[Ca^{2+}]_i$ decay was linearly dependent on $\Delta[Ca^{2+}]_i$ (Figs. 3.17B and D), the possibility that the activity of Ca^{2+} transporters slowed down during repetitive stimulation cannot be excluded. A sublinear increase in the rate of Ca^{2+} sequestration might not be easily distinguished from a linear one. As a result of the activation of voltage-gated Na^+ channels and Na^+/Ca^{2+} exchangers (in normal/forward mode), Na^+ would have accumulated inside the imaged boutons. Regehr (1997) showed that, in presynaptic terminals of cerebellar granule cells, the larger the Ca^{2+} rise, the more Na^+ accumulated, causing the rate of Ca^{2+} removal by Na^+/Ca^{2+} exchangers to slow down. As a result, the decay kinetics prolonged with more APs or a higher stimulation frequency (Regehr, 1997; Scheuss *et al.*, 2006;

Roome *et al.*, 2013). In this study, the decay time course after repetitive stimulation was longer than that in response to a single AP (Figs. 3.9C, 3.10C, and 3.16C). This suggests a possible slow down or even reversal in the activity of Na^+/Ca^{2+} exchangers. However, the decay time course after the 2 s long AP trains was independent of the stimulation frequency (Fig. 3.16C). Even when the decay time constants were only compared between AP trains evoked at ≤ 20 Hz to avoid a speed up caused by saturation of OGB-6F, they did not increase with higher frequencies. Accordingly, a slow down or reversal of Ca^{2+} transporters might partially but not fully account for the supralinear summation of $[Ca^{2+}]_i$.

The finding that exogenous buffers significantly sped up and enhanced the diffusion of Ca^{2+} into the axon suggests that Ca^{2+} from neighbouring boutons might have contributed to the supralinear build-up of $[Ca^{2+}]_i$ within a bouton. However, given that the average inter-bouton distance in layer 5 pyramidal neurons is ~ 7 μm (Salin *et al.*, 1995; Schubert *et al.*, 2006; Romand *et al.*, 2011), $[Ca^{2+}]_i$ from one bouton was unlikely to significantly contribute to the summation of $[Ca^{2+}]_i$ in its proximal neighbours. This idea was supported by a 3D model, in which plasma membrane transporters, intracellular Ca^{2+} uptake, and Ca^{2+} channels were all absent along the axon (data not shown). Following a single AP-evoked Ca^{2+} influx, diffusion of Ca^{2+} from a bouton caused $[Ca^{2+}]_i$ at 7 μm away from it to reach a peak amplitude of 6% of that reached within the bouton (in the presence of 90 μM OGB-6F). It is unlikely that, in the animals used ($P15-20$; with minimal myelination), the axonal membrane is completely devoid of Ca^{2+} transporters. Therefore, this simulation provided an upper estimate of the extent to which $[Ca^{2+}]_i$ accumulated along the axon. Despite this, when Ca^{2+} influx occurred simultaneously in two additional boutons (one on each side and 7 μm away from the main bouton), $[Ca^{2+}]_i$ in the centre bouton still reached a steady state during a 1 s long train of APs evoked at 40 Hz (τ_{rise} = 50 ms). Interestingly, according to this simulation, diffusion of Ca^{2+} from neighbouring boutons could provide a delayed source of Ca^{2+}, and thus, potentially account for the increase in τ_{slow} following repetitive stimulation (Figs. 3.9C, 3.10C, and 3.16C).

Another mechanism that might have contributed to the supralinear build-up

of $[Ca^{2+}]_i$ was activation of presynaptic Ca^{2+}-permeable glutamate receptors, particularly NMDA receptors. Due to a partial voltage-dependent Mg^{2+} block, activation of NMDA receptors upon membrane depolarisation typically produces a supralinear rise in $[Ca^{2+}]_i$. Although it is unknown whether these receptors are expressed on the boutons imaged in this study, their presynaptic expression is generally determined by the postsynaptic cell and hence synapse specific (Banerjee *et al.*, 2016). In particular, in layer 5 pyramidal neurons of the developing mouse visual cortex, only $\sim$ 50% of the boutons produced a supralinear Ca^{2+} rise when glutamate uncaging was coupled with somatically evoked APs (Buchanan *et al.*, 2012). Such a synapse specific expression has also been reported for presynaptic kainate receptors (Scott *et al.*, 2008). In my experiments, a 2 s long AP train evoked at $30 - 50$ Hz caused $[Ca^{2+}]_i$ to sum supralinearly in all of the imaged boutons (Fig. 3.16F). Therefore, activation of presynaptic Ca^{2+}-permeable glutamate receptors was probably not the main underlying mechanism.

It was unlikely that bath application of CPA (25 μM) for 10 min completely emptied presynaptic Ca^{2+} stores. Compared to those at the somata of many cell types (Camello *et al.*, 2002), presynaptic Ca^{2+} stores may have a very slow rate of basal leak. Blockade of SERCA alone did not appreciably deplete presynaptic Ca^{2+} stores in neocortical pyramidal neurons (Simkus and Stricker, 2002a). In addition, the basal fluorescence intensity (*i.e.* F_0) of Cal-520 and OGB-1 in the imaged boutons was not affected by CPA, in contrast to that in synaptic boutons of CA3 pyramidal neurons and hippocampal mossy fibres (Emptage *et al.*, 2001; Scott and Rusakov, 2006). In these studies, an increase in F_0 of OGB-1 indicated a depletion of presynaptic Ca^{2+} stores, which in turn led to a small rise in $[Ca^{2+}]_{rest}$, most likely through activation of store-operated Ca^{2+} channels (Emptage *et al.*, 2001). My finding suggests that leakage of Ca^{2+} from presynaptic stores of layer 5 pyramidal neurons is likely a slow process, and that at least a fraction of the build-up of $[Ca^{2+}]_i$ that remained after addition of CPA arose from CICR.

3.4.5 Functional implications

Following an AP-evoked Ca^{2+} influx, localised domains of elevated $[Ca^{2+}]_i$ around open channels rapidly collapse as a result of diffusion and buffering. The remaining, spatially homogeneous Ca^{2+} is removed by sequestration mechanisms. A low value of κ_E, particularly of fixed buffers, enables Ca^{2+} domains of a high amplitude and large spatial width to build up around Ca^{2+} channels (Delvendahl *et al.*, 2015). Therefore, together with a large number of VGCCs activated in response to a single AP, endogenous fixed buffers with a low κ_E are most likely required for the efficacy and reliability of evoked transmitter release from synaptic boutons of layer 5 pyramidal neurons (Frick *et al.*, 2007). By producing a large increase in the spatially homogeneous $[Ca^{2+}]_i$, they may also allow efficient activation of other Ca^{2+}-dependent cellular processes, including short-term synaptic plasticity (Zucker and Regehr, 2002; Neher and Sakaba, 2008) and gene expression (Benech *et al.*, 1999). In addition, a low value of κ_E means that Ca^{2+} buffers do not strongly compete with Ca^{2+} transporters. As a result, Ca^{2+} is rapidly sequestered after an intracellular Ca^{2+} rise. This ensures that transmitter release remains synchronous during repetitive stimulation (Helmchen *et al.*, 1997; Delvendahl *et al.*, 2015).

In the absence of exogenous buffers, diffusion of Ca^{2+} into the axon does not significantly reduce the peak amplitude of the spatially homogeneous Ca^{2+} rise evoked by a single AP. However, it speeds up the rate of Ca^{2+} decay, and thereby, decreases the time integral of the Ca^{2+} transient. As a result, cellular processes that are dependent on $[Ca^{2+}]_i$ may be affected by the axon diameter. By allowing Ca^{2+} to rapidly escape the boutons, a thick axon may limit the extent to which the spatially homogeneous $[Ca^{2+}]_i$ enhances transmitter release in response to subsequent APs. It may also affect mechanisms, such as intracellular kinases, that integrate the Ca^{2+} signal (Tanaka *et al.*, 2007). As these mechanisms are often triggered by Ca^{2+} in a highly cooperative manner (Tanaka *et al.*, 2007), a small reduction in the time integral of an intracellular Ca^{2+} rise could greatly attenuate their output. Akin to dendritic spines and necks, the diameters of both synaptic boutons and axons

have been shown to undergo activity-dependent modifications (Chereau *et al.*, 2017). These morphological changes may potentially affect the temporal availability of Ca^{2+} to Ca^{2+}-binding proteins within the boutons. Similarly, factors that regulate the apparent mobility of Ca^{2+} may be important determinants of Ca^{2+}-dependent cellular processes. These factors include the expression of mobile Ca^{2+}-binding molecules and proteins, and the presence of physical barriers such as organelles within the boutons.

The supralinear summation of $[Ca^{2+}]_i$ may underlie frequency-dependent recovery (FDR) from depression. FDR has been reported in a range of nerve terminals, including synaptic boutons of layer 5 pyramidal neurons (Dittman and Regehr, 1998; Wang and Kaczmarek, 1998; Fuhrmann *et al.*, 2004). In these presynaptic terminals, FDR is blocked by the slow Ca^{2+} buffer EGTA, indicating a role of the spatially homogeneous Ca^{2+} rise (Dittman and Regehr, 1998; Wang and Kaczmarek, 1998; Fuhrmann *et al.*, 2004). An increase in $[Ca^{2+}]_i$ may influence the rate of recovery from depression by two different mechanisms. First, the rate at which synaptic vesicles are refilled after a depleting stimulus increases with increasing $[Ca^{2+}]_i$ (Hosoi *et al.*, 2007). Second, G$\beta\gamma$, a complex formed by two G-protein subunits, has been shown to compete with synaptotagmin for SNARE binding in a Ca^{2+}-dependent manner (Yoon *et al.*, 2007). A high level of $[Ca^{2+}]_i$ may relieve the SNARE complex from inhibition by constitutively active G$\beta\gamma$ (Leurs *et al.*, 1998; Morisset *et al.*, 2000). This would produce an enhancement in vesicle fusion, seen as a speed up in the recovery kinetics at high levels of $[Ca^{2+}]_i$. Accordingly, by contributing to the supralinear build-up of $[Ca^{2+}]_i$, CICR may not only accelerate vesicle recruitment, but also suppress G$\beta\gamma$-dependent inhibition of transmitter release. As a result, it may prevent a complete depletion of releasable vesicles and sustain transmitter release at high stimulation frequencies.

3.5 Summary

A low Ca^{2+} binding ratio of endogenous buffers and a rapid rate of Ca^{2+} sequestration were found in synaptic boutons of layer 5 pyramidal neurons. Diffusion of Ca^{2+} into the axon was likely the main cause of the initial fast decay of AP-evoked Ca^{2+} transients in the presence of exogenous buffers. In the absence of exogenous buffers, a single AP raised $[Ca^{2+}]_i$ by $\sim$ 5 μM, which returned to the resting level of $\sim$ 50 nM in $\sim$ 100 ms. During repetitive stimulation, activation of CICR contributed to the supralinear build-up of $[Ca^{2+}]_i$. The activity of Ca^{2+} transporters did not significantly saturate, even after $[Ca^{2+}]_i$ was elevated to $\sim$ 10 μM.

Chapter 4

Spontaneous Ca^{2+} transients in neocortical synaptic boutons

4.1 Introduction

Neurotransmitters can be released in response to or independently of presynaptic action potentials (APs). The release of neurotransmitters following an AP requires an increase in $[Ca^{2+}]_i$, the principal source of which is Ca^{2+} influx through voltage-gated Ca^{2+} channels (VGCCs). In contrast, spontaneous transmitter release can occur in the absence of extracellular Ca^{2+} (Fatt and Katz, 1952; Hubbard, 1961). As a result, it is generally thought to arise from the spontaneous fusion of synaptic vesicles with the presynaptic membrane (Katz, 1962). However, recent studies suggest that presynaptic stores provide an intracellular source of Ca^{2+} that can contribute to spontaneous transmission (Llano *et al.*, 2000; Emptage *et al.*, 2001; Simkus and Stricker, 2002a).

The smooth endoplasmic reticulum (ER) is a major constituent of intracellular Ca^{2+} stores. It sequesters Ca^{2+} through the activity of the sarco/endoplasmic reticulum Ca^{2+}-ATPase (SERCA), and releases Ca^{2+} through the ryanodine and/or IP_3 receptor (RyR and IP_3R, respectively). Since 1980s, it has been recognised that the smooth ER extends from the cell body to the axon and nerve terminals of neurons (Westrum and Gray, 1986; Hartter *et al.*, 1987). In olfactory nerve terminals of the frog, the smooth ER can be seen adjacent to synaptic vesicles and as close as 40 nm from the active

zone (Hartter *et al.*, 1987). Moreover, expression of both IP_3 and ryanodine receptors have been reported in a range of nerve terminals, including those in the cerebellum, hippocampus, and neocortex (Sharp *et al.*, 1993; Padua *et al.*, 1996; Llano *et al.*, 2000). Consistent with these observations, a growing number of studies have shown that Ca^{2+}-induced Ca^{2+} release (CICR) contributes to presynaptic Ca^{2+} transients in response to stimulation (Llano *et al.*, 2000; Liang *et al.*, 2002; Scott and Rusakov, 2006; this study). Together, these findings suggest that the smooth ER, with its position close to the presynaptic membrane and its ability to release Ca^{2+}, could potentially trigger vesicle exocytosis.

Within the last two decades, it has become clear that a significant fraction of spontaneous transmission arises from the release of Ca^{2+} from presynaptic stores (Llano *et al.*, 2000; Emptage *et al.*, 2001; Simkus and Stricker, 2002a). A key finding is the observation that spontaneous Ca^{2+} transients (sCaTs) occur in synaptic boutons of cultured hippocampal neurons (Emptage *et al.*, 2001). In these cells, blockade of RyRs reduces the frequency of both sCaTs and miniature excitatory postsynaptic currents (mEPSCs). Consistently, Conti *et al.* (2004) observed sCaTs in cerebellar basket terminals, and found that their amplitudes were similar to those of single AP-evoked Ca^{2+} transients. These findings provide strong evidence that the spontaneous release of Ca^{2+} from presynaptic stores can trigger transmitter release.

This chapter characterised sCaTs in synaptic boutons of layer 5 pyramidal neurons in the rat somatosensory cortex. To elucidate the origin of sCaTs and whether they underlie spontaneous transmitter release, their frequency, together with the frequency of spontaneous postsynaptic currents (sPSCs), was also measured in the presence of pharmacological compounds that interfere with Ca^{2+} release. The results of this chapter extend a growing body of evidence favouring the role of presynaptic Ca^{2+} stores in spontaneous synaptic transmission.

4.2 Materials and methods

4.2.1 Tissue preparation and electrophysiology

$15-20$ day old Wistar rats of either sex were rapidly decapitated and 300 μm thick slices of the rat somatosensory cortex were prepared as detailed in Section 3.2.2. Brain slices were placed in a recording chamber and superfused with a standard ACSF (see Section 3.2.3). All experiments were done at 35 ± 1 °C.

Visually identified pyramidal neurons in layer 5 of the somatosensory cortex were filled through the patch pipette with a standard internal solution (see Section 3.2.3). For fluorescence imaging, two fluorophores were added to the internal solution: 1) Alexa Fluor® 568 (50 μM) or Alexa Fluor® 594 (40 μM), and 2) OGB-1 (80 μM; Life Technologies). Patch pipettes were positioned using an MP-285 manipulator (Sutter Instrument Co.).

Whole-cell recordings were made with a MultiClamp 700A (Molecular Devices; commander version 1.2.10.4). sPSCs were recorded in continuous voltage-clamp at a holding potential of -70 mV. The output current was filtered at 1 kHz using a sample-and-hold amplifier (designed at JCSMR), and acquired at 5 kHz with an ITC-18 computer interface (InstruTech Corporation). Series resistance (R_S), and electrode and whole-cell capacitance were not compensated. R_S was monitored between each sPSC recording period ($3-4$ min long) by applying a brief depolarising voltage step (0.5 mV, 40 ms long; 30 repeats). The resultant current response was filtered at 10 and acquired at 20 kHz.

APs were evoked in current-clamp, by applying 2 ms long somatic current injections ($1-3$ nA). The resultant voltage responses were filtered at 10 and sampled at 20 kHz. Experiments were only done in cells which maintained a resting membrane potential of ≤ -60 mV. Data were acquired using custom-made software implemented in Igor Pro 6.2/6.3 (Wavemetrics), and stored on the hard drive of a MacIntosh PowerMac G5 computer (Apple Inc.). Timings for current and voltage steps were provided by a Master-8 stimulator (A.M.P.I.).

4.2.2 Confocal Ca^{2+} imaging

Fluorescence imaging was done with a Zeiss LSM 510 and a 40x 1.0 NA water-immersion objective, as described in Section 3.2.4. Unless otherwise stated, pyramidal cells were filled with Alexa Fluor® 568 or 594, and OGB-1, for at least 40 min before Ca^{2+} imaging commenced.

In most experiments, Alexa Fluor® 568 or 594, and OGB-1 were excited separately to minimise photo-toxicity. The Ca^{2+}-insensitive fluorophores were excited by 543 nm light from a helium-neon laser (laser power < 0.1 mW). The emitted fluorescence was long-pass filtered for > 560 nm and measured by a photomultiplier tube (PMT). OGB-1 was excited using an argon laser (488 nm; laser power < 0.5 mW), and its fluorescence was long-pass filtered for > 505 nm before being acquired by the same PMT. Bleed-through from Alexa Fluor® 568 or 594 into the fluorescence measurement of OGB-1 would not affect $\Delta[Ca^{2+}]_i$ associated with sCaTs calculated from Eq. 4.1 (Section 4.2.4.2). In experiments in which Alexa Fluor® 594 and OGB-1 were excited simultaneously, fluorescence of OGB-1 was passed through a $500-530$ nm band-pass filter before being acquired.

To reveal the morphology of a patched cell, the fluorescence intensity of Alexa Fluor® 568 or 594 was obtained in z-stacks (typically, 1508×1508 pixels *per* frame; pixel size = 150 nm; dwell time = 0.64 μs *per* pixel; z-interval = 2 μm; open pinhole = 10 Airy units; Fig. 3.4A). The patched cell was confirmed to be a pyramidal neuron if it had a pyramidal-shaped soma, a pronounced apical dendrite, and spines lining along all dendrites. Its axon was then traced, and synaptic boutons were chosen along 1^{st} to 3^{rd} order axon collaterals ($100-300$ μm from the soma; Fig. 3.4B). To reduce laser exposure, fluorescence of OGB-1 was acquired using line scans ($32-44$ pixels *per* line; pixel size = $130-150$ nm; dwell time = 10.24 μs *per* pixel; open pinhole = 12 Airy units), drawn across a bouton and perpendicular to its parent axon collateral (Fig. 3.4C). For measurement of a single AP-evoked Ca^{2+} transient, line scans were taken every 5 ms (Fig. 3.4D). For detection of sCaTs, the sampling interval was 50 ms (Fig. 4.1A). Only boutons that displayed a rapid and clear increase in OGB-1

fluorescence in response to an AP (within 5 ms of AP onset; > 95% boutons) were used for detection of sCaTs.

4.2.3 Pharmacological compounds

Unless otherwise stated, detection of sCaTs was done in the presence of tetrodotoxin (TTX; Affix Scientific, California, USA). The stock solution of TTX (1 mM) was made by dissolving 1 mg of TTX in 3.132 ml of citric acid (0.1 M; BDH Chemicals, Victoria, Australia). On the day that TTX was required for experiments, a small volume of the stock solution was added to the standard ACSF to produce a final concentration of 1 μM. Imaging of sCaTs commenced more than 5 min after addition of TTX, when APs could no longer be generated by somatic current injections.

To promote the occurrence of sCaTs, caffeine (Sigma-Aldrich) was bath-applied for more than 10 min in the presence of TTX. Caffeine was not made into a stock solution, but added directly to the standard ACSF to a final concentration of 20 mM on the day of the experiment.

To investigate whether activation of IP_3Rs contributed to the generation and/or shaped the dynamics of sCaTs, 2-APB (Tocris, Bristol, UK) was bath-applied for more than 10 min in the presence of TTX. The stock solution of 2-APB (16 mM) was made with DMSO as the solvent. On the day that 2-APB was required for experiments, a small volume of the stock solution was added to the standard ACSF to produce a final concentration of 16 μM.

4.2.4 Data analysis

4.2.4.1 Detection and characterisation of sCaTs

Using a custom-made Zeiss TIFF image reader, fluorescence data were imported into Igor Pro 6.3, where further analysis was performed.

Fig. 4.1A shows a 30 s long recording of OGB-1 fluorescence (80 μM) in a synaptic bouton in the presence of TTX (1 μM). To identify sCaTs, two values were calculated: the average OGB-1 fluorescence across the diameter of the bouton (with background fluorescence subtracted), and the total fluorescence of all pixels ($32 - 44$ pixels) in each line scan (*i.e.* including background fluorescence). The average fluorescence was calculated by fitting each line scan with a Gaussian function, the y-offset of which was considered to be background fluorescence (Fig. 3.4D, top left). This was done so that the location of the bouton centre was automatically determined, minimising errors caused by movement of the bouton during imaging. The spatially averaged fluorescence of the bouton (F) was then calculated as the average fluorescence of $6 - 10$ pixels, corresponding to $\pm$ 2 standard deviations around the peak of the Gaussian, minus the background fluorescence. However, due to the small diameter of the imaged boutons, this spatially averaged fluorescence was largely determined by the few brightest pixels (~ 3). As a sCaT should be seen across the entire bouton diameter (sub-micrometer domains of intracellular Ca^{2+} rise were unlikely to be detected), the total fluorescence of all pixels in each line scan (F_T) was also used for detection of sCaTs. As the imaged boutons were loaded with fluorescent dyes through a patch pipette, background fluorescence contributed minimally to the value of F_T.

Once the total fluorescence of all pixels (F_T) and the spatially averaged fluorescence of the bouton (F) had been calculated and plotted against time (green traces in Figs. 4.1B-C, respectively), they were filtered as follows. First, they were digitally high-pass filtered to remove low-frequency fluctuations, likely caused by movement of the

Figure 4.1: Identification of sCaTs. (A) A 30 s long recording of OGB-1 fluorescence in a synaptic bouton in the presence of TTX (1 μM). Arrowheads indicate identified sCaTs. (B) The total fluorescence of all pixels in each line scan (F_T; green) was first high-pass filtered (red) to remove low-frequency fluctuations. Two low-pass filtered signals (pink and blue) were then produced by integrating the high-pass filtered signal over a time window of 200 or 300 ms, respectively. Solid lines represent the cut-off thresholds for the respective signals. (C) Similar to B but with traces calculated from the spatially averaged fluorescence of the bouton (F).

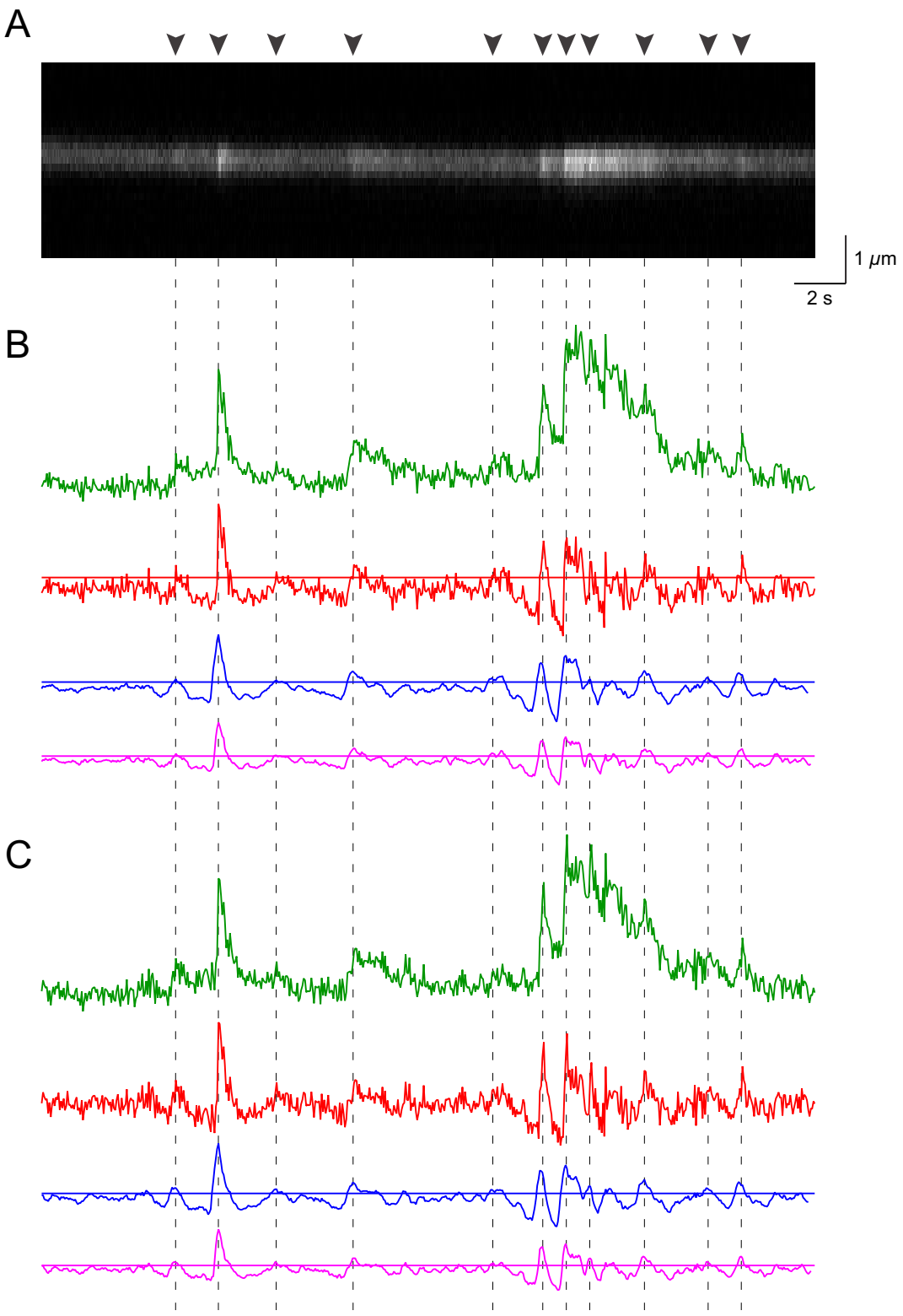

(See previous page for figure legend)

bouton in and out of focus (red traces in Figs. 4.1B-C; end of reject band = 5×10^{-5} Hz; start of pass band = 0.025 Hz). Subsequently, the high-pass filtered signals were low-pass filtered by replacing each value at time t with the sum of 4 or 6 consecutive data points, starting from time t (pink or blue traces, respectively, in Figs. 4.1B-C). The corresponding time windows (200 and 300 ms, respectively) were chosen to match the slow decay time constant (τ_{slow}) of the fluorescence transient measured with 80 μM OGB-1 in response to a single AP (249 $\pm$ 15 ms; n = 18). Both time windows were used to reduce the frequency of false positives and thus increase the specificity of the detection protocol (see below).

To identify sCaTs, a 30 s long section of a recording that contained no visually identified increases in OGB-1 fluorescence was used as baseline (*i.e.*, to estimate the noise standard deviation or σ_{noise}). A sCaT was identified based on the following set of criteria: 1) the high-pass filtered signal of F_T was larger than the mean plus 2 $\times$ σ_{noise} of the corresponding baseline, 2) the low-pass filtered signals of F_T were larger than the mean plus 3 $\times$ σ_{noise} of the corresponding baseline, and 3) the low-pass filtered signals of the spatially averaged fluorescence F were larger than the mean plus 2 $\times$ σ_{noise} of the corresponding baseline. To avoid detection of large fluorescence increases that decayed rapidly, the criteria for low-pass filtered signals had to be met by at least two consecutive data points. Regardless of the total duration, all consecutive data points that satisfied these criteria were attributed to an event. Two events that started within 400 ms of each other were also counted as one. With this set of criteria, 11 sCaTs were identified in the 30 s long recording shown in Fig. 4.1A (arrowheads).

Once identified, the amplitude and decay kinetics of a sCaT was measured from the spatially averaged fluorescence F. The baseline fluorescence (F_0) was determined by averaging over a 1 s time window immediately before its onset (*i.e.*, the first point that passed the set of detection criteria). In the case of multiple transients that occurred within 1 s of each other, F_0 of the following sCaT(s) was the same as that of its predecessor. The relative change in fluorescence associated with each event ($\Delta F/F_0$) was calculated by normalising the change in F to F_0. Its amplitude and

decay time constant (τ) were then estimated by fitting the decay time course of the fluorescence transient with an exponential function $\left(Ae^{-t/\tau}\right)$, over a $0.5-2$ s long period starting at the highest fluorescence increment. The decay kinetics of transients with decay phases straddled by other events were excluded from analysis. The inter-event interval (IEI) between two successive sCaTs was calculated as the difference between their onset times.

Specificity of the detection protocol. Two measures were used to assess the performance of the automated detection protocol. These were the frequency of false positives and the percentage of single AP-evoked Ca^{2+} transients that were not identified. The first measure reflects the specificity of the protocol, whilst the second indicates its sensitivity.

To examine the specificity of the detection protocol, fluorescence of OGB-1 and Alexa Fluor® 594 in dye-filled boutons was acquired simultaneously. As bleed-through of OGB-1 into the fluorescence measurement of the Ca^{2+}-insensitive dye was minimal, any changes in the latter fluorescence were independent of $[Ca^{2+}]_i$. As a result, all events identified by the detection protocol from recordings of Alexa Fluor® 594 fluorescence were false positives.

In 14 boutons with a total of 168 min long recording (12 min *per* bouton), only 3 events were detected from the fluorescence intensity of Alexa Fluor® 594, corresponding to a false positive rate of 0.02 *per* min. In contrast, 55 events were detected from fluorescence of OGB-1, yielding a frequency of sCaTs of 0.33 *per* min. This suggests a high specificity of the detection protocol, with less than 10% of detected events being false positives.

It should be noted here that such a high specificity was only obtained if both low-pass filtered signals, with 200 and 300 ms integration windows (pink and blue traces, respectively, in Figs. 4.1B-C), were used for the detection of sCaTs. When either integration window was used, a total of 14 or 16 events were identified

from fluorescence of Alexa Fluor® 594, and 75 or 77 events identified from OGB-1 fluorescence. As all events identified with the former fluorescence occurred independently of those identified with the latter fluorescence, the rate of false positives was more than 15%. Interestingly, most false positives identified with the 200 ms integration window were not detected by the 300 ms window, and *vice versa*. Therefore, both integration windows were used to increase the specificity of detection.

Sensitivity of the detection protocol. The sensitivity of the automated detection protocol was assessed by evoking single APs during sCaT recordings (with a sampling interval of 50 ms) and checking whether they could be identified by the protocol. In this set of experiments, the fluorescence intensity of OGB-1 was monitored in the absence of TTX so that APs could be evoked. In 17 boutons, a total of 68 APs were evoked by somatic current injections (4 APs *per* bouton). Additionally, five spontaneous APs were detected from voltage recordings at the soma. Out of these 73 APs, 69 APs or 95% produced fluorescence transients that were identified by the detection protocol. The remaining four AP-evoked fluorescence transients had relatively small amplitudes ($\Delta F/F_0 \leq 0.3$, but one with $\Delta F/F_0 = 0.68$). However, the main reason why they escaped detection was because their time integrals (with 200 and/or 300 ms integration windows) were not resolved from the recording noise. A number of single AP-evoked transients with similar amplitudes but less noisy decay phases were, in fact, identified.

Admittedly, the majority of fluorescence transients evoked by single APs had larger amplitudes than sCaTs. Therefore, the percentage of single AP-evoked fluorescence transients that were not identified (5%) provided an overestimation of the sensitivity of the detection protocol. However, the observation that around a quarter of identified sCaTs had $\Delta F/F_0$ smaller than 0.3 (Fig. 4.4D) suggests that the automated detection protocol was able to identify events with small amplitudes, as long as their decay phases could be resolved from the recording noise.

4.2.4.2 Determination of $\Delta[Ca^{2+}]_i$ associated with each sCaT

$\Delta[Ca^{2+}]_i$ associated with each sCaT was calculated from ${}^{\Delta F}/_{F_0}$ of OGB-1 as follows (Lev-Ram *et al.*, 1992):

$$\Delta[Ca^{2+}]_i = \frac{[Ca^{2+}]_{rest} + K_d \times \frac{{}^{\Delta F}/_{F_0}}{({}^{\Delta F}/_{F_0})_{max}}}{1 - \frac{{}^{\Delta F}/_{F_0}}{({}^{\Delta F}/_{F_0})_{max}}} - [Ca^{2+}]_{rest}. \tag{4.1}$$

For this calculation, a value of 50 nM was used for $[Ca^{2+}]_{rest}$ and 300 nM for K_d of OGB-1 (Section 3.3.2 and Chapter 2, respectively). Bleed-through from Alexa Fluor® 568 into the fluorescence measurement of OGB-1 would not affect $\Delta[Ca^{2+}]_i$ calculated from Eq. 4.1, because it was cancelled in the ratio of the two relative changes. $({}^{\Delta F}/_{F_0})_{max}$ of OGB-1 was determined *in situ* for each bouton imaged, by evoking a 1 s long train of APs at 100 Hz at the end of each sCaT imaging period. As this high-frequency train of APs raised $[Ca^{2+}]_i$ to more than 10 μM (Fig. 3.16), OGB-1 was most likely fully saturated; that is, $({}^{\Delta F}/_{F_0})_{100Hz} \approx ({}^{\Delta F}/_{F_0})_{max}$. The latter was thus measured as the average change during the last 500 ms of stimulation.

4.2.4.3 Estimation of $\Delta[Ca^{2+}]_T$ associated with each sCaT

$\Delta[Ca^{2+}]_T$ associated with each sCaT was estimated as follows:

$$\Delta[Ca^{2+}]_T = \Delta[Ca^{2+}]_i \times (1 + \kappa_E + \kappa_D), \tag{4.2}$$

where κ_E and κ_D represent the Ca^{2+} binding ratios of endogenous and exogenous buffers, respectively (Neher and Augustine, 1992). This equation simply states that the total number of Ca^{2+} ions present in a bouton are divided into those that are free, those bound to endogenous buffers, and those bound to exogenous buffers. For this calculation, a value of 7 was used for κ_E (see Section 3.3.4). κ_D was calculated according to Eq. 3.22, with the total concentration of OGB-1 and other exogenous buffers being 90% of that in the patch pipette (see Section 3.3.1).

4.2.4.4 Detection of sPSCs

sPSC recordings were discarded if R_S changed by more than 20% during the time course of the experiment. To estimate R_S, the average current produced by a 0.5 mV voltage step was fitted with the sum of two exponential functions, over a period from 200 μs to 10 ms after the start of the voltage step. R_S was then calculated from the peak amplitude of the fit using Ohm's law.

The technique for detecting sPSCs was published in Simkus and Stricker (2002b). In brief, sPSC recordings were first analysed using a template-matching algorithm (Clements and Bekkers, 1997) implemented in AxoGraph 4.9 (Sydney, Australia). In this process, a spontaneous event was chosen as a template if its amplitude was large but sub-maximal, if its baseline, rise time, and decay time did not overlap another spontaneous event, and if its time course matched the average sPSC time course as determined by eye. Subsequently, to avoid detection of events with amplitudes smaller than the respective recording noise, σ_{noise} in a recording sequence during which there was no sPSC detected by eye was chosen as the cut-off level. Detected events with amplitudes smaller than 2.5 $\times\sigma_{noise}$ were discarded.

The average sPSC time course was estimated after peak-aligning all sPSCs. As other events commonly straddled the decay phase of a sPSC, the time courses were truncated typically after 50% of decay.

4.2.4.5 Statistical analysis

Values are given as mean $\pm$ standard error (S.E.M). Error bars also indicate S.E.M. In each box-and-whisker plot, the ends of the whiskers represent the minimum and maximum values of the respective data set. Unless stated otherwise, statistical comparisons between different experimental conditions were performed with the Student's *t*-test, one-way ANOVA analysis, or a *post-hoc* test (*i.e.* Tukey's honestly significant difference test). To compare the numbers of boutons with and without

sCaTs between different conditions, a 2×2 contingency table was constructed and the χ^2-statistic was used. $p_t < 0.05$, $p_{ANOVA} < 0.05$, $p_{Tukey} < 0.05$, and $p_{\chi^2} < 0.05$ were considered to be significant.

To compare the characteristics of sCaTs and sPSCs in the control condition and after a drug addition, cumulative probability density functions (cPDFs) were formed and compared using the Kolmogorov-Smirnov statistic (p_{KS}). For sCaT characteristics (frequency, IEI, $^{\Delta F}/_{F_0}$, and τ), $p_{KS} < 0.05$ was considered significant. For sPSC amplitude and frequency, the significance level for p_{KS} was taken at $< 10^{-6}$, because of the large sample sizes (more than 2000 events for a $3 - 4$ min long recording).

The χ^2 goodness-of-fit test was used to assess whether the IEIs were exponentially distributed. The expected number of sCaTs in each interval or bin was chosen to be ~ 7 (Snedecor and Cochran, 1989). Depending on the data set, this corresponded to a total (k) of 7 to 13 bins, with a constant expected probability (prob) of 0.143 to 0.077, respectively. With the null hypothesis that the IEIs were exponentially distributed, the upper boundary of each bin was calculated based on the mean IEI (λ) of each data set. That is,

$$\text{boundary} = -\lambda \times \ln(1 - i \times \text{prob}),$$

where $i = 1, 2, ..., k$. The observed number of sCaTs with an IEI within these boundaries was then counted. Subsequently, the χ^2-statistic was calculated from the difference between the observed (O) and expected (E) numbers of sCaTs as follows:

$$\chi^2 = \frac{(O - E)^2}{E}.$$

The number of degrees of freedom was determined as $k - s - 1$, with s representing the number of parameters of the exponential distribution (*i.e.* $s = 1$).

To assess whether $^{\Delta F}/_{F_0}$ associated with an AP or a sCaT decayed mono- or bi-exponentially, fluorescence changes measured in different boutons, under the same

experimental condition, were pooled and averaged. The decay time course of this average response was fitted with an exponential function $\left(Ae^{-t/\tau}\right)$ or the sum of two distinct exponential functions $\left(A_1e^{-t/\tau_1} + A_2e^{-t/\tau_2}\right)$. As a mono-exponential fit is "nested" within a bi-exponential fit (*i.e.*, a bi-exponential fit can be transformed into a mono-exponential fit by making either A_1 or A_2 zero), an *F*-test was used to compare the two fits. The *F*-statistic was calculated as the ratio of the weighted sums of squared errors (χ^2) of the fits (Motulsky and Christopoulos, 2004; Costa *et al.*, 2010). The null hypothesis that the sum of two exponential functions did not provide a significantly better fit than an exponential function was rejected if $p_F < 0.05$.

4.3 Results

4.3.1 Visualising sCaTs

The high-affinity Ca^{2+} indicator OGB-1 (80 μM) was used to monitor small changes in $[Ca^{2+}]_i$ that occurred in the absence of AP firing. Previous studies showed that, in neocortical pyramidal neurons, mEPSCs can occur at a rate as high as 50 Hz, with $1/3$ of them arising from intracellular Ca^{2+} release (Emptage *et al.*, 2001; Simkus and Stricker, 2002a). As each pyramidal neuron in the neocortex receives approximately 10^4 synapses (Larkman, 1991), the frequency of spontaneous Ca^{2+} release *per* nerve terminal was predicted to be low, $\sim$ 3 mHz or once every 5 min (assuming that $1/2$ of all synapses remained intact in brain slices). In support of this, the frequency of sCaTs in basket terminals of cerebellar interneurons is $\sim$ 2 mHz (Conti *et al.*, 2004).

With such a low rate of spontaneous Ca^{2+} release, it was necessary to monitor $[Ca^{2+}]_i$ in each bouton for at least 10 min in order to detect a few sCaTs. Such an extended scanning duration introduced two issues. The first was image drift; that is, whilst being imaged continuously for 10 min, a number of boutons slowly drifted out of focus, perhaps due to heating of the tissue and/or alternating flow directions of the superfusate in a circular recording chamber. To overcome this problem, the

scanning duration was divided into 3 min periods, between which the position of the microscope objective was adjusted to make sure that the imaged bouton remained in focus. Each bouton was imaged for $3-4$ such periods, corresponding to a total duration of $9-12$ min, respectively. Boutons with significant drift during imaging were discarded from further analysis.

The second issue that could have been introduced by the extended scanning duration was photo-damage. To minimise the total time of laser exposure, the fluorescence intensity of OGB-1 was scanned at 50 ms intervals. This sampling interval, although quite long, was only $1/5$ of the slow and $1/4$ of the amplitude-weighted decay time constant of the fluorescence transient measured in response to an AP with 80 μM OGB-1 ($\tau_{slow} = 249 \pm 15$ and $\tau_{w} = 186 \pm 16$ ms, respectively). As the indicator concentration played a major role in shaping the kinetics of presynaptic Ca^{2+} transients (Section 3.3.4), the decay time constant of sCaTs was most likely also around $200-250$ ms, unless a significant amount of CICR occurred, prolonging its decay kinetics. Consequently, with a sampling interval of 50 ms, each sCaT would have been detected with $4-5$ consecutive scans. Dye bleaching was unlikely to occur with a laser power < 0.5 mW (Snapp, 2013); in fact, the baseline fluorescence of OGB-1 did not considerably decrease after 12 min of imaging.

4.3.2 Assessing the frequency of sCaTs over time

Due to the extended imaging duration, it was important to evaluate whether the frequency of sCaTs was affected by the exposure to laser light. Figs. 4.2A and C display the number of sCaTs identified in four 3 min imaging periods in the presence or absence of TTX (1 μM), respectively. Note that boutons imaged in the presence of TTX were different from those imaged without it. It can be seen that, regardless of the presence of TTX, no sCaT was detected during most imaging periods, consistent with their expected frequency. As the underlying distribution of the number of sCaTs identified in each imaging period was unknown, the effect of imaging time on the frequency of sCaTs was assessed by comparing the cumulative probability density

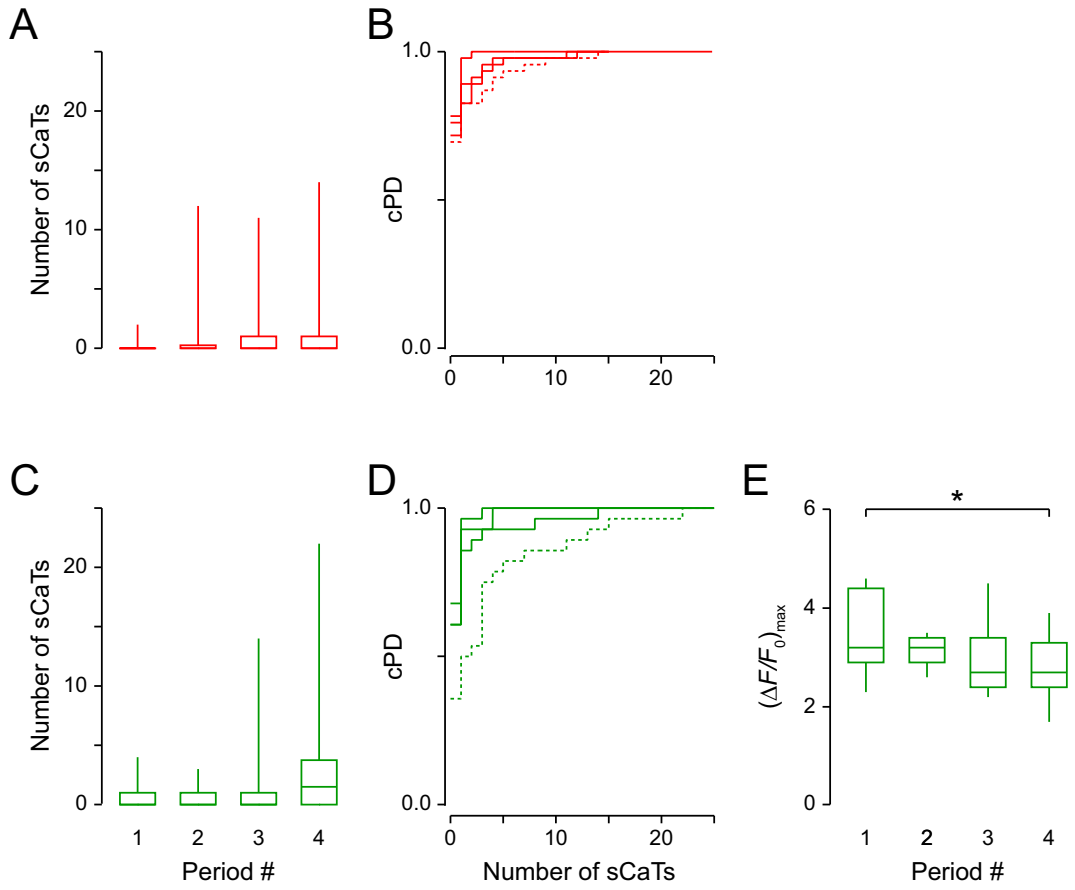

Figure 4.2: Dependence of sCaT frequency on total imaging time. (A) The number of sCaTs identified in four 3 min imaging periods with TTX. (B) The corresponding cPDFs, with dashed line indicating that of the 4th imaging period. (C-D) Same as A-B but without TTX. (E) The maximum fluorescence of OGB-1 $((\Delta F/F_0)_{max})$ measured at the end of each imaging period. n = 46 (A-B), 28 (C-D), and 11 (E). *$p_{Tukey} < 0.05$.

functions (cPDFs) between different recording periods based on the Kolmogorov-Smirnov statistic (Figs. 4.2B and D). In the presence of TTX, the cPDFs were not different from each other (n = 46; $p_{KS} \geq 0.4$). In contrast, in the absence of TTX, whilst the cPDFs of the first three imaging periods were not different from each other (n = 28; $p_{KS} \geq 0.9$), the cPDF of the 4th period was significantly different from those of earlier periods ($p_{KS} \leq 0.04$). This suggests that a total duration of laser exposure longer than 9 min might have increased the frequency of sCaTs.

In 11 out of the 28 boutons that were imaged in the absence of TTX, the

maximum fluorescence of OGB-1 ($(^{\Delta F}/_{F_0})_{\max}$) was measured to investigate whether the regulation of $[Ca^{2+}]_i$ remained constant. $(^{\Delta F}/_{F_0})_{\max}$ of OGB-1 was determined by evoking a 1 s long train of APs at 100 Hz, at the end of each imaging period. According to Eq. 3.4, $(^{\Delta F}/_{F_0})_{\max}$ of the high-affinity indicator OGB-1 depends on $[Ca^{2+}]_{rest}$. Therefore, any change in $(^{\Delta F}/_{F_0})_{\max}$ of OGB-1 would indicate an impairment in the regulation of $[Ca^{2+}]_{rest}$ (Maravall *et al.*, 2000).

Fig. 4.2E displays $(^{\Delta F}/_{F_0})_{\max}$ of OGB-1 measured at the end of the four 3 min imaging periods. On average, $(^{\Delta F}/_{F_0})_{\max}$ decreased over time ($p_{\text{ANOVA}} = 0.049$), with the value measured at the end of the 4$^{\text{th}}$ period significantly smaller than that measured after the 1$^{\text{st}}$ period (3.4 ± 0.2 *vs.* 2.8 ± 0.2; $p_{\text{Tukey}} < 0.05$). This suggests that a total duration of laser exposure longer than 9 min might have increased $[Ca^{2+}]_{rest}$. However, $(^{\Delta F}/_{F_0})_{\max}$ was not different between the first three periods of imaging ($p_{\text{Tukey}} > 0.05$). Therefore, during these periods, the regulation of $[Ca^{2+}]_{rest}$ was not significantly altered, and the majority of sCaTs were unlikely to result from laser-induced dysregulation of $[Ca^{2+}]_i$. Hereafter, synaptic boutons of layer 5 pyramidal cells were only imaged for a total duration of 9 min, with sCaTs identified from the three imaging periods pooled for subsequent analysis.

4.3.3 General characteristics of sCaTs

Fig. 4.3 displays the occurrence of all sCaTs identified in the presence or absence of TTX (red or green, respectively). Without TTX present, an increase in OGB-1 fluorescence was only accepted as a sCaT if it occurred when no AP could be detected in the concurrent somatic voltage recording. Out of 46 boutons that were imaged in the presence of TTX, 19 boutons (41%) did not exhibit any event during the 9 min of imaging. Similarly, no event was identified in 13 out of 36 boutons (36%) that were imaged without TTX. The percentage of boutons with no sCaT was not different between the two conditions ($p_{\chi^2} = 0.6$).

Fig. 4.4 compares the characteristics of sCaTs identified in the presence *vs.* absence of TTX. PDFs and cPDFs were generated for the average frequency, inter-event

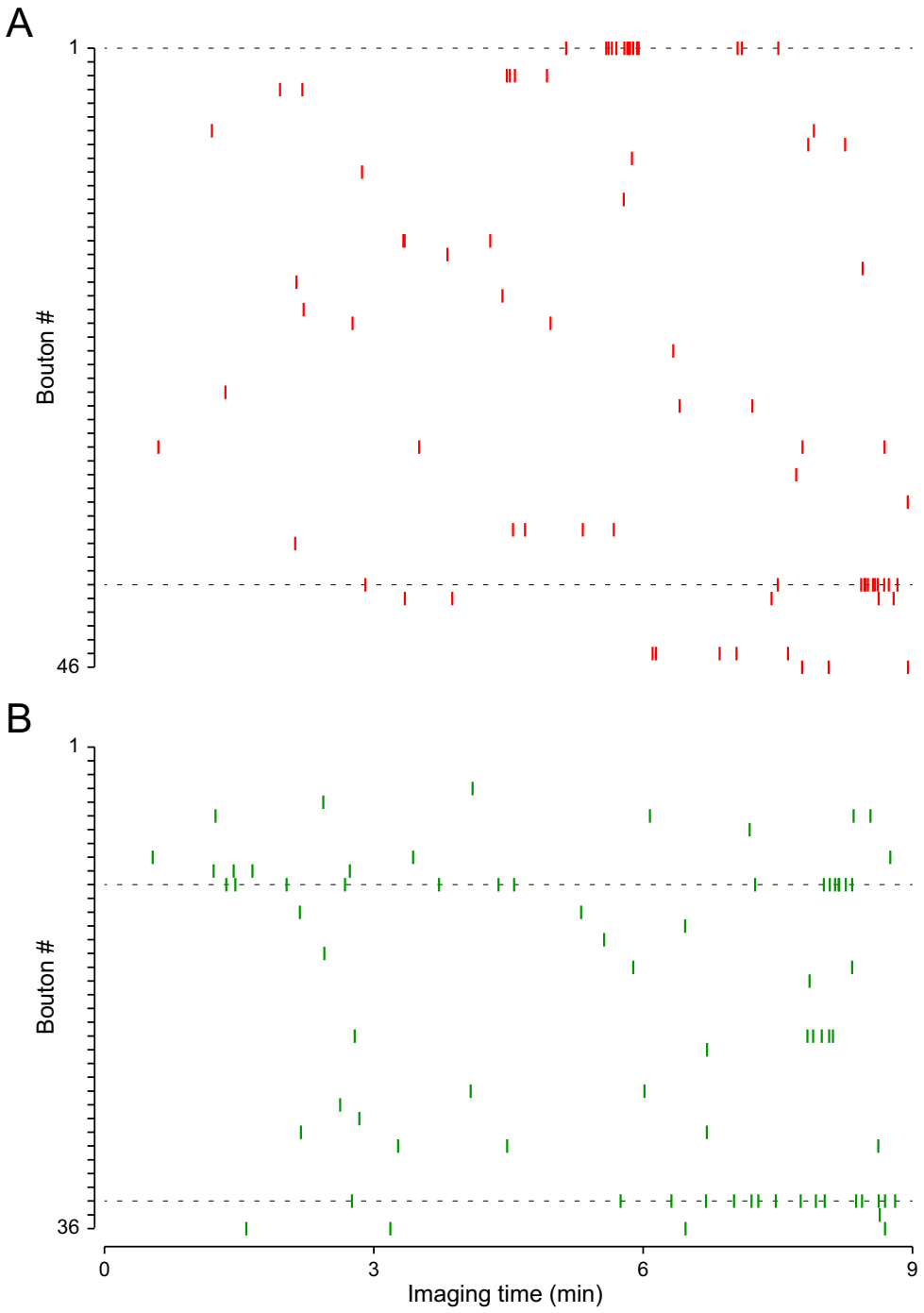

Figure 4.3: Occurrence of sCaTs identified in the presence or absence of TTX. Each tick represents a sCaT identified with or without TTX (1 μM) added to the superfusate (A and B, respectively). Dashed lines indicate boutons with an average sCaT frequency larger than the population mean plus 3 $\times$ SD.

interval (IEI), amplitude, and decay time constant (τ) of sCaTs identified in the two experimental conditions. The average frequency was calculated by dividing the number of events identified in each bouton by the total imaging duration (*i.e.* 9 min). TTX did not affect the average frequency of sCaTs, which was 0.19 $\pm$ 0.05 and 0.23 $\pm$ 0.07 *per* min in the presence and absence of TTX, respectively (p_{KS} = 1.0; Figs. 4.4A). This is in agreement with the finding that TTX did not affect the rate of spontaneous transmitter release in neocortical pyramidal cells (data not shown; also see Simkus and Stricker, 2002b). However, the distribution of IEIs was significantly different between the two experimental conditions (p_{KS} = 0.005; 44 $\pm$ 11 *vs.* 70 $\pm$ 13 s; Fig. 4.4B). The cPDF of the IEIs in the presence of TTX was shifted to the left, indicating an increase in the number of sCaTs with short IEIs. These sCaTs were predominantly from two "active" boutons, each of which exhibited a total of 15 or 12 sCaTs in the 9 min of imaging (boutons # 1 and 40, respectively, marked with dashed lines in Fig. 4.3A). The average frequencies of sCaTs in these boutons exceeded the population mean by more than 3$\times$ the standard deviation. Without TTX present in the superfusate, two such "active" boutons, each with 15 or 16 sCaTs, were also observed (boutons # 11 and 34, respectively, marked with dashed lines in Fig. 4.3B). These two boutons had a longer average IEI compared to the two "active" boutons imaged in the presence of TTX (p_{KS} = 0.0001; 27 $\pm$ 8 *vs.* 20 $\pm$ 11 s, respectively). Together, these "active" boutons suggest a tendency of sCaTs to occur in clusters, probably due to sensitisation of ryanodine or IP_3 receptors.

Figs. 4.4C-D show that TTX did not affect the amplitude and τ of sCaTs ($p_{KS} \geq$ 0.2; $^{\Delta F}/_{F_0}$ = 0.66 $\pm$ 0.06 *vs.* 0.52 $\pm$ 0.05; τ = 0.35 $\pm$ 0.04 *vs.* 0.31 $\pm$ 0.03 s). Fig. 4.4E displays the average time course of sCaTs identified with or without TTX added to the superfusate. Each average time course was generated from $^{\Delta F}/_{F_0}$ of sCaTs identified in the respective experimental condition, after peak-aligning them. In this analysis, events with fluorescence signals remaining above the detection thresholds for more than 0.5 s were excluded so that the decay time course of the average sCaT could be revealed. There were only 4 and 2 such events, out of a total of 78 or 74 events detected with or without TTX, respectively (5 and 3%). In this figure, the peak

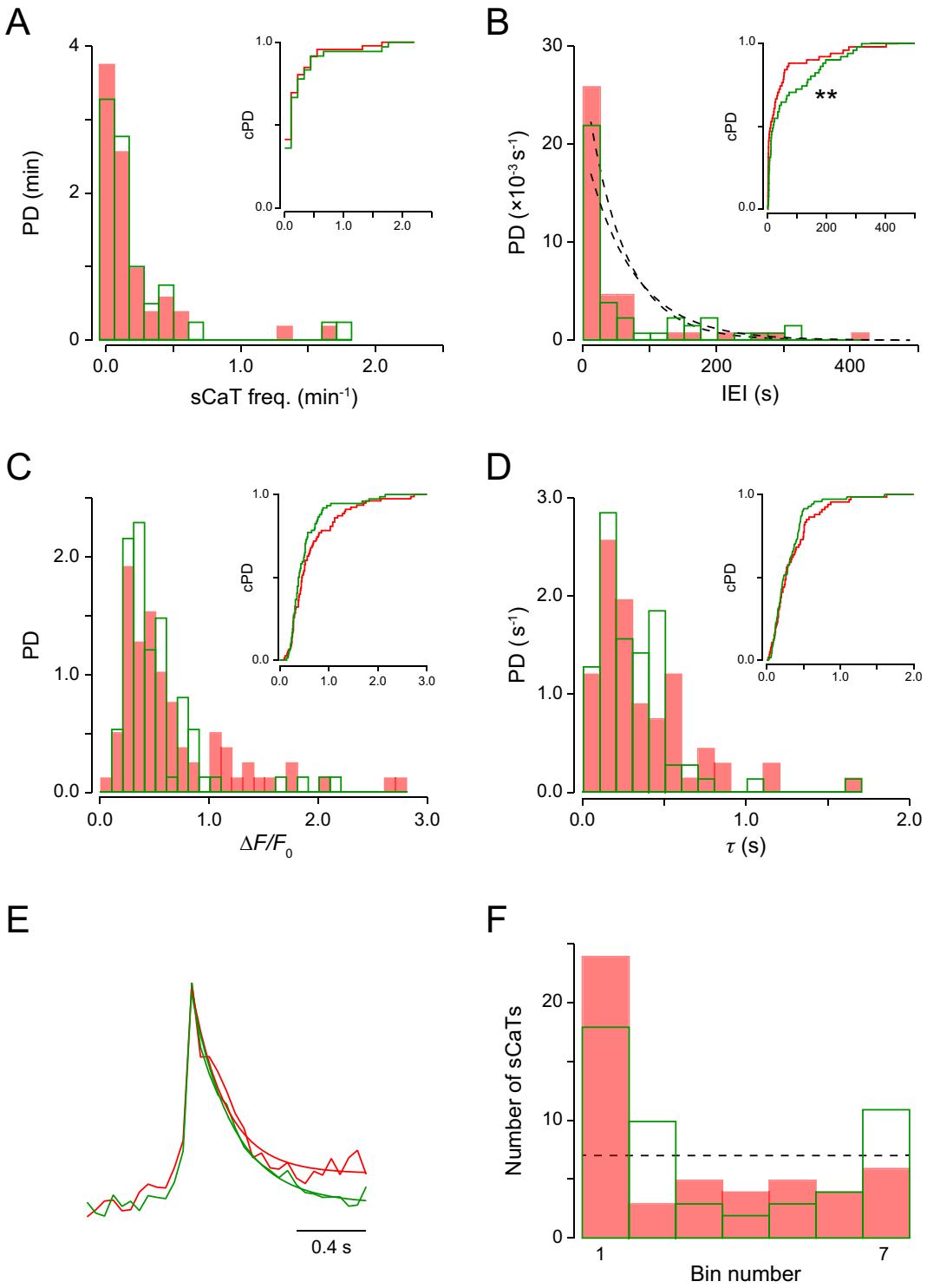

(See next page for figure legend)

Figure 4.4: Characteristics of sCaTs identified in the presence (red) or absence (green) of TTX. (A-D) PDFs of the average frequency, IEI, amplitude, and τ of sCaTs. Insets: the corresponding cPDFs. In B, plots were fitted with an exponential PDF (dashed). (E) The average sCaT time courses (peak-aligned and scaled) measured in the two experimental conditions, with an exponential function fitted to each decay phase. (F) The observed (coloured) *vs.* expected (dashed) numbers of sCaTs. Each bin had an expected probability of 0.143, corresponding to an upper boundary of 6.8, 14.8, 24.7, 37.3, 55.2, 85.7, and ∞ s for IEIs measured in TTX, and 10.9, 23.7, 39.4, 59.7, 88.3, 137.1, and ∞ s for those measured without TTX. ** $p_{KS} < 0.01$.

amplitudes of the average sCaTs had been scaled to match each other, to facilitate a comparison between their time courses. Clearly, the kinetics of sCaTs were not altered by TTX. Unlike fluorescence transients evoked by single APs (Fig. 3.5C), the average sCaTs had their decay phases well-fitted with a single exponential function ($p_F \geq 0.4$). Due to the sampling interval of 50 ms, any fast component in their decay phases could not have been detected. The decay time constant of the average sCaT was 200 $\pm$ 30 or 230 $\pm$ 20 ms, in the presence or absence of TTX, respectively. These values were not different from each other ($p_t = 0.4$). They were also in the range of τ_{slow} and τ_w of the fluorescence transients measured in response to a single AP with 80 μM OGB-1 (249 $\pm$ 15 and 186 $\pm$ 16 ms, respectively). This observation reflects the central role of the indicator concentration in shaping the intracellular Ca^{2+} dynamics. It also argues against significant occurrence of CICR during the decay phase of a sCaT.

Next, I investigated whether the IEIs of sCaTs followed an exponential distribution (*i.e.* whether they were generated by a Poisson process; dashed curves in Fig. 4.4B). To do this, I performed the χ^2 goodness-of-fit test, with intervals or bins of equal probabilities (Fig. 4.4F; see Section 4.2.4.5). The expected number of sCaTs in each bin was chosen to be ~ 7 (dashed line). As each condition, with or without TTX, had a total of 51 IEIs, this corresponded to 7 bins, with each bin having an expected probability of 0.143. With the null hypothesis that the IEIs were exponentially distributed, the upper boundary of each bin was calculated based on the mean IEI of each data set (*i.e.* 44 or 70 s, respectively; see Figure legend). The observed number of sCaTs with an IEI within these boundaries was then counted (red or

green, respectively). Based on the χ^2-statistic, the null hypothesis was rejected for both experimental conditions ($p_{\chi^2} \leq 2 \times 10^{-5}$). A comparison between the observed *vs.* expected numbers of sCaTs reveals an excess of sCaTs within the first bin, corresponding to IEIs $\leq$ 10 s. Therefore, the underlying mechanism was unlikely to be Poisson. Instead, there was a tendency for sCaTs to bunch.

4.3.4 Estimating $\Delta[Ca^{2+}]_i$ associated with sCaTs

To determine $\Delta[Ca^{2+}]_i$ associated with sCaTs, $(\Delta F/F_0)_{max}$ of OGB-1 was measured by evoking a 1 s long train of APs at 100 Hz, in experiments in which TTX was not added to the superfusate. $\Delta[Ca^{2+}]_i$ associated with each sCaT was then calculated from its $\Delta F/F_0$ and $(\Delta F/F_0)_{max}$ measured in the respective bouton, in accordance to Eq. 4.1. In these experiments, cells were filled with OGB-1 for at least 90 min before Ca^{2+} imaging commenced. This was to enable a comparison between spontaneous transients and those evoked by a single AP, and an estimation of $\Delta[Ca^{2+}]_T$ associated with the former.

A total of 38 sCaTs were identified in 19 boutons, imaged after 90 min of whole-cell break-in. This corresponds to an average frequency of 0.22 *per* min. These boutons were included in the above analysis as boutons # 18 to 36 in Fig. 4.3B. The average frequency, IEI, amplitude, and τ of sCaTs identified in these 19 boutons were not different from those observed in the other 18 boutons without TTX present in the superfusate (*i.e.* boutons # 1 to 17 in Fig. 4.3B; $p_{KS} \geq 0.6$; 0.22 $\pm$ 0.10 *vs.* 0.23 $\pm$ 0.10 *per* min; IEI = 67 $\pm$ 18 *vs.* 74 $\pm$ 19 s; $\Delta F/F_0$ = 0.51 $\pm$ 0.06 *vs.* 0.54 $\pm$ 0.07; τ = 0.28 $\pm$ 0.03 *vs.* 0.34 $\pm$ 0.05 s). They were also not different from those observed in the presence of TTX ($p_{KS} \geq 0.2$), except for the IEI (p_{KS} = 0.01).

Fig. 4.5A (green dots and inset) shows the average time course of sCaTs identified in this set of experiments. Here, one event with fluorescence signals remaining above the detection thresholds for more than 0.5 s (3%) was excluded so that the decay kinetics of the average sCaT could be revealed. Again, its decay time course was

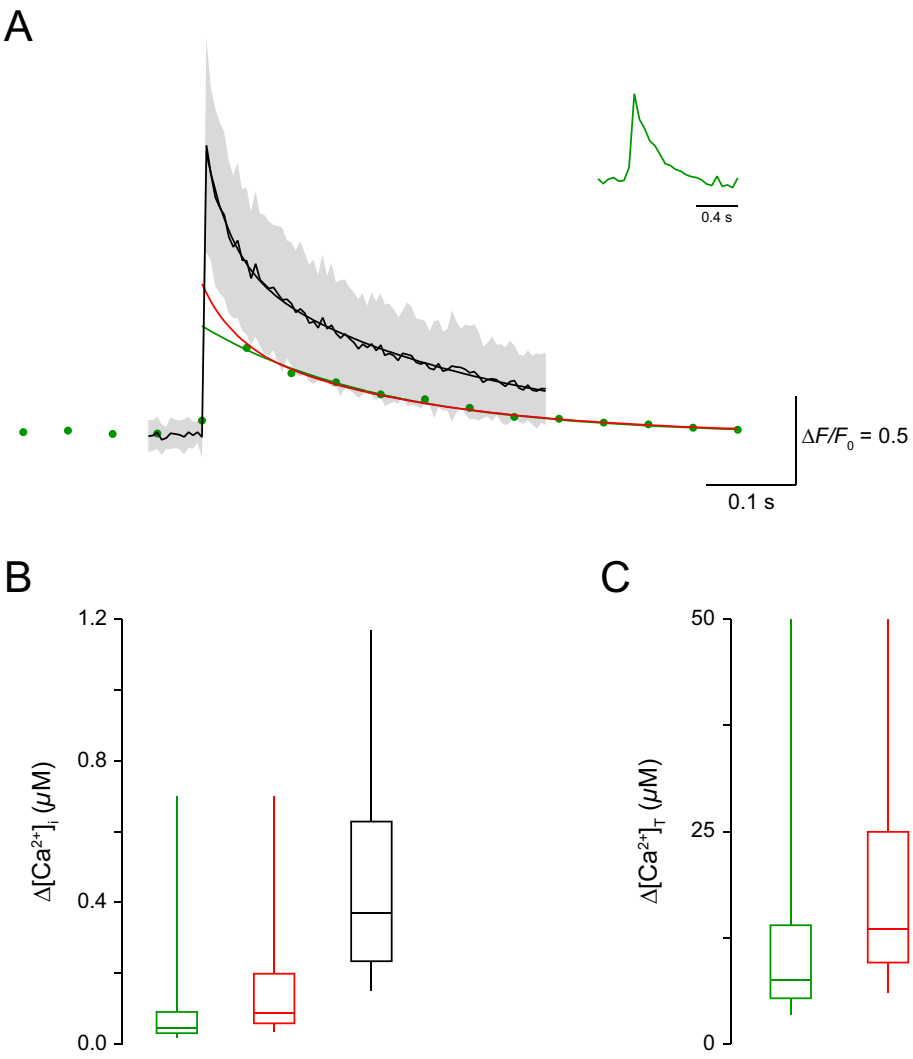

Figure 4.5: Estimating $\Delta[Ca^{2+}]_i$ associated with sCaTs. (A) The average time course of sCaTs measured in the absence of TTX (green dots and inset), compared to the average fluorescence transient measured in response to an AP with 80 μM OGB-1 (black trace; n = 22). The two traces have been aligned by the data points immediately prior to their peak amplitudes. The AP-evoked transient has been fitted with the sum of two exponential functions (black curve). Shaded area represents mean $\pm$ 1 SD. Green curve is a mono-exponential fit to the decay phase of the average sCaT, extrapolated back by 50 ms to the earliest possible time of sCaT initiation. Red curve represents an upper estimate of the peak amplitude of the average sCaT, assuming that it had a bi-exponential decay phase similar to that of the AP-evoked fluorescence transient. (B) Lower and upper estimates of $\Delta[Ca^{2+}]_i$ associated with sCaTs (green and red, respectively), compared to $\Delta[Ca^{2+}]_i$ evoked by an AP measured with 80 μM OGB-1. (C) Lower and upper estimates of $\Delta[Ca^{2+}]_T$ associated with sCaTs.

similar to the late decay phase of the average fluorescence transient evoked by a single AP (also measured with 80 μM OGB-1; black trace; $n = 22$). An exponential fit to the former (green; $p_F = 0.7$) yielded a time constant of 230 $\pm$ 20 ms, a value between τ_{slow} and τ_w of the latter (275 $\pm$ 8 and 182 $\pm$ 7 ms, respectively).

From the measured amplitude of $^{\Delta F}/_{F_0}$, $\Delta[Ca^{2+}]_i$ associated with each sCaT was estimated to be 90 $\pm$ 20 nM, ranging from 19 to 700 nM (Fig. 4.5B, green). This, however, is only a lower estimate of the peak amplitude of the intracellular Ca^{2+} rise. Due to the sampling frequency of 50 ms, which was most likely longer than the rise time of a sCaT, most events would have reached their peak prior to the measured highest fluorescence increment. To get an upper estimate of the peak amplitude, the average fluorescence transient measured in response to a single AP with 80 μM OGB-1 was examined (Fig. 4.5A, black). Its decay time course was bi-exponential ($p_F = 5 \times 10^{-18}$), with its amplitude at 50 ms after the AP onset reduced to 57 $\pm$ 1% of the peak amplitude. Therefore, an upper estimate of the peak fluorescence change associated with each sCaT was calculated by dividing the measured $^{\Delta F}/_{F_0}$ by 0.57 (red curve in Fig. 4.5A). An upper estimate of the corresponding $\Delta[Ca^{2+}]_i$ was then calculated from this value using Eq. 4.1. This yielded values ranging from 35 to 700 nM, with an average of 160 $\pm$ 30 nM (Fig. 4.5B, red). Note that the maximum value of this data set was the same as the maximum value of the lower estimates (*i.e.* 700 nM; red *vs.* green in Fig. 4.5B). This is because the corresponding $^{\Delta F}/_{F_0}$, when divided by 0.57, was larger than $\left(^{\Delta F}/_{F_0}\right)_{max}$ of OGB-1 measured in the respective bouton. Therefore, the upper estimate of $\Delta[Ca^{2+}]_i$ for this sCaT was kept the same as its lower estimate. Together, these calculations show that, in the presence of 80 μM OGB-1, an average sCaT raised $[Ca^{2+}]_i$ by $20 - 36\%$ of that evoked by a single AP (450 $\pm$ 60 nM).

To estimate the total Ca^{2+} flux associated with each sCaT, the lower and upper estimates of $\Delta[Ca^{2+}]_i$ were multiplied by the total Ca^{2+} binding ratios plus 1 (Eq. 4.2); multiplication of $\Delta[Ca^{2+}]_i$ by the Ca^{2+} binding ratios of endogenous and exogenous buffers (κ_E and κ_D, respectively) yielded the total concentration of Ca^{2+} ions that were bound to all buffers. In this calculation, a value of 7, measured at the peak of

single AP-evoked Ca^{2+} transients, was used for κ_E (see Section 3.3.4). This resulted in a lower estimate of 11 $\pm$ 2 μM and an upper estimate of 19 $\pm$ 2 μM for the total change in Ca^{2+} ($\Delta[Ca^{2+}]_T$; Fig. 4.5C, green and red, respectively). Dividing these values by $(1 + \kappa_E)$ yielded $\Delta[Ca^{2+}]_i$ in the absence of exogenous buffers ($\Delta[Ca^{2+}]_{i,0}$). $\Delta[Ca^{2+}]_{i,0}$ was $1.4 - 2.3$ μM, corresponding to $25 - 45\%$ of that evoked by a single AP.

4.3.5 The IP_3R blocker 2-APB did not affect sCaT frequency

As sCaTs were observed in the presence of TTX, which blocks voltage-gated Na^+ channels and prevents AP firing, it was hypothesised that they arose from Ca^{2+} release from presynaptic Ca^{2+} stores. To investigate whether Ca^{2+} release through IP_3Rs gave rise to sCaTs, their frequency was measured in the presence of the IP_3R antagonist 2-APB. A concentration of 16 μM was used; this was approximately the concentration that most effectively inhibited spontaneous transmitter release in neocortical pyramidal neurons (Simkus and Stricker, 2002a).

Fig. 4.6A shows the occurrence of all sCaTs identified in 12 boutons in the presence of TTX and 2-APB. The percentage of boutons with no sCaT (25%) was not different from the control condition (p_{χ^2} = 0.3). A total of 17 events were identified, corresponding to an average frequency of 0.16 *per* min. This average frequency was not different from that measured in the presence of only TTX (p_{KS} = 0.9; 0.16 $\pm$ 0.04 *vs.* 0.19 $\pm$ 0.05 *per* min; Fig. 4.6B). The amplitude and τ of sCaTs were also not affected by 2-APB ($p_{KS} \geq 0.4$; $^{\Delta F}/_{F_0}$ = 0.66 $\pm$ 0.06 *vs.* 0.57 $\pm$ 0.08; τ = 0.35 $\pm$ 0.04 *vs.* 0.30 $\pm$ 0.06 s; Figs. 4.6C-D). The distribution of IEIs in 2-APB was not characterised and compared to that in the control condition due to their small number (n = 8 IEIs).

Fig. 4.6E shows the average time course of sCaTs measured in 2-APB compared to that in the control condition. To generate this average time course, one event with fluorescence signals remaining above the detection thresholds for more than 0.5 s (6%) was excluded so that the decay time course of the average sCaT measured in

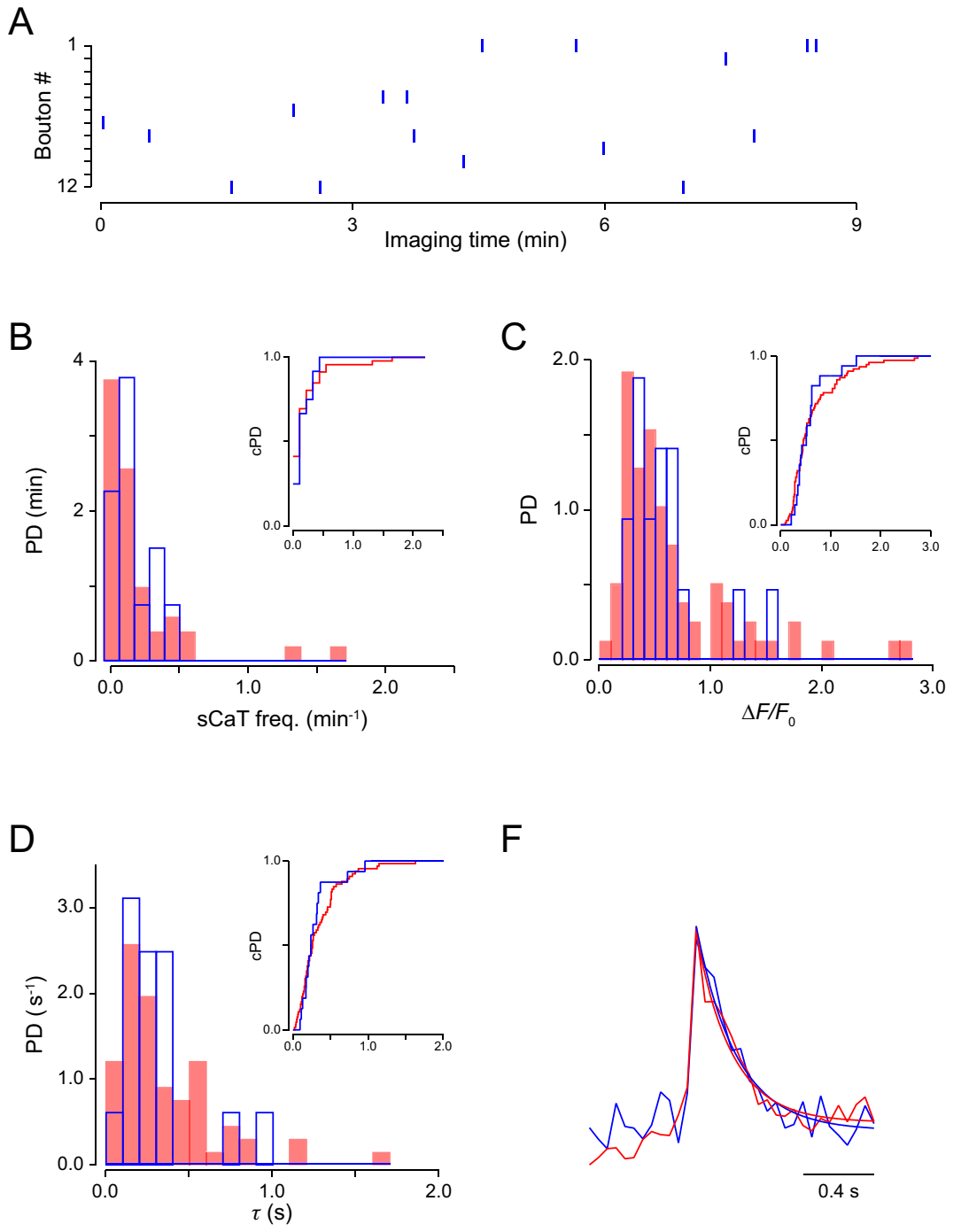

Figure 4.6: 2-APB did not affect the frequency and dynamics of sCaTs. (A) All spontaneous events identified in the presence of 2-APB and TTX (16 and 1 μM, respectively). (B-D) PDFs of the average frequency, amplitude, and τ of sCaTs identified in the control condition (red) and in 2-APB (blue). Insets: The corresponding cPDFs. (F) The average sCaT time courses (peak-aligned and scaled) measured in the two experimental conditions, with an exponential function fitted to each decay phase.

2-APB could be revealed. An exponential fit to the decay phase of the average sCaT (p_F = 1.0) yielded a τ of 230 $\pm$ 30 ms, not different from that of the control (200 $\pm$ 30 ms; $p_t = 0.7$). Together, the findings that addition of 2-APB did not alter the frequency, amplitude, and kinetics of sCaTs argue against a significant contribution of Ca^{2+} release through IP_3 receptors to their generation and dynamics.

4.3.6 Caffeine increased the frequency of sCaTs and sPSCs

To investigate whether Ca^{2+} release through RyRs gave rise to sCaTs, their frequency was measured in the presence of the RyR agonist caffeine (20 mM; $EC_{50} \sim 5$ mM, according to Porta *et al.*, 2011). Fig. 4.7A displays the occurrence of all sCaTs identified in the presence of TTX and caffeine. For comparison, the occurrence of all sCaTs identified in the control condition, with only TTX present in the superfusate, was also presented (Fig. 4.7B). As described above, no sCaT was identified in 19 out of 46 boutons (41%) that were imaged with only TTX. After addition of caffeine, the percentage of boutons that did not exhibit any event was 24% (*i.e.* 9 out of 37), not different from that in the control condition (p_{χ^2} = 0.10).

Fig. 4.8 compares the characteristics of sCaTs identified in the presence of caffeine to those identified in the control condition. Addition of caffeine significantly increased the average frequency of sCaTs by 90 $\pm$ 30%, from 0.19 $\pm$ 0.05 to 0.36 $\pm$ 0.07 *per* min (p_{KS} = 0.02; Figs. 4.8A). However, the distribution of IEIs was not different between the two experimental conditions (p_{KS} = 0.10; 44 $\pm$ 11 *vs.* 57 $\pm$ 9 s; Fig. 4.8B). Caffeine also did not affect the amplitude and τ of sCaTs ($p_{KS} \geq 0.2$; $^{\Delta F}/_{F_0}$ = 0.66 $\pm$ 0.06 *vs.* 0.58 $\pm$ 0.03; τ = 0.35 $\pm$ 0.04 *vs.* 0.33 $\pm$ 0.03 s; Figs. 4.8C-D). Therefore, caffeine-induced events and those observed in the control condition likely arose from the same process.

Fig. 4.8E displays the average time course of sCaTs identified in the control condition and after addition of caffeine. In this analysis, one event with fluorescence signals remaining above the detection thresholds for more than 0.5 s (0.8%) was excluded

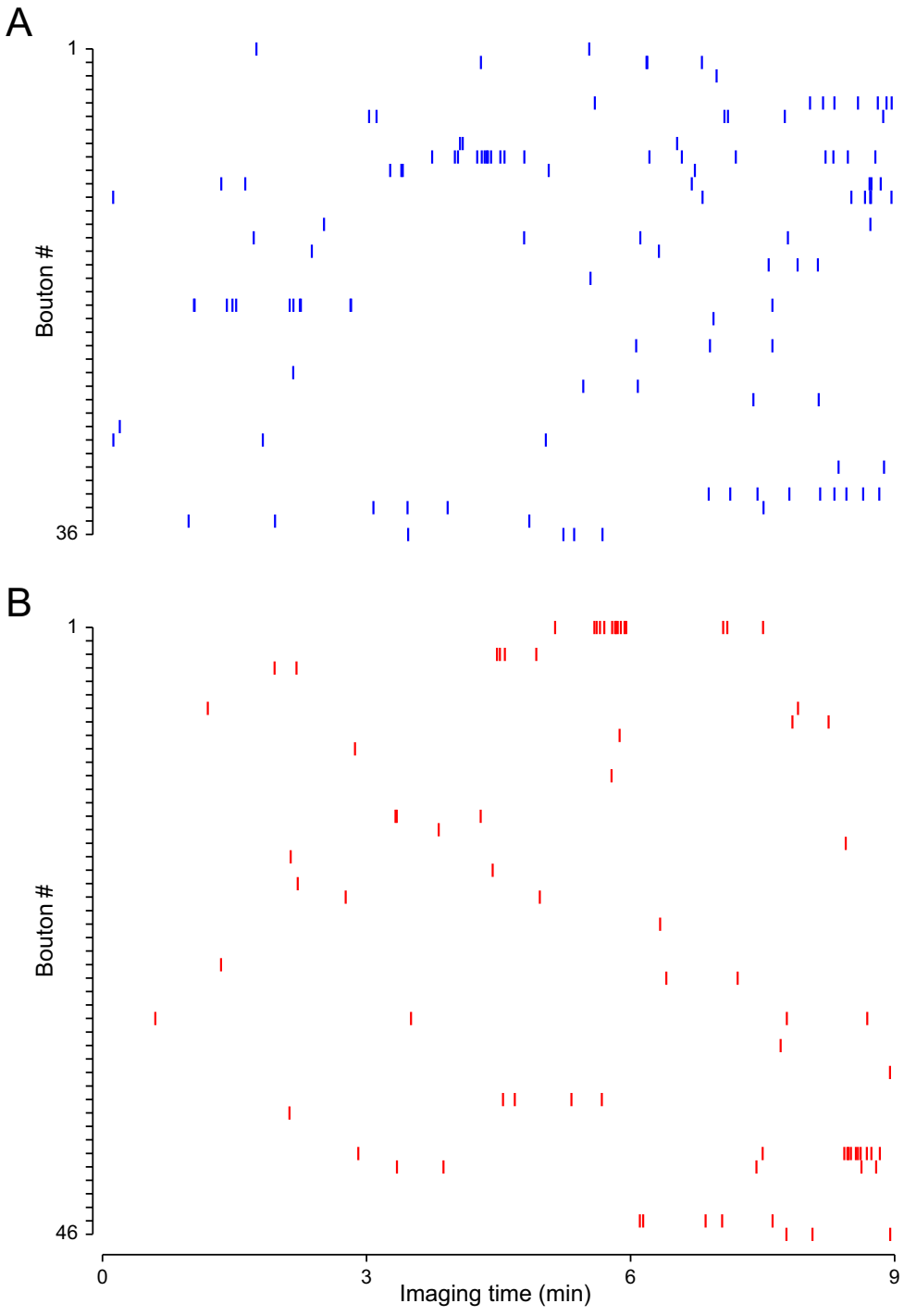

Figure 4.7: sCaTs identified in the presence or absence of caffeine. Each tick represents a spontaneous event identified with or without caffeine (20 mM) added to the superfusate (A or B, respectively). TTX was present in all experiments.

so that the decay time course of the average sCaT measured in caffeine could be revealed. Again, the kinetics of the average sCaT was not altered by caffeine. An exponential fit to its decay phase (p_F = 0.08) yielded a τ of 230 $\pm$ 20 ms, not different from that in the control condition (200 $\pm$ 30 ms; $p_t = 0.4$). This suggests that Ca^{2+} release through RyRs was brief and did not considerably persist during the decay phase of sCaTs.

The χ^2 goodness-of-fit test was performed to assess whether the IEIs, measured in the presence of caffeine, were exponentially distributed (dashed curve in Fig. 4.8B). In Fig. 4.8F, the observed and expected numbers of sCaTs were plotted (blue and dashed, respectively). With $\sim$ 7 sCaTs expected in each bin, there was a total of 13 bins (n = 92 IEIs), each with an expected probability of 0.077. The upper boundary of each bin was calculated using the mean IEI, which was 57 s (see Figure legend). Based on the χ^2-statistic, the null hypothesis that the IEIs followed an exponential distribution was rejected ($p_{\chi^2} = 2 \times 10^{-8}$). This suggests that the release of Ca^{2+} through RyRs, in the presence of caffeine, was unlikely to be a Poisson process. As seen in the control condition, there was an excess of sCaTs with IEIs $\leq$ 10 s.

In this set of experiments, the frequency of sPSCs was also measured to examine the extent to which 20 mM caffeine increased the rate of spontaneous transmitter release in layer 5 pyramidal cells. The majority of sPSCs were of excitatory synaptic origin, as addition of the $GABA_A$ receptor blocker gabazine did not affect their frequency and amplitude (data not shown; also see Simkus and Stricker, 2002b). Fig. 4.9A illustrates a typical recording sequence (2 s long), before the addition of TTX and caffeine (red) and after they were added to the superfusate (blue). During the control period with a total recording duration of 4 min, 4,522 sPSCs were detected; their instantaneous frequencies are plotted in Fig. 4.9B ($t < 0$). The average instantaneous frequency was 45 $\pm$ 1 Hz and the amplitude -11.9 ± 0.1 pA. After addition of TTX and caffeine at $t = 0$ and the resumption of the recording after a gap of 6 min, 6,230 events were detected in the subsequent 3 min. The respective instantaneous frequencies are presented in Fig. 4.9B for $t \geq 6$ min. The average instantaneous frequency during this period was 67 $\pm$ 1 Hz, corresponding to an increase by 51

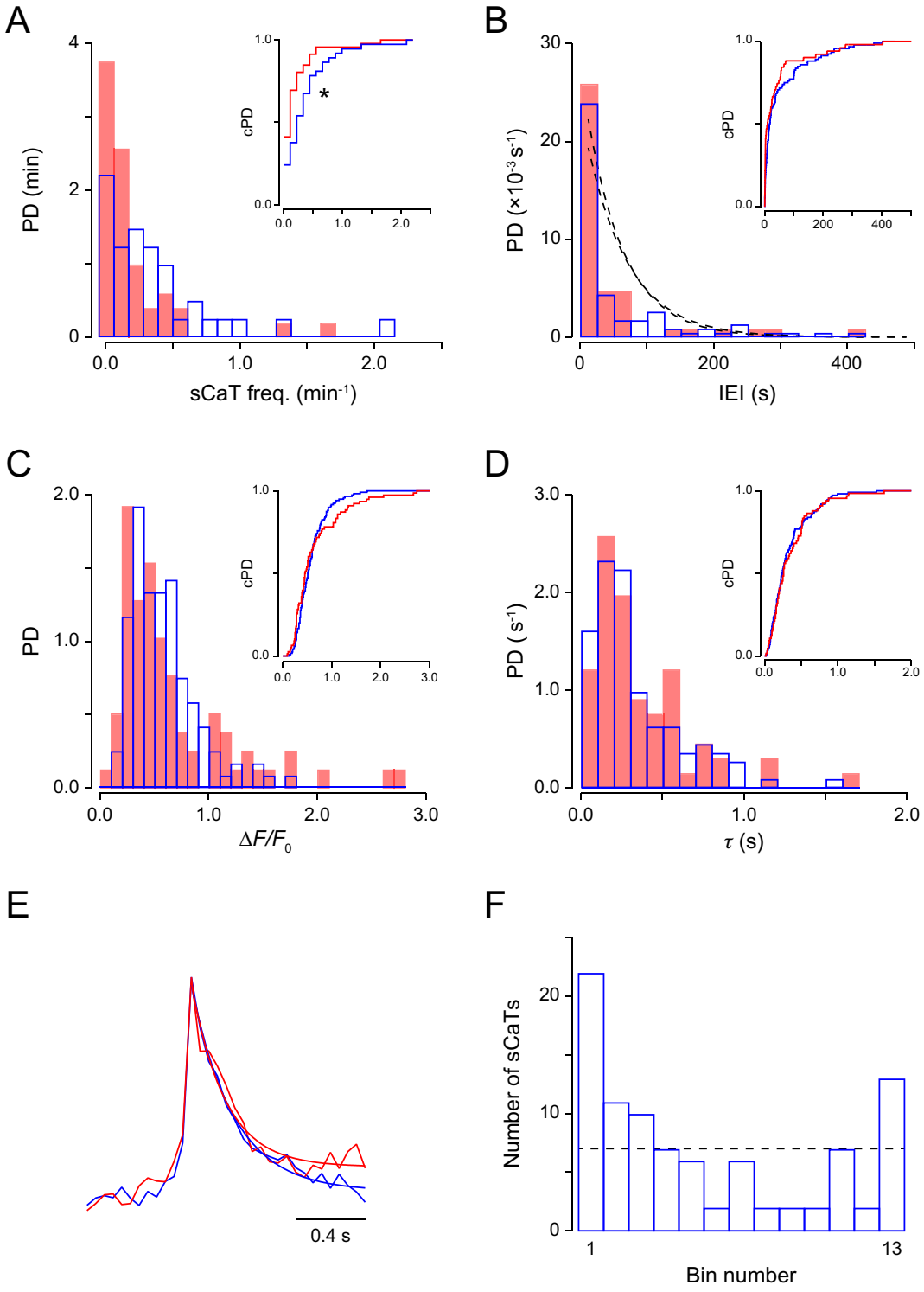

(See next page for figure legend)

Figure 4.8: Characteristics of sCaTs identified after addition of caffeine (blue) compared to those identified in the control condition (red). (A-D) PDFs of the average frequency, IEI, amplitude, and τ of sCaTs. Insets: the corresponding cPDFs. TTX was present in the superfusate in all experiments. In B, plots were fitted with an exponential PDF (dashed). (E) The average sCaT time courses (peak-aligned and scaled) measured in the two experimental conditions, with an exponential function fitted to each decay phase. (F) The observed (blue) *vs.* expected (dashed) numbers of sCaTs. Each bin had an expected probability of 0.077, corresponding to an upper boundary of 4.5, 9.5, 14.9, 20.9, 27.5, 35.1, 43.9, 54.2, 66.9, 83.2, 106.2, 145.5, and ∞ s. * $p_{KS} < 0.05$.

$\pm$ 1% ($p_{KS} \ll 10^{-6}$; Fig. 4.9C). Such an increase in frequency could have arisen if the sPSC amplitude became larger in caffeine. However, sPSCs identified in caffeine had an average amplitude of -13.2 ± 0.2 pA, not different from that measured in the control condition (p_{KS} = 0.07; Fig. 4.9D). The time course of sPSCs was also not affected by caffeine (Fig. 4.9F). Fig. 4.9E displays the instantaneous frequency, averaged for every 0.5 min and normalised to the average value during control. It can be seen that the increase in the instantaneous frequency was maintained throughout the recording period. Accordingly, in this cell, caffeine increased the frequency of sPSCs, without significantly affecting their amplitudes.

Fig. 4.9G presents the average of the instantaneous sPSC frequency in three cells that fulfilled the quality criterion for sPSC recordings (*i.e.* < 20% change in access resistance). Caffeine increased the instantaneous frequency in all of these cells by 47 $\pm$ 14%, from 61 $\pm$ 9 Hz to 88 $\pm$ 11 Hz. In contrast, it inconsistently affected the sPSC amplitude, with no change in one cell (p_{KS} = 0.07; Fig. 4.9D) and a decrease by 10 $\pm$ 1% in the two remaining cells ($p_{KS} \leq 10^{-8}$; -11.6 ± 0.1 *vs.* -10.3 ± 0.1 pA, and -9.5 ± 0.1 *vs.* -8.6 ± 0.1 pA). Thus, in layer 5 pyramidal cells, the stimulatory effect of caffeine on the occurrence of sCaTs was paralleled by its effect on sPSC frequency. This finding led to the hypothesis that sCaTs might underlie spontaneous transmitter release, as has been proposed in synaptic boutons of cultured hippocampal pyramidal neurons (Emptage *et al.*, 2001).

It should be noted here that, as TTX was absent during the control period but added to the superfusate together with caffeine, the extent to which caffeine increased the frequency of sPSCs might have been underestimated. However, this was unlikely

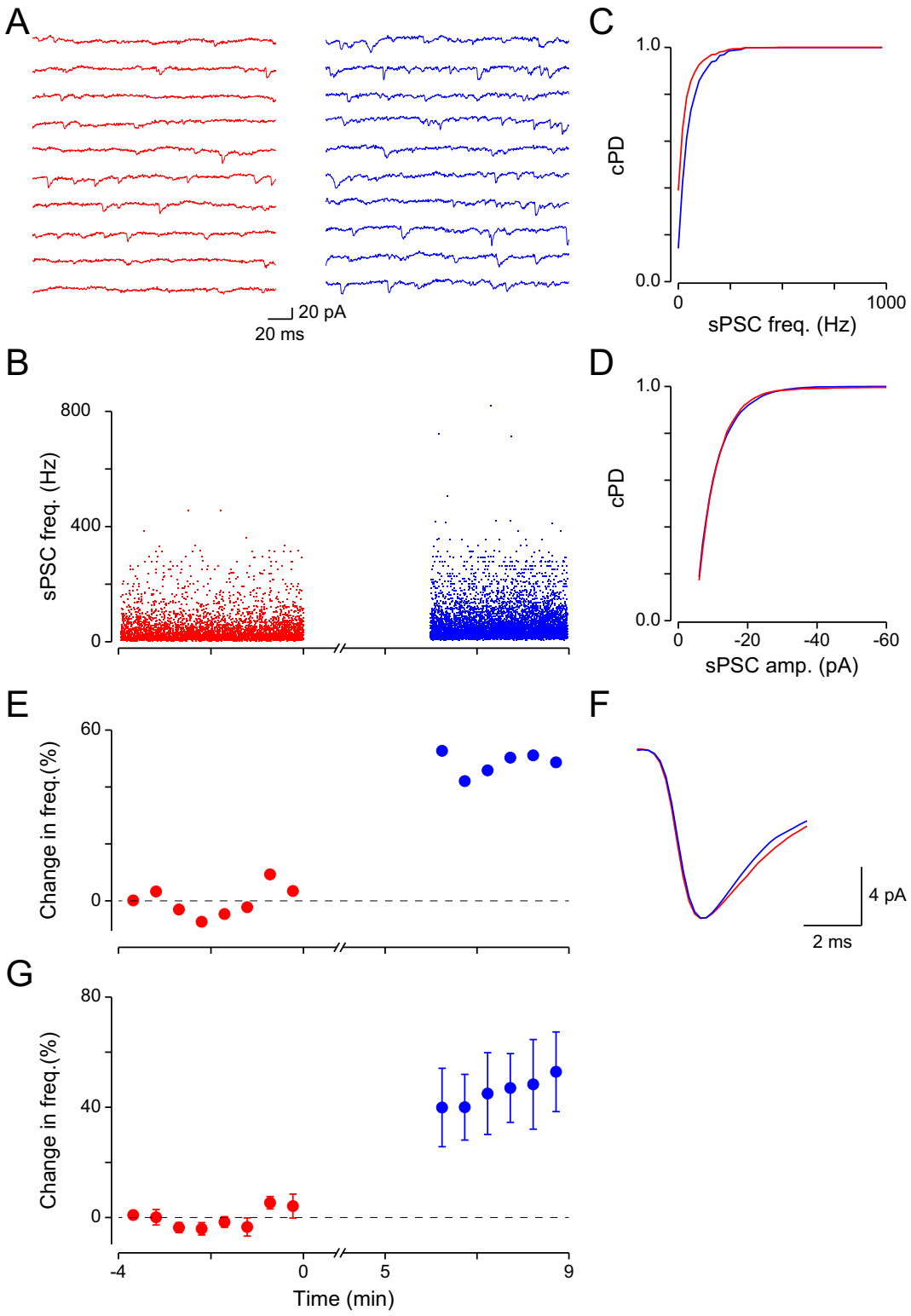

(See next page for figure legend)

Figure 4.9: Caffeine increased the frequency of sPSCs. (A) A 2 s long recording sequence before (red) and after (blue) addition of caffeine and TTX (20 mM and 1 μM, respectively). (B) The instantaneous frequency of individual sPSCs in a layer 5 pyramidal cell, shown for the control period ($t < 0$ min) and after caffeine and TTX were added ($t = 0$ min). (C-D) cPDFs of the instantaneous frequency and amplitude of sPSCs before and after addition of caffeine. (E) The change in instantaneous frequency, averaged for every 0.5 min, of the data in B. (F) The average time courses of sPSCs measured during control and in caffeine. (G) The overall change in instantaneous frequency, averaged for every 0.5 min, in three different cells. In (E-G), dashed lines indicate no change with respect to the average of the 4 min control period.

because, in a different set of experiments ($n = 3$), addition of only TTX did not decrease the frequency of sPSCs (data not shown; also see Simkus and Stricker, 2002b).

4.4 Discussion

This chapter provided direct evidence for the occurrence of sCaTs in synaptic boutons of layer 5 pyramidal neurons. In the absence of exogenous buffers, each sCaT raised $[Ca^{2+}]_i$ by $1.4 - 2.3$ μM. Additionally, it was found that 1) the mechanism underlying sCaTs was unlikely to be Poisson, 2) the average frequency of sCaTs increased after addition of the RyR agonist caffeine, but was unaffected by the IP_3R blocker 2-APB, and 3) both caffeine and 2-APB did not affect the amplitude and decay time course of sCaTs. Together, these findings suggest that a large fraction of sCaTs might have been a result of the spontaneous and brief release of Ca^{2+} through RyRs.

4.4.1 Mechanism(s) underlying sCaTs

4.4.1.1 Intracellular Ca^{2+} release through RyRs

Spontaneously occurring Ca^{2+} transients have previously been observed at the lizard neuromuscular junction (Melamed-Book *et al.*, 1999), synaptic boutons of cultured hippocampal neurons (Emptage *et al.*, 2001), and basket terminals of cerebellar

interneurons (Conti *et al.*, 2004). In these nerve terminals, the frequency of sCaTs was decreased or increased by a high or low concentration of ryanodine, respectively (Emptage *et al.*, 2001; Conti *et al.*, 2004). Similar Ca^{2+} transients have also been reported in dendrites of hippocampal pyramidal neurons, in which their frequency is independent of the activation of ionotropic receptors, but modulated by blockers and agonists of intracellular Ca^{2+} release (Manita and Ross, 2009). Together, these findings indicate that the spontaneous release of Ca^{2+} is a common feature of intracellular stores in neurons.

The observation of sCaTs during whole-cell recordings in TTX and at somatic membrane potentials ≤ -60 mV suggests that sCaTs predominantly arose from intracellular Ca^{2+} release, consistent with previous studies (Melamed-Book *et al.*, 1999; Emptage *et al.*, 2001; Conti *et al.*, 2004; Manita and Ross, 2009). At these membrane potentials, P/Q- and N-type VGCCs, which are the main source of AP-evoked Ca^{2+} transients in synaptic boutons of neocortical pyramidal neurons ($\geq$ 70%; Koester and Sakmann, 2000; Yu *et al.*, 2010), are not appreciably activated (Nowycky *et al.*, 1985; Currie and Fox, 1997). Although Ca^{2+} influx through L- and T-type Ca^{2+} channels, and NMDA receptors, can lead to activation of RyRs (Wang *et al.*, 2001; Manita and Ross, 2009; Tang *et al.*, 2011; Reese and Kavalali, 2015), blockade of VGCCs and NMDA receptors did not affect the frequency of mEPSCs in neocortical pyramidal neurons (Simkus and Stricker, 2002b). Therefore, it is unlikely that VGCCs and/or presynaptic NMDA receptors significantly contributed to the generation of sCaTs.

A number of findings support the conclusion that the spontaneous release of Ca^{2+} occurred mainly through RyRs. First, the amplitude and kinetics of sCaTs in the control condition was the same as those measured after addition of caffeine. Second, the IP_3R antagonist 2-APB did not affect the frequency, amplitude, and decay time constant of sCaTs. Third, less than 5% of the observed sCaTs had fluorescence signals remaining above the detection thresholds for more than 0.5 s. Such sustained Ca^{2+} elevations are preferentially mediated by IP_3Rs, whereas activation of RyRs generally produces a rapid rise in $[Ca^{2+}]_i$, with a time to peak of less than 10 ms

(Wang *et al.*, 2001; Miyazaki and Ross, 2013). However, because of the long sampling interval of 50 ms, the rise time and peak amplitude of most sCaTs were not resolved or detected. Therefore, a contribution of IP_3R-mediated Ca^{2+} release cannot be completely excluded. In fact, in the absence of G-protein activation, 2-APB was found to reduce the frequency of mEPSCs in neocortical layer 2/3 pyramidal neurons (Simkus and Stricker, 2002a). This indicates that IP_3Rs are likely to be constitutively active. Additionally, during synaptic activity, activation of presynaptic metabotropic receptors and subsequently IP_3Rs could promote the occurrence of sCaTs (Manita and Ross, 2009).

The lack of a significant effect of 2-APB could be due to the small number of sCaTs observed in this study. Due to their low frequency, a large number of boutons would need to be imaged to demonstrate a statistically significant reduction in the frequency of sCaTs. This is also one of the reasons why I used an agonist, rather than an antagonist, to investigate whether RyRs mediated sCaTs. The main reason I did not attempt to block RyRs was the unavailability of a blocker that has a high specificity and produces unambiguous results. To my knowledge, the only specific blocker of all RyR isoforms is the plant alkaloid, ryanodine, which causes a complete closure of the channels at high concentrations (≥ 200 μM; Buck *et al.*, 1992). However, between 1 and 100 μM, ryanodine increases the open probability of RyRs, while stabilising them in sub-conducting states (Buck *et al.*, 1992). As these two actions produce opposing effects on the overall Ca^{2+} conductance, the effects of ryanodine are not easy to interpret. For instance, $20 - 30$ μM of ryanodine abolished sCaTs in synaptic boutons and dendrites of hippocampal pyramidal neurons (Emptage *et al.*, 2001; Manita and Ross, 2009). Yet, 10 μM of ryanodine increased the frequency of sCaTs in cerebellar basket terminals (Conti *et al.*, 2004). In addition, Simkus and Stricker (2002a) found that 20 μM of ryanodine (bath-applied for more than 20 min) failed to produce a complete block of RyR-mediated mEPSCs in neocortical pyramidal neurons. Because of the low frequency of sCaTs and the varying effects of ryanodine, I chose to investigate the origin of sCaTs by stimulating RyRs with caffeine.

4.4.1.2 Characteristics of the underlying mechanism(s)

Although sCaTs displayed a decay time course similar to that of a single AP-evoked Ca^{2+} transient, their amplitude was, on average, only $25 - 45\%$ of the latter. This finding is not surprising, considering that different sources of Ca^{2+} most likely underlay these transients. In addition, the open probability of a Ca^{2+} channel, whether it is voltage-gated or not, is most likely very low at rest. Therefore, unless it was significantly amplified by nearby Ca^{2+} channels, a sCaT was unlikely to be as large as an AP-evoked Ca^{2+} transient.

The non-exponential distribution of the IEIs suggests that sCaTs might not be generated by a Poisson process. In fact, the large number of sCaTs with short IEIs indicates that they occurred in clusters. Temporal bunching of sCaTs and RyR-mediated Ca^{2+} sparks has been described in basket terminals of cerebellar interneurons (Conti *et al.*, 2004) and cardiac myocytes (Parker and Wier, 1997), respectively. Similar to those observed in cardiac myocytes, a cluster of sCaTs was often accompanied with a small but sustained increase in the basal fluorescence of OGB-1 (Fig. 4.1). A prolonged elevation in the spatially homogeneous $[Ca^{2+}]_i$ might have sensitised the same or nearby RyRs (Laver, 2007), thereby generating clusters of sCaTs.

It is interesting that 34% of the boutons that were imaged (44 out of 131) displayed no sCaT in the 9 min of imaging. This percentage of "inactive" boutons is larger than that expected for a Poisson process. With an overall average of 2.2 sCaTs *per* bouton, the probability of observing a bouton with no sCaT would have been only 11%. Although the mechanism underlying sCaTs was unlikely to be Poisson, the fact that sCaTs were not detected in 34% of the boutons may indicate variability in the expression of RyRs, ER Ca^{2+} content, and/or resting $[Ca^{2+}]_i$ between presynaptic terminals.

4.4.2 The number of RyRs associated with each sCaT

The present results allow a rough estimation of the number of RyRs that generated individual sCaTs. With a value of $\Delta[Ca^{2+}]_T$ of $11-19$ μM, and assuming that the average volume of the imaged boutons was 0.36 μm^3 (Rollenhagen and Lübke, personal communication), a total of 2,400−4,100 Ca^{2+} ions were released into the cytosol. To approximate the number of RyRs that were open, their mean unitary current was assumed to be 0.5 pA (for quasi-physiological ionic conditions; Mejia-Alvarez *et al.*, 1999; Kettlun *et al.*, 2003). Their mean open time was additionally assumed to be 1 ms (Xu and Meissner, 1998; Cannell *et al.*, 2013). With these assumptions, the opening of each RyR releases $\sim$ 1,600 Ca^{2+} ions. Therefore, a sCaT was generated by the activation of $2-3$ RyRs. Although this value is only a rough estimate, it is in the range of the number of RyRs producing "Ca^{2+} sparks" in cardiac myocytes ($4-6$ RyRs; Wang *et al.*, 2001). This suggests that a sCaT might be equivalent to a "Ca^{2+} spark".

4.4.3 Functional consequences of sCaTs

In the imaged boutons, individual sCaTs increased $[Ca^{2+}]_i$ by $25-45\%$ of that evoked by a single AP. In addition, caffeine increased the frequency of not only sCaTs but also sPSCs. Based on these results, it is proposed that sCaTs can trigger vesicular exocytosis, and therefore, underlie the Ca^{2+}-dependent fraction of spontaneous transmission in neocortical pyramidal neurons (Simkus and Stricker, 2002a). To test this hypothesis, future work will need to simultaneously measure presynaptic sCaTs and postsynaptic mEPSCs. Whether they contribute to spontaneous transmitter release or not, sCaTs may also play important roles in the formation and maintenance of synapses in the absence of neuronal activity (McKinney *et al.*, 1999; Bouchard *et al.*, 2003; Tyler and Pozzo-Miller, 2003).

4.5 Summary

In synaptic boutons of layer 5 pyramidal neurons, sCaTs were likely to arise from the spontaneous and brief release of Ca^{2+} through RyRs. Each sCaT raised $[Ca^{2+}]_i$ by $1.4 - 2.3$ μM, and corresponded to the activation of $2 - 3$ RyRs.

Chapter 5

Conclusion

For a variety of nerve terminals, especially the calyx of Held (Helmchen *et al.*, 1997; Kim *et al.*, 2005; Muller *et al.*, 2007) and mossy fibre boutons (Liang *et al.*, 2002; Lauri *et al.*, 2003; Scott and Rusakov, 2006; Scott *et al.*, 2008; Delvendahl *et al.*, 2015), factors that underlie the spatially homogeneous $[Ca^{2+}]_i$ have been characterised. However, only a few studies have imaged $[Ca^{2+}]_i$ in synaptic boutons of neocortical pyramidal neurons (Cox *et al.*, 2000; Koester and Sakmann, 2000; Buchanan *et al.*, 2012). In particular, at the start of this thesis, there was no study that had systematically characterised factors that shaped the presynaptic Ca^{2+} dynamics in layer 5 pyramidal neurons. This thesis aimed to measure AP-evoked and spontaneous Ca^{2+} transients in synaptic boutons of these neurons, in order to determine the endogenous Ca^{2+} binding ratio and the rate constant of Ca^{2+} sequestration, to reveal the Ca^{2+} dynamics in the absence of exogenous buffers, and to provide evidence for Ca^{2+} release from presynaptic stores.

5.1 Key findings and implications

In Chapter 2, the Ca^{2+} binding affinities (K_d) of several fluorescent Ca^{2+} indicators were measured in calibrating solutions that mimicked the patch-clamp internal solution. It was shown that Maxchelator, a freely available computer program, provided inaccurate estimates of the K_d values of commonly used Ca^{2+} buffers, such as EGTA and HEDTA. In addition, the purity of EGTA was not as advertised by

the manufacturer. Therefore, the use of Maxchelator and the assumption of 100% buffer purity yielded inaccurate and inconsistent estimates of the free concentration of Ca^{2+} in Ca^{2+}-buffer solutions. This has implications for the published values of K_d of Ca^{2+} dyes and thus of $[Ca^{2+}]_i$, suggesting that they may have an error of up to 200%. To avoid this pitfall, the free $[Ca^{2+}]$ in the calibrating solutions was measured with a Ca^{2+}-selective macroelectrode. This allowed an accurate determination of the K_d values of the fluorescent Ca^{2+} indicators. In the subsequent chapters, these measured K_d values enabled $[Ca^{2+}]_i$ to be calculated from the fluorescence intensity of the Ca^{2+} indicators.

In Chapter 3, AP-evoked Ca^{2+} transients were measured in synaptic boutons of layer 5 pyramidal neurons. Based on these measurements, the endogenous Ca^{2+} binding ratio (κ_E), the rate constant of Ca^{2+} sequestration, and the amplitude and time course of an AP-evoked Ca^{2+} transient with no added buffer were estimated in accordance with the single-compartment model (Neher and Augustine, 1992). It was found that the imaged boutons had a very small value of κ_E. This allowed $[Ca^{2+}]_i$ to rise by $\sim$ 5 μM in response a single AP and in the absence of exogenous buffers. A low κ_E and a large Ca^{2+} rise may be required for the efficacy, reliability, and synchronicity of evoked transmitter release, and facilitate the induction of Ca^{2+}-dependent cellular processes.

Additionally, Chapter 3 demonstrated that, in a small bouton-type synapse, diffusion of Ca^{2+} into the axon can significantly speed up the decay time course of an AP-evoked Ca^{2+} transient. Based on the estimated values of κ_E and the total Ca^{2+} influx, a 3D reaction-diffusion model was created to reproduce the measured Ca^{2+} transients. This model showed that, due to the small size of the imaged boutons and the fact that they were *boutons en passant*, Ca^{2+} was able to escape into the axon immediately after an AP-evoked Ca^{2+} influx. Therefore, a bouton-type synapse is not a truly single compartment, where diffusion is negligible. Any changes to the axon diameter or the apparent mobility of Ca^{2+} would affect the rate of Ca^{2+} decay. Consistently, in the presence of fluorescent Ca^{2+} indicators, which increased the diffusion of Ca^{2+} into the axon, an AP-evoked Ca^{2+} transient exhibited an initial

fast drop, followed by a much slower decay. The slow decay phase was mainly determined by Ca^{2+} sequestration mechanisms, including intracellular Ca^{2+} uptake. In contrast, the dynamics of the spatially homogeneous $[Ca^{2+}]_i$ in these boutons were unlikely shaped by saturation of endogenous Ca^{2+} buffers or by buffers with slow Ca^{2+} binding kinetics.

Chapter 3 also demonstrated a supralinear summation of $[Ca^{2+}]_i$ during high-frequency trains of APs. Facilitation of presynaptic Ca^{2+} currents and saturation of Ca^{2+} sequestration were unlikely to underlie this phenomenon. Instead, it most likely arose from Ca^{2+} release from intracellular stores. The supralinear build-up of $[Ca^{2+}]_i$ may have considerable biological significance, such as induction of activity-dependent presynaptic plasticity.

By providing direct evidence for spontaneous Ca^{2+} transients (sCaTs), chapter 4 showed that presynaptic Ca^{2+} stores may also contribute to spontaneous transmitter release. As in synaptic boutons of hippocampal neurons and cerebellar basket terminals (Emptage *et al.*, 2001; Conti *et al.*, 2004), the observed sCaTs were most likely a result of spontaneous and brief release of Ca^{2+} through ryanodine receptors. In the absence of exogenous buffers, the change in $[Ca^{2+}]_i$ associated with each sCaT was almost half of that evoked by a single AP. This suggests that sCaTs could potentially trigger transmitter release, if synaptic vesicles are located in the vicinity (≤ 100 nm) of the open channels. The value of κ_E, determined in Chapter 3, allowed the total Ca^{2+} flux associated with each sCaT to be estimated. This in turn allowed a rough estimation of the number of ryanodine receptors involved in its generation. It was concluded that a sCaT could be produced by the activation of $2-3$ ryanodine receptors, and thus, was equivalent to a "Ca^{2+} spark" in cardiac myocytes.

5.2 Concluding remark

This thesis revealed important factors that shape the spatially homogeneous $[Ca^{2+}]_i$ in synaptic boutons of neocortical pyramidal neurons. It also extends a growing body

of evidence supporting the role of presynaptic Ca^{2+} stores in synaptic transmission and short-term plasticity. Mutations or alterations in the expression of Ca^{2+} channels, buffers, and transporters have been suggested to underlie a multitude of neurological disorders, ranging from migraine, epilepsy, to neurodegenerative diseases (Schwaller *et al.*, 2002; Brini and Carafoli, 2009; Bezprozvanny, 2011; Brini and Carafoli, 2011; Catterall, 2011; Del Prete *et al.*, 2014). In addition, dysfunction of presynaptic Ca^{2+} stores, which impairs neurotransmitter release and disrupts the induction of synaptic plasticity, might be an early pathogenic event leading to Alzheimer's disease (Zhang *et al.*, 2009). Therefore, a detailed investigation of mechanisms that control the presynaptic Ca^{2+} dynamics, and how they regulate synaptic transmission and plasticity, promises important insights into the pathogenesis of neurological disorders and may offer therapeutic targets.

Appendix A

Estimation of dye saturation

The maximum change in fluorescence of OGB-1 ($(\Delta F/F_0)_{\max}$) was determined by comparing its relative changes ($\Delta F/F_0$) during two trains of APs at different frequencies. This analysis was based on Maravall *et al.* (2000). Here, Eq. 3.3 is re-derived to extend beyond the assumption of linear summation of $[Ca^{2+}]_i$ during the AP trains. A similar derivation was found in Appendix A of Maravall *et al.* (2000).

The fluorescence intensity (F) of a non-ratiometric Ca^{2+} indicator can be written as

$$\begin{aligned} F &= S_D[D] + S_{DCa}[DCa] \\ &= S_D([D]_T - [DCa]) + S_{DCa}[DCa] \\ &= S_D[D]_T + (S_{DCa} - S_D)[DCa], \end{aligned}$$

where S_D and S_{DCa} are constants that describe the brightness of the indicator when it is free of and bound to Ca^{2+}, respectively, $[D]_T$ is the total concentration of the indicator, $[DCa]$ is the concentration of Ca^{2+}-bound indicator molecules, and $[D]$ is the concentration of free indicator molecules. By analogy, the baseline fluorescence (F_0) of the Ca^{2+} indicator can be written as

$$F_0 = S_D[D]_T + (S_{DCa} - S_D)[DCa]_0,$$

where $[\mathrm{DCa}]_0$ is the concentration of Ca^{2+}-bound indicator molecules at baseline. Accordingly, during a train of APs, the change in fluorescence intensity of the Ca^{2+} indicator can be expressed as

$$\begin{aligned}\Delta F &= F - F_0 \\ &= (S_{\mathrm{DCa}} - S_{\mathrm{D}})([\mathrm{DCa}] - [\mathrm{DCa}]_0) \\ &= (S_{\mathrm{DCa}} - S_{\mathrm{D}})\Delta[\mathrm{DCa}]. \end{aligned} \tag{A.1}$$

Eq. A.1 shows that the change in fluorescence intensity of a non-ratiometric Ca^{2+} indicator is proportional to the change in concentration of Ca^{2+}-bound indicator molecules; that is, $\Delta F \propto \Delta[\mathrm{DCa}]$. Based on the law of mass action,

$$[\mathrm{DCa}] = \frac{[\mathrm{D}]_{\mathrm{T}}[\mathrm{Ca}^{2+}]_{\mathrm{i}}}{K_{\mathrm{d}} + [\mathrm{Ca}^{2+}]_{\mathrm{i}}}. \tag{A.2}$$

Therefore,

$$\begin{aligned}\Delta F &\propto \left(\frac{[\mathrm{Ca}^{2+}]_{\mathrm{i}}}{K_{\mathrm{d}} + [\mathrm{Ca}^{2+}]_{\mathrm{i}}} - \frac{[\mathrm{Ca}^{2+}]_{\mathrm{rest}}}{K_{\mathrm{d}} + [\mathrm{Ca}^{2+}]_{\mathrm{rest}}} \right) \\ &\propto \left[\frac{K_{\mathrm{d}}([\mathrm{Ca}^{2+}]_{\mathrm{i}} - [\mathrm{Ca}^{2+}]_{\mathrm{rest}})}{(K_{\mathrm{d}} + [\mathrm{Ca}^{2+}]_{\mathrm{i}})(K_{\mathrm{d}} + [\mathrm{Ca}^{2+}]_{\mathrm{rest}})} \right] \\ &\propto \left[\frac{\Delta[\mathrm{Ca}^{2+}]_{\mathrm{i}}}{(K_{\mathrm{d}} + [\mathrm{Ca}^{2+}]_{\mathrm{i}})(K_{\mathrm{d}} + [\mathrm{Ca}^{2+}]_{\mathrm{rest}})} \right]. \end{aligned}$$

Let Q be the ratio between the fluorescence changes during two trains of APs at different frequencies v_1 and v_2; that is, $Q = \frac{(\Delta F/F_0)_{v_2}}{(\Delta F/F_0)_{v_1}}$. Then,

$$
\begin{aligned}
Q &= \frac{(\Delta F)_{v_2}}{(\Delta F)_{v_1}} \\
&= \frac{\Delta[\mathrm{Ca}^{2+}]_{v_2}}{\Delta[\mathrm{Ca}^{2+}]_{v_1}} \times \frac{K_\mathrm{d} + [\mathrm{Ca}^{2+}]_{v_1}}{K_\mathrm{d} + [\mathrm{Ca}^{2+}]_{v_2}}.
\end{aligned} \tag{A.3}
$$

Let $\Delta[\mathrm{Ca}^{2+}]$ be simplified as Δ. The second factor on the right-hand side of Eq. A.3 is thus

$$
\begin{aligned}
\frac{K_\mathrm{d} + [\mathrm{Ca}^{2+}]_{v_1}}{K_\mathrm{d} + [\mathrm{Ca}^{2+}]_{v_2}} &= \frac{K_\mathrm{d} + \Delta_1 + [\mathrm{Ca}^{2+}]_\mathrm{rest}}{K_\mathrm{d} + \Delta_2 + [\mathrm{Ca}^{2+}]_\mathrm{rest}} \\
&= \frac{K_\mathrm{d} + \Delta_1 + [\mathrm{Ca}^{2+}]_\mathrm{rest} + (\Delta_2 - \Delta_2)}{K_\mathrm{d} + \Delta_2 + [\mathrm{Ca}^{2+}]_\mathrm{rest}} \\
&= 1 + \frac{\Delta_1 - \Delta_2}{K_\mathrm{d} + \Delta_2 + [\mathrm{Ca}^{2+}]_\mathrm{rest}} \\
&= 1 + \frac{\Delta_1 - \Delta_2}{K_\mathrm{d} + \Delta_2 + [\mathrm{Ca}^{2+}]_\mathrm{rest}} \times \frac{\Delta_2}{\Delta_2} \\
&= 1 + \frac{\Delta_2}{K_\mathrm{d} + \Delta_2 + [\mathrm{Ca}^{2+}]_\mathrm{rest}} \times \frac{\Delta_1 - \Delta_2}{\Delta_2} \\
&= 1 + \frac{\Delta_2}{K_\mathrm{d} + \Delta_2 + [\mathrm{Ca}^{2+}]_\mathrm{rest}} \times \left(\frac{\Delta_1}{\Delta_2} - 1 \right).
\end{aligned}
$$

As $[\mathrm{Ca}^{2+}]_\mathrm{rest} \ll \Delta_2$, this factor can be approximated as

$$
\begin{aligned}
\frac{K_\mathrm{d} + [\mathrm{Ca}^{2+}]_{v_1}}{K_\mathrm{d} + [\mathrm{Ca}^{2+}]_{v_2}} &\approx 1 + \frac{\Delta_2 + [\mathrm{Ca}^{2+}]_\mathrm{rest}}{K_\mathrm{d} + \Delta_2 + [\mathrm{Ca}^{2+}]_\mathrm{rest}} \times \left(\frac{\Delta_1}{\Delta_2} - 1 \right) \\
&\approx 1 + \frac{[\mathrm{Ca}^{2+}]_{v_2}}{K_\mathrm{d} + [\mathrm{Ca}^{2+}]_{v_2}} \times \left(\frac{\Delta_1}{\Delta_2} - 1 \right).
\end{aligned}
$$

Using the law of mass action (Eq. A.2), this can be re-written as

$$
\frac{K_\mathrm{d} + [\mathrm{Ca}^{2+}]_{v_1}}{K_\mathrm{d} + [\mathrm{Ca}^{2+}]_{v_2}} \approx 1 + \frac{[\mathrm{DCa}]_{v_2}}{[\mathrm{D}]_\mathrm{T}} \times \left(\frac{\Delta_1}{\Delta_2} - 1 \right). \tag{A.4}
$$

Let x_{v_2} be the level of saturation of the Ca^{2+} indicator during an AP train at frequency v_2. According to Eq. A.1,

$$\begin{aligned} x_{v_2} &= \frac{\left(\Delta F/F_0\right)_{v_2}}{\left(\Delta F/F_0\right)_{\max}} \\ &= \frac{\left(\Delta F\right)_{v_2}}{\left(\Delta F\right)_{\max}} \\ &= \frac{\left(\Delta [\mathrm{DCa}]\right)_{v_2}}{\left(\Delta [\mathrm{DCa}]\right)_{\max}} \\ &= \frac{[\mathrm{DCa}]_{v_2} - [\mathrm{DCa}]_0}{[\mathrm{DCa}]_{\max} - [\mathrm{DCa}]_0} \\ &= \frac{[\mathrm{DCa}]_{v_2} - [\mathrm{DCa}]_0}{[\mathrm{D}]_\mathrm{T} - [\mathrm{DCa}]_0} \\ &= \frac{\dfrac{[\mathrm{DCa}]_{v_2}}{[\mathrm{D}]_\mathrm{T}} - \dfrac{[\mathrm{DCa}]_0}{[\mathrm{D}]_\mathrm{T}}}{1 - \dfrac{[\mathrm{DCa}]_0}{[\mathrm{D}]_\mathrm{T}}}. \end{aligned}$$

Rearranging this equation yields

$$\frac{[\mathrm{DCa}]_{v_2}}{[\mathrm{D}]_\mathrm{T}} = \left(1 - \frac{[\mathrm{DCa}]_0}{[\mathrm{D}]_\mathrm{T}}\right) x_{v_2} + \frac{[\mathrm{DCa}]_0}{[\mathrm{D}]_\mathrm{T}}. \tag{A.5}$$

Using Eqs. A.4 and A.5, Eq. A.3 can be re-written as follows:

$$Q = \frac{\Delta_2}{\Delta_1} \times \left\{1 + \left[\left(1 - \frac{[\mathrm{DCa}]_0}{[\mathrm{D}]_\mathrm{T}}\right) x_{v_2} + \frac{[\mathrm{DCa}]_0}{[\mathrm{D}]_\mathrm{T}}\right] \times \left(\frac{\Delta_1}{\Delta_2} - 1\right)\right\}.$$

Consequently,

$$x_{v_2} = \frac{\dfrac{Q\dfrac{\Delta_1}{\Delta_2} - 1}{\dfrac{\Delta_1}{\Delta_2} - 1} - \dfrac{[\mathrm{DCa}]_0}{[\mathrm{D}]_\mathrm{T}}}{1 - \dfrac{[\mathrm{DCa}]_0}{[\mathrm{D}]_\mathrm{T}}}.$$

References

Adler, E. M., Augustine, G. J., Duffy, S. N., and Charlton, M. P. (1991). Alien intracellular calcium chelators attenuate neurotransmitter release at the squid giant synapse. *J Neurosci* 11, 1496–507.

Alabi, A. A. and Tsien, R. W. (2013). Perspectives on kiss-and-run: role in exocytosis, endocytosis, and neurotransmission. *Annu Rev Physiol* 75, 393–422.

Ali, A. B. and Nelson, C. (2006). Distinct Ca^{2+} channels mediate transmitter release at excitatory synapses displaying different dynamic properties in rat neocortex. *Cereb Cortex* 16, 386–93.

Allbritton, N. L., Meyer, T., and Stryer, L. (1992). Range of messenger action of calcium ion and inositol 1,4,5-trisphosphate. *Science* 258, 1812–5.

Altimimi, H. F. and Schnetkamp, P. P. (2007). Na^+/Ca^{2+}-K^+ exchangers (NCKX): functional properties and physiological roles. *Channels (Austin)* 1, 62–9.

Alvarez-Leefmans, F. J., Gamino, S. M., and Rink, T. J. (1984). Intracellular free magnesium in neurones of Helix aspersa measured with ion-selective micro-electrodes. *J Physiol* 354, 303–17.

Atluri, P. P. and Regehr, W. G. (1996). Determinants of the time course of facilitation at the granule cell to Purkinje cell synapse. *J Neurosci* 16, 5661–71.

Atluri, P. P. and Regehr, W. G. (1998). Delayed release of neurotransmitter from cerebellar granule cells. *J Neurosci* 18, 8214–27.

Augustine, G. J. (1990). Regulation of transmitter release at the squid giant synapse by presynaptic delayed rectifier potassium current. *J Physiol* 431, 343–64.

Augustine, G. J., Charlton, M. P., and Smith, S. J. (1985). Calcium entry and transmitter release at voltage-clamped nerve terminals of squid. *J Physiol* 367, 163–81.

Augustine, G. J. and Eckert, R. (1984). Divalent cations differentially support transmitter release at the squid giant synapse. *J Physiol* 346, 257–71.

Augustine, G. J. and Neher, E. (1992). Calcium requirements for secretion in bovine chromaffin cells. *J Physiol* 450, 247–71.

Babai, N., Kochubey, O., Keller, D., and Schneggenburger, R. (2014). An alien divalent ion reveals a major role for Ca^{2+} buffering in controlling slow transmitter release. *J Neurosci* 34, 12622–35.

Bacaj, T., Wu, D., Yang, X., Morishita, W., Zhou, P., Xu, W., Malenka, R. C., and Sudhof, T. C. (2013). Synaptotagmin-1 and synaptotagmin-7 trigger synchronous and asynchronous phases of neurotransmitter release. *Neuron* 80, 947–59.

Banerjee, A., Larsen, R. S., Philpot, B. D., and Paulsen, O. (2016). Roles of presynaptic NMDA receptors in neurotransmission and plasticity. *Trends Neurosci* 39, 26–39.

Bao, J., Li, J. J., and Perl, E. R. (1998). Differences in Ca^{2+} channels governing generation of miniature and evoked excitatory synaptic currents in spinal laminae I and II. *J Neurosci* 18, 8740–50.

Barrett, E. F. and Stevens, C. F. (1972). The kinetics of transmitter release at the frog neuromuscular junction. *J Physiol* 227, 691–708.

Baughman, J. M., Perocchi, F., Girgis, H. S., Plovanich, M., Belcher-Timme, C. A., Sancak, Y., Bao, X. R., Strittmatter, L., Goldberger, O., Bogorad, R. L., Koteliansky, V., and Mootha, V. K. (2011). Integrative genomics identifies MCU as an essential component of the mitochondrial calcium uniporter. *Nature* 476, 341–5.

Baylor, S. M. and Hollingworth, S. (1998). Model of sarcomeric Ca^{2+} movements, including ATP Ca^{2+} binding and diffusion, during activation of frog skeletal muscle. *J Gen Physiol* 112, 297–316.

Beck, A., Nieden, R. Z., Schneider, H. P., and Deitmer, J. W. (2004). Calcium release from intracellular stores in rodent astrocytes and neurons in situ. *Cell Calcium* 35, 47–58.

Beierlein, M., Fioravante, D., and Regehr, W. G. (2007). Differential expression of posttetanic potentiation and retrograde signaling mediate target-dependent short-term synaptic plasticity. *Neuron* 54, 949–59.

Benech, J. C., Crispino, M., Kaplan, B. B., and Giuditta, A. (1999). Protein synthesis in presynaptic endings from squid brain: modulation by calcium ions. *J Neurosci Res* 55, 776–81.

Bennett, M. V. (1997). Gap junctions as electrical synapses. *J Neurocytol* 26, 349–66.

Bennett, M. V., Aljure, E., Nakajima, Y., and Pappas, G. D. (1963). Electrotonic junctions between teleost spinal neurons: electrophysiology and ultrastructure. *Science* 141, 262–4.

Bers, D. M. (1982). A simple method for the accurate determination of free Ca^{2+} in Ca-EGTA solutions. *Am J Physiol* 242, C404–8.

Bers, D. M., Patton, C. W., and Nuccitelli, R. (2010). A practical guide to the preparation of Ca^{2+} buffers. *Methods Cell Biol* 99, 1–26.

Bertram, R., Sherman, A., and Stanley, E. F. (1996). Single-domain/bound calcium hypothesis of transmitter release and facilitation. *J Neurophysiol* 75, 1919–31.

Best, A. R. and Regehr, W. G. (2009). Inhibitory regulation of electrically coupled neurons in the inferior olive is mediated by asynchronous release of GABA. *Neuron* 62, 555–65.

Betz, W. J. (1970). Depression of transmitter release at the neuromuscular junction of the frog. *J Physiol* 206, 629–44.

Beutner, D., Voets, T., Neher, E., and Moser, T. (2001). Calcium dependence of exocytosis and endocytosis at the cochlear inner hair cell afferent synapse. *Neuron* 29, 681–90.

Bezprozvanny, I. (2011). Role of inositol 1,4,5-trisphosphate receptors in pathogenesis of Huntington's disease and spinocerebellar ataxias. *Neurochem Res* 36, 1186–97.

Bezprozvanny, I., Bezprozvannaya, S., and Ehrlich, B. E. (1994). Caffeine-induced inhibition of inositol(1,4,5)-trisphosphate-gated calcium channels from cerebellum. *Mol Biol Cell* 5, 97–103.

Bezprozvanny, I. and Ehrlich, B. E. (1994). Inositol (1,4,5)-trisphosphate ($InsP_3$)-gated Ca^{2+} channels from cerebellum: conduction properties for divalent cations and regulation by intraluminal calcium. *J Gen Physiol* 104, 821–56.

Bezprozvanny, I. B., Ondrias, K., Kaftan, E., Stoyanovsky, D. A., and Ehrlich, B. E. (1993). Activation of the calcium release channel (ryanodine receptor) by heparin and other polyanions is calcium dependent. *Mol Biol Cell* 4, 347–52.

Bhalla, A., Chicka, M. C., Tucker, W. C., and Chapman, E. R. (2006). Ca^{2+}-synaptotagmin directly regulates t-SNARE function during reconstituted membrane fusion. *Nat Struct Mol Biol* 13, 323–30.

Bianchi, K., Rimessi, A., Prandini, A., Szabadkai, G., and Rizzuto, R. (2004). Calcium and mitochondria: mechanisms and functions of a troubled relationship. *Biochim Biophys Acta* 1742, 119–31.

Biber, A., Schmid, G., and Hempel, K. (1984). Calmodulin content in specific brain areas. *Exp Brain Res* 56, 323–6.

Billups, B. and Forsythe, I. D. (2002). Presynaptic mitochondrial calcium sequestration influences transmission at mammalian central synapses. *J Neurosci* 22, 5840–7.

Bischofberger, J., Geiger, J. R., and Jonas, P. (2002). Timing and efficacy of Ca^{2+} channel activation in hippocampal mossy fiber boutons. *J Neurosci* 22, 10593–602.

Blankenship, J. E. and Kuno, M. (1968). Analysis of spontaneous subthreshold activity in spinal motoneurons of the cat. *J Neurophysiol* 31, 195–209.

Blatow, M., Caputi, A., Burnashev, N., Monyer, H., and Rozov, A. (2003). Ca^{2+} buffer saturation underlies paired pulse facilitation in calbindin-D28k-containing terminals. *Neuron* 38, 79–88.

Blaustein, M. P., Juhaszova, M., Golovina, V. A., Church, P. J., and Stanley, E. F. (2002). Na^{+}/Ca^{2+} exchanger and PMCA localization in neurons and astrocytes: functional implications. *Ann N Y Acad Sci* 976, 356–66.

Blaustein, M. P., Kao, J. P. Y., and Matteson, D. R. (2004). Active transport. In *Cellular Physiology: Mosby's Physiology Monograph Series* 149–175. Elsevier, Philadelphia, Pennsylvania, USA 1st (first) edn.

Blaustein, M. P. and Lederer, W. J. (1999). Sodium/calcium exchange: its physiological implications. *Physiol Rev* 79, 763–854.

Bollmann, J. H. and Sakmann, B. (2005). Control of synaptic strength and timing by the release-site Ca^{2+} signal. *Nat Neurosci* 8, 426–34.

Bollmann, J. H., Sakmann, B., and Borst, J. G. (2000). Calcium sensitivity of glutamate release in a calyx-type terminal. *Science* 289, 953–7.

Bonanomi, D., Benfenati, F., and Valtorta, F. (2006). Protein sorting in the synaptic vesicle life cycle. *Prog Neurobiol* 80, 177–217.

Bootman, M. D., Collins, T. J., Mackenzie, L., Roderick, H. L., Berridge, M. J., and Peppiatt, C. M. (2002). 2-aminoethoxydiphenyl borate (2-APB) is a reliable blocker of store-operated Ca^{2+} entry but an inconsistent inhibitor of $InsP_3$-induced Ca^{2+} release. *FASEB J* 16, 1145–50.

Borst, J. G. and Sakmann, B. (1996). Calcium influx and transmitter release in a fast CNS synapse. *Nature* 383, 431–4.

Borst, J. G. and Sakmann, B. (1998a). Calcium current during a single action potential in a large presynaptic terminal of the rat brainstem. *J Physiol* 506 (Pt 1), 143–57.

Borst, J. G. and Sakmann, B. (1998b). Facilitation of presynaptic calcium currents in the rat brainstem. *J Physiol* 513 (Pt 1), 149–55.

Bouchard, R., Pattarini, R., and Geiger, J. D. (2003). Presence and functional significance of presynaptic ryanodine receptors. *Prog Neurobiol* 69, 391–418.

Boyd, I. A. and Martin, A. R. (1956). Spontaneous subthreshold activity at mammalian neural muscular junctions. *J Physiol* 132, 61–73.

Boyman, L., Williams, G. S., Khananshvili, D., Sekler, I., and Lederer, W. J. (2013). NCLX: the mitochondrial sodium calcium exchanger. *J Mol Cell Cardiol* 59, 205–13.

Brager, D. H., Cai, X., and Thompson, S. M. (2003). Activity-dependent activation of presynaptic protein kinase C mediates post-tetanic potentiation. *Nat Neurosci* 6, 551–2.

Brenowitz, S. D. and Regehr, W. G. (2007). Reliability and heterogeneity of calcium signaling at single presynaptic boutons of cerebellar granule cells. *J Neurosci* 27, 7888–98.

Breustedt, J. and Schmitz, D. (2004). Assessing the role of GLUK5 and GLUK6 at hippocampal mossy fiber synapses. *J Neurosci* 24, 10093–8.

Breustedt, J., Vogt, K. E., Miller, R. J., Nicoll, R. A., and Schmitz, D. (2003). Alpha1e-containing Ca^{2+} channels are involved in synaptic plasticity. *Proc Natl Acad Sci U S A* 100, 12450–5.

Brini, M. and Carafoli, E. (2009). Calcium pumps in health and disease. *Physiol Rev* 89, 1341–78.

Brini, M. and Carafoli, E. (2011). The plasma membrane Ca^{2+} ATPase and the plasma membrane sodium calcium exchanger cooperate in the regulation of cell calcium. *Cold Spring Harb Perspect Biol* 3.

Brocard, J. B., Rajdev, S., and Reynolds, I. J. (1993). Glutamate-induced increases in intracellular free Mg^{2+} in cultured cortical neurons. *Neuron* 11, 751–7.

Brock, L. G., Coombs, J. S., and Eccles, J. C. (1952). The recording of potentials from motoneurones with an intracellular electrode. *J Physiol* 117, 431–60.

Brose, N., Petrenko, A. G., Sudhof, T. C., and Jahn, R. (1992). Synaptotagmin: a calcium sensor on the synaptic vesicle surface. *Science* 256, 1021–5.

Buchanan, K. A., Blackman, A. V., Moreau, A. W., Elgar, D., Costa, R. P., Lalanne, T., Tudor Jones, A. A., Oyrer, J., and Sjostrom, P. J. (2012). Target-specific expression of presynaptic NMDA receptors in neocortical microcircuits. *Neuron* 75, 451–66.

Buck, E., Zimanyi, I., Abramson, J. J., and Pessah, I. N. (1992). Ryanodine stabilizes multiple conformational states of the skeletal muscle calcium release channel. *J Biol Chem* 267, 23560–7.

Bucurenciu, I., Bischofberger, J., and Jonas, P. (2010). A small number of open Ca^{2+} channels trigger transmitter release at a central GABAergic synapse. *Nat Neurosci* 13, 19–21.

Bucurenciu, I., Kulik, A., Schwaller, B., Frotscher, M., and Jonas, P. (2008). Nanodomain coupling between Ca^{2+} channels and Ca^{2+} sensors promotes fast and efficient transmitter release at a cortical GABAergic synapse. *Neuron* 57, 536–45.

Bull, R. and Marengo, J. J. (1993). Sarcoplasmic reticulum release channels from frog skeletal muscle display two types of calcium dependence. *FEBS Lett* 331, 223–7.

Burgalossi, A., Jung, S., Meyer, G., Jockusch, W. J., Jahn, O., Taschenberger, H., O'Connor, V. M., Nishiki, T., Takahashi, M., Brose, N., and Rhee, J. S. (2010). SNARE protein recycling by alphaSNAP and betaSNAP supports synaptic vesicle priming. *Neuron* 68, 473–87.

Burkhardt, P., Hattendorf, D. A., Weis, W. I., and Fasshauer, D. (2008). Munc18a controls SNARE assembly through its interaction with the syntaxin N-peptide. *EMBO J* 27, 923–33.

Caillard, O., Moreno, H., Schwaller, B., Llano, I., Celio, M. R., and Marty, A. (2000). Role of the calcium-binding protein parvalbumin in short-term synaptic plasticity. *Proc Natl Acad Sci U S A* 97, 13372–7.

Camello, C., Lomax, R., Petersen, O. H., and Tepikin, A. V. (2002). Calcium leak from intracellular stores - the enigma of calcium signalling. *Cell Calcium* 32, 355–61.

Cannell, M. B., Kong, C. H., Imtiaz, M. S., and Laver, D. R. (2013). Control of sarcoplasmic reticulum Ca^{2+} release by stochastic RyR gating within a 3D model of the cardiac dyad and importance of induction decay for CICR termination. *Biophys J* 104, 2149–59.

Cao, Y. Q. and Tsien, R. W. (2010). Different relationship of N- and P/Q-type Ca^{2+} channels to channel-interacting slots in controlling neurotransmission at cultured hippocampal synapses. *J Neurosci* 30, 4536–46.

Carter, A. G. and Regehr, W. G. (2002). Quantal events shape cerebellar interneuron firing. *Nat Neurosci* 5, 1309–18.

Carter, A. G., Vogt, K. E., Foster, K. A., and Regehr, W. G. (2002). Assessing the role of calcium-induced calcium release in short-term presynaptic plasticity at excitatory central synapses. *J Neurosci* 22, 21–8.

Catterall, W. A. (2011). Voltage-gated calcium channels. *Cold Spring Harb Perspect Biol* 3, a003947.

Catterall, W. A., Leal, K., and Nanou, E. (2013). Calcium channels and short-term synaptic plasticity. *J Biol Chem* 288, 10742–9.

Cavazzini, M., Bliss, T., and Emptage, N. (2005). Ca^{2+} and synaptic plasticity. *Cell Calcium* 38, 355–67.

Chad, J. E. and Eckert, R. (1984). Calcium domains associated with individual channels can account for anomalous voltage relations of Ca^{2+}-dependent responses. *Biophys J* 45, 993–9.

Chamberlain, B. K., Volpe, P., and Fleischer, S. (1984). Inhibition of calcium-induced calcium release from purified cardiac sarcoplasmic reticulum vesicles. *J Biol Chem* 259, 7547–53.

Chapman, E. R. (2008). How does synaptotagmin trigger neurotransmitter release? *Annu Rev Biochem* 77, 615–41.

Charlton, M. P. and Bittner, G. D. (1978). Presynaptic potentials and facilitation of transmitter release in the squid giant synapse. *J Gen Physiol* 72, 487–511.

Charvin, N., L'Eveque, C., Walker, D., Berton, F., Raymond, C., Kataoka, M., Shoji-Kasai, Y., Takahashi, M., De Waard, M., and Seagar, M. J. (1997). Direct interaction of the calcium sensor protein synaptotagmin I with a cytoplasmic domain of the alpha1a subunit of the P/Q-type calcium channel. *EMBO J* 16, 4591–6.

Chen, S. R., Li, X., Ebisawa, K., and Zhang, L. (1997). Functional characterization of the recombinant type 3 Ca^{2+} release channel (ryanodine receptor) expressed in HEK293 cells. *J Biol Chem* 272, 24234–46.

Chen, T. W., Wardill, T. J., Sun, Y., Pulver, S. R., Renninger, S. L., Baohan, A., Schreiter, E. R., Kerr, R. A., Orger, M. B., Jayaraman, V., Looger, L. L., Svoboda, K., and Kim, D. S. (2013). Ultrasensitive fluorescent proteins for imaging neuronal activity. *Nature* 499, 295–300.

Chereau, R., Saraceno, G. E., Angibaud, J., Cattaert, D., and Nagerl, U. V. (2017). Superresolution imaging reveals activity-dependent plasticity of axon morphology linked to changes in action potential conduction velocity. *Proc Natl Acad Sci U S A* 114, 1401–1406.

Choi, B. J., Imlach, W. L., Jiao, W., Wolfram, V., Wu, Y., Grbic, M., Cela, C., Baines, R. A., Nitabach, M. N., and McCabe, B. D. (2014). Miniature neurotransmission regulates Drosophila synaptic structural maturation. *Neuron* 82, 618–34.

Choy, J. (2011). *PhD Thesis: Adrenergic neuromodulation of transmitter release in rat neocortex*. Thesis.

Cibulsky, S. M. and Sather, W. A. (1999). Block by ruthenium red of cloned neuronal voltage-gated calcium channels. *J Pharmacol Exp Ther* 289, 1447–53.

Clements, J. D. (1996). Transmitter timecourse in the synaptic cleft: its role in central synaptic function. *Trends Neurosci* 19, 163–71.

Clements, J. D. and Bekkers, J. M. (1997). Detection of spontaneous synaptic events with an optimally scaled template. *Biophys J* 73, 220–9.

Cole, K. S. (1949). Dynamic electrical characteristics of the squid axon membrane. *Arch Sci Physiol* 3, 3–25.

Colegrove, S. L., Albrecht, M. A., and Friel, D. D. (2000a). Dissection of mitochondrial Ca^{2+} uptake and release fluxes in situ after depolarization-evoked $[Ca^{2+}]_i$ elevations in sympathetic neurons. *J Gen Physiol* 115, 351–70.

Colegrove, S. L., Albrecht, M. A., and Friel, D. D. (2000b). Quantitative analysis of mitochondrial Ca^{2+} uptake and release pathways in sympathetic neurons. Reconstruction of the recovery after depolarization-evoked $[Ca^{2+}]_i$ elevations. *J Gen Physiol* 115, 371–88.

Collin, T., Chat, M., Lucas, M. G., Moreno, H., Racay, P., Schwaller, B., Marty, A., and Llano, I. (2005a). Developmental changes in parvalbumin regulate presynaptic Ca^{2+} signaling. *J Neurosci* 25, 96–107.

Collin, T., Marty, A., and Llano, I. (2005b). Presynaptic calcium stores and synaptic transmission. *Curr Opin Neurobiol* 15, 275–81.

Collingridge, G. L., Peineau, S., Howland, J. G., and Wang, Y. T. (2010). Long-term depression in the CNS. *Nat Rev Neurosci* 11, 459–73.

Colomo, F. and Erulkar, S. D. (1968). Miniature synaptic potentials at frog spinal neurones in the presence of tertodotoxin. *J Physiol* 199, 205–21.

Connor, J. A., Kretz, R., and Shapiro, E. (1986). Calcium levels measured in a presynaptic neurone of Aplysia under conditions that modulate transmitter release. *J Physiol* 375, 625–42.

Conti, R., Tan, Y. P., and Llano, I. (2004). Action potential-evoked and ryanodine-sensitive spontaneous Ca^{2+} transients at the presynaptic terminal of a developing CNS inhibitory synapse. *J Neurosci* 24, 6946–57.

Coombs, J. S., Curtis, D. R., and Eccles, J. C. (1957). The interpretation of spike potentials of motoneurones. *J Physiol* 139, 198–231.

Costa, K., Kleinstein, S., and Hershberg, U. (2010). *Model Fitting and Error Estimation*. http://clip.med.yale.edu/courses/brdu/Costa_ODE.pdf, Accessed on 18/08/2015.

Cox, C. L., Denk, W., Tank, D. W., and Svoboda, K. (2000). Action potentials reliably invade axonal arbors of rat neocortical neurons. *Proc Natl Acad Sci U S A* 97, 9724–8.

Cummings, D. D., Wilcox, K. S., and Dichter, M. A. (1996). Calcium-dependent paired-pulse facilitation of miniature EPSC frequency accompanies depression of EPSCs at hippocampal synapses in culture. *J Neurosci* 16, 5312–23.

Currie, K. P. and Fox, A. P. (1997). Comparison of N- and P/Q-type voltage-gated calcium channel current inhibition. *J Neurosci* 17, 4570–9.

Cuttle, M. F., Tsujimoto, T., Forsythe, I. D., and Takahashi, T. (1998). Facilitation of the presynaptic calcium current at an auditory synapse in rat brainstem. *J Physiol* 512 (Pt 3), 723–9.

Dale, H. (1937). Transmission of Nervous Effects by Acetylcholine: Harvey Lecture, May 20, 1937. *Bull N Y Acad Med* 13, 379–96.

Daw, M. I., Tricoire, L., Erdelyi, F., Szabo, G., and McBain, C. J. (2009). Asynchronous transmitter release from cholecystokinin-containing inhibitory interneurons is widespread and target-cell independent. *J Neurosci* 29, 11112–22.

de Juan-Sanz, J., Holt, G. T., Schreiter, E. R., de Juan, F., Kim, D. S., and Ryan, T. A. (2017). Axonal Endoplasmic Reticulum Ca^{2+} Content Controls Release Probability in CNS Nerve Terminals. *Neuron* 93, 867–881 e6.

De Robertis, E. D. and Bennett, H. S. (1955). Some features of the submicroscopic morphology of synapses in frog and earthworm. *J Biophys Biochem Cytol* 1, 47–58.

Del Castillo, J. and Katz, B. (1954). The effect of magnesium on the activity of motor nerve endings. *J Physiol* 124, 553–9.

Del Castillo, J. and Katz, B. (1955). Local activity at a depolarized nerve-muscle junction. *J Physiol* 128, 396–411.

Del Castillo, J. and Stark, L. (1952). The effect of calcium ions on the motor end-plate potentials. *J Physiol* 116, 507–15.

Del Prete, D., Checler, F., and Chami, M. (2014). Ryanodine receptors: physiological function and deregulation in Alzheimer disease. *Mol Neurodegener* 9, 21.

Delaney, K. R. and Tank, D. W. (1994). A quantitative measurement of the dependence of short-term synaptic enhancement on presynaptic residual calcium. *J Neurosci* 14, 5885–902.

Delaney, K. R., Zucker, R. S., and Tank, D. W. (1989). Calcium in motor nerve terminals associated with posttetanic potentiation. *J Neurosci* 9, 3558–67.

Delvendahl, I., Jablonski, L., Baade, C., Matveev, V., Neher, E., and Hallermann, S. (2015). Reduced endogenous Ca^{2+} buffering speeds active zone Ca^{2+} signaling. *Proc Natl Acad Sci U S A* 112, E3075–84.

DeMaria, C. D., Soong, T. W., Alseikhan, B. A., Alvania, R. S., and Yue, D. T. (2001). Calmodulin bifurcates the local Ca^{2+} signal that modulates P/Q-type Ca^{2+} channels. *Nature* 411, 484–9.

Diao, J., Su, Z., Lu, X., Yoon, T. Y., Shin, Y. K., and Ha, T. (2010). Single-vesicle fusion assay reveals Munc18-1 binding to the SNARE core is sufficient for stimulating membrane fusion. *ACS Chem Neurosci* 1, 168–174.

Dingledine, R., Borges, K., Bowie, D., and Traynelis, S. F. (1999). The glutamate receptor ion channels. *Pharmacol Rev* 51, 7–61.

DiPolo, R. and Beauge, L. (1979). Physiological role of ATP-driven calcium pump in squid axon. *Nature* 278, 271–3.

Diril, M. K., Wienisch, M., Jung, N., Klingauf, J., and Haucke, V. (2006). Stonin 2 is an AP-2-dependent endocytic sorting adaptor for synaptotagmin internalization and recycling. *Dev Cell* 10, 233–44.

Dittman, J. S. and Regehr, W. G. (1998). Calcium dependence and recovery kinetics of presynaptic depression at the climbing fiber to Purkinje cell synapse. *J Neurosci* 18, 6147–62.

Dodge, J., F. A. and Rahamimoff, R. (1967). Co-operative action a calcium ions in transmitter release at the neuromuscular junction. *J Physiol* 193, 419–32.

Dulubova, I., Khvotchev, M., Liu, S., Huryeva, I., Sudhof, T. C., and Rizo, J. (2007). Munc18-1 binds directly to the neuronal SNARE complex. *Proc Natl Acad Sci U S A* 104, 2697–702.

Dulubova, I., Sugita, S., Hill, S., Hosaka, M., Fernandez, I., Sudhof, T. C., and Rizo, J. (1999). A conformational switch in syntaxin during exocytosis: role of munc18. *EMBO J* 18, 4372–82.

Eccles, J., Katz, B., and Kuffler, S. (1941). Nature of the "endplate potential" in curarized muscle. *J Neurophysiol* 4, 362–387.

Eccles, J. C. (1990). Developing concepts of the synapses. *J Neurosci* 10, 3769–81.

Eccles, J. C., Katz, B., and Kuffler, S. W. (1942). Effect of eserine on neuromuscular transmission. *J Neurophysiol* 5, 211–230.

Eccles, J. C. and McGeer, P. L. (1979). Ionotropic and metabotropic neurotransmission. *Trends Neurosci* 2, 39–40.

Edwards, R. H. (2007). The neurotransmitter cycle and quantal size. *Neuron* 55, 835–58.

Eggermann, E., Bucurenciu, I., Goswami, S. P., and Jonas, P. (2012). Nanodomain coupling between Ca^{2+} channels and sensors of exocytosis at fast mammalian synapses. *Nat Rev Neurosci* 13, 7–21.

Eggermann, E. and Jonas, P. (2011). How the 'slow' Ca^{2+} buffer parvalbumin affects transmitter release in nanodomain-coupling regimes. *Nat Neurosci* 15, 20–2.

Eilers, J. and Konnerth, A. (2009). Dye loading with patch pipettes. *Cold Spring Harb Protoc* 2009, pdb prot5201.

Elliott, T. R. (1905). The action of adrenalin. *J Physiol* 32, 401–67.

Emptage, N. J., Reid, C. A., and Fine, A. (2001). Calcium stores in hippocampal synaptic boutons mediate short-term plasticity, store-operated Ca^{2+} entry, and spontaneous transmitter release. *Neuron* 29, 197–208.

Engelman, H. S. and MacDermott, A. B. (2004). Presynaptic ionotropic receptors and control of transmitter release. *Nat Rev Neurosci* 5, 135–45.

Ermolyuk, Y. S., Alder, F. G., Surges, R., Pavlov, I. Y., Timofeeva, Y., Kullmann, D. M., and Volynski, K. E. (2013). Differential triggering of spontaneous glutamate release by P/Q-, N- and R-type Ca^{2+} channels. *Nat Neurosci* 16, 1754–63.

Faas, G. C. and Mody, I. (2014). Measuring the steady-state properties of Ca^{2+} indicators with a set of calibrated [Ca^{2+}] solutions. *Cold Spring Harb Protoc* 2014, 758–62.

Faas, G. C., Raghavachari, S., Lisman, J. E., and Mody, I. (2011). Calmodulin as a direct detector of Ca^{2+} signals. *Nat Neurosci* 14, 301–4.

Faas, G. C., Schwaller, B., Vergara, J. L., and Mody, I. (2007). Resolving the fast kinetics of cooperative binding: Ca^{2+} buffering by calretinin. *PLoS Biol* 5, e311.

Fabiato, A. and Fabiato, F. (1975). Contractions induced by a calcium-triggered release of calcium from the sarcoplasmic reticulum of single skinned cardiac cells. *J Physiol* 249, 469–95.

Fabiato, A. and Fabiato, F. (1978). Calcium-induced release of calcium from the sarcoplasmic reticulum of skinned cells from adult human, dog, cat, rabbit, rat, and frog hearts and from fetal and new-born rat ventricles. *Ann N Y Acad Sci* 307, 491–522.

Fatt, P. and Katz, B. (1950). Some observations on biological noise. *Nature* 166, 597–8.

Fatt, P. and Katz, B. (1952). Spontaneous subthreshold activity at motor nerve endings. *J Physiol* 117, 109–128.

Featherstone, D. E. and Shippy, S. A. (2008). Regulation of synaptic transmission by ambient extracellular glutamate. *Neuroscientist* 14, 171–81.

Fedchyshyn, M. J. and Wang, L. Y. (2005). Developmental transformation of the release modality at the calyx of Held synapse. *J Neurosci* 25, 4131–40.

Felmy, F., Neher, E., and Schneggenburger, R. (2003). Probing the intracellular calcium sensitivity of transmitter release during synaptic facilitation. *Neuron* 37, 801–11.

Felmy, F. and Schneggenburger, R. (2004). Developmental expression of the Ca^{2+}-binding proteins calretinin and parvalbumin at the calyx of Held of rats and mice. *Eur J Neurosci* 20, 1473–82.

Feng, T. P. (1941). Studies on the neuromuscular junction XXVI. The changes of the end-plate potential during and after prolonged stimulation. *Chin J Physiol* 16, 341–372.

Fernandez-Chacon, R., Konigstorfer, A., Gerber, S. H., Garcia, J., Matos, M. F., Stevens, C. F., Brose, N., Rizo, J., Rosenmund, C., and Sudhof, T. C. (2001). Synaptotagmin I functions as a calcium regulator of release probability. *Nature* 410, 41–9.

Fill, M. and Copello, J. A. (2002). Ryanodine receptor calcium release channels. *Physiol Rev* 82, 893–922.

Fioravante, D., Chu, Y., Myoga, M. H., Leitges, M., and Regehr, W. G. (2011). Calcium-dependent isoforms of protein kinase C mediate posttetanic potentiation at the calyx of Held. *Neuron* 70, 1005–19.

Fischer von Mollard, G., Mignery, G. A., Baumert, M., Perin, M. S., Hanson, T. J., Burger, P. M., Jahn, R., and Sudhof, T. C. (1990). rab3 is a small GTP-binding protein exclusively localized to synaptic vesicles. *Proc Natl Acad Sci U S A* 87, 1988–92.

Flourakis, M., Van Coppenolle, F., Lehen'kyi, V., Beck, B., Skryma, R., and Prevarskaya, N. (2006). Passive calcium leak via translocon is a first step for iPLA2-pathway regulated store operated channels activation. *FASEB J* 20, 1215–7.

Forsythe, I. D., Tsujimoto, T., Barnes-Davies, M., Cuttle, M. F., and Takahashi, T. (1998). Inactivation of presynaptic calcium current contributes to synaptic depression at a fast central synapse. *Neuron* 20, 797–807.

Foskett, J. K., White, C., Cheung, K. H., and Mak, D. O. (2007). Inositol trisphosphate receptor Ca^{2+} release channels. *Physiol Rev* 87, 593–658.

Frank, C. A., Kennedy, M. J., Goold, C. P., Marek, K. W., and Davis, G. W. (2006). Mechanisms underlying the rapid induction and sustained expression of synaptic homeostasis. *Neuron* 52, 663–77.

Franzini-Armstrong, C. (1975). Membrane particles and transmission at the triad. *Fed Proc* 34, 1382–9.

Fredj, N. B. and Burrone, J. (2009). A resting pool of vesicles is responsible for spontaneous vesicle fusion at the synapse. *Nat Neurosci* 12, 751–8.

Frerking, M., Borges, S., and Wilson, M. (1997). Are some minis multiquantal? *J Neurophysiol* 78, 1293–304.

Frick, A., Feldmeyer, D., Helmstaedter, M., and Sakmann, B. (2008). Monosynaptic connections between pairs of L5a pyramidal neurons in columns of juvenile rat somatosensory cortex. *Cereb Cortex* 18, 397–406.

Frick, A., Feldmeyer, D., and Sakmann, B. (2007). Postnatal development of synaptic transmission in local networks of L5a pyramidal neurons in rat somatosensory cortex. *J Physiol* 585, 103–16.

Fruen, B. R., Bardy, J. M., Byrem, T. M., Strasburg, G. M., and Louis, C. F. (2000). Differential Ca^{2+} sensitivity of skeletal and cardiac muscle ryanodine receptors in the presence of calmodulin. *Am J Physiol Cell Physiol* 279, C724–33.

Fuhrmann, G., Cowan, A., Segev, I., Tsodyks, M., and Stricker, C. (2004). Multiple mechanisms govern the dynamics of depression at neocortical synapses of young rats. *J Physiol* 557, 415–38.

Fuortes, M. G., Frank, K., and Becker, M. C. (1957). Steps in the production of motoneuron spikes. *J Gen Physiol* 40, 735–52.

Gabso, M., Neher, E., and Spira, M. E. (1997). Low mobility of the Ca^{2+} buffers in axons of cultured Aplysia neurons. *Neuron* 18, 473–81.

Galante, M. and Marty, A. (2003). Presynaptic ryanodine-sensitive calcium stores contribute to evoked neurotransmitter release at the basket cell-Purkinje cell synapse. *J Neurosci* 23, 11229–34.

Geiger, J. R. and Jonas, P. (2000). Dynamic control of presynaptic Ca^{2+} inflow by fast-inactivating K^{+} channels in hippocampal mossy fiber boutons. *Neuron* 28, 927–39.

Geppert, M., Goda, Y., Hammer, R. E., Li, C., Rosahl, T. W., Stevens, C. F., and Sudhof, T. C. (1994). Synaptotagmin I: a major Ca^{2+} sensor for transmitter release at a central synapse. *Cell* 79, 717–27.

Gerber, S. H., Rah, J. C., Min, S. W., Liu, X., de Wit, H., Dulubova, I., Meyer, A. C., Rizo, J., Arancillo, M., Hammer, R. E., Verhage, M., Rosenmund, C., and Sudhof, T. C. (2008). Conformational switch of syntaxin-1 controls synaptic vesicle fusion. *Science* 321, 1507–10.

Ghosh, T. K., Eis, P. S., Mullaney, J. M., Ebert, C. L., and Gill, D. L. (1988). Competitive, reversible, and potent antagonism of inositol 1,4,5-trisphosphate-activated calcium release by heparin. *J Biol Chem* 263, 11075–9.

Gollasch, M., Hescheler, J., Quayle, J. M., Patlak, J. B., and Nelson, M. T. (1992). Single calcium channel currents of arterial smooth muscle at physiological calcium concentrations. *Am J Physiol* 263, C948–52.

Gomis, A., Burrone, J., and Lagnado, L. (1999). Two actions of calcium regulate the supply of releasable vesicles at the ribbon synapse of retinal bipolar cells. *J Neurosci* 19, 6309–17.

Goswami, S. P., Bucurenciu, I., and Jonas, P. (2012). Miniature IPSCs in hippocampal granule cells are triggered by voltage-gated Ca^{2+} channels via microdomain coupling. *J Neurosci* 32, 14294–304.

Graham, J. and Gerard, R. W. (1946). Membrane potentials and excitation of impaled single muscle fibers. *J Cell Comp Physiol* 28, 99–117.

Gray, E. G. (1959). Axo-somatic and axo-dendritic synapses of the cerebral cortex: an electron microscope study. *J Anat* 93, 420–33.

Gregory, R. B., Rychkov, G., and Barritt, G. J. (2001). Evidence that 2-aminoethyl diphenylborate is a novel inhibitor of store-operated Ca^{2+} channels in liver cells, and acts through a mechanism which does not involve inositol trisphosphate receptors. *Biochem J* 354, 285–90.

Groemer, T. W. and Klingauf, J. (2007). Synaptic vesicles recycling spontaneously and during activity belong to the same vesicle pool. *Nat Neurosci* 10, 145–7.

Groffen, A. J., Martens, S., Diez Arazola, R., Cornelisse, L. N., Lozovaya, N., de Jong, A. P., Goriounova, N. A., Habets, R. L., Takai, Y., Borst, J. G., Brose, N., McMahon, H. T., and Verhage, M. (2010). Doc2b is a high-affinity Ca^{2+} sensor for spontaneous neurotransmitter release. *Science* 327, 1614–8.

Grynkiewicz, G., Poenie, M., and Tsien, R. Y. (1985). A new generation of Ca^{2+} indicators with greatly improved fluorescence properties. *J Biol Chem* 260, 3440–50.

Gulyas-Kovacs, A., de Wit, H., Milosevic, I., Kochubey, O., Toonen, R., Klingauf, J., Verhage, M., and Sorensen, J. B. (2007). Munc18-1: sequential interactions with the fusion machinery stimulate vesicle docking and priming. *J Neurosci* 27, 8676–86.

Habets, R. L. and Borst, J. G. (2005). Post-tetanic potentiation in the rat calyx of Held synapse. *J Physiol* 564, 173–87.

Habets, R. L. and Borst, J. G. (2006). An increase in calcium influx contributes to post-tetanic potentiation at the rat calyx of Held synapse. *J Neurophysiol* 96, 2868–76.

Hagler, J., D. J. and Goda, Y. (2001). Properties of synchronous and asynchronous release during pulse train depression in cultured hippocampal neurons. *J Neurophysiol* 85, 2324–34.

Hammes, G. G. and Levison, S. A. (1964). A kinetic investigation of the interaction of adenosine-5'-triphosphate with divalent metal ions. *Biochemistry* 3, 1504–6.

Han, Y., Kaeser, P. S., Sudhof, T. C., and Schneggenburger, R. (2011). RIM determines Ca^{2+} channel density and vesicle docking at the presynaptic active zone. *Neuron* 69, 304–16.

Hansford, R. G. and Lakatta, E. G. (1987). Ryanodine releases calcium from sarcoplasmic reticulum in calcium-tolerant rat cardiac myocytes. *J Physiol* 390, 453–67.

Harkins, A. B., Kurebayashi, N., and Baylor, S. M. (1993). Resting myoplasmic free calcium in frog skeletal muscle fibers estimated with fluo-3. *Biophys J* 65, 865–81.

Harlow, M. L., Ress, D., Stoschek, A., Marshall, R. M., and McMahan, U. J. (2001). The architecture of active zone material at the frog's neuromuscular junction. *Nature* 409, 479–84.

Hartter, D. E., Burton, P. R., and Laveri, L. A. (1987). Distribution and calcium-sequestering ability of smooth endoplasmic reticulum in olfactory axon terminals of frog brain. *Neuroscience* 23, 371–86.

Hashimoto, T., Ishii, T., and Ohmori, H. (1996). Release of Ca^{2+} is the crucial step for the potentiation of IPSCs in the cultured cerebellar Purkinje cells of the rat. *J Physiol* 497 (Pt 3), 611–27.

Hata, Y., Slaughter, C. A., and Sudhof, T. C. (1993). Synaptic vesicle fusion complex contains unc-18 homologue bound to syntaxin. *Nature* 366, 347–51.

Hefft, S. and Jonas, P. (2005). Asynchronous GABA release generates long-lasting inhibition at a hippocampal interneuron-principal neuron synapse. *Nat Neurosci* 8, 1319–28.

Heidelberger, R., Heinemann, C., Neher, E., and Matthews, G. (1994). Calcium dependence of the rate of exocytosis in a synaptic terminal. *Nature* 371, 513–5.

Helmchen, F., Borst, J. G., and Sakmann, B. (1997). Calcium dynamics associated with a single action potential in a CNS presynaptic terminal. *Biophys J* 72, 1458–71.

Helmchen, F., Imoto, K., and Sakmann, B. (1996). Ca^{2+} buffering and action potential-evoked Ca^{2+} signaling in dendrites of pyramidal neurons. *Biophys J* 70, 1069–81.

Helmchen, F. and Tank, D. W. (2015). A single-compartment model of calcium dynamics in nerve terminals and dendrites. *Cold Spring Harb Protoc* 2015, 155–67.

Heuser, J. E., Reese, T. S., Dennis, M. J., Jan, Y., Jan, L., and Evans, L. (1979). Synaptic vesicle exocytosis captured by quick freezing and correlated with quantal transmitter release. *J Cell Biol* 81, 275–300.

Hodgkin, A. I. and Huxley, A. F. (1939). Action potentials recorded from inside a nerve fibre. *Nature* 144, 710–711.

Hof, P. R., Glezer, I., Conde, F., Flagg, R. A., Rubin, M. B., Nimchinsky, E. A., and Vogt Weisenhorn, D. M. (1999). Cellular distribution of the calcium-binding proteins parvalbumin, calbindin, and calretinin in the neocortex of mammals: phylogenetic and developmental patterns. *J Chem Neuroanat* 16, 77–116.

Holderith, N., Lorincz, A., Katona, G., Rozsa, B., Kulik, A., Watanabe, M., and Nusser, Z. (2012). Release probability of hippocampal glutamatergic terminals scales with the size of the active zone. *Nat Neurosci* 15, 988–97.

Hosoi, N., Sakaba, T., and Neher, E. (2007). Quantitative analysis of calcium-dependent vesicle recruitment and its functional role at the calyx of Held synapse. *J Neurosci* 27, 14286–98.

Hu, C., Ahmed, M., Melia, T. J., Sollner, T. H., Mayer, T., and Rothman, J. E. (2003). Fusion of cells by flipped SNAREs. *Science* 300, 1745–9.

Hu, H. Z., Gu, Q., Wang, C., Colton, C. K., Tang, J., Kinoshita-Kawada, M., Lee, L. Y., Wood, J. D., and Zhu, M. X. (2004). 2-aminoethoxydiphenyl borate is a common activator of TRPV1, TRPV2, and TRPV3. *J Biol Chem* 279, 35741–8.

Hu, S. H., Latham, C. F., Gee, C. L., James, D. E., and Martin, J. L. (2007). Structure of the Munc18c/Syntaxin4 N-peptide complex defines universal features of the N-peptide binding mode of Sec1/Munc18 proteins. *Proc Natl Acad Sci U S A* 104, 8773–8.

Hubbard, J. (1961). The effect of calcium and magnesium on the spontaneous release of transmitter from mammalian motor nerve endings. *J Physiol* 159, 507–517.

Hubbard, J. I., Stenhouse, D., and Eccles, R. M. (1967). Origin of synaptic noise. *Science* 157, 330–1.

Hughes, J. R. (1958). Post-tetanic potentiation. *Physiol Rev* 38, 91–113.

Inchauspe, C. G., Martini, F. J., Forsythe, I. D., and Uchitel, O. D. (2004). Functional compensation of P/Q by N-type channels blocks short-term plasticity at the calyx of Held presynaptic terminal. *J Neurosci* 24, 10379–83.

Indriati, D. W., Kamasawa, N., Matsui, K., Meredith, A. L., Watanabe, M., and Shigemoto, R. (2013). Quantitative localization of Cav2.1 (P/Q-type) voltage-dependent calcium channels in Purkinje cells: somatodendritic gradient and distinct somatic coclustering with calcium-activated potassium channels. *J Neurosci* 33, 3668–78.

Inui, M., Saito, A., and Fleischer, S. (1987a). Isolation of the ryanodine receptor from cardiac sarcoplasmic reticulum and identity with the feet structures. *J Biol Chem* 262, 15637–42.

Inui, M., Saito, A., and Fleischer, S. (1987b). Purification of the ryanodine receptor and identity with feet structures of junctional terminal cisternae of sarcoplasmic reticulum from fast skeletal muscle. *J Biol Chem* 262, 1740–7.

Ionescu, L., Cheung, K. H., Vais, H., Mak, D. O., White, C., and Foskett, J. K. (2006). Graded recruitment and inactivation of single $InsP_3$ receptor Ca^{2+}-release channels: implications for quantal [corrected] Ca^{2+} release. *J Physiol* 573, 645–62.

Iremonger, K. J. and Bains, J. S. (2007). Integration of asynchronously released quanta prolongs the postsynaptic spike window. *J Neurosci* 27, 6684–91.

Ishikawa, T., Kaneko, M., Shin, H. S., and Takahashi, T. (2005). Presynaptic N-type and P/Q-type Ca^{2+} channels mediating synaptic transmission at the calyx of Held of mice. *J Physiol* 568, 199–209.

Israel, M., Gautron, J., and Lesbats, B. (1968). [Isolation of the synaptic vesicles of the electric organ of the torpedo and localization of acetylcholine at their level]. *C R Acad Sci Hebd Seances Acad Sci D* 266, 273–5.

Iwasaki, S., Momiyama, A., Uchitel, O. D., and Takahashi, T. (2000). Developmental changes in calcium channel types mediating central synaptic transmission. *J Neurosci* 20, 59–65.

Jackman, S. L. and Regehr, W. G. (2017). The Mechanisms and Functions of Synaptic Facilitation. *Neuron* 94, 447–464.

Jackman, S. L., Turecek, J., Belinsky, J. E., and Regehr, W. G. (2016). The calcium sensor synaptotagmin 7 is required for synaptic facilitation. *Nature* 529, 88–91.

Jackson, M. B., Konnerth, A., and Augustine, G. J. (1991). Action potential broadening and frequency-dependent facilitation of calcium signals in pituitary nerve terminals. *Proc Natl Acad Sci U S A* 88, 380–4.

Jackson, M. B. and Redman, S. J. (2003). Calcium dynamics, buffering, and buffer saturation in the boutons of dentate granule-cell axons in the hilus. *J Neurosci* 23, 1612–21.

Jahn, R. and Fasshauer, D. (2012). Molecular machines governing exocytosis of synaptic vesicles. *Nature* 490, 201–7.

Jia, Y., Wang, X., Varty, L., Rizzo, C. A., Yang, R., Correll, C. C., Phelps, P. T., Egan, R. W., and Hey, J. A. (2004). Functional TRPV4 channels are expressed in human airway smooth muscle cells. *Am J Physiol Lung Cell Mol Physiol* 287, L272–8.

Johnson, J. W. and Ascher, P. (1987). Glycine potentiates the NMDA response in cultured mouse brain neurons. *Nature* 325, 529–31.

Jonas, P. and Burnashev, N. (1995). Molecular mechanisms controlling calcium entry through AMPA-type glutamate receptor channels. *Neuron* 15, 987–90.

Jung, N. and Haucke, V. (2007). Clathrin-mediated endocytosis at synapses. *Traffic* 8, 1129–36.

Kaeser, P. S., Deng, L., Fan, M., and Sudhof, T. C. (2012). RIM genes differentially contribute to organizing presynaptic release sites. *Proc Natl Acad Sci U S A* 109, 11830–5.

Kaeser, P. S., Deng, L., Wang, Y., Dulubova, I., Liu, X., Rizo, J., and Sudhof, T. C. (2011). RIM proteins tether Ca^{2+} channels to presynaptic active zones via a direct PDZ-domain interaction. *Cell* 144, 282–95.

Kaeser, P. S. and Regehr, W. G. (2014). Molecular mechanisms for synchronous, asynchronous, and spontaneous neurotransmitter release. *Annu Rev Physiol* 76, 333–63.

Kaftan, E. J., Ehrlich, B. E., and Watras, J. (1997). Inositol 1,4,5-trisphosphate ($InsP_3$) and calcium interact to increase the dynamic range of $InsP_3$ receptor-dependent calcium signaling. *J Gen Physiol* 110, 529–38.

Kamer, K. J. and Mootha, V. K. (2015). The molecular era of the mitochondrial calcium uniporter. *Nat Rev Mol Cell Biol* 16, 545–53.

Kamiya, H. and Zucker, R. S. (1994). Residual Ca^{2+} and short-term synaptic plasticity. *Nature* 371, 603–6.

Kanamori, T., Kanai, M. I., Dairyo, Y., Yasunaga, K., Morikawa, R. K., and Emoto, K. (2013). Compartmentalized calcium transients trigger dendrite pruning in Drosophila sensory neurons. *Science* 340, 1475–8.

Katz, B. (1962). The Croonian Lecture: The transmission of impulses from nerve to muscle, and the subcellular unit of synaptic action. *Proc R Soc Lond B Biol Sci* 155.

Katz, B. and Miledi, R. (1965a). The effect of calcium on acetylcholine release from motor nerve terminals. *Proc R Soc Lond B Biol Sci* 161, 496–503.

Katz, B. and Miledi, R. (1965b). The measurement of synaptic delay, and the time course of acetylcholine release at the neuromuscular junction. *Proc R Soc Lond B Biol Sci* 161, 483–95.

Katz, B. and Miledi, R. (1967). Ionic requirements of synaptic transmitter release. *Nature* 215, 651.

Katz, B. and Miledi, R. (1968). The role of calcium in neuromuscular facilitation. *J Physiol* 195, 481–92.

Katz, B. and Miledi, R. (1969). Tetrodotoxin-resistant electric activity in presynaptic terminals. *J Physiol* 203, 459–87.

Kettlun, C., Gonzalez, A., Rios, E., and Fill, M. (2003). Unitary Ca^{2+} current through mammalian cardiac and amphibian skeletal muscle ryanodine receptor Channels under near-physiological ionic conditions. *J Gen Physiol* 122, 407–17.

Khodakhah, K. and Ogden, D. (1995). Fast activation and inactivation of inositol trisphosphate-evoked Ca^{2+} release in rat cerebellar Purkinje neurones. *J Physiol* 487 (Pt 2), 343–58.

Kim, M. H., Korogod, N., Schneggenburger, R., Ho, W. K., and Lee, S. H. (2005). Interplay between Na^{+}/Ca^{2+} exchangers and mitochondria in Ca^{2+} clearance at the calyx of Held. *J Neurosci* 25, 6057–65.

Kirichok, Y., Krapivinsky, G., and Clapham, D. E. (2004). The mitochondrial calcium uniporter is a highly selective ion channel. *Nature* 427, 360–4.

Kisfali, M., Lrincz, T., and Vizi, E. S. (2013). Comparison of Ca^{2+} transients and $[Ca^{2+}]_i$ in the dendrites and boutons of non-fast-spiking GABAergic hippocampal interneurons using two-photon laser microscopy and high- and low-affinity dyes. *J Physiol* 591, 5541–53.

Klapstein, G. J., Vietla, S., Lieberman, D. N., Gray, P. A., Airaksinen, M. S., Thoenen, H., Meyer, M., and Mody, I. (1998). Calbindin-D28k fails to protect hippocampal neurons against ischemia in spite of its cytoplasmic calcium buffering properties: evidence from calbindin-D28k knockout mice. *Neuroscience* 85, 361–73.

Kochubey, O., Han, Y., and Schneggenburger, R. (2009). Developmental regulation of the intracellular Ca^{2+} sensitivity of vesicle fusion and Ca^{2+}-secretion coupling at the rat calyx of Held. *J Physiol* 587, 3009–23.

Kochubey, O., Lou, X., and Schneggenburger, R. (2011). Regulation of transmitter release by Ca^{2+} and synaptotagmin: insights from a large CNS synapse. *Trends Neurosci* 34, 237–46.

Kochubey, O. and Schneggenburger, R. (2011). Synaptotagmin increases the dynamic range of synapses by driving Ca^{2+}-evoked release and by clamping a near-linear remaining Ca^{2+} sensor. *Neuron* 69, 736–48.

Koester, H. J. and Johnston, D. (2005). Target cell-dependent normalization of transmitter release at neocortical synapses. *Science* 308, 863–6.

Koester, H. J. and Sakmann, B. (2000). Calcium dynamics associated with action potentials in single nerve terminals of pyramidal cells in layer 2/3 of the young rat neocortex. *J Physiol* 529 Pt 3, 625–46.

Kombian, S. B., Hirasawa, M., Mouginot, D., Chen, X., and Pittman, Q. J. (2000). Short-term potentiation of miniature excitatory synaptic currents causes excitation of supraoptic neurons. *J Neurophysiol* 83, 2542–53.

Konishi, M., Olson, A., Hollingworth, S., and Baylor, S. M. (1988). Myoplasmic binding of fura-2 investigated by steady-state fluorescence and absorbance measurements. *Biophys J* 54, 1089–104.

Koo, S. J., Markovic, S., Puchkov, D., Mahrenholz, C. C., Beceren-Braun, F., Maritzen, T., Dernedde, J., Volkmer, R., Oschkinat, H., and Haucke, V. (2011). SNARE motif-mediated sorting of synaptobrevin by the endocytic adaptors clathrin assembly lymphoid myeloid leukemia (CALM) and AP180 at synapses. *Proc Natl Acad Sci U S A* 108, 13540–5.

Korogod, N., Lou, X., and Schneggenburger, R. (2005). Presynaptic Ca^{2+} requirements and developmental regulation of posttetanic potentiation at the calyx of Held. *J Neurosci* 25, 5127–37.

Korogod, N., Lou, X., and Schneggenburger, R. (2007). Posttetanic potentiation critically depends on an enhanced Ca^{2+} sensitivity of vesicle fusion mediated by presynaptic PKC. *Proc Natl Acad Sci U S A* 104, 15923–8.

Kretz, R., Shapiro, E., and Kandel, E. R. (1982). Post-tetanic potentiation at an identified synapse in Aplysia is correlated with a Ca^{2+}-activated K^+ current in the presynaptic neuron: evidence for Ca^{2+} accumulation. *Proc Natl Acad Sci U S A* 79, 5430–4.

Kukkonen, J. P., Lund, P. E., and Akerman, K. E. (2001). 2-aminoethoxydiphenyl borate reveals heterogeneity in receptor-activated Ca^{2+} discharge and store-operated Ca^{2+} influx. *Cell Calcium* 30, 117–29.

Kwon, H. B. and Sabatini, B. L. (2011). Glutamate induces de novo growth of functional spines in developing cortex. *Nature* 474, 100–4.

Lai, F. A., Erickson, H. P., Rousseau, E., Liu, Q. Y., and Meissner, G. (1988). Purification and reconstitution of the calcium release channel from skeletal muscle. *Nature* 331, 315–9.

Lando, L. and Zucker, R. S. (1994). Ca^{2+} cooperativity in neurosecretion measured using photolabile Ca^{2+} chelators. *J Neurophysiol* 72, 825–30.

Larkman, A. U. (1991). Dendritic morphology of pyramidal neurones of the visual cortex of the rat: III. Spine distributions. *J Comp Neurol* 306, 332–43.

Lattanzio, J., F. A., Schlatterer, R. G., Nicar, M., Campbell, K. P., and Sutko, J. L. (1987). The effects of ryanodine on passive calcium fluxes across sarcoplasmic reticulum membranes. *J Biol Chem* 262, 2711–8.

Lauri, S. E., Bortolotto, Z. A., Nistico, R., Bleakman, D., Ornstein, P. L., Lodge, D., Isaac, J. T., and Collingridge, G. L. (2003). A role for Ca^{2+} stores in kainate receptor-dependent synaptic facilitation and LTP at mossy fiber synapses in the hippocampus. *Neuron* 39, 327–41.

Laver, D. R. (2007). Ca^{2+} stores regulate ryanodine receptor Ca^{2+} release channels via luminal and cytosolic Ca^{2+} sites. *Biophys J* 92, 3541–55.

Le Meur, K., Galante, M., Angulo, M. C., and Audinat, E. (2007). Tonic activation of NMDA receptors by ambient glutamate of non-synaptic origin in the rat hippocampus. *J Physiol* 580, 373–83.

Lee, A., Zhou, H., Scheuer, T., and Catterall, W. A. (2003). Molecular determinants of Ca^{2+}/calmodulin-dependent regulation of Cav2.1 channels. *Proc Natl Acad Sci U S A* 100, 16059–64.

Lee, D., Lee, K. H., Ho, W. K., and Lee, S. H. (2007). Target cell-specific involvement of presynaptic mitochondria in post-tetanic potentiation at hippocampal mossy fiber synapses. *J Neurosci* 27, 13603–13.

Lee, M. C., Yasuda, R., and Ehlers, M. D. (2010). Metaplasticity at single glutamatergic synapses. *Neuron* 66, 859–70.

Lee, S. H., Rosenmund, C., Schwaller, B., and Neher, E. (2000a). Differences in Ca^{2+} buffering properties between excitatory and inhibitory hippocampal neurons from the rat. *J Physiol* 525 Pt 2, 405–18.

Lee, S. H., Schwaller, B., and Neher, E. (2000b). Kinetics of Ca^{2+} binding to parvalbumin in bovine chromaffin cells: implications for [Ca^{2+}] transients of neuronal dendrites. *J Physiol* 525 Pt 2, 419–32.

Lerma, J. (2003). Roles and rules of kainate receptors in synaptic transmission. *Nat Rev Neurosci* 4, 481–95.

Leurs, R., Smit, M. J., Alewijnse, A. E., and Timmerman, H. (1998). Agonist-independent regulation of constitutively active G-protein-coupled receptors. *Trends Biochem Sci* 23, 418–22.

Lev-Ram, V., Miyakawa, H., Lasser-Ross, N., and Ross, W. N. (1992). Calcium transients in cerebellar Purkinje neurons evoked by intracellular stimulation. *J Neurophysiol* 68, 1167–77.

Li, F., Pincet, F., Perez, E., Eng, W. S., Melia, T. J., Rothman, J. E., and Tareste, D. (2007a). Energetics and dynamics of SNAREpin folding across lipid bilayers. *Nat Struct Mol Biol* 14, 890–6.

Li, L., Bischofberger, J., and Jonas, P. (2007b). Differential gating and recruitment of P/Q-, N-, and R-type Ca^{2+} channels in hippocampal mossy fiber boutons. *J Neurosci* 27, 13420–9.

Li, M., Jiang, J., and Yue, L. (2006). Functional characterization of homo- and heteromeric channel kinases TRPM6 and TRPM7. *J Gen Physiol* 127, 525–37.

Li-Smerin, Y., Levitan, E. S., and Johnson, J. W. (2001). Free intracellular Mg^{2+} concentration and inhibition of NMDA responses in cultured rat neurons. *J Physiol* 533, 729–43.

Liang, Y., Yuan, L. L., Johnston, D., and Gray, R. (2002). Calcium signaling at single mossy fiber presynaptic terminals in the rat hippocampus. *J Neurophysiol* 87, 1132–7.

Liley, A. and North, K. (1953). An electrical investigation of effects of repetitive stimulation on mammalian neuromuscular junction. *J Neurophysiol* 16, 509–527.

Linden, M., Andersson, G., Gellerfors, P., and Nelson, B. D. (1984). Subcellular distribution of rat liver porin. *Biochim Biophys Acta* 770, 93–6.

Llano, I., DiPolo, R., and Marty, A. (1994). Calcium-induced calcium release in cerebellar Purkinje cells. *Neuron* 12, 663–73.

Llano, I., Gonzalez, J., Caputo, C., Lai, F. A., Blayney, L. M., Tan, Y. P., and Marty, A. (2000). Presynaptic calcium stores underlie large-amplitude miniature IPSCs and spontaneous calcium transients. *Nat Neurosci* 3, 1256–65.

Llinas, R., Steinberg, I. Z., and Walton, K. (1981a). Presynaptic calcium currents in squid giant synapse. *Biophys J* 33, 289–321.

Llinas, R., Steinberg, I. Z., and Walton, K. (1981b). Relationship between presynaptic calcium current and postsynaptic potential in squid giant synapse. *Biophys J* 33, 323–51.

Llinas, R., Sugimori, M., and Silver, R. B. (1992). Microdomains of high calcium concentration in a presynaptic terminal. *Science* 256, 677–9.

Loewi, O. (1924). Über humorale übertragbarkeit der Herznervenwirkung. *Pflugers Arch Gesamte Physiol Menschen Tiere* 204, 629–640.

Lou, X., Scheuss, V., and Schneggenburger, R. (2005). Allosteric modulation of the presynaptic Ca^{2+} sensor for vesicle fusion. *Nature* 435, 497–501.

Lu, T. and Trussell, L. O. (2000). Inhibitory transmission mediated by asynchronous transmitter release. *Neuron* 26, 683–94.

Lubke, J., Egger, V., Sakmann, B., and Feldmeyer, D. (2000). Columnar organization of dendrites and axons of single and synaptically coupled excitatory spiny neurons in layer 4 of the rat barrel cortex. *J Neurosci* 20, 5300–11.

Luthi, D., Spichiger, U., Forster, I., and McGuigan, J. A. (1997). Calibration of Mg^{2+}-selective macroelectrodes down to 1 mumol l-1 in intracellular and Ca^{2+}-containing extracellular solutions. *Exp Physiol* 82, 453–67.

Lytton, J., Li, X. F., Dong, H., and Kraev, A. (2002). K^+-dependent Na^+/Ca^{2+} exchangers in the brain. *Ann N Y Acad Sci* 976, 382–93.

Lytton, J., Westlin, M., Burk, S. E., Shull, G. E., and MacLennan, D. H. (1992). Functional comparisons between isoforms of the sarcoplasmic or endoplasmic reticulum family of calcium pumps. *J Biol Chem* 267, 14483–9.

Ma, H., Zhong, L., Inesi, G., Fortea, I., Soler, F., and Fernandez-Belda, F. (1999). Overlapping effects of S3 stalk segment mutations on the affinity of Ca^{2+}-ATPase (SERCA) for thapsigargin and cyclopiazonic acid. *Biochemistry* 38, 15522–7.

Ma, J. (1993). Block by ruthenium red of the ryanodine-activated calcium release channel of skeletal muscle. *J Gen Physiol* 102, 1031–56.

Magleby, K. L. and Zengel, J. E. (1976). Augmentation: A process that acts to increase transmitter release at the frog neuromuscular junction. *J Physiol* 257, 449–70.

Majewska, A., Brown, E., Ross, J., and Yuste, R. (2000). Mechanisms of calcium decay kinetics in hippocampal spines: role of spine calcium pumps and calcium diffusion through the spine neck in biochemical compartmentalization. *J Neurosci* 20, 1722–34.

Mak, D. O., McBride, S., and Foskett, J. K. (1998). Inositol 1,4,5-trisphosphate [correction of tris-phosphate] activation of inositol trisphosphate [correction of tris-phosphate] receptor Ca^{2+} channel by ligand tuning of Ca^{2+} inhibition. *Proc Natl Acad Sci U S A* 95, 15821–5.

Mak, D. O., McBride, S., and Foskett, J. K. (1999). ATP regulation of type 1 inositol 1,4,5-trisphosphate receptor channel gating by allosteric tuning of Ca^{2+} activation. *J Biol Chem* 274, 22231–7.

Mak, D. O., McBride, S., and Foskett, J. K. (2001a). ATP regulation of recombinant type 3 inositol 1,4,5-trisphosphate receptor gating. *J Gen Physiol* 117, 447–56.

Mak, D. O., McBride, S., and Foskett, J. K. (2001b). Regulation by Ca^{2+} and inositol 1,4,5-trisphosphate ($InsP_3$) of single recombinant type 3 $InsP_3$ receptor channels. Ca^{2+} activation uniquely distinguishes types 1 and 3 $InsP_3$ receptors. *J Gen Physiol* 117, 435–46.

Malsam, J., Kreye, S., and Sollner, T. H. (2008). Membrane fusion: SNAREs and regulation. *Cell Mol Life Sci* 65, 2814–32.

Manita, S. and Ross, W. N. (2009). Synaptic activation and membrane potential changes modulate the frequency of spontaneous elementary Ca^{2+} release events in the dendrites of pyramidal neurons. *J Neurosci* 29, 7833–45.

Mank, M., Reiff, D. F., Heim, N., Friedrich, M. W., Borst, A., and Griesbeck, O. (2006). A FRET-based calcium biosensor with fast signal kinetics and high fluorescence change. *Biophys J* 90, 1790–6.

Manseau, F., Marinelli, S., Mendez, P., Schwaller, B., Prince, D. A., Huguenard, J. R., and Bacci, A. (2010). Desynchronization of neocortical networks by asynchronous release of GABA at autaptic and synaptic contacts from fast-spiking interneurons. *PLoS Biol* 8.

Maravall, M., Mainen, Z. F., Sabatini, B. L., and Svoboda, K. (2000). Estimating intracellular calcium concentrations and buffering without wavelength ratioing. *Biophys J* 78, 2655–67.

Markram, H., Lubke, J., Frotscher, M., Roth, A., and Sakmann, B. (1997). Physiology and anatomy of synaptic connections between thick tufted pyramidal neurones in the developing rat neocortex. *J Physiol* 500 (Pt 2), 409–40.

Marmont, G. (1949). Studies on the axon membrane. I. A new method. *J Cell Comp Physiol* 34, 351–382.

Maruyama, T., Kanaji, T., Nakade, S., Kanno, T., and Mikoshiba, K. (1997). 2APB, 2-aminoethoxydiphenyl borate, a membrane-penetrable modulator of Ins(1,4,5)P_3-induced Ca^{2+} release. *J Biochem* 122, 498–505.

Matthews, E. A. and Dietrich, D. (2015). Buffer mobility and the regulation of neuronal calcium domains. *Front Cell Neurosci* 9, 48.

Matthews, E. A., Schoch, S., and Dietrich, D. (2013). Tuning local calcium availability: cell-type-specific immobile calcium buffer capacity in hippocampal neurons. *J Neurosci* 33, 14431–45.

Matveev, V., Sherman, A., and Zucker, R. S. (2002). New and corrected simulations of synaptic facilitation. *Biophys J* 83, 1368–73.

Maughan, D. W. and Godt, R. E. (1999). Parvalbumin concentration and diffusion coefficient in frog myoplasm. *J Muscle Res Cell Motil* 20, 199–209.

Maximov, A. and Sudhof, T. C. (2005). Autonomous function of synaptotagmin 1 in triggering synchronous release independent of asynchronous release. *Neuron* 48, 547–54.

Mayer, M. L. (2005). Glutamate receptor ion channels. *Curr Opin Neurobiol* 15, 282–8.

Mayer, M. L., Westbrook, G. L., and Guthrie, P. B. (1984). Voltage-dependent block by Mg^{2+} of NMDA responses in spinal cord neurones. *Nature* 309, 261–3.

McGuigan, J. A., Kay, J. W., and Elder, H. Y. (2006). Critical review of the methods used to measure the apparent dissociation constant and ligand purity in Ca^{2+} and Mg^{2+} buffer solutions. *Prog Biophys Mol Biol* 92, 333–70.

McGuigan, J. A., Kay, J. W., and Elder, H. Y. (2014). An improvement to the ligand optimisation method (LOM) for measuring the apparent dissociation constant and ligand purity in Ca^{2+} and Mg^{2+} buffer solutions. *Prog Biophys Mol Biol* 116, 203–11.

McGuigan, J. A., Kay, J. W., Elder, H. Y., and Luthi, D. (2007). Comparison between measured and calculated ionised concentrations in Mg^{2+} /ATP, Mg^{2+} /EDTA and Ca^{2+} /EGTA buffers; influence of changes in temperature, pH and pipetting errors on the ionised concentrations. *Magnes Res* 20, 72–81.

McGuigan, J. A., Luthi, D., and Buri, A. (1991). Calcium buffer solutions and how to make them: a do it yourself guide. *Can J Physiol Pharmacol* 69, 1733–49.

McGuigan, J. A. and Stumpff, F. (2013). Calculated and measured [Ca^{2+}] in buffers used to calibrate Ca^{2+} macroelectrodes. *Anal Biochem* 436, 29–35.

McGuigan, J. A. S., Kay, J. W., and Elder, H. Y. (2017). Ionised concentrations in calcium and magnesium buffers: Standards and precise measurement are mandatory. *Prog Biophys Mol Biol* 126, 48–64.

McKinney, R. A., Capogna, M., Durr, R., Gahwiler, B. H., and Thompson, S. M. (1999). Miniature synaptic events maintain dendritic spines via AMPA receptor activation. *Nat Neurosci* 2, 44–9.

McPherson, P. S., Kim, Y. K., Valdivia, H., Knudson, C. M., Takekura, H., Franzini-Armstrong, C., Coronado, R., and Campbell, K. P. (1991). The brain ryanodine receptor: a caffeine-sensitive calcium release channel. *Neuron* 7, 17–25.

Medine, C. N., Rickman, C., Chamberlain, L. H., and Duncan, R. R. (2007). Munc18-1 prevents the formation of ectopic SNARE complexes in living cells. *J Cell Sci* 120, 4407–15.

Meinrenken, C. J., Borst, J. G., and Sakmann, B. (2002). Calcium secretion coupling at calyx of Held governed by nonuniform channel-vesicle topography. *J Neurosci* 22, 1648–67.

Meissner, G. (1986). Ryanodine activation and inhibition of the Ca^{2+} release channel of sarcoplasmic reticulum. *J Biol Chem* 261, 6300–6.

Mejia-Alvarez, R., Kettlun, C., Rios, E., Stern, M., and Fill, M. (1999). Unitary Ca^{2+} current through cardiac ryanodine receptor channels under quasi-physiological ionic conditions. *J Gen Physiol* 113, 177–86.

Melamed-Book, N., Kachalsky, S. G., Kaiserman, I., and Rahamimoff, R. (1999). Neuronal calcium sparks and intracellular calcium "noise". *Proc Natl Acad Sci U S A* 96, 15217–21.

Millan, C., Castro, E., Torres, M., Shigemoto, R., and Sanchez-Prieto, J. (2003). Co-expression of metabotropic glutamate receptor 7 and N-type Ca^{2+} channels in single cerebrocortical nerve terminals of adult rats. *J Biol Chem* 278, 23955–62.

Miller, D. J. and Smith, G. L. (1984). EGTA purity and the buffering of calcium ions in physiological solutions. *Am J Physiol* 246, C160–6.

Minelli, A., Castaldo, P., Gobbi, P., Salucci, S., Magi, S., and Amoroso, S. (2007). Cellular and subcellular localization of Na^+-Ca^{2+} exchanger protein isoforms, NCX1, NCX2, and NCX3 in cerebral cortex and hippocampus of adult rat. *Cell Calcium* 41, 221–34.

Minta, A., Kao, J. P., and Tsien, R. Y. (1989). Fluorescent indicators for cytosolic calcium based on rhodamine and fluorescein chromophores. *J Biol Chem* 264, 8171–8.

Missiaen, L., Callewaert, G., De Smedt, H., and Parys, J. B. (2001). 2-Aminoethoxydiphenyl borate affects the inositol 1,4,5-trisphosphate receptor, the intracellular Ca^{2+} pump and the non-specific Ca^{2+} leak from the non-mitochondrial Ca^{2+} stores in permeabilized A7r5 cells. *Cell Calcium* 29, 111–6.

Misura, K. M., Scheller, R. H., and Weis, W. I. (2000). Three-dimensional structure of the neuronal-Sec1-syntaxin 1a complex. *Nature* 404, 355–62.

Miyawaki, A., Llopis, J., Heim, R., McCaffery, J. M., Adams, J. A., Ikura, M., and Tsien, R. Y. (1997). Fluorescent indicators for Ca^{2+} based on green fluorescent proteins and calmodulin. *Nature* 388, 882–7.

Miyazaki, K. and Ross, W. N. (2013). Ca^{2+} sparks and puffs are generated and interact in rat hippocampal CA1 pyramidal neuron dendrites. *J Neurosci* 33, 17777–88.

Mochida, S., Sheng, Z. H., Baker, C., Kobayashi, H., and Catterall, W. A. (1996). Inhibition of neurotransmission by peptides containing the synaptic protein interaction site of N-type Ca^{2+} channels. *Neuron* 17, 781–8.

Montero, M., Brini, M., Marsault, R., Alvarez, J., Sitia, R., Pozzan, T., and Rizzuto, R. (1995). Monitoring dynamic changes in free Ca^{2+} concentration in the endoplasmic reticulum of intact cells. *EMBO J* 14, 5467–75.

Morisset, S., Rouleau, A., Ligneau, X., Gbahou, F., Tardivel-Lacombe, J., Stark, H., Schunack, W., Ganellin, C. R., Schwartz, J. C., and Arrang, J. M. (2000). High constitutive activity of native H3 receptors regulates histamine neurons in brain. *Nature* 408, 860–4.

Motulsky, H. and Christopoulos, A. (2004). *Fitting models to biological data using linear and non-linear regression: A practical guide to curve fitting.* Oxford University Press, New York, USA.

Mulkey, R. M. and Zucker, R. S. (1992). Posttetanic potentiation at the crayfish neuromuscular junction is dependent on both intracellular calcium and sodium ion accumulation. *J Neurosci* 12, 4327–36.

Muller, A., Kukley, M., Stausberg, P., Beck, H., Muller, W., and Dietrich, D. (2005). Endogenous Ca^{2+} buffer concentration and Ca^{2+} microdomains in hippocampal neurons. *J Neurosci* 25, 558–65.

Muller, M., Felmy, F., and Schneggenburger, R. (2008). A limited contribution of Ca^{2+} current facilitation to paired-pulse facilitation of transmitter release at the rat calyx of Held. *J Physiol* 586, 5503–20.

Muller, M., Felmy, F., Schwaller, B., and Schneggenburger, R. (2007). Parvalbumin is a mobile presynaptic Ca^{2+} buffer in the calyx of Held that accelerates the decay of Ca^{2+} and short-term facilitation. *J Neurosci* 27, 2261–71.

Murthy, V. N. and Stevens, C. F. (1999). Reversal of synaptic vesicle docking at central synapses. *Nat Neurosci* 2, 503–7.

Nagai, T., Sawano, A., Park, E. S., and Miyawaki, A. (2001). Circularly permuted green fluorescent proteins engineered to sense Ca^{2+}. *Proc Natl Acad Sci U S A* 98, 3197–202.

Nagerl, U. V., Novo, D., Mody, I., and Vergara, J. L. (2000). Binding kinetics of calbindin-D(28k) determined by flash photolysis of caged Ca^{2+}. *Biophys J* 79, 3009–18.

Nagy, G., Kim, J. H., Pang, Z. P., Matti, U., Rettig, J., Sudhof, T. C., and Sorensen, J. B. (2006). Different effects on fast exocytosis induced by synaptotagmin 1 and 2 isoforms and abundance but not by phosphorylation. *J Neurosci* 26, 632–43.

Nakamura, Y., Harada, H., Kamasawa, N., Matsui, K., Rothman, J. S., Shigemoto, R., Silver, R. A., DiGregorio, D. A., and Takahashi, T. (2015). Nanoscale distribution of presynaptic Ca^{2+} channels and its impact on vesicular release during development. *Neuron* 85, 145–58.

Naraghi, M. (1997). T-jump study of calcium binding kinetics of calcium chelators. *Cell Calcium* 22, 255–68.

Naraghi, M. and Neher, E. (1997). Linearized buffered Ca^{2+} diffusion in microdomains and its implications for calculation of $[Ca^{2+}]$ at the mouth of a calcium channel. *J Neurosci* 17, 6961–73.

Neher, E. (1995). The use of fura-2 for estimating Ca buffers and Ca fluxes. *Neuropharmacology* 34, 1423–42.

Neher, E. (1998). Usefulness and limitations of linear approximations to the understanding of Ca^{2+} signals. *Cell Calcium* 24, 345–57.

Neher, E. (2013). Quantitative aspects of calcium fluorimetry. *Cold Spring Harb Protoc* 2013, 918–24.

Neher, E. and Augustine, G. J. (1992). Calcium gradients and buffers in bovine chromaffin cells. *J Physiol* 450, 273–301.

Neher, E. and Marty, A. (1982). Discrete changes of cell membrane capacitance observed under conditions of enhanced secretion in bovine adrenal chromaffin cells. *Proc Natl Acad Sci U S A* 79, 6712–6.

Neher, E. and Sakaba, T. (2008). Multiple roles of calcium ions in the regulation of neurotransmitter release. *Neuron* 59, 861–72.

Neher, E. and Taschenberger, H. (2013). Transients in global Ca^{2+} concentration induced by electrical activity in a giant nerve terminal. *J Physiol* 591, 3189–95.

Nicoll, R. A. (2017). A Brief History of Long-Term Potentiation. *Neuron* 93, 281–290.

Niki, I., Yokokura, H., Sudo, T., Kato, M., and Hidaka, H. (1996). Ca^{2+} signaling and intracellular Ca^{2+} binding proteins. *J Biochem* 120, 685–98.

Niswender, C. M. and Conn, P. J. (2010). Metabotropic glutamate receptors: physiology, pharmacology, and disease. *Annu Rev Pharmacol Toxicol* 50, 295–322.

Noguchi, J., Matsuzaki, M., Ellis-Davies, G. C., and Kasai, H. (2005). Spine-neck geometry determines NMDA receptor-dependent Ca^{2+} signaling in dendrites. *Neuron* 46, 609–22.

Novak, P., Gorelik, J., Vivekananda, U., Shevchuk, A. I., Ermolyuk, Y. S., Bailey, R. J., Bushby, A. J., Moss, G. W., Rusakov, D. A., Klenerman, D., Kullmann, D. M., Volynski, K. E., and Korchev, Y. E. (2013). Nanoscale-targeted patch-clamp recordings of functional presynaptic ion channels. *Neuron* 79, 1067–77.

Nowak, L., Bregestovski, P., Ascher, P., Herbet, A., and Prochiantz, A. (1984). Magnesium gates glutamate-activated channels in mouse central neurones. *Nature* 307, 462–5.

Nowycky, M. C., Fox, A. P., and Tsien, R. W. (1985). Three types of neuronal calcium channel with different calcium agonist sensitivity. *Nature* 316, 440–3.

Ohana, O. and Sakmann, B. (1998). Transmitter release modulation in nerve terminals of rat neocortical pyramidal cells by intracellular calcium buffers. *J Physiol* 513 (Pt 1), 135–48.

Oheim, M. (1995). *Methodische voraussetzungen zur untersuchung der calcium diffusion und calcium pufferung im cytosol lebender chromaffinzellen*. Thesis.

Olinger, E., Schwaller, B., Loffing, J., Gailly, P., and Devuyst, O. (2012). Parvalbumin: calcium and magnesium buffering in the distal nephron. *Nephrol Dial Transplant* 27, 3988–94.

O'Malley, D. M., Burbach, B. J., and Adams, P. R. (1999). Fluorescent calcium indicators: subcellular behavior and use in confocal imaging. *Methods Mol Biol* 122, 261–303.

Otis, T. S., Staley, K. J., and Mody, I. (1991). Perpetual inhibitory activity in mammalian brain slices generated by spontaneous GABA release. *Brain Res* 545, 142–50.

Otsu, Y., Shahrezaei, V., Li, B., Raymond, L. A., Delaney, K. R., and Murphy, T. H. (2004). Competition between phasic and asynchronous release for recovered synaptic vesicles at developing hippocampal autaptic synapses. *J Neurosci* 24, 420–33.

Oxenoid, K., Dong, Y., Cao, C., Cui, T., Sancak, Y., Markhard, A. L., Grabarek, Z., Kong, L., Liu, Z., Ouyang, B., Cong, Y., Mootha, V. K., and Chou, J. J. (2016). Architecture of the mitochondrial calcium uniporter. *Nature* 533, 269–73.

Padua, R. A., Nagy, J. I., and Geiger, J. D. (1996). Subcellular localization of ryanodine receptors in rat brain. *Eur J Pharmacol* 298, 185–9.

Palade, P. (1987). Drug-induced Ca^{2+} release from isolated sarcoplasmic reticulum. I. Use of pyrophosphate to study caffeine-induced Ca^{2+} release. *J Biol Chem* 262, 6135–41.

Palay, S. L. (1956). Synapses in the central nervous system. *J Biophys Biochem Cytol* 2, 193–202.

Palmer, A. E., Jin, C., Reed, J. C., and Tsien, R. Y. (2004). Bcl-2-mediated alterations in endoplasmic reticulum Ca^{2+} analyzed with an improved genetically encoded fluorescent sensor. *Proc Natl Acad Sci U S A* 101, 17404–9.

Palmer, L. M. and Stuart, G. J. (2006). Site of action potential initiation in layer 5 pyramidal neurons. *J Neurosci* 26, 1854–63.

Pang, Z. P., Shin, O. H., Meyer, A. C., Rosenmund, C., and Sudhof, T. C. (2006). A gain-of-function mutation in synaptotagmin-1 reveals a critical role of Ca^{2+}-dependent soluble N-ethylmaleimide-sensitive factor attachment protein receptor complex binding in synaptic exocytosis. *J Neurosci* 26, 12556–65.

Parker, I. and Wier, W. G. (1997). Variability in frequency and characteristics of Ca^{2+} sparks at different release sites in rat ventricular myocytes. *J Physiol* 505 (Pt 2), 337–44.

Patton, C., Thompson, S., and Epel, D. (2004). Some precautions in using chelators to buffer metals in biological solutions. *Cell Calcium* 35, 427–31.

Pelled, D., Lloyd-Evans, E., Riebeling, C., Jeyakumar, M., Platt, F. M., and Futerman, A. H. (2003). Inhibition of calcium uptake via the sarco/endoplasmic reticulum Ca^{2+}-ATPase in a mouse model of Sandhoff disease and prevention by treatment with N-butyldeoxynojirimycin. *J Biol Chem* 278, 29496–501.

Pereda, A. E. (2014). Electrical synapses and their functional interactions with chemical synapses. *Nat Rev Neurosci* 15, 250–263.

Perin, M. S., Fried, V. A., Mignery, G. A., Jahn, R., and Sudhof, T. C. (1990). Phospholipid binding by a synaptic vesicle protein homologous to the regulatory region of protein kinase C. *Nature* 345, 260–3.

Perocchi, F., Gohil, V. M., Girgis, H. S., Bao, X. R., McCombs, J. E., Palmer, A. E., and Mootha, V. K. (2010). MICU1 encodes a mitochondrial EF hand protein required for Ca^{2+} uptake. *Nature* 467, 291–6.

Plovanich, M., Bogorad, R. L., Sancak, Y., Kamer, K. J., Strittmatter, L., Li, A. A., Girgis, H. S., Kuchimanchi, S., De Groot, J., Speciner, L., Taneja, N., Oshea, J., Koteliansky, V., and Mootha, V. K. (2013). MICU2, a paralog of MICU1, resides within the mitochondrial uniporter complex to regulate calcium handling. *PLoS One* 8, e55785.

Pohle, J. and Bischofberger, J. (2014). Supralinear dendritic Ca^{2+} signalling in young developing CA1 pyramidal cells. *J Physiol* 592, 4931–49.

Porta, M., Zima, A. V., Nani, A., Diaz-Sylvester, P. L., Copello, J. A., Ramos-Franco, J., Blatter, L. A., and Fill, M. (2011). Single ryanodine receptor channel basis of caffeine's action on Ca^{2+} sparks. *Biophys J* 100, 931–8.

Preiano, B. S., Guerini, D., and Carafoli, E. (1996). Expression and functional characterization of isoforms 4 of the plasma membrane calcium pump. *Biochemistry* 35, 7946–53.

Pumplin, D. W., Reese, T. S., and Llinas, R. (1981). Are the presynaptic membrane particles the calcium channels? *Proc Natl Acad Sci U S A* 78, 7210–3.

Raffaello, A., De Stefani, D., Sabbadin, D., Teardo, E., Merli, G., Picard, A., Checchetto, V., Moro, S., Szabo, I., and Rizzuto, R. (2013). The mitochondrial calcium uniporter is a multimer that can include a dominant-negative pore-forming subunit. *EMBO J* 32, 2362–76.

Raingo, J., Khvotchev, M., Liu, P., Darios, F., Li, Y. C., Ramirez, D. M., Adachi, M., Lemieux, P., Toth, K., Davletov, B., and Kavalali, E. T. (2012). VAMP4 directs synaptic vesicles to a pool that selectively maintains asynchronous neurotransmission. *Nat Neurosci* 15, 738–45.

Raymond, C. R. and Redman, S. J. (2002). Different calcium sources are narrowly tuned to the induction of different forms of LTP. *J Neurophysiol* 88, 249–55.

Reese, A. L. and Kavalali, E. T. (2015). Spontaneous neurotransmission signals through store-driven Ca^{2+} transients to maintain synaptic homeostasis. *Elife* 4.

Regehr, W. G. (1997). Interplay between sodium and calcium dynamics in granule cell presynaptic terminals. *Biophys J* 73, 2476–88.

Regehr, W. G. (2012). Short-term presynaptic plasticity. *Cold Spring Harb Perspect Biol* 4, a005702.

Regehr, W. G., Delaney, K. R., and Tank, D. W. (1994). The role of presynaptic calcium in short-term enhancement at the hippocampal mossy fiber synapse. *J Neurosci* 14, 523–37.

Rettig, J., Heinemann, C., Ashery, U., Sheng, Z. H., Yokoyama, C. T., Catterall, W. A., and Neher, E. (1997). Alteration of Ca^{2+} dependence of neurotransmitter release by disruption of Ca^{2+} channel/syntaxin interaction. *J Neurosci* 17, 6647–56.

Rettig, J., Sheng, Z. H., Kim, D. K., Hodson, C. D., Snutch, T. P., and Catterall, W. A. (1996). Isoform-specific interaction of the alpha1a subunits of brain Ca^{2+} channels with the presynaptic proteins syntaxin and SNAP-25. *Proc Natl Acad Sci U S A* 93, 7363–8.

Rickman, C., Medine, C. N., Bergmann, A., and Duncan, R. R. (2007). Functionally and spatially distinct modes of munc18-syntaxin 1 interaction. *J Biol Chem* 282, 12097–103.

Rizzoli, S. O. and Betz, W. J. (2005). Synaptic vesicle pools. *Nat Rev Neurosci* 6, 57–69.

Robertson, J. D. (1956). The ultrastructure of a reptilian myoneural junction. *J Biophys Biochem Cytol* 2, 381–94.

Rodkey, T. L., Liu, S., Barry, M., and McNew, J. A. (2008). Munc18a scaffolds SNARE assembly to promote membrane fusion. *Mol Biol Cell* 19, 5422–34.

Romand, S., Wang, Y., Toledo-Rodriguez, M., and Markram, H. (2011). Morphological development of thick-tufted layer V pyramidal cells in the rat somatosensory cortex. *Front Neuroanat* 5, 5.

Roome, C. J., Power, E. M., and Empson, R. M. (2013). Transient reversal of the sodium/calcium exchanger boosts presynaptic calcium and synaptic transmission at a cerebellar synapse. *J Neurophysiol* 109, 1669–80.

Rossi, B., Maton, G., and Collin, T. (2008). Calcium-permeable presynaptic AMPA receptors in cerebellar molecular layer interneurones. *J Physiol* 586, 5129–45.

Rossi, B., Ogden, D., Llano, I., Tan, Y. P., Marty, A., and Collin, T. (2012). Current and calcium responses to local activation of axonal NMDA receptors in developing cerebellar molecular layer interneurons. *PLoS One* 7, e39983.

Rousseau, E., Ladine, J., Liu, Q. Y., and Meissner, G. (1988). Activation of the Ca^{2+} release channel of skeletal muscle sarcoplasmic reticulum by caffeine and related compounds. *Arch Biochem Biophys* 267, 75–86.

Rozov, A., Burnashev, N., Sakmann, B., and Neher, E. (2001). Transmitter release modulation by intracellular Ca^{2+} buffers in facilitating and depressing nerve terminals of pyramidal cells in layer 2/3 of the rat neocortex indicates a target cell-specific difference in presynaptic calcium dynamics. *J Physiol* 531, 807–26.

Rusakov, D. A. and Kullmann, D. M. (1998). Extrasynaptic glutamate diffusion in the hippocampus: ultrastructural constraints, uptake, and receptor activation. *J Neurosci* 18, 3158–70.

Sabatini, B. L., Oertner, T. G., and Svoboda, K. (2002). The life cycle of Ca^{2+} ions in dendritic spines. *Neuron* 33, 439–52.

Sah, P., Hestrin, S., and Nicoll, R. A. (1989). Tonic activation of NMDA receptors by ambient glutamate enhances excitability of neurons. *Science* 246, 815–8.

Sakaba, T. (2008). Two Ca^{2+}-dependent steps controlling synaptic vesicle fusion and replenishment at the cerebellar basket cell terminal. *Neuron* 57, 406–19.

Sakaba, T. and Neher, E. (2001). Calmodulin mediates rapid recruitment of fast-releasing synaptic vesicles at a calyx-type synapse. *Neuron* 32, 1119–31.

Sala, F. and Hernandez-Cruz, A. (1990). Calcium diffusion modeling in a spherical neuron. Relevance of buffering properties. *Biophys J* 57, 313–24.

Salin, P., Tseng, G. F., Hoffman, S., Parada, I., and Prince, D. A. (1995). Axonal sprouting in layer V pyramidal neurons of chronically injured cerebral cortex. *J Neurosci* 15, 8234–45.

Sancak, Y., Markhard, A. L., Kitami, T., Kovacs-Bogdan, E., Kamer, K. J., Udeshi, N. D., Carr, S. A., Chaudhuri, D., Clapham, D. E., Li, A. A., Calvo, S. E., Goldberger, O., and Mootha, V. K. (2013). EMRE is an essential component of the mitochondrial calcium uniporter complex. *Science* 342, 1379–82.

Sanchez, G., Hidalgo, C., and Donoso, P. (2003). Kinetic studies of calcium-induced calcium release in cardiac sarcoplasmic reticulum vesicles. *Biophys J* 84, 2319–30.

Sankaranarayanan, R., Li, Y., Greensmith, D. J., Eisner, D. A., and Venetucci, L. (2016). Biphasic decay of the Ca transient results from increased sarcoplasmic reticulum Ca leak. *J Physiol* 594, 611–23.

Sara, Y., Virmani, T., Deak, F., Liu, X., and Kavalali, E. T. (2005). An isolated pool of vesicles recycles at rest and drives spontaneous neurotransmission. *Neuron* 45, 563–73.

Saviane, C. and Silver, R. A. (2006). Fast vesicle reloading and a large pool sustain high bandwidth transmission at a central synapse. *Nature* 439, 983–7.

Scheuss, V., Yasuda, R., Sobczyk, A., and Svoboda, K. (2006). Nonlinear $[Ca^{2+}]$ signaling in dendrites and spines caused by activity-dependent depression of Ca^{2+} extrusion. *J Neurosci* 26, 8183–94.

Schmidt, H., Arendt, O., Brown, E. B., Schwaller, B., and Eilers, J. (2007). Parvalbumin is freely mobile in axons, somata and nuclei of cerebellar Purkinje neurones. *J Neurochem* 100, 727–35.

Schmidt, H., Brown, E. B., Schwaller, B., and Eilers, J. (2003). Diffusional mobility of parvalbumin in spiny dendrites of cerebellar Purkinje neurons quantified by fluorescence recovery after photobleaching. *Biophys J* 84, 2599–608.

Schmidt, H., Schwaller, B., and Eilers, J. (2005). Calbindin D28k targets myo-inositol monophosphatase in spines and dendrites of cerebellar Purkinje neurons. *Proc Natl Acad Sci U S A* 102, 5850–5.

Schneggenburger, R. and Neher, E. (2000). Intracellular calcium dependence of transmitter release rates at a fast central synapse. *Nature* 406, 889–93.

Schneggenburger, R. and Neher, E. (2005). Presynaptic calcium and control of vesicle fusion. *Curr Opin Neurobiol* 15, 266–74.

Schneggenburger, R. and Rosenmund, C. (2015). Molecular mechanisms governing Ca^{2+} regulation of evoked and spontaneous release. *Nat Neurosci* 18, 935–41.

Schnetkamp, P. P. (1995). Calcium homeostasis in vertebrate retinal rod outer segments. *Cell Calcium* 18, 322–30.

Schonn, J. S., Maximov, A., Lao, Y., Sudhof, T. C., and Sorensen, J. B. (2008). Synaptotagmin-1 and -7 are functionally overlapping Ca^{2+} sensors for exocytosis in adrenal chromaffin cells. *Proc Natl Acad Sci U S A* 105, 3998–4003.

Schousboe, A., Bak, L. K., and Waagepetersen, H. S. (2013). Astrocytic control of biosynthesis and turnover of the neurotransmitters glutamate and GABA. *Front Endocrinol (Lausanne)* 4, 102.

Schubert, D., Kotter, R., Luhmann, H. J., and Staiger, J. F. (2006). Morphology, electrophysiology and functional input connectivity of pyramidal neurons characterizes a genuine layer Va in the primary somatosensory cortex. *Cereb Cortex* 16, 223–36.

Schwaller, B. (2010). Cytosolic Ca^{2+} buffers. *Cold Spring Harb Perspect Biol* 2, a004051.

Schwaller, B., Meyer, M., and Schiffmann, S. (2002). 'New' functions for 'old' proteins: the role of the calcium-binding proteins calbindin D-28k, calretinin and parvalbumin, in cerebellar physiology. Studies with knockout mice. *Cerebellum* 1, 241–58.

Scimemi, A. and Diamond, J. S. (2012). The number and organization of Ca^{2+} channels in the active zone shapes neurotransmitter release from Schaffer collateral synapses. *J Neurosci* 32, 18157–76.

Scott, R., Lalic, T., Kullmann, D. M., Capogna, M., and Rusakov, D. A. (2008). Target-cell specificity of kainate autoreceptor and Ca^{2+}-store-dependent short-term plasticity at hippocampal mossy fiber synapses. *J Neurosci* 28, 13139–49.

Scott, R. and Rusakov, D. A. (2006). Main determinants of presynaptic Ca^{2+} dynamics at individual mossy fiber-CA3 pyramidal cell synapses. *J Neurosci* 26, 7071–81.

Seidler, N. W., Jona, I., Vegh, M., and Martonosi, A. (1989). Cyclopiazonic acid is a specific inhibitor of the Ca^{2+}-ATPase of sarcoplasmic reticulum. *J Biol Chem* 264, 17816–23.

Sharp, A. H., McPherson, P. S., Dawson, T. M., Aoki, C., Campbell, K. P., and Snyder, S. H. (1993). Differential immunohistochemical localization of inositol 1,4,5-trisphosphate- and ryanodine-sensitive Ca^{2+} release channels in rat brain. *J Neurosci* 13, 3051–63.

Shen, J., Tareste, D. C., Paumet, F., Rothman, J. E., and Melia, T. J. (2007). Selective activation of cognate SNAREpins by Sec1/Munc18 proteins. *Cell* 128, 183–95.

Sheng, Z. H., Rettig, J., Takahashi, M., and Catterall, W. A. (1994). Identification of a syntaxin-binding site on N-type calcium channels. *Neuron* 13, 1303–13.

Sheng, Z. H., Yokoyama, C. T., and Catterall, W. A. (1997). Interaction of the synprint site of N-type Ca^{2+} channels with the C2b domain of synaptotagmin I. *Proc Natl Acad Sci U S A* 94, 5405–10.

Shilling, D., Mak, D. O., Kang, D. E., and Foskett, J. K. (2012). Lack of evidence for presenilins as endoplasmic reticulum Ca^{2+} leak channels. *J Biol Chem* 287, 10933–44.

Shleper, M., Kartvelishvily, E., and Wolosker, H. (2005). D-serine is the dominant endogenous coagonist for NMDA receptor neurotoxicity in organotypic hippocampal slices. *J Neurosci* 25, 9413–7.

Shoshan-Barmatz, V., De Pinto, V., Zweckstetter, M., Raviv, Z., Keinan, N., and Arbel, N. (2010). VDAC, a multi-functional mitochondrial protein regulating cell life and death. *Mol Aspects Med* 31, 227–85.

Simkus, C. R. and Stricker, C. (2002a). The contribution of intracellular calcium stores to mEPSCs recorded in layer II neurones of rat barrel cortex. *J Physiol* 545, 521–35.

Simkus, C. R. and Stricker, C. (2002b). Properties of mEPSCs recorded in layer II neurones of rat barrel cortex. *J Physiol* 545, 509–20.

Simon, S. M. and Llinas, R. R. (1985). Compartmentalization of the submembrane calcium activity during calcium influx and its significance in transmitter release. *Biophys J* 48, 485–98.

Snapp, E. L. (2013). Photobleaching methods to study Golgi complex dynamics in living cells. *Methods Cell Biol* 118, 195–216.

Snedecor, G. and Cochran, W. (1989). *Statistical Methods*. Iowa State University Press, Iowa, USA eighth edn.

Soler, F., Plenge-Tellechea, F., Fortea, I., and Fernandez-Belda, F. (1998). Cyclopiazonic acid effect on Ca^{2+}-dependent conformational states of the sarcoplasmic reticulum ATPase. Implication for the enzyme turnover. *Biochemistry* 37, 4266–74.

Stauffer, T. P., Guerini, D., and Carafoli, E. (1995). Tissue distribution of the four gene products of the plasma membrane Ca^{2+} pump. A study using specific antibodies. *J Biol Chem* 270, 12184–90.

Stein, A., Weber, G., Wahl, M. C., and Jahn, R. (2009). Helical extension of the neuronal SNARE complex into the membrane. *Nature* 460, 525–8.

Stocca, G., Schmidt-Hieber, C., and Bischofberger, J. (2008). Differential dendritic Ca^{2+} signalling in young and mature hippocampal granule cells. *J Physiol* 586, 3795–811.

Strehler, E. E. and Zacharias, D. A. (2001). Role of alternative splicing in generating isoform diversity among plasma membrane calcium pumps. *Physiol Rev* 81, 21–50.

Stuart, G. J., Dodt, H. U., and Sakmann, B. (1993). Patch-clamp recordings from the soma and dendrites of neurons in brain slices using infrared video microscopy. *Pflugers Arch* 423, 511–8.

Stuenkel, E. L. (1994). Regulation of intracellular calcium and calcium buffering properties of rat isolated neurohypophysial nerve endings. *J Physiol* 481 (Pt 2), 251–71.

Stumpff, F. and McGuigan, J. A. (2014). Measuring Ca^{2+} binding to short chain fatty acids and gluconate with a Ca^{2+} electrode: role of the reference electrode. *Anal Biochem* 459, 46–52.

Sudhof, T. C. (1995). The synaptic vesicle cycle: a cascade of protein-protein interactions. *Nature* 375, 645–53.

Sudhof, T. C. (2013). Neurotransmitter release: the last millisecond in the life of a synaptic vesicle. *Neuron* 80, 675–90.

Sudhof, T. C. (2014). The molecular machinery of neurotransmitter release (Nobel lecture). *Angew Chem Int Ed Engl* 53, 12696–717.

Sugita, S., Han, W., Butz, S., Liu, X., Fernandez-Chacon, R., Lao, Y., and Sudhof, T. C. (2001). Synaptotagmin VII as a plasma membrane Ca^{2+} sensor in exocytosis. *Neuron* 30, 459–73.

Sullivan, J. M. (2007). A simple depletion model of the readily releasable pool of synaptic vesicles cannot account for paired-pulse depression. *J Neurophysiol* 97, 948–50.

Sun, J., Pang, Z. P., Qin, D., Fahim, A. T., Adachi, R., and Sudhof, T. C. (2007). A dual-Ca^{2+}-sensor model for neurotransmitter release in a central synapse. *Nature* 450, 676–82.

Sun, J. Y. and Wu, L. G. (2001). Fast kinetics of exocytosis revealed by simultaneous measurements of presynaptic capacitance and postsynaptic currents at a central synapse. *Neuron* 30, 171–82.

Sutton, M. A., Ito, H. T., Cressy, P., Kempf, C., Woo, J. C., and Schuman, E. M. (2006). Miniature neurotransmission stabilizes synaptic function via tonic suppression of local dendritic protein synthesis. *Cell* 125, 785–99.

Sutton, M. A., Wall, N. R., Aakalu, G. N., and Schuman, E. M. (2004). Regulation of dendritic protein synthesis by miniature synaptic events. *Science* 304, 1979–83.

Sutton, R. B., Fasshauer, D., Jahn, R., and Brunger, A. T. (1998). Crystal structure of a SNARE complex involved in synaptic exocytosis at 2.4 A resolution. *Nature* 395, 347–53.

Tada, M., Takeuchi, A., Hashizume, M., Kitamura, K., and Kano, M. (2014). A highly sensitive fluorescent indicator dye for calcium imaging of neural activity in vitro and in vivo. *Eur J Neurosci* 39, 1720–8.

Takahashi, M., Billups, B., Rossi, D., Sarantis, M., Hamann, M., and Attwell, D. (1997). The role of glutamate transporters in glutamate homeostasis in the brain. *J Exp Biol* 200, 401–9.

Takamori, S., Holt, M., Stenius, K., Lemke, E. A., Gronborg, M., Riedel, D., Urlaub, H., Schenck, S., Brugger, B., Ringler, P., Muller, S. A., Rammner, B., Grater, F., Hub, J. S., De Groot, B. L., Mieskes, G., Moriyama, Y., Klingauf, J., Grubmuller, H., Heuser, J., Wieland, F., and Jahn, R. (2006). Molecular anatomy of a trafficking organelle. *Cell* 127, 831–46.

Tan, W. and Colombini, M. (2007). VDAC closure increases calcium ion flux. *Biochim Biophys Acta* 1768, 2510–5.

Tanaka, K., Khiroug, L., Santamaria, F., Doi, T., Ogasawara, H., Ellis-Davies, G. C., Kawato, M., and Augustine, G. J. (2007). Ca^{2+} requirements for cerebellar long-term synaptic depression: role for a postsynaptic leaky integrator. *Neuron* 54, 787–800.

Tang, A. H., Karson, M. A., Nagode, D. A., McIntosh, J. M., Uebele, V. N., Renger, J. J., Klugmann, M., Milner, T. A., and Alger, B. E. (2011). Nerve terminal nicotinic acetylcholine receptors initiate quantal GABA release from perisomatic interneurons by activating axonal T-type (Cav3) Ca^{2+} channels and Ca^{2+} release from stores. *J Neurosci* 31, 13546–61.

Tang, Y. and Zucker, R. S. (1997). Mitochondrial involvement in post-tetanic potentiation of synaptic transmission. *Neuron* 18, 483–91.

Tank, D. W., Regehr, W. G., and Delaney, K. R. (1995). A quantitative analysis of presynaptic calcium dynamics that contribute to short-term enhancement. *J Neurosci* 15, 7940–52.

Thastrup, O., Cullen, P. J., Drobak, B. K., Hanley, M. R., and Dawson, A. P. (1990). Thapsigargin, a tumor promoter, discharges intracellular Ca^{2+} stores by specific inhibition of the endoplasmic reticulum Ca^{2+}-ATPase. *Proc Natl Acad Sci U S A* 87, 2466–70.

Thomas, D., Tovey, S. C., Collins, T. J., Bootman, M. D., Berridge, M. J., and Lipp, P. (2000). A comparison of fluorescent Ca^{2+} indicator properties and their use in measuring elementary and global Ca^{2+} signals. *Cell Calcium* 28, 213–23.

Tian, L., Hires, S. A., Mao, T., Huber, D., Chiappe, M. E., Chalasani, S. H., Petreanu, L., Akerboom, J., McKinney, S. A., Schreiter, E. R., Bargmann, C. I., Jayaraman, V., Svoboda, K., and Looger, L. L. (2009). Imaging neural activity in worms, flies and mice with improved GCaMP calcium indicators. *Nat Methods* 6, 875–81.

Tripathy, A., Xu, L., Mann, G., and Meissner, G. (1995). Calmodulin activation and inhibition of skeletal muscle Ca^{2+} release channel (ryanodine receptor). *Biophys J* 69, 106–19.

Tsien, R. Y. (1980). New calcium indicators and buffers with high selectivity against magnesium and protons: design, synthesis, and properties of prototype structures. *Biochemistry* 19, 2396–404.

Tsien, R. Y. (1988). Fluorescence measurement and photochemical manipulation of cytosolic free calcium. *Trends Neurosci* 11, 419–24.

Tsien, R. Y. (1989). Fluorescent probes of cell signaling. *Annu Rev Neurosci* 12, 227–53.

Tsien, R. Y., Pozzan, T., and Rink, T. J. (1982). Calcium homeostasis in intact lymphocytes: cytoplasmic free calcium monitored with a new, intracellularly trapped fluorescent indicator. *J Cell Biol* 94, 325–34.

Tu, H., Nelson, O., Bezprozvanny, A., Wang, Z., Lee, S. F., Hao, Y. H., Serneels, L., De Strooper, B., Yu, G., and Bezprozvanny, I. (2006). Presenilins form ER Ca^{2+} leak channels, a function disrupted by familial Alzheimer's disease-linked mutations. *Cell* 126, 981–93.

Tu, H., Wang, Z., and Bezprozvanny, I. (2005). Modulation of mammalian inositol 1,4,5-trisphosphate receptor isoforms by calcium: a role of calcium sensor region. *Biophys J* 88, 1056–69.

Tyler, W. J. and Pozzo-Miller, L. (2003). Miniature synaptic transmission and BDNF modulate dendritic spine growth and form in rat CA1 neurones. *J Physiol* 553, 497–509.

van den Bogaart, G., Thutupalli, S., Risselada, J. H., Meyenberg, K., Holt, M., Riedel, D., Diederichsen, U., Herminghaus, S., Grubmuller, H., and Jahn, R. (2011). Synaptotagmin-1 may be a distance regulator acting upstream of SNARE nucleation. *Nat Struct Mol Biol* 18, 805–12.

Van der Kloot, W. (1988a). Estimating the timing of quantal releases during end-plate currents at the frog neuromuscular junction. *J Physiol* 402, 595–603.

Van der Kloot, W. (1988b). The kinetics of quantal releases during end-plate currents at the frog neuromuscular junction. *J Physiol* 402, 605–26.

Vanden Abeele, F., Bidaux, G., Gordienko, D., Beck, B., Panchin, Y. V., Baranova, A. V., Ivanov, D. V., Skryma, R., and Prevarskaya, N. (2006). Functional implications of calcium permeability of the channel formed by pannexin 1. *J Cell Biol* 174, 535–46.

Verhage, M. and Sorensen, J. B. (2008). Vesicle docking in regulated exocytosis. *Traffic* 9, 1414–24.

Verkhratsky, A. (2005). Physiology and pathophysiology of the calcium store in the endoplasmic reticulum of neurons. *Physiol Rev* 85, 201–79.

Vincenzi, F. F., Hinds, T. R., and Raess, B. U. (1980). Calmodulin and the plasma membrane calcium pump. *Ann N Y Acad Sci* 356, 232–44.

Vites, A. M. and Pappano, A. J. (1992). Ruthenium red selectively prevents Ins(1,4,5)P_3-but not caffeine-gated calcium release in avian atrium. *Am J Physiol* 262, H268–77.

Voets, T., Nilius, B., Hoefs, S., van der Kemp, A. W., Droogmans, G., Bindels, R. J., and Hoenderop, J. G. (2004). TRPM6 forms the Mg^{2+} influx channel involved in intestinal and renal Mg^{2+} absorption. *J Biol Chem* 279, 19–25.

von Waldeyer-Hartz, H. W. G. (1891). Ueber einige neuere forschungen im gebiete der anatomie des central nerven systems. *Dtsch med Wochenschr* 17, 1213–1356.

Vyleta, N. P. and Jonas, P. (2014). Loose coupling between Ca^{2+} channels and release sensors at a plastic hippocampal synapse. *Science* 343, 665–70.

Wadel, K., Neher, E., and Sakaba, T. (2007). The coupling between synaptic vesicles and Ca^{2+} channels determines fast neurotransmitter release. *Neuron* 53, 563–75.

Wagenknecht, T., Grassucci, R., Frank, J., Saito, A., Inui, M., and Fleischer, S. (1989). Three-dimensional architecture of the calcium channel/foot structure of sarcoplasmic reticulum. *Nature* 338, 167–70.

Wang, L. Y. and Augustine, G. J. (2014). Presynaptic nanodomains: a tale of two synapses. *Front Cell Neurosci* 8, 455.

Wang, L. Y. and Kaczmarek, L. K. (1998). High-frequency firing helps replenish the readily releasable pool of synaptic vesicles. *Nature* 394, 384–8.

Wang, L. Y., Neher, E., and Taschenberger, H. (2008). Synaptic vesicles in mature calyx of Held synapses sense higher nanodomain calcium concentrations during action potential-evoked glutamate release. *J Neurosci* 28, 14450–8.

Wang, S. Q., Song, L. S., Lakatta, E. G., and Cheng, H. (2001). Ca^{2+} signalling between single L-type Ca^{2+} channels and ryanodine receptors in heart cells. *Nature* 410, 592–6.

Weber, T., Zemelman, B. V., McNew, J. A., Westermann, B., Gmachl, M., Parlati, F., Sollner, T. H., and Rothman, J. E. (1998). SNAREpins: minimal machinery for membrane fusion. *Cell* 92, 759–72.

Westrum, L. E. and Gray, E. G. (1986). New observations on the substructure of the active zone of brain synapses and motor endplates. *Proc R Soc Lond B Biol Sci* 229, 29–38.

Wiederhold, K. and Fasshauer, D. (2009). Is assembly of the SNARE complex enough to fuel membrane fusion? *J Biol Chem* 284, 13143–52.

Wilhelm, B. G., Groemer, T. W., and Rizzoli, S. O. (2010). The same synaptic vesicles drive active and spontaneous release. *Nat Neurosci* 13, 1454–6.

Williams, C., Chen, W., Lee, C. H., Yaeger, D., Vyleta, N. P., and Smith, S. M. (2012). Coactivation of multiple tightly coupled calcium channels triggers spontaneous release of GABA. *Nat Neurosci* 15, 1195–7.

Williams, D. A., Head, S. I., Bakker, A. J., and Stephenson, D. G. (1990). Resting calcium concentrations in isolated skeletal muscle fibres of dystrophic mice. *J Physiol* 428, 243–56.

Woehler, A., Lin, K. H., and Neher, E. (2014). Calcium-buffering effects of gluconate and nucleotides, as determined by a novel fluorimetric titration method. *J Physiol* 592, 4863–75.

Wu, K. D., Lee, W. S., Wey, J., Bungard, D., and Lytton, J. (1995). Localization and quantification of endoplasmic reticulum Ca^{2+}-ATPase isoform transcripts. *Am J Physiol* 269, C775–84.

Wu, L. G., Westenbroek, R. E., Borst, J. G., Catterall, W. A., and Sakmann, B. (1999). Calcium channel types with distinct presynaptic localization couple differentially to transmitter release in single calyx-type synapses. *J Neurosci* 19, 726–36.

Wu, X. S. and Wu, L. G. (2001). Protein kinase c increases the apparent affinity of the release machinery to Ca^{2+} by enhancing the release machinery downstream of the Ca^{2+} sensor. *J Neurosci* 21, 7928–36.

Wyllie, D. J., Behe, P., and Colquhoun, D. (1998). Single-channel activations and concentration jumps: comparison of recombinant NR1a/NR2a and NR1a/NR2d NMDA receptors. *J Physiol* 510 (Pt 1), 1–18.

Xu, J., Mashimo, T., and Sudhof, T. C. (2007). Synaptotagmin-1, -2, and -9: Ca^{2+} sensors for fast release that specify distinct presynaptic properties in subsets of neurons. *Neuron* 54, 567–81.

Xu, J., Pang, Z. P., Shin, O. H., and Sudhof, T. C. (2009). Synaptotagmin-1 functions as a Ca^{2+} sensor for spontaneous release. *Nat Neurosci* 12, 759–66.

Xu, J. and Wu, L. G. (2005). The decrease in the presynaptic calcium current is a major cause of short-term depression at a calyx-type synapse. *Neuron* 46, 633–45.

Xu, L., Mann, G., and Meissner, G. (1996). Regulation of cardiac Ca^{2+} release channel (ryanodine receptor) by Ca^{2+}, H^{+}, Mg^{2+}, and adenine nucleotides under normal and simulated ischemic conditions. *Circ Res* 79, 1100–9.

Xu, L. and Meissner, G. (1998). Regulation of cardiac muscle Ca^{2+} release channel by sarcoplasmic reticulum lumenal Ca^{2+}. *Biophys J* 75, 2302–12.

Xu, L., Tripathy, A., Pasek, D. A., and Meissner, G. (1999). Ruthenium red modifies the cardiac and skeletal muscle Ca^{2+} release channels (ryanodine receptors) by multiple mechanisms. *J Biol Chem* 274, 32680–91.

Xu, T., Naraghi, M., Kang, H., and Neher, E. (1997). Kinetic studies of Ca^{2+} binding and Ca^{2+} clearance in the cytosol of adrenal chromaffin cells. *Biophys J* 73, 532–45.

Yasuda, R., Nimchinsky, E. A., Scheuss, V., Pologruto, T. A., Oertner, T. G., Sabatini, B. L., and Svoboda, K. (2004). Imaging calcium concentration dynamics in small neuronal compartments. *Sci STKE* 2004, pl5.

Yawo, H. (1999). Protein kinase C potentiates transmitter release from the chick ciliary presynaptic terminal by increasing the exocytotic fusion probability. *J Physiol* 515 (Pt 1), 169–80.

Yoon, E. J., Gerachshenko, T., Spiegelberg, B. D., Alford, S., and Hamm, H. E. (2007). Gbetagamma interferes with Ca^{2+}-dependent binding of synaptotagmin to the soluble N-ethylmaleimide-sensitive factor attachment protein receptor (SNARE) complex. *Mol Pharmacol* 72, 1210–9.

Yu, Y., Maureira, C., Liu, X., and McCormick, D. (2010). P/Q and N channels control baseline and spike-triggered calcium levels in neocortical axons and synaptic boutons. *J Neurosci* 30, 11858–69.

Zador, A. and Koch, C. (1994). Linearized models of calcium dynamics: formal equivalence to the cable equation. *J Neurosci* 14, 4705–15.

Zengel, J. E., Magleby, K. L., Horn, J. P., McAfee, D. A., and Yarowsky, P. J. (1980). Facilitation, augmentation, and potentiation of synaptic transmission at the superior cervical ganglion of the rabbit. *J Gen Physiol* 76, 213–31.

Zhang, C., Wu, B., Beglopoulos, V., Wines-Samuelson, M., Zhang, D., Dragatsis, I., Sudhof, T. C., and Shen, J. (2009). Presenilins are essential for regulating neurotransmitter release. *Nature* 460, 632–6.

Zhang, X., Kim-Miller, M. J., Fukuda, M., Kowalchyk, J. A., and Martin, T. F. (2002). Ca^{2+}-dependent synaptotagmin binding to SNAP-25 is essential for Ca^{2+}-triggered exocytosis. *Neuron* 34, 599–611.

Zhong, N., Beaumont, V., and Zucker, R. S. (2001). Roles for mitochondrial and reverse mode Na^{+}/Ca^{2+} exchange and the plasmalemma Ca^{2+} ATPase in post-tetanic potentiation at crayfish neuromuscular junctions. *J Neurosci* 21, 9598–607.

Zhou, P., Pang, Z. P., Yang, X., Zhang, Y., Rosenmund, C., Bacaj, T., and Sudhof, T. C. (2013). Syntaxin-1 N-peptide and Habc-domain perform distinct essential functions in synaptic vesicle fusion. *EMBO J* 32, 159–71.

Zhou, Y. and Danbolt, N. C. (2013). GABA and Glutamate Transporters in Brain. *Front Endocrinol (Lausanne)* 4, 165.

Zhou, Z. and Neher, E. (1993). Mobile and immobile calcium buffers in bovine adrenal chromaffin cells. *J Physiol* 469, 245–73.

Zhu, J. J. and Connors, B. W. (1999). Intrinsic firing patterns and whisker-evoked synaptic responses of neurons in the rat barrel cortex. *J Neurophysiol* 81, 1171–83.

Zucker, R. S. and Regehr, W. G. (2002). Short-term synaptic plasticity. *Annu Rev Physiol* 64, 355–405.